Biomechanical assessment and monitoring of thermal ablation using Harmonic Motion Imaging for Focused Ultrasound (HMIFU)

Gary Yi Hou

Submitted in partial fulfillment of the

requirements for the degree

of Doctor of Philosophy

in the Graduate School of Arts and Sciences

COLUMBIA UNIVERSITY

2014

ABSTRACT

Biomechanical assessment and monitoring of thermal ablation using Harmonic Motion Imaging for Focused Ultrasound (HMIFU)

Gary Yi Hou

Cancer remains, one of the major public health problems in the United States as well as many other countries worldwide. According to According to the World Health Organization, cancer is currently the leading cause of death worldwide, accounting for 7.6 million deaths annually, and 25% of the annual death was due to Cancer during the year of 2011. In the long history of the cancer treatment field, many treatment options have been established up to date. Traditional procedures include surgical procedures as well as systemic therapies such as biologic therapy, chemotherapy, hormone therapy, and radiation therapy. Nevertheless, side-effects are often associated with such procedures due to the systemic delivery across the entire body.

Recently technologies have been focused on localized therapy under minimally or noninvasive procedure with imaging-guidance, such as cryoablation, laser ablation, radio-frequency (RF) ablation, and High Intensity F-ocused Ultrasound (HIFU). HIFU is a non-invasive procedure aims to coagulate tissue thermally at a localized focal zone created with noninvasively emitting a set of focused ultrasound beams while the surrounding healthy tissues remain relatively untreated. Harmonic Motion Imaging for Focused Ultrasound (HMIFU) is a dynamic, radiation-force-based imaging technique, which utilizes a single HIFU transducer by

emitting an Amplitude-modulated (AM) beam to both thermally ablate the tumor while inducing a stable oscillatory tissue displacement at its focal zone. The oscillatory response is then estimated by a cross-correlation based motion tracking technique on the signal collected by a confocally-aligned diagnostic transducer. HMIFU addresses the most critical aspect and one of the major unmet needs of HIFU treatment, which is the ability to perform real-time monitoring and mapping of tissue property change during the HIFU treatment.

In this dissertation, both the assessment and monitoring aspects of HMIFU have been investigated fundamentally and experimentally through development of both a 1-D and 2-D based system. The performance assessment of HMIFU technique in depicting the lesion size increase as well as the lesion-to-background displacement contrast was first demonstrated using a 3D, FE-based interdisciplinary simulation framework. Through the development of 1-D HMIFU system, a multi-parametric monitoring approach was presented where presented where the focal HMI displacement, phase shift ($\Delta\varphi$), and correlation coefficients were monitored along with thermocouple and PCD under the HIFU treatment sequence with boiling and slow denaturation. For HIFU treatments with slow denaturation, consistent displacement increase-then-decrease trend was observed, indicating tissue softening-then-stiffening and phase shift increased with treatment time in agreement with mechanical testing outcomes. The correlation coefficient remained high throughout the entire treatment time under a minimized broadband energy and boiling mechanism. Contrarily, both displacement and phase shift changes lacked consistency under HIFU treatment sequences with boiling due to the presence of strong boiling mechanism confirmed by both PCD and thermocouple monitoring. In order to facilitate its clinical translation, a fully-integrated, clinically 2D real-time HMIFU system was also developed, which is capable of providing 2D real-time streaming during HIFU treatment up to 15 Hz

without interruption. Reproducibility studies of the system showed consistent displacement estimation on tissue-mimicking phantoms as well as monitoring of tissue-softening-then-stiffening phase change across 16 out of 19 liver specimens (Increasing rate in phase shift ($\Delta\varphi$): 0.73±0.69 %/s, Decreasing rate in phase shift ($\Delta\varphi$): 0.60±0.19 %/s) along with thermocouple monitoring (Increasing: 0.84±1.15 %/ °C, Decreasing: 2.03± 0.93%/ °C) and validation of tissue stiffening using mechanical testing. In addition, the 2-D HMIFU system feasibility on preclinical pancreatic tumor mice model was also demonstrated *in vivo*, where HMI displacement decreases were observed across three of five treatment locations on the kP(f)c model at 20.8±6.84, 18.6±1.46, and 24.0±5.43%, as well as across four of the seven treatment locations on the KPC model at 39.5±2.98%, 34.5±21.5%, 16.0±3.05%, and 35.0±3.12% along with H&E histological confirmation. In order to improve the quantitative monitoring aspect of HMIFU, a novel, model-independent method for the estimating Young's modulus based on strain profile was also implemented, where 1-D HMIFU system showed feasibilities on polyacrylamide phantom ($E_{HMI}/E \approx 2.3$) and liver specimen ($E_{HMI}/E \approx 8.1$), and 2-D HMIFU system showed feasibilities on copolymer phantom($E_{HMI}/E \approx 30.4$), liver specimen($E_{HMI}/E \approx 211.3$), as well as HIFU treated liver specimen($E_{HMI,end}/E_{HMI,beginning} \approx 5.96$). In conclusion, the outcomes from the aforementioned studies successfully showed the feasibility of both HMIFU systems in multi-parametric monitoring of HIFU treatment with slow denaturation and boiling, which prepares its stage towards clinical translation.

Table of Contents

LIST OF TABLES

LIST OF FIGURES

ACKNOWLEDGMENTS

"If I have seen further it is by standing on the shoulders of giants."

- Isaac Newton, Letter to Robert Hooke, February 5, 1675

In the fall of 2008, I have started my thesis study without much research experience, none in the field of ultrasound. Therefore first and foremost, I would like to express my most sincere gratitude towards my thesis advisor Professor Elisa Konofagou for supporting my dissertation work throughout my thesis study. It has been my pleasure to be selected as a member of the Harmonic Motion Imaging Project Team in her laboratory, where I have been able to grow throughout my dissertation work both as a person and a student because of the meaningful and resourceful environment.

Secondly, I am able to complete my dissertation today because I had the fortune and pleasure to work with some of the brightest scientists and engineers I have ever known in my life. From the ways to become a good engineer to ways to become a good person, they have taught me with their priceless knowledge and shared with me their endless amount of experience that they have learned after overcoming an insurmountable amount of obstacles and challenges. I will always remember and improve myself from the values, experience, and knowledge that I have learned from them throughout my dissertation in my future life. I hereby express my most humble gratitude towards my mentors, colleagues, and collaborators throughout my dissertation work.

Lastly, I would like to thank my parents and family for their unconditional love, guidance, and encouragement throughout my dissertation work. Mother and Father, this dissertation is dedicated to you.

Chapter 1. Introduction

1.1 Cancer

Cancer has been one of the major public health problems in the United States as well as many other countries across the globe; it is the leading cause of death worldwide, accounting for 7.6 million deaths annually (World Health Organization, 2013). Approximately one in four deaths in the United States is due to cancer during the year of 2011 [1]. From the perspective of microenvironment, a tumor is defined as an uncontrolled growth of body tissue, and its type can be classified as either benign or malignant but only malignant tumors are categorized as cancer. Benign tumor types usually grow with clear boundaries and do not invade the surrounding tissue or spread out to other parts of the body; however, its presence may exert anatomical hindrance on peripheral structures such as organ, blood vessels, or nerves, when then requires surgery [2]. In comparison to benign type, malignant types are usually composed of neoplasmic cells as well as heterogeneous vasculatures at its periphery embedded with a collagen-rich matrix [3-5]. More importantly, the malignant type tumors are more invasive, destructive and spread to other sites and cause ischemia and necrosis due to intensive consumption rate of energy and nutrients. A salient feature of the metastatic progression of malignant type tumors hosts the ability to differentiate and colonize the same or different organ sites, where typical sites of metastatic relapse from solid tumors types include breast tumors (to bone, lungs, liver, and brain), lung adenocarcinomas (to brain, bones, adrenal gland and liver), skin melanomas (to lungs, brain, skin, and liver), colorectal (to liver and lung), pancreatic (to liver and lungs), prostate (to bone), sarcoma (to lung), and uveal melanoma (toliver) [6].

1.2 Cancer treatment

1.2.1 Conventional Cancer treatment

Until now, numerous therapy options are available for the treatment of benign and malignant tumors. Surgical procedures usually entail removal of the entire tumor with 100% of excised cells [7]. However, surgical risks are numerous including bleeding or infection. In turn, several medical treatments can be performed as alternative treatment procedures: Systemic therapy uses chemotherapeutics that are designed to annihilate or inhibit the DNA of rapidly dividing cells, which are injected into a vein or taken orally. These substances travel through the bloodstream, reaching and affecting cells all over the body. Systemic therapy includes biologic therapy, chemotherapy, and hormone therapy [7]. Some patients may be treated by systemic therapy before surgery (i.e., neoadjuvant therapy) in order to shrink the tumor. Neoadjuvant therapy has been found to be as effective as therapy given after surgery in terms of survival rate, disease progression, and distant recurrence [8]. Adjuvant therapy is given to patients after surgery in order to elucidate any undetected cancer cells that may have migrated to nearby organs or other parts of the body [8]. Physicians decide whether or not to perform adjuvant therapy based on tumor size, biopsy, histology, and the presence of cancer in axillary nodes. Systemic therapy may be used in treating patient with metastasis cancer. Chemotherapy is another clinically-used cancer treatment method that requires oral intake or intravenous injection of a drug. These drugs can kill cancer cells, but may also damage normal cells leading to several patient side-effects, such as fatigue, nausea and vomiting, loss of appetite, hair loss, mouth sores, changes in menstrual cycle, etc. Permanent side-effects can include early menopause and infertility[9] due to the prolonged duration of the treatment cycle. For example, the total

treatment cycle usually lasts for 3 to 6 months for chemotherapy on breast cancer and is typically administered to patients with metastatic cancer. Chemotherapy has also been shown effective when administered surgery in order to minimize the possibility of metastatic responses of certain tumors as a result of resection. Radiation therapy applies high-energy X-rays to deprive cancer cells of their multiplication potential. The radiation beam can be applied externally or internally (using radioactive seeds). Treatment is usually administered five days a week over a period of several weeks. Each treatment lasts only a few minutes and is usually painless. Common side-effects of radiation therapy include skin burns in the treated area and fatigue. Past examples of cancers treated with radiation therapy include skin cancer, prostate carcinomas, cervic carcinomas, lymphonomas, and head and neck carcinomas [10].

1.2.1 Noninvasive and minimally invasive cancer therapy

Technological advancements over the last decade have increased interest in less invasive treatment of patients with localized tumor. Currently available minimally invasive image-guided tumor ablation techniques include cryoablation, laser ablation, radio-frequency (RF) ablation, and High Intensity Focused Ultrasound (HIFU). It is noteworthy that if the tumor is detected early, minimally invasive tumor treatment could be performed to improve the survival rate. Thus, minimally invasive or non-invasive image-guided tumor ablation treatments are both alternative methods to surgery. Cryoablation, also known as cryosurgery, is the process of using freezing temperatures to destroy cancer cells and commonly applies to prostate or breast cancer tumors. A cryoprobe circulating liquid nitrogen is inserted into the tumor under ultrasound guidance, causing the cells to freeze [11]. The tumor is frozen, thawed, and refrozen until the tumor cells

are completely destroyed. Coagulation therapies such as laser therapy, microwave therapy, radio-frequency ablation therapy aims at treating tumors through thermal dosage utilizing the heat-susceptibility aspect of cancerous cells. Microwave ablation therapy is a minimally invasive technique mainly used for treating hepatic tumors with ultrasonographic guidance. The heat-emitting probe generates frequencies up to thousands of MHz range and attached to a microwave generator, which once activated, produce dielectric heat by stimulation of water molecules within he tissue and cells in order to deliver thermal energy of 70-90 W for 30-60 seconds[12]. Interstitial laser thermotherapy is a minimally invasive technique for treating small cancer. Needle probes are placed percutaneously under ultrasound or magnetic-resonance imaging (MRI) guidance, to deliver laser energy into a tumor to slowly heat and destroy the tumor cells[12].

Radio-frequency (RF) ablation is a rapidly emerging technology as a minimally invasive alternative to lumpectomy. For this treatment, a needle-like or star-burst electrode is injected around the tumor tissue and the tip of the electrode is positioned at the center of the tumor. The tip causes frictional heat generated by an electromagnetic wave with frequency between audio and infrared. The electrode is connected to a function generator producing alternating current and the electrical current flows and raises the local temperature up to 95°C maintaining it for about 15 minutes. Since the first clinical feasibility study in 1999, several clinical studies have utilized RF ablation in tumors of various organs such as liver, breast, brain, bone, adrenal gland, prostate kidney, pancreas, spine, rectroperioneum [13]. Nevertheless, the abovementioned treatment techniques requires interventional procedure which may induces surgical-like complications such as infection, thus are limited in the noninvasive aspect as a treatment modality.

1.2.1 High Intensity Focused Ultrasound

High-Intensity Focused Ultrasound (HIFU)[14-17] or Focused ultrasound (FUS) ablation is a non-invasive procedure and uses a high level of acoustic energy that is converted to heat in order to coagulate tissue (thermal lesions), while the surrounding tissues remain relatively unheated. The rapid temperature rise at the transducer focus that causes tissue coagulation is at least 20 up to over 100 C^o and results in immediate protein denaturation and coagulative necrosis [16, 18]. The extent of the tissue damaged is determined both by the temperature elevation and the treatment time[19]. Due to its ability to cause irreversible cell damage in tissues, HIFU has been capable of treating early-stage cancer by inducing thermal and mechanical (or, cavitation) effects on cells in order to annihilate their function. Due to its noninvasive, non-ionizing, extracorporeal advantageous aspect, HIFU treatment constitutes a promising method for non-invasive treatment of benign or malignant solid tumors such as the brain, liver, uterus, kidney, prostate, bone and breast [15].

1.2.1 Monitoring methods for High Intensity Focused Ultrasound

For every therapeutic technique, there consists of three different stages: 1) Surgical planning, e.g., tumor localization, 2) Therapy Stage, e.g., tumor treatment, 3) Treatment Assessment, e.g., confirmation of effective treatment or death of cancer death. For both planning and assessment techniques, many techniques have been developed over the past few decades such as Computed Tomography, Magnetic Resonance Imaging (MRI), Ultrasound, as well as Optical Imaging. Nevertheless, insurmountable challenges still exist for the Therapy Stage, where the area of interest (therapy) often undergoes rapid, irreversible property changes at both

macroscopic and microscopic change under strong environmental change due to the therapeutic effects. Therefore, a crucial area of interest in the field of surgical monitoring is the development of novel, cost effective monitoring techniques with high Signal-to-Noise Ratio (SNR), spatial resolution, and temporal resolution. HIFU aims at thermally coagulating the tissue at the focus of the transducer through application of a continuous high energy acoustic beam. Irreversible cell damage, also known as a thermal lesion, is formed through absorption of focal acoustic energy in soft tissues. Moreover, it can be confined only in the focal region without inducing irreversible thermal damage to the surrounding medium. In the past, the ability of HIFU to induce noninvasive, localized and irreversible tissue necrosis has led to numerous investigations of its application for solid tumor ablation [18, 20-27]. Nevertheless, a few major hurdles still exist in the path of widespread clinical translation of HIFU surgery, especially the aspect of ability of effective monitoring: This includes both the capability of efficient monitoring of lesion formation as well as online characterization of the effective region of treatment (thermal lesion), i.e., the optimization of detecting the onset of lesion formation.

Until now, numerous imaging approaches have been established and implemented for HIFU lesion monitoring and treatment assessment in both MRI [28-31] and ultrasound [14, 32-34]. MRI is currently held as the standard noninvasive guidance and monitoring of HIFU because it can provide quantitative spatial maps of the induced temperature rise at high spatial resolution. Widely known as MR-guided focused ultrasound surgery (MRgFUS) [28-31, 35], the system includes a MR-compatible focused ultrasound transducer whose focus lies inside the target tumor region while T1-weighted images are acquired to detect the tumor and monitor the treatment based on the mapped temperature change. The temperature map by MRgFUS is estimated based on changes in the tissue proton-resonance frequency, which is associated with

the water proton chemical shift resulting from rupture, stretching, or bending of hydrogen bonds in a temperature elevated environment [36]. Among the ultrasound based techniques, detection criteria can be categorized under three different physical measurements: B-mode, temperature elevation, and elasticity change. Conventional B-mode imaging [14, 33, 34] detects thermal lesion formation based on its associated hyperechoic change. However, the nature of the backscattered signal change is highly dependent on the onset of boiling and its uncertainty often limits the reliability of B-mode imaging as an optimal onset lesion detection technique [18, 37, 38]. Non-invasive temperature-induced echo-shift imaging relies on the changes of tissue sound speed in the backscattered ultrasound signal. Although limited by an upper limit in detectable temperature rise [39] , this technique has been validated theoretically and experimentally in thermal lesion assessment [40] and real-time monitoring of HIFU lesion formation *in vitro* [41, 42]. Acousto-optic sensing is another cost-effective modality capable of monitoring the change in tissue optical absorption and scattering using a modulated light under HIFU beams during the treatment [43, 44]. Other backscattered signal-based techniques have also utilized either the change (Anand and Kaczkowski, 2004) or rise (Nandlall *et al.*, 2011) in harmonics using spectral analysis in order to detect the onset of thermal lesion formation.

A common shortfall amongst the previously mentioned techniques is the lack of ability to provide quantification of the underlying tissue property change during the HIFU treatment procedure. In response to this need, another field has been developed aside from the aforementioned techniques that are focused on imaging-based characterization of the mechanical properties of HIFU-induced thermal lesion. This stems from the fact that previous studies have shown there is a strong correlation between pathological tissue and tissue stiffness varies before, during, and after thermal ablation treatment. The next chapter will focus on the basic principles

behind tissue mechanics, as well as an overview on the elasticity based imaging techniques and the elasticity based HIFU monitoring techniques, following by the description of the technique to be presented, Harmonic Motion Imaging, its principle, and the specific aims associated with HMI completed for this dissertation.

Chapter 2. Background and significance

2.1 Tissue mechanics

2.1.1 Tissue elasticity and elasticity imaging

Manual palpation has been served as a standard of screening method for physicians to diagnose tissue abnormalities for centuries. The underlying principle behind palpation stems from the mechanism of the pathological process when the growth of malignant tumors or scarring of tissues replaces the healthy tissues to form fibrotic tissues, which lead to increase of local tissue stiffness [45-51]. Therefore, the study of soft tissue biomechanics is of particular significance given the elasticity of soft tissues have been shown to be closely associated with their biological properties across from the both microscopic and macroscopic structural levels [52]. It has been shown that pathological tissues can be evidently identified based on the change in tissue elastic properties, *i.e.*, breast tumors exhibiting hard nodules in comparison to that of the normal breast tissues [53], nonalcoholic fatty liver disease exhibiting stiffer liver tissue under fibrosis [54], calcific aortic tissues exhibiting calcified nodes stiffer than the medium tissue [55, 56] and abdominal aortic aneurysmal lesions exhibiting local softening and stiffening [57, 58].

The stiffness value of the tissue can be usually quantified by several mechanical parameters such as Young's modulus (E), Bulk Modulus (κ), or Shear modulus (μ). Young's modulus is defined as the measure of a material's resistance to a compressive deformation. In other words, the Young's modulus is defined as the ratio of the stress (σ) to the deformation (i.e., strain $\varepsilon = \Delta L/L$ where L is the original length). Various types of pathological tissues such as

sirrhous carcinoma of breast, liver metastasis, prostatic carcinoma, and thyroid cancer exhibit higher Young's moduli whereas some types of breast cancer types including intraductal and papillary carcinoma are softer than normal surrounding tissues [54, 59]. In general, soft tissues are known to be anisotropic, viscoelastic and nonlinear [60]. Nevertheless, linear elasticity is often considered as a reasonable assumption under relatively small strains (less than 10%), where the applied stress and corresponding strain are related such as $\sigma = E\,\varepsilon$, where E is the Young's Modulus. Furthermore, the linear elasticity, with assumption of homogeneous, elastic, isotropic, and small strain in a continuous 3D medium can be derived from Hooke's Law such as:

$$\sigma_{ij} = \lambda \delta_{ij} \varepsilon_{kk} + 2\mu \varepsilon_{ij}, \qquad (1)$$

Where λ and μ are the Lamé (Elastic) Coefficients, ε_{ij} is the strain, σ_{ij} is the stress and δ_{ij} is the Kronecker delta (i.e, δ =1 for $i = j$ and δ = 0 for $i \neq j$). In the case of simple uniaxial stress, the strain can be can be related to Young's Modulus (E)and Poisson's ratio (ν) as:

$$\varepsilon_{ij} = \frac{1+\nu}{E}\sigma_{ij} - \frac{\nu}{E}\delta_{ij}\sigma_{kk}, \qquad (2)$$

where the Young's modulus, Poisson's ratio, and Lamé (Elastic) Coefficients are related as follows:

$$\lambda = \frac{E\nu}{(1+\nu)(1-2\nu)}, \text{ and } \mu = \frac{E}{2(1+\nu)}, \qquad (3)$$

With the assumption of incompressibility, where the Poisson's ratio (ν) is 0.4999, the shear modulus, defined as the shear stress to shear strain (angular deformation), can be linked with the Young's modulus as:

$$\mu = \frac{E}{2(1+\nu)} = \frac{E}{3}, \text{ or } E = 3G \qquad (4)$$

Also, the Bulk Modulus (κ), or the elastic modulus, which represents the molecular structure of soft tissue properties, can be related to the Lamé (Elastic) Coefficients as follows:

$$\kappa = \lambda + \frac{2}{3}\mu \qquad (5)$$

It is also noteworthy that the shear modulus is more widely used to estimate tissue properties as its magnitude may change by second orders of magnitude depending on the tissue type and pathological conditions, whereas the variation of bulk modulus is much smaller (less than order of magnitude) [61, 62]. The main reason behind this characteristic is that the bulk properties are determined mainly by the molecular structure while shear properties are determined by the higher level of tissue organization [63].

Given the interesting distinctive contrast in elasticity across various types of pathological soft tissues types, numerous mechanical imaging modalities have been developed to detect and diagnose tissue abnormalities using either ultrasound or MRI. Elasticity imaging is classified as a noninvasive method to quantify tissue mechanical properties *in situ* —based on the palpation principle— utilizing tissue response under either external perturbation such as static [64] and dynamic Elastography [65, 66], and Magnetic Resonance Imaging(MRI)-based Magnetic Resonance Elastography (MRE) [67-70]. In static Elastography, a small external compression is applied and the resulting tissue deformation or strain detected through radiofrequency (RF) signals is estimated using motion estimation techniques such as cross-correlation. Dynamic

Elastography such as Sonoelasticity imaging utilizes a mechanical exciter to generate external vibrations at low frequency between 100 to 300 Hz, which disturbs the region of interest imaged by an ultrasound imaging probe. The underlying tissues stiffness is mapped in a binary format using a Doppler shift based algorithm, where normal tissue exhibits significant motion, i.e., Doppler shifts while the stiffer regions exhibit no significant movement. In MRE, shear waves within the tissue are first induced by an external mechanical exciter. Displacements resulting from the propagation of such shear waves are recorded through a motion-sensitizing gradient sequence. As a result, the underlying mechanical properties can be directly estimated based on the shear wave velocity. Another external excitation based method is Transient Elastography, which couples the ultrasound transducer with a vibrating piston, where the transducer captures RF signals containing low frequency shear wave producd by the vibrating piston ranging between 50 to 500 Hz [71, 72].

Unlike the previously mentioned methods that rely on external excitation, several techniques have been developed that measure tissue deformations from internal perturbation methods such as vibroacoustography, Shearwave Imaging, Acoustic Radiation Force Impulse (ARFI) Imaging. Vibroacoustography [73] utilized two confocal therapeutic ultrasound beams to generate a localized oscillatory radiation force in tissues. Acting as a localized acoustic source, the transmitted acoustic reflection is recorded by a hydrophone. Several studies have shown that such oscillatory acoustic radiation force can be generated in biological soft tissues internally at variable depths [62, 74-83].

Shear wave imaging was first proposed by Sarvazyan *et al.* (1998), who reported quantifying the shear modulus from shear waves generated by an impulse acoustic radiation force excitation. Supersonic shear wave imaging [84-87] was later developed to map the shear

modulus based on a plane wave excitation approach that entailed a set of excitation points along the axial direction. Another recently developed shear wave imaging techniques based on radiation force excitation is SDUV, which estimates tissue viscosity and elasticity based on the phase of the shear wave using RF signals from pulse-echo transducer and a burst excitation from a separate focused transducer.

Acoustic Radiation Force Impulse(ARFI) elasticity imaging [88] is another unique internal perturbation imaging technique which can be implemented on any commercial scanner and diagnostic probe. ARFI relies on two sequences: a pushing sequence consists of focused beam with higher intensities for durations of tens to hundreds of microseconds, followed by a standard pulse-echo imaging pulse to detect the tissue relaxation response following the push. The ARFI technique only requires a single diagnostic probe and has been shown feasibility of implementing onto a commercially available ultrasound scanner.

Until now, an extensive amount of feasibility studies for applying elasticity imaging in quantifying tissue elastic properties has been shown for numerous applications such as cardiovascular [89-93], breast [79, 94, 95], liver [72, 96-99], kidney [87, 97, 100], muscle [101, 102], brain [97], bone [103], and prostate [104, 105] under various pathological conditions. Some elasticity imaging techniques have recently been successfully translated to commercially available ultrasound scanners. Techniques such as SSI, SWEI, and ARFI imaging have also been successfully translated to the clinic. The applications of elasticity imaging also spread to the monitoring of various types of thermal ablation treatments, which will be described in the following section.

2.1.2 Monitoring tissue elasticity under thermal ablation

Another emerging application for the ultrasound–based elasticity imaging techniques has been the assessment and monitoring of changes in tissue mechanical properties during minimally and non-invasive treatment procedures and following therapies such as microwave and Radio Frequency (RF) ablation [106-109], High Intensity Focused Ultrasound (HIFU) ablation [110-119], hyperthermia [120], histotripsy [87, 121-123], and cryoablation [124]. Different studies have been conducted over the past decades on clinical implementation of HIFU-based methods [125-129]. Several studies have been shown capable to depicting various thermal effects on the tissue mechanical properties [85, 86, 109, 113, 130, 131] where different soft tissues were found to show different thermal behaviors [85]. It has been shown that different soft tissues undergo (reversible) softening followed by (irreversible) stiffening phase beyond certain temperature [85, 112, 132].

The fundamental reason for which elasticity imaging can monitor the HIFU lesion is the underlying contrast between the stiffness of HIFU-induced lesion compared to that of the untreated condition. MR-based tissue elasticity imaging, namely magnetic resonance elastography (MRE) [69, 133-135] was shown feasible in HIFU monitoring [136]. In MRE, shear waves within the tissue are first induced by an external mechanical exciter. Displacements resulting from the propagation of such shear waves are recorded through a motion-sensitizing gradient sequence. As a result, the underlying mechanical properties can be directly estimated based on the shear wave velocity. Wu *et al.* (2001) showed that the MRE was capable of quantitatively estimating the differences in shear modulus between the HIFU lesion and the untreated tissue, indicating that the ablated regions were stiffer than the untreated ones. In addition to MRE, other ultrasound-based elasticity imaging studies also investigated the Young's

Modulus of HIFU lesions for comparative analyses with mechanical testing. In Sonoelasticity Imaging [137], Zhang *et al.* (2010) applied dynamic mechanical analysis (DMA) to measure the Young's Modulus of *ex vivo* bovine liver lesions following *in vivo* HIFU and found the HIFU lesion-to-background Young's Modulus ratio to be as high as 12 to 1. Other such comparative studies between outcomes of elasticity imaging and mechanical testing on HIFU lesions have been performed on *in vitro* canine liver [138], *in vitro* porcine liver [139] and *ex vivo* bovine muscle [136]. Based on these studies, the Young's Modulus of the HIFU lesions was found to be 2 to 12 times higher than the untreated tissue.

Given the clear contrast in mechanical properties between the HIFU-induced thermal lesions compared to those of normal tissues, imaging the HIFU lesions based on their distinct mechanical properties has been investigated by numerous techniques. Ultrasound elastography [140] has been shown capable of assessing the extent of thermal lesions based on this strain difference [138, 141-144]. Following HIFU *in vivo,* strain imaging showed a significant decrease in the average strain within the treated region with respect to the peripheral normal tissue in both *ex vivo* prostate [145] and *ex vivo* liver [146]. Vibroacoustography [147] utilized two confocal therapeutic ultrasound beams to generate a localized oscillatory radiation force in tissues. Acting as a localized acoustic source, the transmitted acoustic reflection is recorded by a hydrophone. Several studies have shown that such oscillatory acoustic radiation force can be generated in biological soft tissues internally at variable depths [62, 74-83]. On the other hand, the potential of using an acoustic radiation force for monitoring thermal lesion formation during HIFU surgery was first reported by Konofagou *et al.* (2001) who showed the feasibility of using Vibroacoustography for monitoring of the temperature during thermal therapy and thermal lesion formation.

Ultrasound-based tissue elasticity imaging techniques are developed based on the fact that HIFU lesions correspond to significant tissue stiffening. The Acoustic Radiation Force Impulse (ARFI) imaging technique utilizes a modified linear array transducer to transmit a high-intensity continuous wave pulse, i.e., a localized radiation force and subsequently perform a standard-pulse-echo sequence in order to obtain the tissue relaxation response following force application using a one dimensional (1D) cross-correlation technique [148]. In previous studies, ARFI was shown capable of detecting thermal lesions in both *in vitro* and *in vivo* tissues [149, 150] where the stimulated displacement was much smaller in the coagulated tissue than in the untreated tissue. Recently, ARFI imaging has also been shown feasible in monitoring HIFU treatment using a cost-effective conventional imaging platform n combination with a curvilinear imaging probe operated under a customized beam excitation sequence [151]. Supersonic Shear Wave Imaging (SSI) [152, 153] is also capable of providing high frame rates mapping the changes in local shear modulus through an *in situ* plane shear wave induced by focused acoustic radiation force under HIFU treatment [115]. Nevertheless, MRE relies on the costly MRI system while its frame rate performance is limited 0.5-10 Hz and both SSI and ARFI requires the HIFU treatment to be turned off during its imaging sequences despite the fact that one of the primordial unsolved issues of HIFU is the long duration of its procedures. It is therefore important to implement a monitoring technique capable of providing high frame rate, real-time feedback without interrupting the treatment.

2.2 Harmonic Motion Imaging for Focused Ultrasound (HMIFU)

Localized harmonic motion (LHM) imaging [81] is a dynamic radiation force technique, which utilizes two sets of therapeutic beams from a pair of confocally aligned HIFU transducers excited under burst mode for noninvasive tissue probing. Simultaneously acquired RF signals are used for estimation of the induced focal tissue oscillatory motion. Applying a similar excitation principle as Vibroacoustography, this technique is a localized, noninvasive, non-ionizing, cost-effective alternative for HIFU ablation guidance, real-time monitoring, and lesion detection. Recently, Maleke and Konofagou *et al*. introduced an amplitude-modulated (AM) version of the HMI method that produced a harmonic radiation force using a single-element FUS transducer instead of the previous configuration that used two confocal transducers. Using AM ultrasound waves offers the advantages of a simpler transducer design and a sustained application of the radiation force, establishing a stable vibration location deep inside the tissue. The imaging transducer can either be a pulse-echo transducer or a phased array transducer, as long as the frequencies of the imaging and HIFU transducers are sufficiently distinct so that the high power HIFU beam can be filtered out prior to post-processing. The designed HMI system allows the resulting harmonic tissue motion to be imaged and monitored during force application using a cross-correlation based motion estimation technique. A major advantage of this technique is the real-time feedback of the associated variation in the tissue mechanical properties during the force application. Since HMI applies an oscillatory motion and estimates axial displacements, the motion induced in the tissue is independent of the duration of the applied force, assuming the tissue elasticity stays constant (no softening/hardening) during force application.

As HIFU is slowly emerging as a promising thermal ablation technology for minimal, or non-invasive, non-ionizing, extracorporeal treatment of various diseases, the potential of HIFU treatment as a non-invasive surgical tool has been demonstrated in several clinical applications for treatment of tumors of the prostate, liver, breast, kidney and pancreas, as well as uterine fibroids. Currently, the two major limitations of HIFU treatment lie in include the difficulty of monitoring the changes in temperature and tissue mechanical properties as well as the lack of ability to optimally control precise thermal exposure upon lesion formation. In order to address such existing issues, HMI has been further extended as a HIFU treatment monitoring technique because the AM-HMI method can be applied throughout the treatment, i.e., for simultaneous HMI and ablation during the entire treatment. The integrated system is named HMIFU for Harmonic Motion Imaging for Focused Ultrasound. In HMIFU, a focused transducer is used to induce focal ablation while a confocal pulse-echo transducer is simultaneously used to image the tissue and estimate the HMI displacement and phase shift, which will be further discussed in Chapter 4, section 4.1. The HMI focal measurements are used to monitor and assess the contrast in underlying viscoelastic properties between lesion and medium.

HIFU using HMIFU is typically composed of three stages: 1) Surgical planning, e.g., tumor localization, 2) HIFU application with real-time monitoring, and 3) HIFU lesion assessment. The excitation waveform of the transducer is controlled at a relatively lower intensity of HMI for stages 1 and 3 whereas stage 2 involves a higher intensity. Further details are provided elsewhere [154]. Previously, experimental studies have shown the feasibility of HMIFU *in vitro* [155]*, ex vivo* [154] and *in vivo* [156, 157]. In addition, past simulation studies showed initial feasibility in monitoring the onset of thermal lesion formation based on the change

in the tissue mechanical response [158]. Through the development of an interdisciplinary framework comprising an acoustic, FE-based mechanical response, and image formation module, [159] and [160] investigated feasibilities in the tumor localization and coagulation detection using 1-D imaging and direct measurements, respectively.

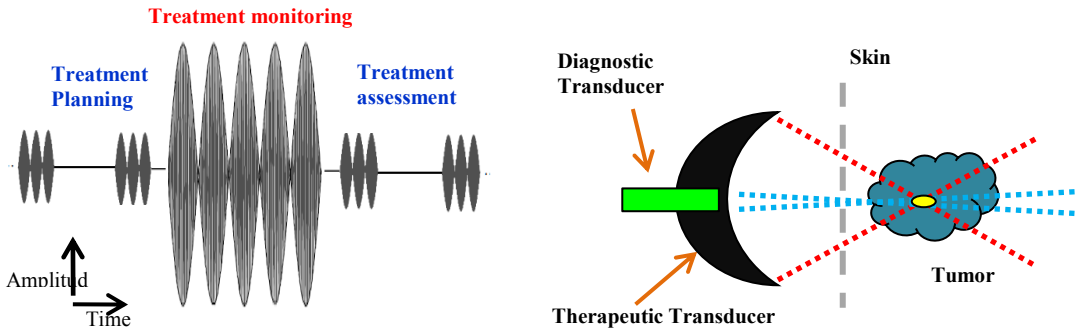

(a) (b)

Figure 2.1. Principle of HMIFU. The input HIFU signal (a) is composed of amplitude-modulated HIFU beams for both treatment planning/assessment and monitoring. The HMIFU set up (b) is composed of a pair of confocally-aligned diagnostic and therapeutic probe and aims to monitor the non-invasive HIFU treatment of any tissue abnormalities such as tumor.

2.3 Overview and significance

This dissertation first focuses on the development and experimental validation of a finite element based three-dimensional (3D) complementary framework used for performance assessment of HMIFU on thermal lesion formed during HIFU treatment. Following the validation of HMIFU *in silico*, we then proceed to develop and optimize 1D and 2D HMIFU system for assessment of acoustical and biomechanical property change of biological tissues under two protocols: slow denaturation or boiling. Following the system development, feasibility studies of 2D pre-clinical system for biological tissues and tumor applications *ex vivo* and *in vivo* would be tested under both treatment protocols. Lastly, we plan to implement a model-independent modulus estimation algorithm using HMIFU for quantitative assessment and monitoring the viscoelasticity change of biological tissue and tumor under HIFU treatment. The dissertation is structured as follows: Chapter 2 overviews the basics of tissue mechanics, including the tissue elasticity properties under normal, pathological, under thermal ablation treatments, as well as numerous imaging techniques that are capable of imaging the elasticity property of soft tissue underlying these conditions. Lastly, the principles of the technique to be presented in this dissertation, Harmonic Motion Imaging for Focused Ultrasound (HMIFU) will be introduced. Chapter 3 summarizes an interdisciplinary theoretical framework for performance assessment of HMIFU and overviews each of the developed modules including an acoustic, thermal, mechanical simulation, and ultrasound image formation and displacement estimation along with *ex vivo* experimental validation. Chapter 4 and 5 introduces two systems: A 1D system for fundamental investigation of acoustical, thermal, and viscoelasticity property change under two types of clinically-used HIFU treatment: 1) HIFU treatment with boiling and 2) HIFU treatment with slow denaturation. Consequently, the development of another fully integrated,

clinically translatable, real-time 2D HMIFU system will be discussed along with feasibilities demonstrated in tissue-mimicking phantom as well as biological specimen. Chapter 6 will discuss further application implementation of the 2D HMIFU system for pancreatic tumor treatment using transgenic KPC model mice *in vivo*. Chapter 7 will be focused on the development of a model-independent modulus estimation algorithm using HMIFU for quantitative assessment and monitoring of the viscoelasticity changes of biological tissues and tumors under HIFU. Lastly, chapter 8 summarizes the findings shown in this dissertation and indicates future directions.

Chapter 3. Theoretical framework for performance assessment of HMIFU

3.1 Introduction

In this chapter, a comprehensive theoretical model has been developed in order to assess the performance of HMIFU in stage 3), i.e., HIFU lesion assessment fundamentally. As previously mentioned, HMIFU is composed of three stages: 1) Surgical planning, e.g., tumor localization, 2) HIFU application with real-time monitoring, and 3) HIFU lesion assessment. The excitation waveform of the transducer is controlled at a relatively lower intensity of HMI for stages 1 and 3 whereas stage 2 involves a higher intensity. Previously, the first set of HMI simulation studies were conducted in order to assess the initial feasibility in monitoring the onset of thermal lesion formation based on the change in the tissue mechanical response, which was then validated against experimental findings *in vitro* [158, 161]. In addition, several interdisciplinary framework comprising an acoustic, FE-based mechanical response, and image formation module were also developed in order to assess the, feasibilities in the tumor localization and coagulation detection using 1-D imaging and direct measurements, respectively [160, 162].

Nevertheless, a theoretical framework study on the feasibility of HIFU lesion detection has yet to be developed, i.e., in order to assess the capability of HMI for HIFU lesion localization and quantification based on a geometry independent, complete 3D analysis with consideration of nonlinear acoustic wave propagation during lesion formation under ablative AM-HIFU beam (i.e., Stage 2 of HMIFU). Our hypothesis is that HMIFU is fundamentally capable of detecting

HIFU lesions based on the aforementioned change in stiffness and correctly depict the increase in HIFU lesion size with treatment duration. In order to validate this hypothesis, a comprehensive, easily implementable 3-D model (Figure 3.1) has been developed, which links 1) a nonlinear-acoustics based model coupled with the Bioheat Transfer (BHT) equation solver for simulating both the pressure field and lesion map, 2) a finite-element (FE) based mechanics module for simulating the acoustical-mechanical response in the focal region within a simulated tissue-mimicking phantom, and 3) an image-formation model, which validates the feasibility of our RF based motion-estimation technique.

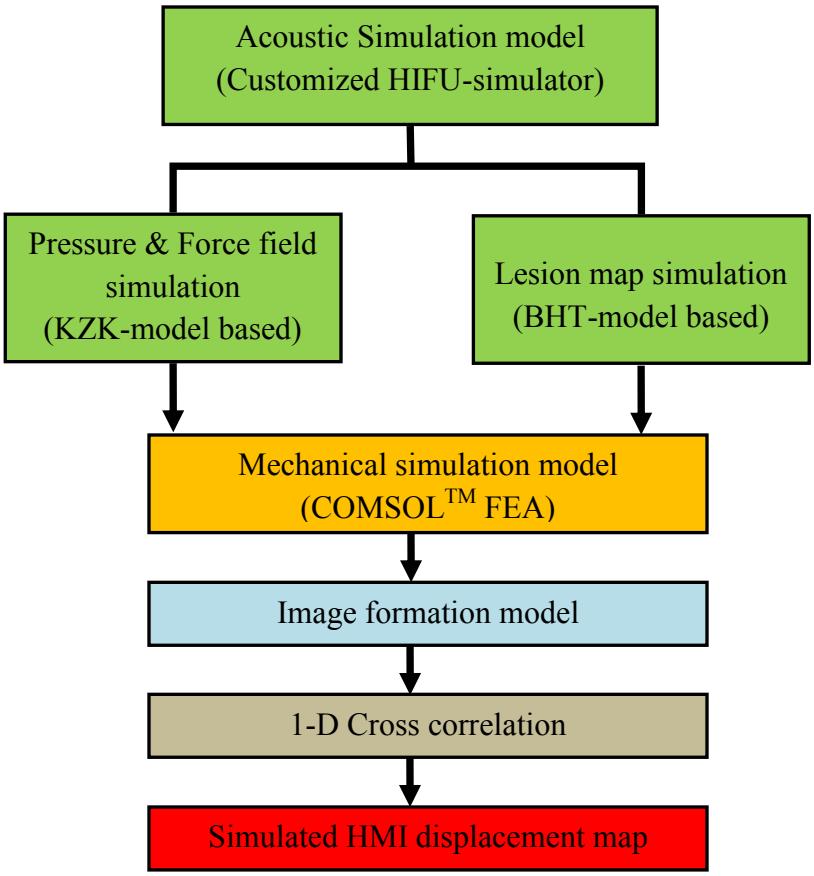

Figure 3.1. Theoretical framework flow diagram. The three modules within the frame are: Customized HIFU Simulator (green), FE mechanical response (yellow), and 2D convolutional model (blue) followed by 1D cross-correlation (brown)

The developed simulation framework is comprised of three modules: a nonlinear-acoustics based model coupled with a Bioheat Transfer (BHT) equation solver, a finite-element (FE) based mechanics module, and an image-formation model. All three modules have been linked in the following order: (1) the nonlinear-acoustic module simulates the acoustic intensity and radiation force maps; (2) the BHT module simulates the size and distribution of the thermal lesion using the acoustic intensity map simulated in step (1); (3) following assignment of the lesion-to-background Young's modulus based on existing literature, the FE mechanics module

calculates the acoustic-mechanical motion response map using both the simulated acoustic intensity and lesion map (from (1) and (2)); (4) the image-formation module simulates the RF signals before and after the motion response calculated from step (3); (5) a cross-correlation technique was applied on simulated RF signals from step (4) for the estimation of the displacements. In the subsequent sections, details of each module are described separately, followed by *ex vivo* experiments using canine liver specimens were performed to validate the results from each module of the simulation framework under the same input parameters.

3.2 Methods

3.2.1 Acoustic and thermal simulation module

The acoustic and thermal simulation module used for this theoretical framework was derived and improved from an existing HIFU-Simulator [163]. The HIFU simulator was customized to the HMI configuration. The HIFU simulation framework assumes a 2D axisymmetric propagation geometry and is composed of two parts: 1) a Khokhlov-Zabolotskaya-Kuznetsov (KZK) [164] based nonlinear acoustic module for simulation of the pressure and intensity field, and 2) a conventional BHT-based thermal module for simulation of the temperature change and a binary lesion map based on the calculated thermal dose surrounding the focal region.

In this study, the objective was solely to validate that the HMIFU is capable of detecting HIFU lesions based on the relative change in stiffness (lesion-to-background contrast) and of accurately depicting the increase in HIFU lesion size at distinct exposure durations. Therefore,

in order to overcome the limitation of the acoustic simulation module, the geometry of the transducer was defined as plane circular, i.e., with an equivalent surface area to the experimental transducer. In other words, both the distribution and magnitude of the experimental force field was approximated in simulations. Two modifications were applied to the HIFU-simulator. First, the HIFU transducer used in HMI is a spherical transducer with a void center, i.e., outer radius of 70 mm and inner radius of 45 mm. The reduction in the active surface area corresponded to the experimental annular void that accommodated the pulse-echo transducer. In order to approximate the actual pressure field, the original spherical geometry with a void center was converted into a plane circular shape with radius of 57 mm but equivalent surface area and *apparent F-number*, $\frac{f}{d}$, where f is the focal length, d is diameter of the transducer, which can be derived using Fraunhofer diffraction of Gaussian beams in the case of a generic spherical transducer [165, 166] such that:

$$\frac{f}{d} = \sqrt{\frac{\ell}{7\lambda}}, \qquad (1)$$

where, ℓ and λ represents the axial focal spot diameter and wavelength, respectively. In this study, the apparent F-numbers were 0.86 and 0.88 under the adapted (customized plane circular simulated transducer) and experimental geometries. The simulated *in situ* acoustic intensities were 196 W/cm^2 and 942 W/cm^2 under imaging and ablation settings, respectively. Secondly, the input signal to the HIFU transducer is amplitude modulated, i.e., it is composed of both the carrier and modulation frequencies, thus the excitation sequence in the BHT module of the model was modified from a binary signal to one oscillating at twice the AM frequency used in experiments. A complete set of simulation parameters can be found in Tables 3.1 and 3.2 [167, 168]. In HIFU-simulator, the focusing is calculated by assuming a uniform pressure distribution

on the transducer surface with the phase shift corresponding to a quadratic approximation of a spherical converging wave. It is noteworthy that the theory of KZK has a paraxial assumption limiting its accuracy within 20˚ of the axis of propagation [169]. This implies that transducers with a F-number smaller than 1.74 will suffer a loss of accuracy. However, previous studies [170] have been performed under this limitation and considered such inaccuracies to be minor in practice [169].

Medium 1: Water	
Parameter	*Value*
Speed of sound (m/s)	1482
Mass density (kg/m^3)	1000
Attenuation at 1 MHz (dB/m)	0.217
Power of attenuation vs. frequency curve	2
Nonlinear parameter	3.5
Medium 2: Liver	
Parameter	*Value*
Speed of sound (m/s)	1597
Mass density (kg/m^3)	1050
Attenuation at 1 MHz (dB/m)	75
Power of attenuation vs. frequency curve	1.5
Nonlinear parameter	7.9

Table 3.1. Simulation parameters for KZK module in HIFU Simulator

Medium 1: Water	
Parameter	*Value*
Heat capacity (J/Kg/K)	4180
Thermal conductivity (W/m/K)	0.6
Perfusion rate (Kg/m^3/s)	0
Medium 2: Liver	
Parameter	*Value*
Heat capacity (J/Kg/K)	3510
Thermal conductivity (W/m/K)	0.51
Perfusion rate (Kg/m^3/s)	0

Table 3.2. Simulation parameters for BHT module in HIFU Simulator

3.2.2 Finite-Element-Analysis mechanical simulation module

In order to calculate the oscillatory tissue response induced by the acoustic HMI radiation force, both the simulated acoustic intensity fields and lesion maps were translated into a COMSOL^{TM} (Comsol Inc., Burlington, MA, U.S.A.) based 3D FE geometry through MATLAB (Mathworks, Natick, MA, U.S.A.). The acoustic intensity field was first approximated into the HMI force field through the conventional plane-wave body force equation [171, 172]

$$F = \frac{2\alpha I}{c}, \qquad (2)$$

where I is the simulated intensity field, α is the absorption coefficient, and c is the speed of sound. The equation was derived based on the propagation of a plane wave in a linearly viscous fluid and neglects the contribution from scattering mechanism in the computation of momentum transfer, because the absorption is the dominant attenuation mechanism in soft tissues [173]. Similarly, the generated lesion maps were also translated onto a 3D simulated phantom. As mentioned in the introduction, previous studies have found a lesion-to-background Young's modulus ratio of 2-12 [136, 138, 139, 154, 174]. Since the stiffness of the HIFU lesion increases with the exposure duration, the modulus of simulated HIFU lesion map after a 0-, 10-, 20- or 30-s HIFU exposure was assigned to be 1, 3, 6, or 9 times that of the background (10 kPa), respectively. As a first order of approximation, the temperature rise within the formed HIFU lesion was assumed uniform, i.e., the assigned modulus was assumed to be homogeneous across the lesion in each case. In order to retain the accuracy of the estimated focal displacement at low computational cost, a finer mesh was applied surrounding the focus of the HMI force field, i.e., the distance between neighboring nodes inside and outside the force field was set to be 0.085 mm and 0.57 mm, respectively (Figure 3.2a, Table 3.3). The HMI force field was moved in a

raster-scan format in order to compute the displacements within a region of interest (ROI) within an axial view surrounding the thermal lesion.

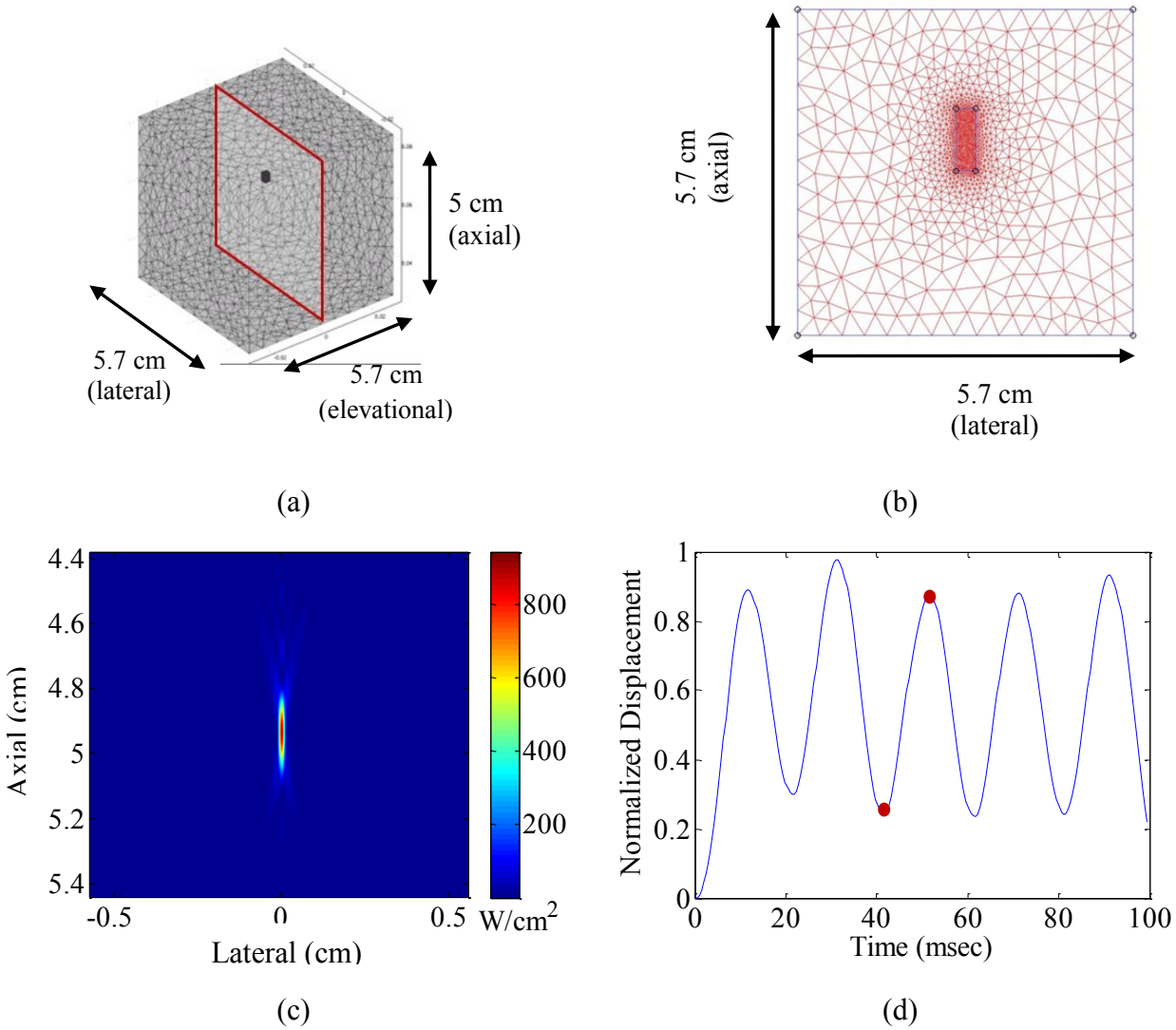

Figure 3.2. Theoretical framework flow diagram. The three modules within the frame are: Customized HIFU Simulator (green), FE mechanical response (yellow), and 2D convolutional model (blue) followed by 1D cross-correlation (brown)

FE analysis parameters		
Parameter	3D transient	3D static
	Value	*Value*
No. of vertex elements	16	16
No. of edge elements	140	204
No. of boundary elements	>2100	>2600
No. of elements	>17000	>26000
Computation time	>300 min per point	<10 min per point

Table 3.3. FE mesh parameters using COMSOL^{TM}. The computational time per point in the simulation were 10 minutes and 4.5 hours under static and dynamic, respectively.

Simulations: 3D static versus 3D dynamic simulation

In previously reported studies [159, 160], transient analysis was used to evaluate the simulated mechanical response profile in 1D imaging and direct measurements, respectively. In this paper, we investigated the full two dimensional (2D) displacement profile based on the true three dimensional (3D) HMI problem, i.e., without axisymmetric assumptions while maintaining a reasonable computational cost. Here, a static computational approach was performed instead of the conventional dynamic approach such that in a linear, purely elastic medium while ignoring any initial transient forces, the peak-to-peak steady-state displacement under the dynamic sinusoidal HMI force was assumed equivalent to the displacement induced by a single quasi-static deformation using the maximum HMI force (Figure 3.2d). As a result, this method allowed us to obtain displacement profiles at a 96% reduction in computational time compared to the dynamic method. In order to demonstrate equivalency of the 3D static alternative to that of the 3D dynamic method, 1D comparison of the dynamic and static analysis was performed along

the central plane through the HIFU lesion. For a lesion-to-background modulus contrast of 3, 6 and 9 (which corresponds to lesions formed at 10-, 20-, and 30-s HIFU exposure, respectively), the lesion-to-background displacement contrast values under static and dynamic analyses were found to be comparable, i.e., 2.50, 4.11 and 5.41, and 2.42, 3.93 and 5.33, respectively; hence validating the assumed equivalence (Figure 3.3).

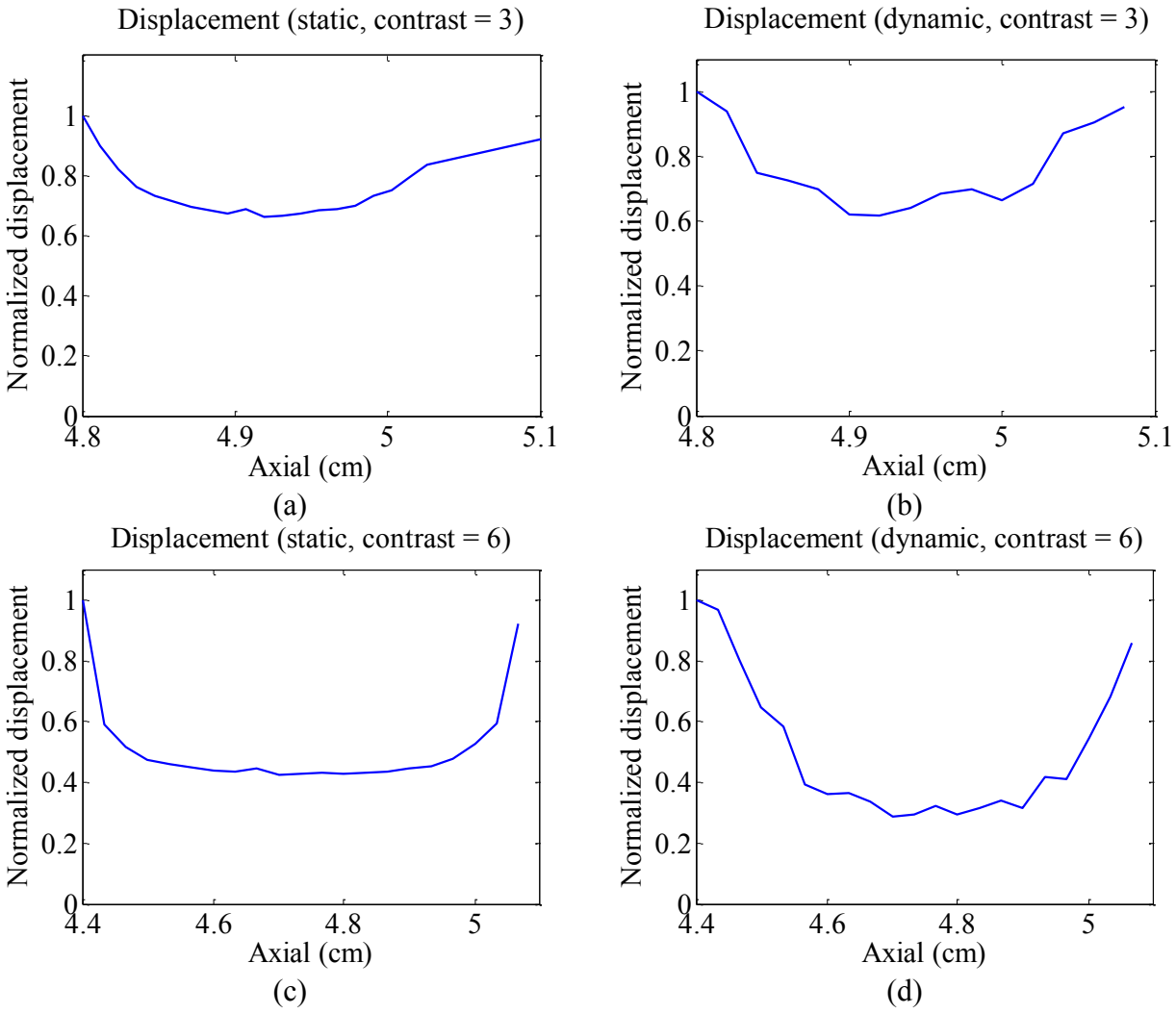

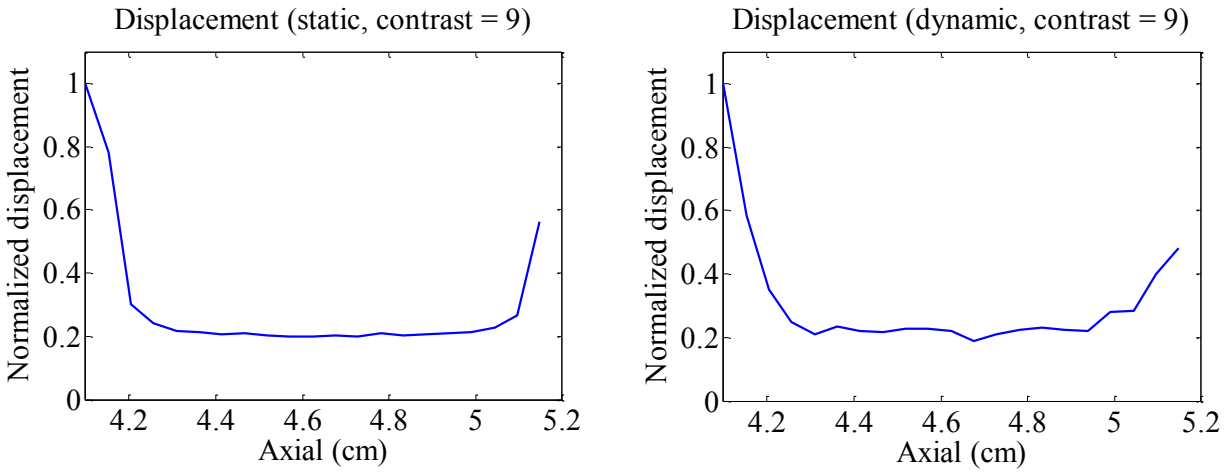

(e) (f)

Figure 3.3. 1D analysis showing feasibility of static replacing dynamic analysis approach. (a), (c), (e), static, and (b), (d), (f), dynamic raster-scan were performed in a single line with length of 3, 7, and 11 mm along the axial direction enclosing the expected lesion depth on simulated lesion maps with modulus contrast of 3, 6, and 9, respectively.

3.2.3 Image Formation and Displacement estimation module

Once the FE displacement solution was generated, it was applied in a series of simulated ultrasound radio-frequency (RF) signals in MATLAB 2008b (Mathworks, Natic, MA, U.S.A.) generated using a 2D linear convolutional scattering model [175, 176]. The simulated linear array had 128 elements, center frequency of 7.5 MHz, beamwidth of 1 mm, 60% bandwidth with a sampling frequency of 80 MHz. Additive Gaussian random noise at 40 dB was implemented to all simulated RF signals. As previously mentioned, in the FE mechanics module section, the FE-computed outputs are the displacement maps obtained by moving the HMI force field within

a region of interest (ROI) surrounding the thermal lesion. Therefore, estimating the displacement using our RF-based motion estimation algorithm needed to be repeated for every coordinate investigated during raster scan simulation, i.e., every pixel of the FE-generated mechanical response map. This procedure is as follows: 1) tissue motion was induced using the FE-generated mechanical response map on all of the simulated RF frames generated by the 2D linear convolutional scattering model; 2) only the center line of every RF frame was selected to simulate the acquisition from a single-element, pulse-echo transducer used in the experiments; 3) a 1-D cross-correlation technique [177] was applied on the RF signals using a window size of 1 mm and 85% overlap. As a result, displacements are estimated from step 1) to step 3), representing the peak-to-peak displacement. In order to estimate the 2D displacement map, this sequence was repeated for every coordinate investigated in the FE module. Lastly, upon completion of the 2D displacement map, a 3 x 3 median filter was used in conjunction with bilinear interpolation to enhance the visualization.

3.2.4 *Ex vivo* experimental validation

In order to validate the theoretical findings ex vivo, HMIFU experiments were also conducted under the same systemic parameters as the theoretical investigations. For sample preparation, fresh canine liver specimens were excised immediately after animal sacrifice and immersed into a Phosphate buffered saline (PBS) solution at room temperature. All procedures were approved by the Institutional Animal Care and Use Committee of Columbia University. Each specimen was fixed using a metallic needle on an acoustic absorber submerged in a de-ionized and degassed water bath. The 1-D HMIFU system (Further details described in Chapter 4) was comprised of a 4.5MHz focused (outer diameter 70 mm, inner diameter 45 mm, focal

depth 5 cm) transducer (Imasonic S.A., Voray/l'Ognon, France) used to vibrate the tissue using an AM frequency of 25 Hz. The active element was fabricated utilizing a 1-3 piezocomposite technique and materials such as a large number of lead zirconate titanate ceramic (PZT) rods embedded into a matrix of epoxy or polyurethane [178, 179]. A confocally-aligned, 7.5 MHz single element pulse-echo transducer (Panametrics, Waltham, MA, U.S.A.) (diameter 15 mm, focal length 6 cm) was used for simultaneous acquisition of the RF signals (Fig 3.4).

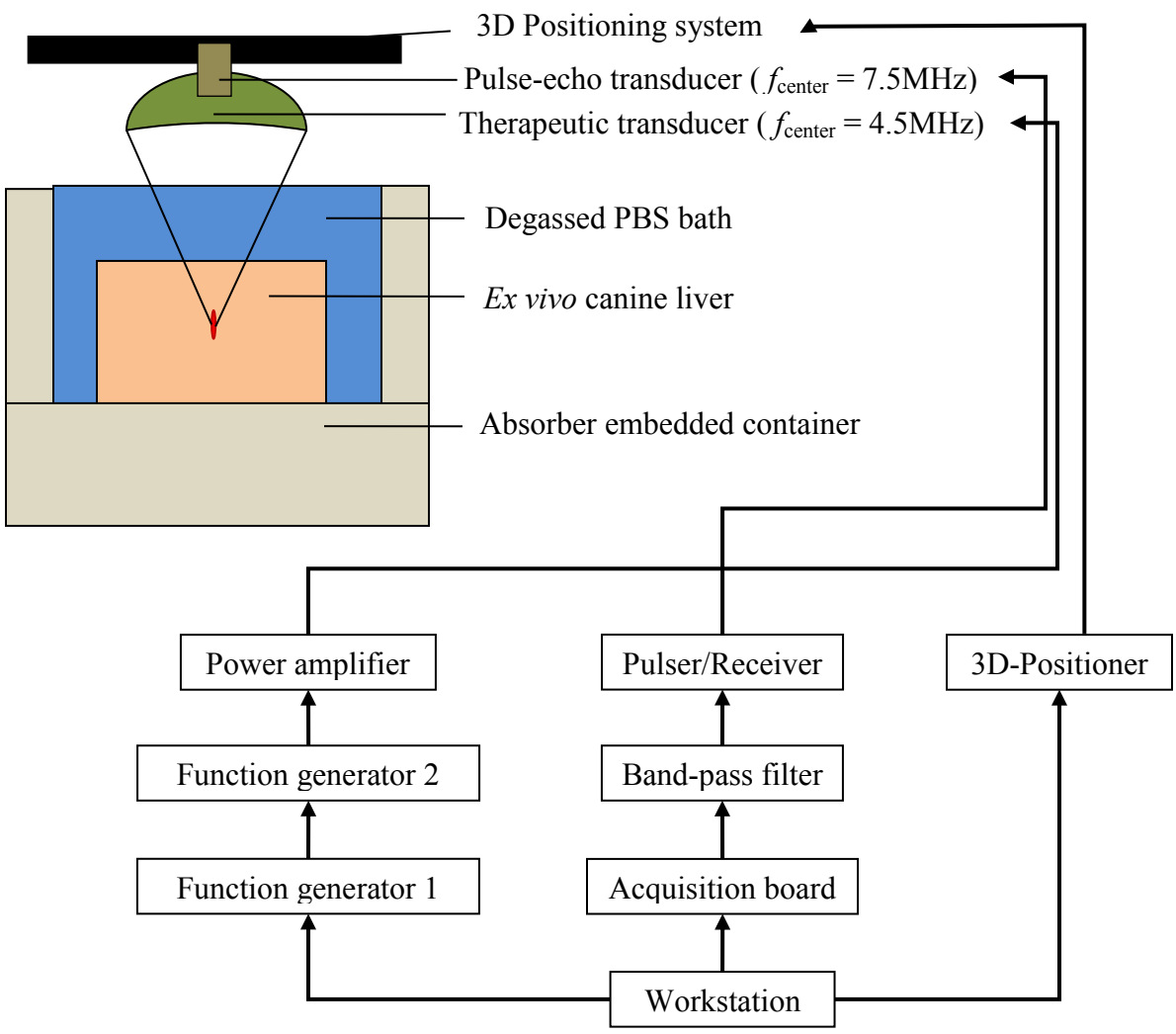

Figure 3.4. 1-D HMIFU experimental set up. The focal depth of the HIFU is 5 cm, i.e., the propagational medium consists of 3 cm water and 2 cm soft tissue, which is same as simulation. Note the 3D positioning system is responsible for HMI raster scan.

The extrapolated *in situ* acoustic intensities were 363 W/cm^2 and 1452 W/cm^2 under imaging and ablation settings, respectively. The focal acoustic beam profile was characterized through a hydrophone based calibration experiment. The HIFU transducer assembly was framed onto a metallic clamp in a degassed water tank. A hydrophone (HGN-0200, Onda Corp,

Sunnyvale, CA, USA) is attached to a PC-controlled 3D axis positioning system (Velmex Inc., Bloomfield, NY, USA), which enabled the mechanical translation during raster scanning. The acquired RF signals were filtered through an analog band-pass filter (Reactel, Inc., Gaithersburg, Maryland, USA) with cutoff frequencies of f_{c1} = 5.84 MHz and f_{c2} = 8.66 MHz (at -60dB) and recorded using a data acquisition unit (Gage applied, Lockport, IL) at a sampling frequency of 80 MHz. 2D-HMI displacement maps were obtained through raster scans before and after lesion formation across a 1-cm^2 region of interest (ROI) surrounding the HIFU lesion (Figure 3.5).

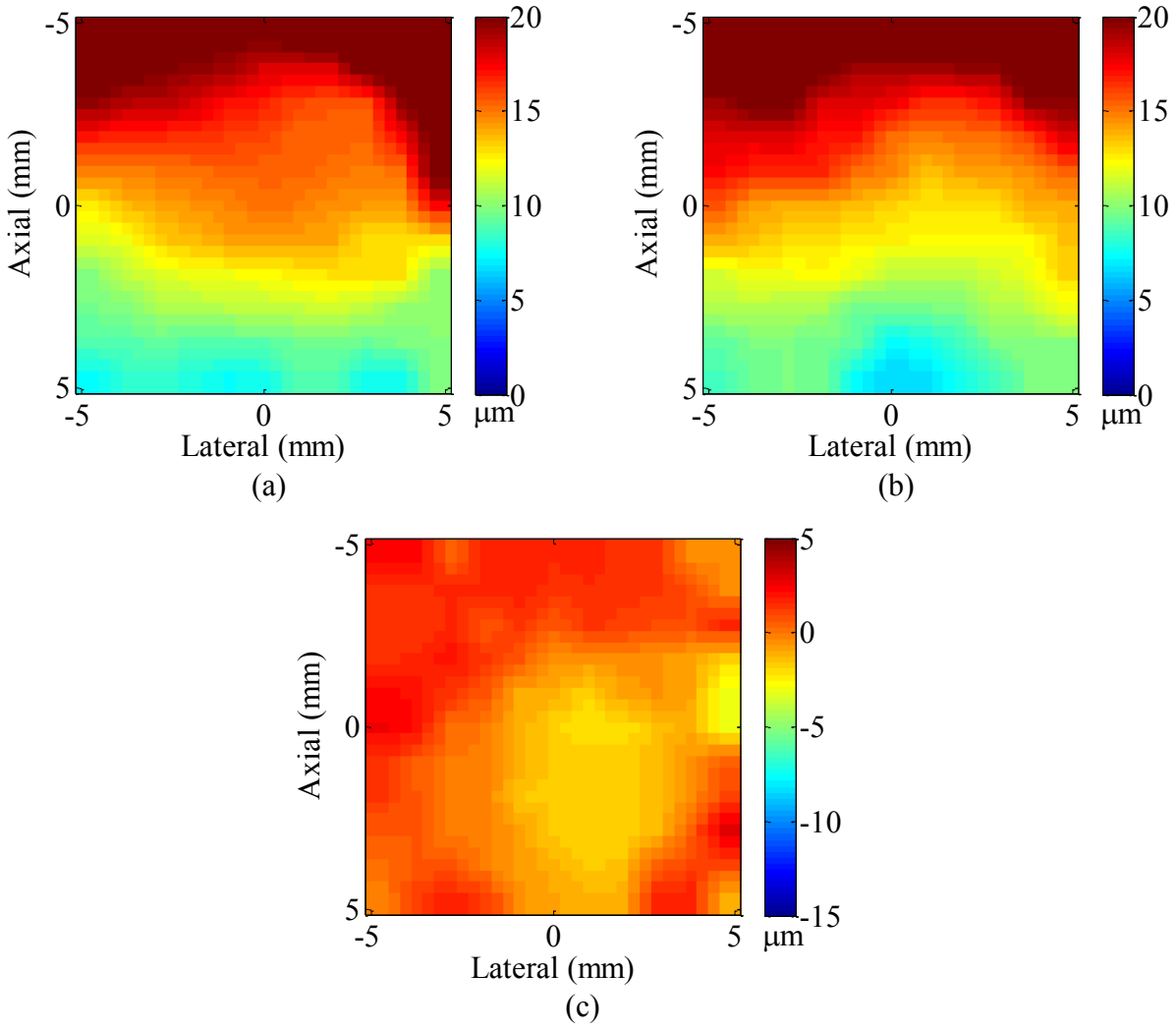

Figure 3.5. HMI experimental displacement map: (a) Before HIFU exposure, (b) after HIFU exposure, and (c) after minus before, i.e., HMI displacement contrast map.

2D-HMI displacement maps were formed as follows: at every acquisition point during the raster scan, a M-mode consisting of 600 RF lines was acquired using the single-element, pulse-echo transducer at a frame rate of 5.4 kHz. Displacements were then estimated using a 1-D normalized cross-correlation (window size of 1 mm and 85% overlap) technique on the received RF signals. Subsequently, a third-order median filter was applied in conjunction with

bilinear interpolation on the displacement map to enhance the image resolution. Based on findings from previous studies, the stiffness increased with HIFU exposure; thus a decrease of displacement was expected within the thermal lesion [154]. The same method was repeated in the 10-, 20-, and 30-s HIFU treatment cases on three separate liver samples. All liver specimens were sectioned along the raster scan plane immediately following the ablation protocol and gross pathology images were acquired upon completion of the study and thresholded in contrast and brightness using Microsoft Office® Picture Manager in order to enhance the visualization of the formed lesions.

3.3 Results

3.3.1 Acoustic and thermal simulation module

Based on the customization of the HIFU simulator mentioned in the methods section, the simulated pressure distribution is based on an approximated intensity field from a plane-circular transducer with equivalent active surface area. Figure 3.6 compares the maps of the simulated intensity fields obtained from the original (Figure 3.6a) and adapted (customized plane circular simulated transducer) (Figure 3.6b) geometries to the experimental case (Figure 3.6c), indicating a closer agreement in both magnitude and pressure distribution after customization. Regarding the consequences of assuming a plane circular transducer with equivalent surface area in simulations, a similar emitted power is obtained but with a difference in the shape of the beam profile (simulation: axial 1.75 x lateral 0.29 mm vs. experimental: axial 2.0 x lateral 0.25 mm).

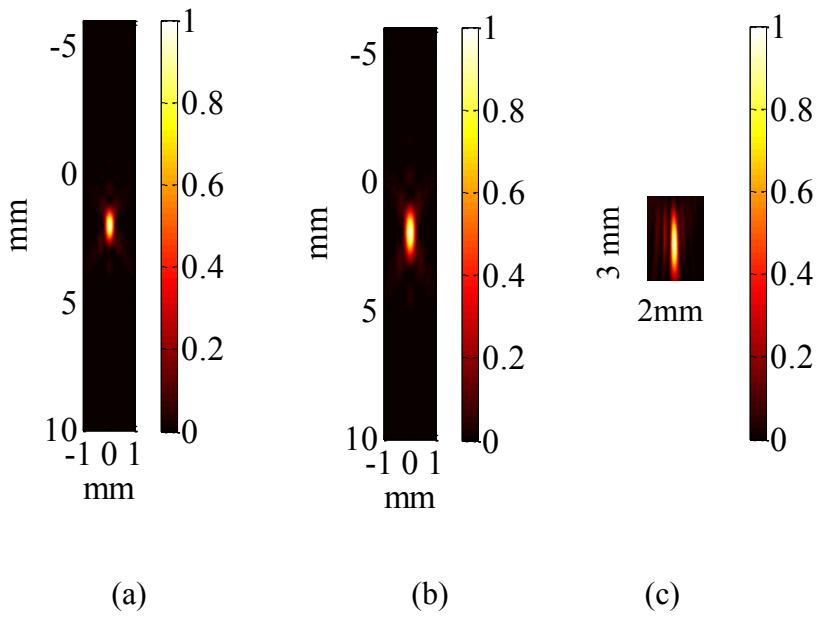

Figure 3.6. (a) -6dB simulated force field without the customization (1.15 mm x 0.26 mm), (b) simulated force field with customization(1.75 x 0.29 mm), (c) experimental beam profile (2.0 x 0.25 mm). At the electric power of 0.20 W, the simulated original, simulated adapted, and experimental acoustic intensities were 21.3 W/cm^2, 17.5 W/cm^2, and 18.5 W/cm^2, respectively. Therefore, a closer agreement between simulations and experiments in the absolute magnitude of the acoustic intensities was achieved by implementing the adapted geometry. However, by ignoring the center aperture in the simulated transducer geometry, difference remains between the experimental and customized simulated force fields.

3.3.2 Finite-Element-Analysis mechanical simulation module

In this finite element module, the simulated intensity map from the previously developed acoustic module was truncated to its -6dB Full-Width-at-Half-Maximum (FWHM) before incorporating into the simulated phantom of the finite element mesh. The AM implementation of HIFU excitation was confirmed through calculation of the low-amplitude oscillatory component in the temperature rise computed by the BHT module (Figure 3.7).

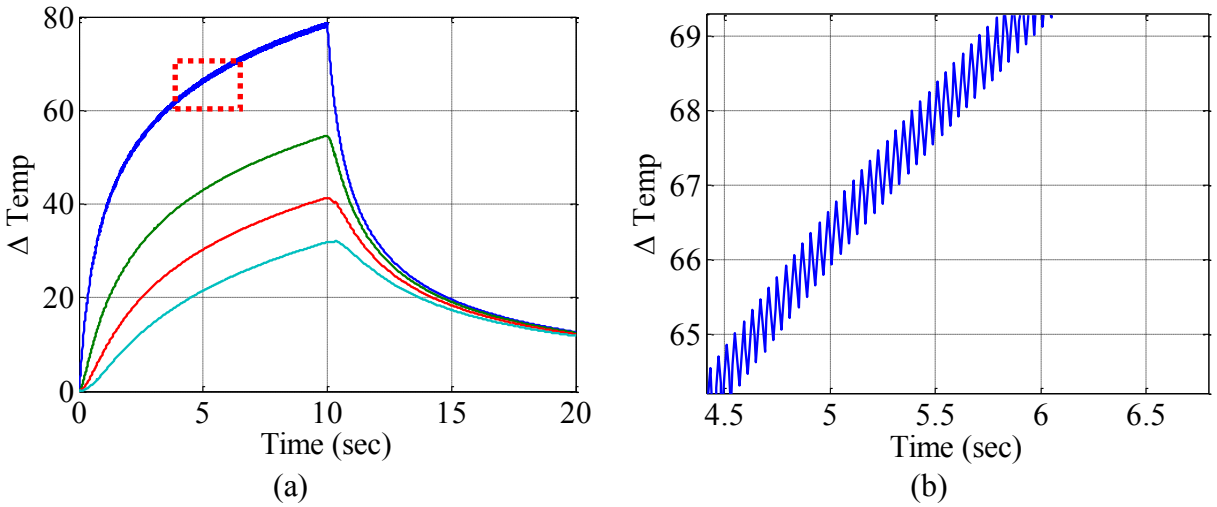

Figure 3.7. (a) Four representative temperature monitoring curves. From top to bottom: in the focus (navy), 0.2 (green), 0.4 (red) and 0.6 mm (cyan) laterally away from the focus, respectively (10 sec HIFU exposure followed by 10 seconds cooling), (b) finer view of a window indicated by the red box in (a), showing the temperature elevation with an oscillatory pattern due to implementation of AM-HIFU beam.

Assuming a 3D ellipsoidal shape, the transverse area of the simulated HIFU lesion incraesed under 10-, 20-, and 30-second HIFU exposure, respectively (Table 3.4), and the lesion

sizes were validated with previously available experimental gross pathology [180]. As previously mentioned, the HIFU lesion maps were assigned to have a lesion-to-background Young's modulus ratio of 1,3,6, and 9 for treatment durations of 0, 10, 20, and 30 seconds with the background remaining constant at 10 kPa (Figure 3.8).

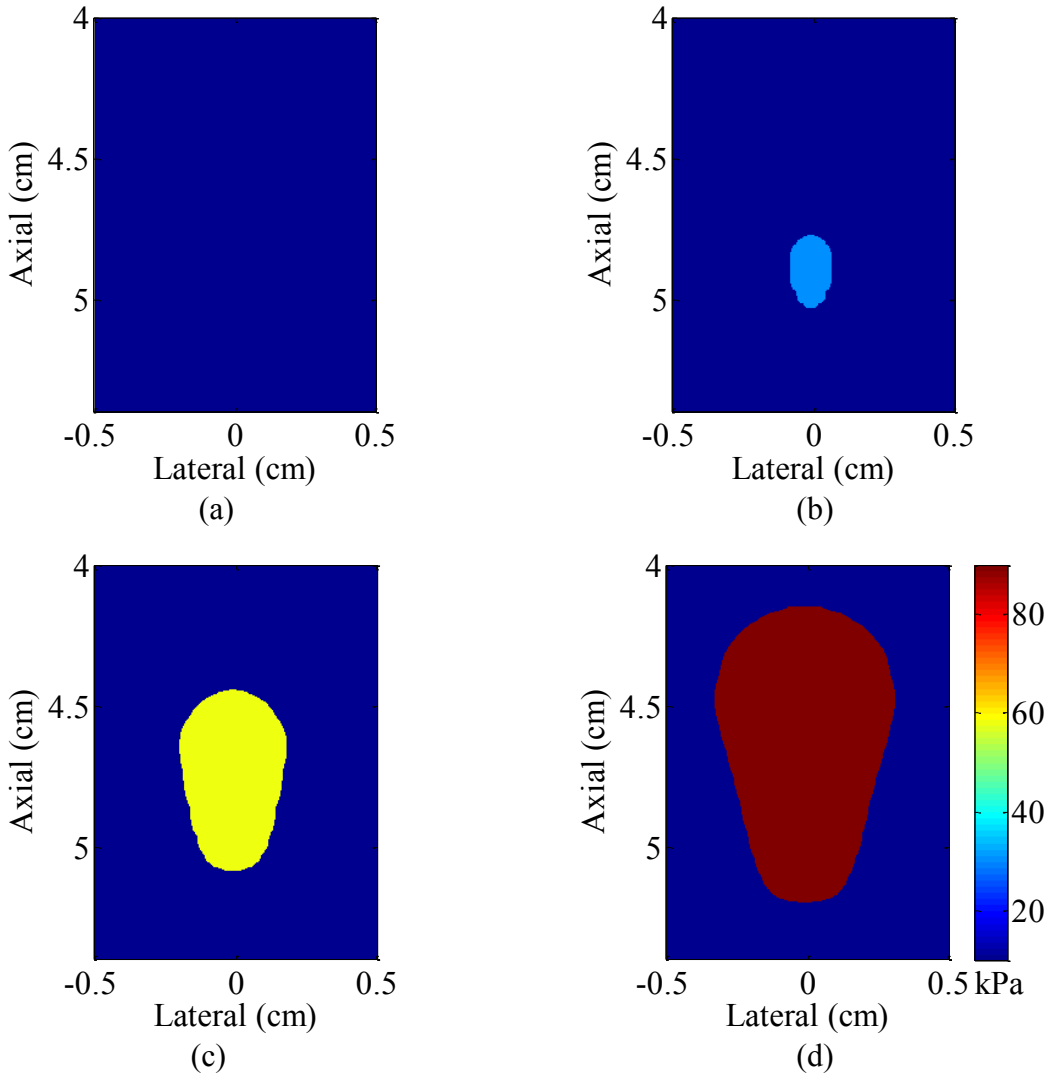

Figure 3.8. Input lesion map assigned at different Young's modulus. Simulated lesion formed under (a) 0 sec, (b) 10 sec, (c) 20 sec and (d) 30 sec HIFU exposure.

Accordingly, the generated displacement profile showed increase of lesion-to-background ratio for the 10-, 20-, and 30-s HIFU exposure case, respectively (Figure 3.9, Table 3.5).

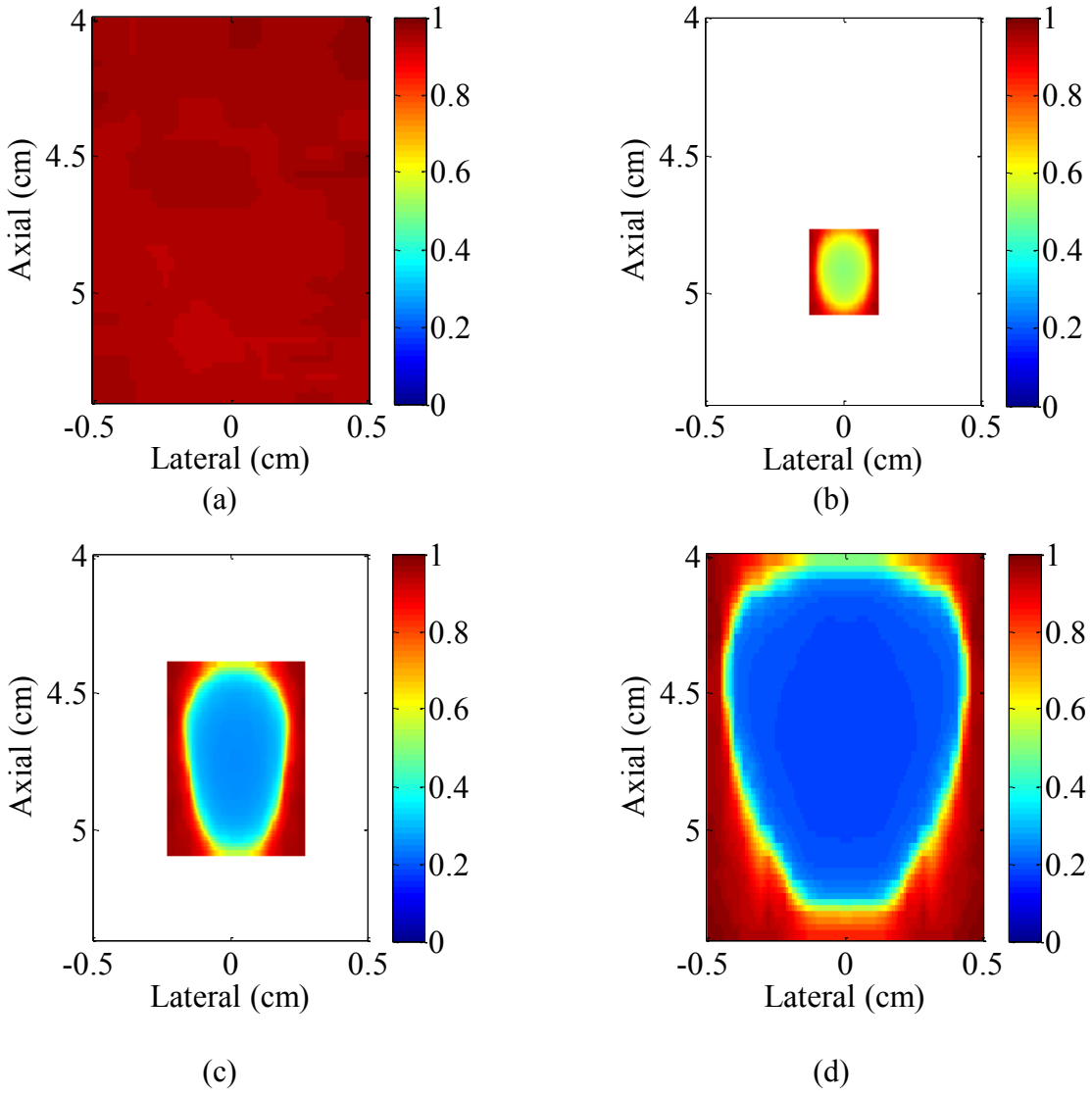

Figure 3.9. Output displacement map generated by FE raster-scan: Displacement map for lesion formed under (a) 0 sec, (b) 10 sec, (c) 20 sec and (d) 30 sec HIFU exposure.

3.3.3 Image Formation and Displacement estimation module

Consequently, the estimated HMI displacement maps (Figure 3.10) also depicted similar increase in both the lesion size and lesion-to-background contrast at the same HIFU exposure durations with a mean average error (over three HIFU exposure cases) of 8.48% and 12.7%, respectively in reference to the true displacement calculated by the finite-element mechanics module (Table 3.4, Table 3.5).

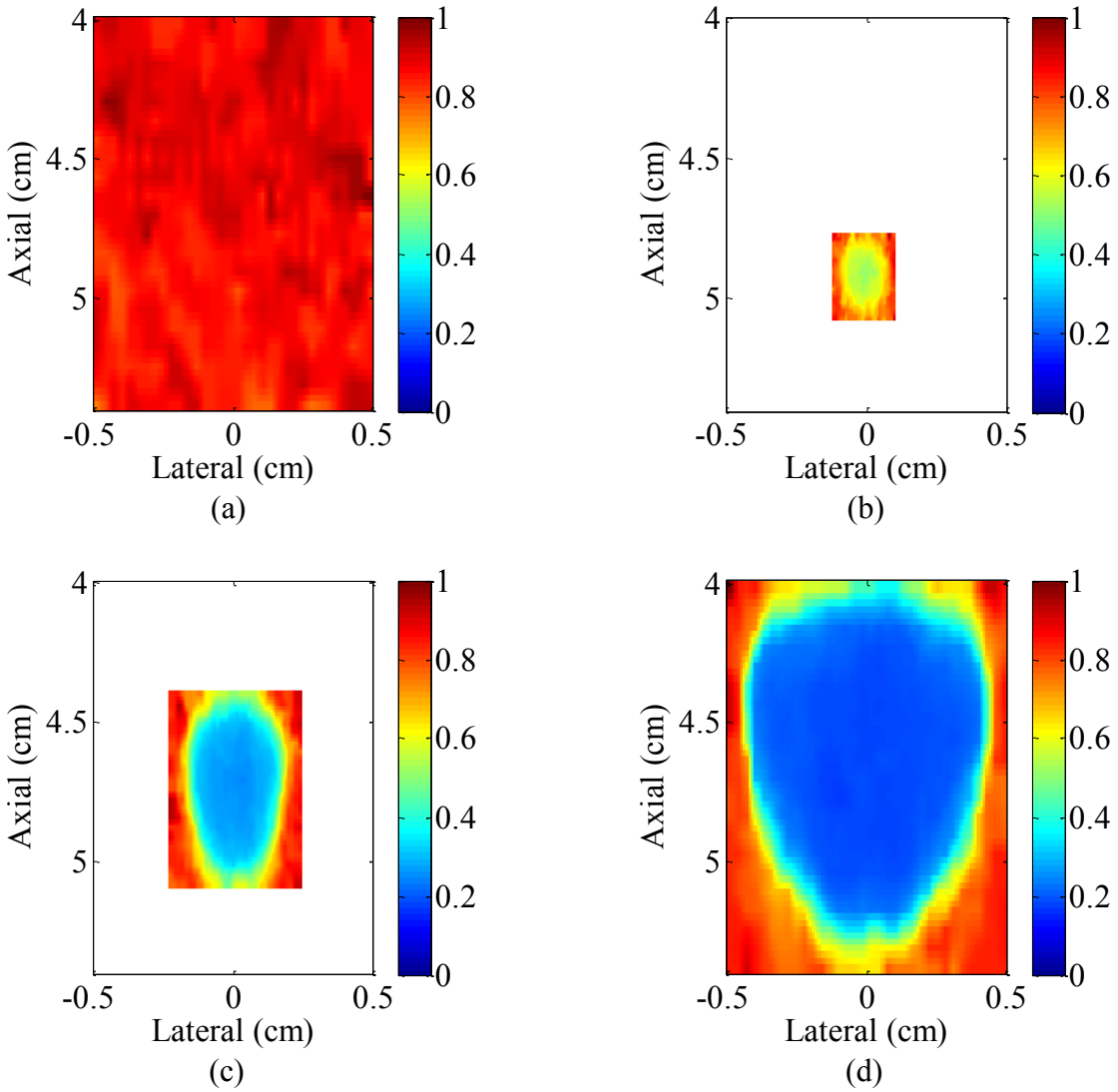

Figure 3.10. Estimated HMI displacement map: Displacement map for lesion formed under (a) 0 sec, (b) 10 sec, (c) 20 sec and (d) 30 sec HIFU exposure.

3.3.4 *Ex vivo* experimental validation

The 2D estimated HMI contrast maps were shown to be in moderate agreement with gross pathology images obtained after completion of the HMI experiments (Table 3.4) in depicting the lesion boundaries as well as the growth in lesion size with an average error of

7.57 %. As previously mentioned, the HMI contrast maps were generated by computing the difference between the two HMI displacement map obtained before and after HIFU exposure. It was also shown that the HMI lesion-to-background displacement contrast linearly increased with the treatment time, i.e., indicating a positive correlation between stiffness and HIFU exposure duration (Figure 3.11).

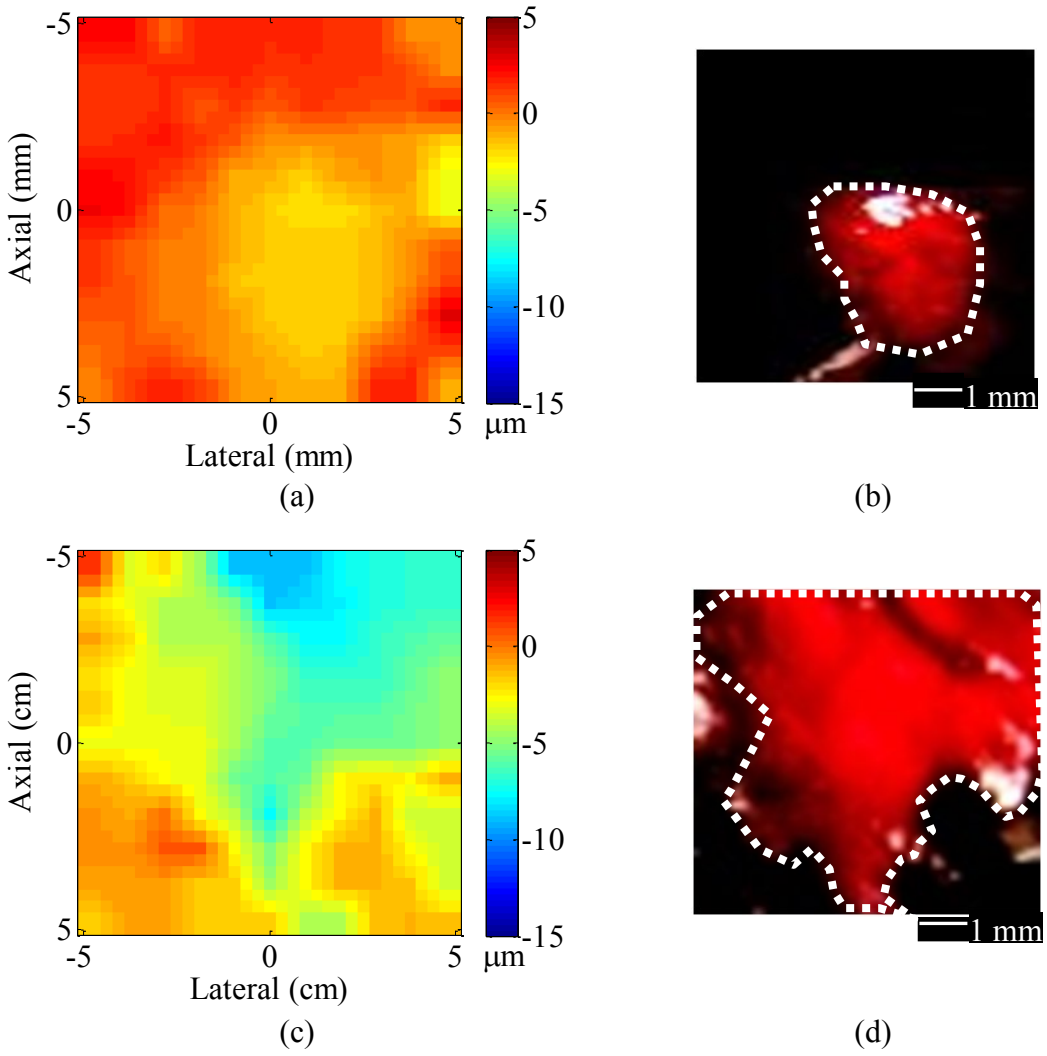

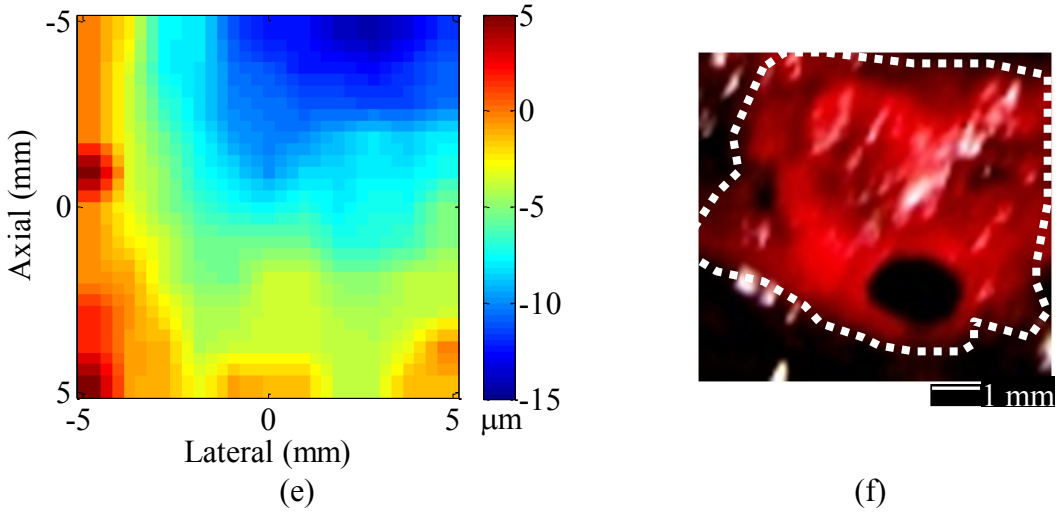

(e) (f)

Figure 3.11. HMI displacement contrast map of lesion formed under (a) 10 sec, (c) 20 sec and (e) 30 sec HIFU exposure. Gross pathology for lesion formed under (b) 10 sec, (d) 20 sec and (f) 30 sec HIFU exposure. White contour lines have been manually added to facilitate depiction of the induced lesion (bright red).

HIFU exposure time (sec) / Lesion Size (mm^2)	10	20	30
Simulation (FE)	13.6	72.0	319.3
Simulation (HMI)	16.2	73.1	334.7
Experimental HMI	26.2	94.2	206.2
Gross pathology	28.2	83.3	201.1

Table 3.4. Comparison of simulated, experimentally mapped HMI lesion sizes. Note the consistent increments in sizes with HIFU exposure duration for all cases.

Lesion-to-background contrast \ HIFU exposure time (sec)	10	20	30
Simulation (FE)	1.83	3.69	5.39
Simulation (HMI)	1.65	3.19	4.59
Experimental HMI	1.19	1.28	1.78

Table 3.5. Comparison of simulated and experimentally mapped HMI lesion-to-background contrast. Note the consistent increments in contrast with HIFU exposure duration for all cases.

3.4 Discussion

HIFU remains the only non-contact, non-ionizing, noninvasive technique for tumor treatment based on thermally inducing cell necrosis with high energy acoustic beams. However, improvements are needed for HIFU in its real-time monitoring and onset lesion detection. To date, numerous techniques for HIFU imaging in both the field of MRI and ultrasound have been developed based on the associated changes in temperature (e.g., MRgFUS, echo shift-based imaging), B-mode, or tissue elasticity (e.g., MRE, Elastography). HMI is a dynamic ultrasound elasticity imaging technique using a simple configuration, i.e., a pair of confocally-aligned HIFU and diagnostic transducers, for respectively inducing focal oscillatory motion while estimating the displacement in real time. HMIFU applies HMI for tumor localization, simultaneous monitoring of HIFU surgery as well as assessment of treatment outcomes. Previous experimental studies have demonstrated the feasibility of HMI and HMIFU *in vitro*, *ex vivo*, and *in vivo*. Previous theoretical studies have investigated the planning and monitoring stages using 1D imaging and direct measurements. In this paper, a theoretical framework was developed to

assess the fundamental capability of the third stage in the HMIFU process, i.e., thermal lesion mapping. The hypothesis was that HMIFU is capable of detecting HIFU lesions based on the change in stiffness and can accurately depict the increase in HIFU lesion size at distinct exposure durations. The objective of this study was to test this hypothesis through the development of a comprehensive 3D theoretical framework that could include the nonlinear wave propagation within a geometry-independent medium. The developed framework included a customized nonlinear acoustic and BHT module for simulation of both the acoustic field and lesion maps, a FE-based mechanical response module, and an image formation module. The simulated findings from the complete sets of the 2D analysis were validated with experiments using canine liver specimens *ex vivo* and the same experimental parameters as in the simulations. Both the simulation and experimental findings demonstrate the feasibility of HMI in both inducing the lesion and detecting the onset of coagulation at different treatment durations based on the change in elasticity [136, 138, 139, 146, 154, 174] as well as quantifying the increase in lesion size with respect to treatment duration [19, 146, 154, 181].

Simulations

In the FE mechanics module, the displacement maps clearly depicted the increase in the lesion size i.e., 13.6, 72.0, 319.3 mm^2 with treatment duration (10-,20-,and 30-s HIFU treatment, respectively). Similarly, an increase in the lesion-to-background ratio (1.83, 3.69, 5.39) was obtained for the modulus contrast of 3, 6, and 9, respectively. Note that the computed displacement profiles had lower values compared to the experimental case (Figure 3.11a,11b,11c). In our framework, we assumed a purely elastic medium with a constant

absorption and no scattering, which may not fully represent the actual tissue properties. The theoretical and experimental studies of tissue viscoelasticity using HMI have been completed in a separate study [182] as well as additional studies to be mentioned in Chapter 4. In addition, a significant contribution to the total body force was found to be induced by the increased sidelobes specific to the transducer geometry used [183], which were not taken into account in this study. Nevertheless, the FE-based framework provided an easily implementable, geometry independent, full 3D model that can be adapted to a variety of configurations.

In the estimated HMI displacement profile in simulations, both the mapped lesion sizes as well as the lesion-to-background displacement contrasts increased with the assigned modulus contrast and treatment time (Tables 3.4 and 3.5). Therefore, the hypothesis that HMIFU is capable of detecting lesions under different HIFU exposure times based on the associated lesion-to-background stiffness increase was validated through the presented framework. Average errors of 8.5% and 12.7% were respectively found in the HMI estimation of the lesion-to-background displacement contrast and lesion size (Table 3.5). Nevertheless, the aforementioned findings demonstrated the value of the developed framework in predicting the performance of HMI under a specific set of parameters and design of the experimental HMIFU system.

Experiments

In the experimental HMI displacement maps, both the detected lesion-to-background displacement contrast and lesion size showed an increased with treatment time, which is in agreement with findings from the theoretical framework (Tables 3.4 and 3.5). Therefore, the experimental findings could validate the theoretical framework and prove the hypothesis

regarding the capability of HMIFU to map the increase in both lesion size and stiffness with the HIFU exposure time. As shown, there was a difference in the lesion-to-background displacement ratio between the simulations and experiments, which could be due to the lower rate of increase of lesion modulus compared to what was modeled in simulations. This will be further investigated in future studies. Some discrepancies were found in both the lesion size and displacement contrast between the simulations and experiments. This is in part due to the use of a convolutional model in simulations, the ignored change of absorption in simulations, the depth-dependent attenuation in experiments (Figure 3.5a, 3.5b), the difference in SNR and the boundary effects due to hepatic pores and vessels. Framework improvements are ongoing taking these effects into account.

3.5 Conclusions and Summary

In conclusion, a 3D, FE-based simulation framework comprised of a nonlinear wave propagation model coupled with a Bioheat Transfer (BHT) module, a finite-element (FE) based mechanics module and an image-formation model, was developed for assessing the feasibility of HMIFU lesion mapping. In both simulations and experiments, HMI was capable of depicting the lesion size increase as well as the lesion-to-background displacement contrast. Therefore, given the experimental validation of this theoretical framework, it can be used to design and predict experimental HMIFU systems. In the following chapter, the design, development, and experimental validation of two separate experimental HMIFU systems will be discussed. The two platforms to be discussed are: 1) a 1D-based platform used for *in vitro* and *ex vivo* based study, as well as 2) a 2D-based platform for preclinical and clinical translation of HMIFU. In

addition, the outcomes of multi-parametric studies using the developed platforms will also be discussed, where investigations were performed to optimize biomechanical, acoustical, and thermal monitoring of lesion formation using two types of clinically implemented HIFU treatment sequences.

Chapter 4. 1-D HMIFU system based HIFU treatment monitoring

4.1 Introduction

4.1.1 1D-HMIFU System

In this chapter, the development a 1D-based platform is described, which was composed by a HIFU transducer coupled with a single-element pulse-echo transducer. This chapter will first introduce the 1D-HMIFU system, followed by two optimization studies utilizing the 1D-HMIFU system for a multi-parametric monitoring of HIFU treatment with boiling and slow denaturation based on HMI displacement, phase shift, temperature, and Passive Cavitation Detection (PCD), and mechanical testing. The subsequent chapter 5 will focus on the development of a pre-clinical 2D-HMIFU system along with its preliminary feasibility as well as another multi-parametric optimization study using HMI displacement, temperature, and mechanical testing.

The prior prototype of the 1D-HMIFU system comprised of a 4.75MHz focused Lead Zirconate Titanate (PZT) (outer diameter 80 mm, inner diameter 16.5 mm, focal depth 9 cm) transducer (Riverside Research Institute, New York, NY) for vibrating tissues at an AM frequency of 25 Hz, and a confocal 7.5 MHz single-element pulse-echo transducer (Olympus-NDT, Waltham, MA, U.S.A.) with a diameter of 15 mm and a focal length of 6 cm for simultaneous RF signals acquisition [154]. During raster scan imaging, the coupled transducers were adjusted mechanically through a 3D translational system (Velmex Inc., Bloomfield, NY,

U.S.A.) for targeting and raster scan purposes. The received RF signals were band-pass filtered (Reactel, Inc., Gaithersburg, Maryland, USA) with cutoff frequencies of f_{c1} = 5.84 MHz and f_{c2} = 8.66 MHz (at -60dB) and recorded along with the excitation signal representing the force profile and a dual-channel data acquisition unit (Gage applied, Lockport, IL, U.S.A.) at a sampling frequency of 80 MHz. Subsequently, a 1-D normalized cross-correlation technique[177] was used to estimate the displacement and axial compressive strains were estimated using a least-square estimator on the RF signals [184]. Further details of the additional improvement on the 1D-HMIFU system will be discussed in sections 4.1.3 and 4.1.8, respectively.

4.1.2 Multi-Parametric HIFU monitoring using 1-D HMIFU System

Monitoring of HIFU treatment remains as the most challenging and critical aspects of its clinical translation requiring both high frame rate and spatial resolution within the localized focal zone. To date, several techniques have been developed with an interest in monitoring the focal tissue environment under HIFU treatment. MRI-guided Focused Ultrasound (MRgFUS) [28-31, 35, 185] is the current standard monitoring modality which provides a focal temperature map at a feed-back frame rate of 0.1 to 2 Hz and millimeter resolution. It is based on changes in the tissue proton-resonance frequency, which is associated with the water proton chemical shift resulting from rupture, stretching, or bending of hydrogen bonds in a temperature elevated environment [36]. Acousto-optic sensing is a recently developed, cost-effective modality capable of monitoring the change in tissue optical absorption and scattering using a modulated light with HIFU beams during treatment [43, 44]. Several acoustic echo signal-based techniques [186, 187]

have also utilized either changes or rise in harmonics through spectral analysis of the backscattered signals in order to detect thermal lesion formation.

HIFU tissue elasticity imaging focuses on detecting and monitoring the onset and progress of tissue elasticity and/or viscosity throughout the entire treatment. Currently, several techniques have investigated and proven its potential in HIFU monitoring including Magnetic Resonance Elastography (MRE) [69, 133-135], Supersonic Shear Wave Imaging (SSI) [152, 153], Acoustic Radiation Force Impulse (ARFI) Imaging [151], and Harmonic Motion Imaging for Focused Ultrasound [154, 188]. Both MRE and SSI are capable of monitoring the change of tissue mechanical properties through estimation of the shear wave velocity, where the tissue motion is induced either by an external mechanical exciter (MRE) or *in situ* plane wave generated using a series of focused acoustic beams (SSI). ARFI has recently shown feasible in ablating and monitoring formation of thermal lesions through operation of a customized beam sequence using a conventional curvilinear imaging probe [151]. Each of the aforementioned monitoring technique possesses unique advantages: MRE is capable of quantitatively monitoring shear modulus changes with sub-millimeter spatial resolution through the entire ablation sequence, SSI is capable of assessing the shear modulus change of high frame rates under a frame acquisition rate up to 10,000 frames/sec and a shear modulus mapping rate up to 0.333 frames/sec) [115], and ARFI imaging is capable of utilizing a cost-effective conventional imaging system to induce and monitor lesion formation.

Nevertheless, MRE can be costly while operating at frame rates of 0.5-10 Hz and one of the primordial unsolved issues of HIFU, lies with the long duration of the procedures. Therefore, real-time feedback on the effectiveness of lesioning is warranted. This is achieved by providing information on the success of the treatment (i.e., coagulation) in real time, i.e., fast and before

having moved to the next site of treatment. Therefore, it is important to develop monitoring techniques that can achieve the cost-effectiveness without the use of MRI, providing true real time capability in ideal registration with the treatment, i.e., maintaining high frame rates at the kHz range in localized HIFU focal zone, while not interrupting or slowing down the HIFU treatment Harmonic Motion Imaging for Focused Ultrasound (HMIFU) couples a HIFU transducer emitting an Amplitude-modulated (AM) beam for inducing stable oscillatory tissue probing at its focal zone while the response is acquired through a confocally-aligned pulse-echo imaging transducer [154]. Band-pass filtering is performed on the RF signals from pulse-echo imaging transducer in order to remove the interference from the HIFU beam, and the oscillatory tissue motion is then estimated using a 1D cross-correlation method.

Several HMIFU feasibility studies have been completed for *in vitro* [81, 189], *ex vivo* [154], and *in vivo* [156, 157] applications. However, monitoring HIFU ablation with boiling was not studied using this technique. In HIFU treatment, tissue boiling usually occurs at the focal region when tissue is being exposed at the highest acoustic intensity, where bubbles may form from thermal mechanisms such as boiling of fluid in blood or tissue, or mechanical mechanisms such as growth of tiny cavitation nuclei inside the tissue by the negative pressure of the induced nonlinear acoustic waves [190, 191]. Occurrence of the formation of such boiling bubbles is unpredictable and the nonlinear wave induced at high intensities may lead to an increased absorption, i.e., higher thermal dosage, thus presenting a potential challenge for the currently existing temperature estimation-based monitoring modalities. Nevertheless, in the literature of HIFU treatment on cancerous tissues, numerous studies have indicated the importance of high intensities (2-20 kW/cm^2) capable of inducing boiling [129, 192, 193] given the resistive nature and proliferated vasculature among cancerous cells [194]. Additionally, a group of studies have

investigated the histological changes between normal and cancerous cells following HIFU treatment and inferred that effective cell death in cancerous tissues requires higher intensities compared to those under normal conditions [195, 196]. Despite this interesting aspect, the performance of current clinical monitoring techniques using B-mode or MRI is limited under HIFU treatment with boiling. The B-mode is only capable of indicating hyperechoic regions denoting formation of bubbles, yet the bubbles are unstable and do not necessarily delineate the entire lesion extent [197]. On the other hand, the temperature monitoring using MRI loses its accuracy as the initiation of boiling is unlikely to be registered as 100 ºC or above, which could potentially question the accuracy of any ablation volume calculation using MR-based thermal dosage [191].

Therefore, it is crucial to assess the performance of HMIFU under such boiling conditions using high acoustic power levels where HIFU treatment is proposed to be more effective and efficient through both thermal (protein denaturation due to heat-shock) and mechanical (cavitation) damage. Moreover, amongst the previous studies, focal displacement has been the only tracking parameter representing a qualitative and relative change of stiffness of focal tissue accounting for both acoustic and mechanical changes under HIFU treatment. To further improve the assessment quality of HMIFU, therefore, requires a comprehensive and complementary assessment of focal tissue mechanical properties. Here, a multi-parametric monitoring study is proposed, which investigates four different parameters, namely displacement, phase shift, compressive strain, and 2D mapping to monitor and assess the tissue stiffness change during and following HIFU treatment. From our previous work [132] the peak-to-peak amplitude of HMI focal displacement first increases then decreases as tissue undergoes softening-followed by-stiffening during slow thermal ablation, which is the pattern of stiffness

change under slow denaturation [198, 199]. Nevertheless, lesions induced by high power with boiling forms much more rapidly thus stiffening occurs much earlier in time during treatment period. We therefore hypothesize that a multi-parametric monitoring approach would improve the HMIFU reliability in the sense that 1) focal phase shift ($\Delta\varphi$) will serve to decouple changes in mechanical and acoustical tissue responses; 2) compressive strains would serve to confirm the displacement assessment within the focal region, and 3) the 2D HMI displacement image will accurately delineate the lesion margins. In this study, we present a multi-parametric approach to enhance the reliability of the HMIFU technique for real-time HIFU treatment with the capability of 1) monitoring thermal lesion formation under HIFU-induced boiling, 2) comprehensive lesion assessment using three main HMI parameters, and 3) decoupling changes in mechanical from those in acoustical tissue properties under HIFU treatment.

4.1.3 HMIFU Monitoring parameters

a. HMI focal Displacement

In HMIFU, the amplitude-modulated HIFU beams induce a sinusoidal displacement profile at the geometric focus. The motion originates from the acoustic radiation force generated due to the energy absorption from the HIFU beam, which was previously derived and indicated as follows [171, 172]:

$$F = \frac{2\alpha I}{c}, \qquad (1)$$

where I is the *in situ* acoustic intensity field, α is the acoustic absorption coefficient, and c is the speed of sound. The relationship between induced displacement and excitation force can be described from the general theory of wave propagation within a linear elastic medium:

$$\rho \frac{\partial^2 u}{\partial^2 t} = (K + \frac{\mu}{3}) \nabla(\nabla \cdot u) + \mu \Delta u + \rho F, \quad (2)$$

where ρ is the density of the medium, K is the bulk modulus, μ is the shear modulus, F is the volumetric force, and u is the induced displacement. Note that in this study, we focus our investigation along the propagation direction (z), i.e., $F = F$ (z), and μ (z). In HMIFU, an oscillatory response is induced at the HIFU focal zone due to the AM-HIFU excitation (Figure 4. 1(d)), namely the HMI displacement. Although the displacement may also arise from thermal expansion and variation in speed of sound, they are considered to be much smaller than the oscillatory mechanical motion generated by the acoustic radiation force from the AM-HIFU beam in the case of HMI as we have reported elsewhere [154]. This HMI displacement is monitored throughout the entire HIFU treatment duration. The relative change of the peak-to-peak HMI displacement amplitude with respect to the displacement at the baseline, i.e., at the beginning of the HIFU treatment, can be correlated with the relative change in local tissue stiffness as the thermal lesion develops. Until now, the displacement parameter has been the main parameter used; nevertheless, displacement is a qualitative parameter which accounts for changes in both the acoustic and mechanical properties at the focus during HIFU treatment. For example, displacement may not clearly reveal the relative changes in tissue stiffness when stiffening occurred along with increase of acoustic absorption, i.e., increased displacement amplitude. Therefore, complementary approaches are required to improve the reliability of HMIFU.

b. Relative change in phase shift

Within the acoustic focal zone where displacement is monitored, another parameter, phase shift, can also be monitored (Figure 4.1). The phase shift refers to the phase angle difference between the applied force and induced displacement profile. In the frequency domain, the complex modulus can be derived from calculating the ratio between the oscillatory excitation force and the induced displacement with a delay φ [182],

$$\frac{\sigma(\omega)}{\varepsilon(\omega)} = \frac{\sigma_0 e^{i\omega t}}{\varepsilon_0 e^{i(\omega t-\varphi)}} = G' + iG'', \qquad (3)$$

where σ_0 is the pressure amplitude, ω is the modulation frequency, ε_0 is the strain amplitude, i^2 = -1, G' is the shear storage modulus, G'' is the shear loss modulus, φ is the phase angle between force and displacement profile, and t is the time. The phase angle between these two functions is simply the ratio between G' (elasticity) and G'' (viscosity).

$$\frac{G'}{G''} = \frac{1}{\tan(\varphi)} \qquad (4)$$

The phase shift is capable of providing the ratio of the shear storage to the shear loss modulus, i.e., the ratio of the tissue elasticity to the viscosity. Although phase shift by itself requires quantification using shear or Young's modulus, it nevertheless represents a standard biomechanical parameter independent of changes in the tissue acoustic properties. As the Young's modulus represents tissue elasticity, the phase shift is a model-independent biomechanical parameter that can be used to assess the tissue viscoelasticity. Also, the HMI phase shift is a localized parameter that is estimated using the only the phase of focal displacement and force during the force application. In this study, we will investigate the

relative change in the difference of phase shift degree across the monitoring stage with respect to starting time of treatment (t_0), namely $\Delta\varphi$, or namely, the relative change in focal phase shift ($\Delta\varphi$). The reader is referred to Vappou et al., (2009) for a comprehensive viscoelasticity investigation using HMI.

$$\Delta\varphi = \varphi(t) - \varphi(t_0) \qquad (5)$$

c. Compressive Strain

In the presented HMIFU study, compressive strains can be estimated at adjacent regions of the focal zone in the axial direction (ε_{zz}), which can be estimated through calculation of the spatial derivative of the displacement:

$$\varepsilon_{zz} = \frac{\partial u_z}{\partial z}, \qquad (7)$$

Where ε denotes the strain tensor, z denotes the axial direction, and **U** denotes the displacement vector. In this study, we studied three cases of the axial compressive strains during monitoring for treatment of 10W at 10, 20, and 30 seconds, respectively. Strain monitoring cases from other treatment parameters were not included due to poor signal to noise ratio (SNR) amongst the estimated focal displacements.

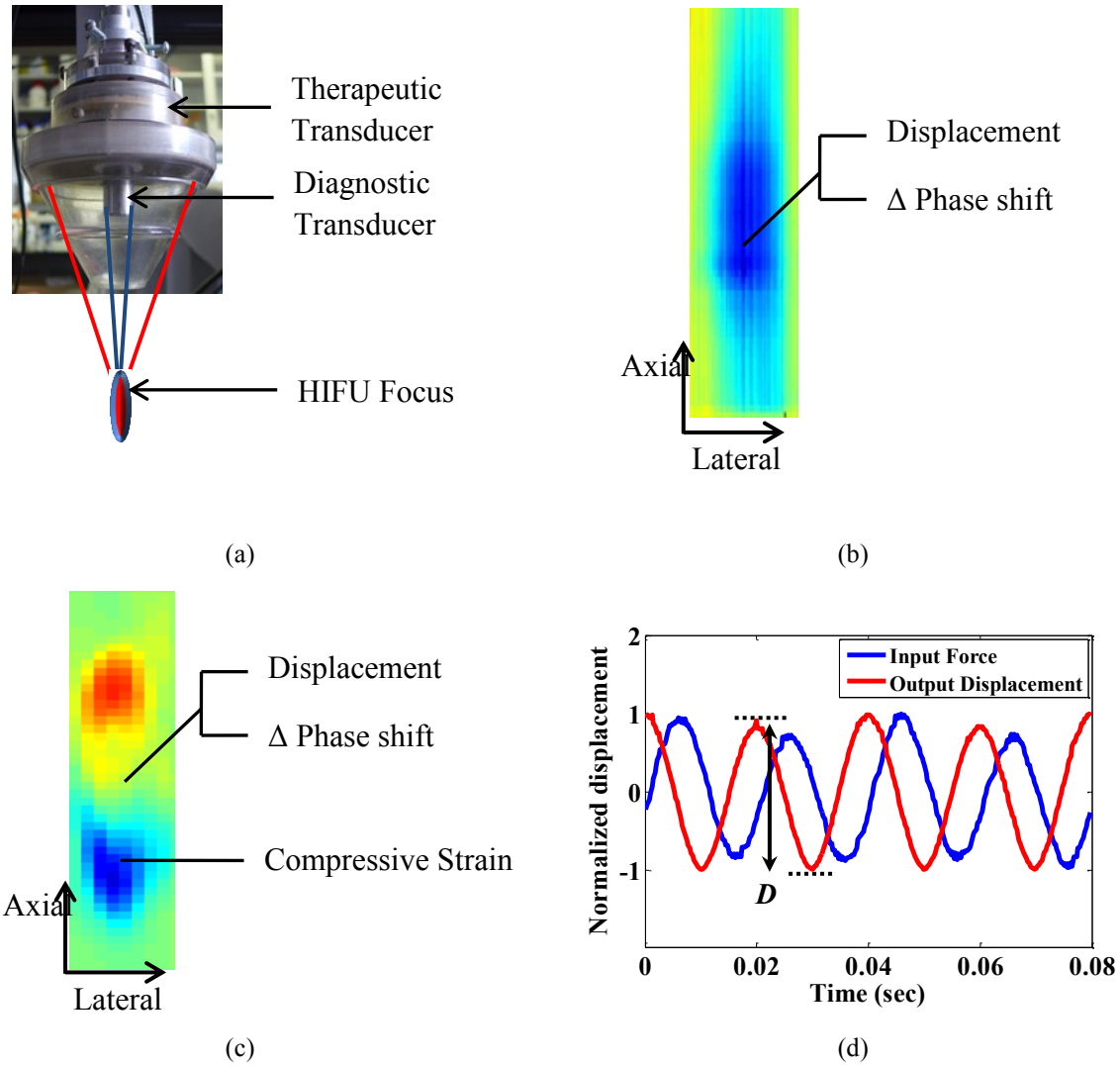

Figure 4.1. (a) The schematic description of HMIFU multi-parametric framework. (b) 1-cycle of HMI focal displacement M-mode. Both Δφ and displacement are estimated from values extracted within the focal region. (c) Strain distribution estimated using least square estimation on the same 1-cycle HMI focal displacement M-mode as (c). Note that only compressive strain is being investigated here. (d) Δφ corresponds to the phase angle difference between the registered input force (Blue curve) and induced focal displacement (Red). The D indicated here refers to the HMI focal displacement, which is the peak-to-peak displacement in the oscillatory response under AM-HIFU beam excitation.

Experimental protocol

Canine livers (subject=7, lobes = 28) were excised immediately upon animal sacrifice and immersed into a degassed Phosphate buffered saline (PBS) solution bath maintained at room temperature. All procedures were approved by the Institutional Animal Care and Use Committee (IACUC) of Columbia University. Each specimen was fixed using metallic needles onto an acoustic absorber submerged in a de-ionized and degassed PBS tank. The HMIFU system was comprised of a 4.75MHz focused Lead Zirconate Titanate (PZT) (outer diameter 80 mm, inner diameter 16.5 mm, focal depth 9 cm) transducer (Riverside Research Institute, New York, NY) for probing tissue with an AM frequency of 25 Hz, and a confocal 7.5 MHz single-element pulse-echo transducer (Olympus-NDT, Waltham, MA, U.S.A.) with a diameter of 15 mm and a focal length of 6 cm for simultaneous RF signals acquisition at a frame rate of 4 kHz. Raster scans were completed by mechanically moving the transducers through a 3D translational system (Velmex Inc., Bloomfield, NY, U.S.A.) for targeting and raster scan purposes (Figure 4.2).

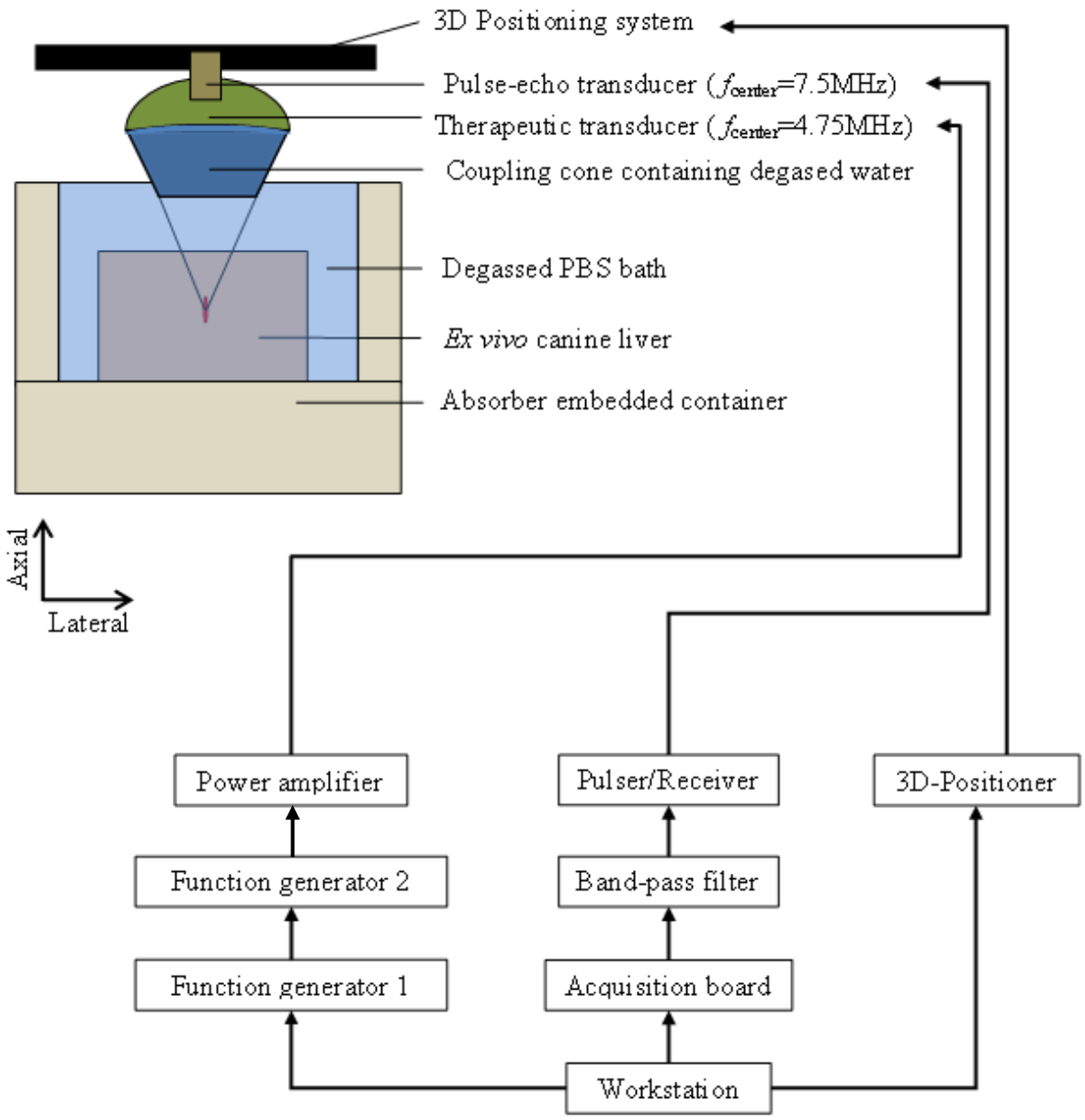

Figure 4.2. HMIFU experimental set up and data flow. The focal depth of the HIFU is 9 cm and the focal spot lies at 3.4 cm below of the tip of the coupling cone containing degassed water. Note the 3D positioning system is responsible for HMI raster scan.

The extrapolated *in situ* focal acoustic intensity and power was equal to 5546 W/cm^2, 7164 W/cm^2, and 9067 W/cm^2, at 8W, 10W, and 11W, respectively. The treatment power and duration were selected to fall within the boiling regime range and so as to investigate the performance of HMI under different power and duration as typically used in HIFU [200]. The received RF signals were band-pass filtered (Reactel, Inc., Gaithersburg, Maryland, USA) with cutoff frequencies of f_{c1} = 5.84 MHz and f_{c2} = 8.66 MHz (at -60dB) and recorded along with the excitation signal representing the force profile and a dual-channel data acquisition unit (Gage applied, Lockport, IL, U.S.A.) at a sampling frequency of 80 MHz (Figure 4.2). Subsequently, a 1-D normalized cross-correlation (window size of 3.85 mm and 90% overlap) technique [177] was used to estimate the incremental HMI displacement and axial compressive strains were estimated using a least-square estimator on the RF signals [184]. In each HMIFU treatment, 2D transverse HMI displacement maps were also obtained through raster scan acquisition before and after lesion formation. A 3 x 3 median filter was applied on the displacement profiles in order to enhance the SNR of the displacement map. Lesion-to-displacement contrast values were assessed by taking the ratio of HMI focal displacement outside to that inside of the mapped thermal lesion on the 2D transverse HMI displacement map after the HIFU treatment. In order to confirm the presence of tissue boiling at the proposed treatment level, Passive Cavitation Detection (PCD) monitoring was also performed by operating the conically-aligned pulse-echo transducer in passive mode in conjunction with thermocouple measurement. Focal temperature monitoring was performed by inserting a T-type bare wire thermocouple with diameter of 25 μm (Omega Inc., Stamford, CT) inside the tissue. The diameter of the thermocouple was chosen to be smaller than 1/10 of the carrier wavelength in order to minimize reflection and viscous heating artifacts [201].

4.1.4 Results

First, PCD monitoring were investigated at the three acoustic power levels of 8, 10, and 11 W for 30 seconds, respectively, where all spectrograms detected significant increase in broadband noise, indicating formation of strong bubble dynamics likely to be induced by tissue boiling (Figures 4.3a, 4.3b, 4.3c) [200].

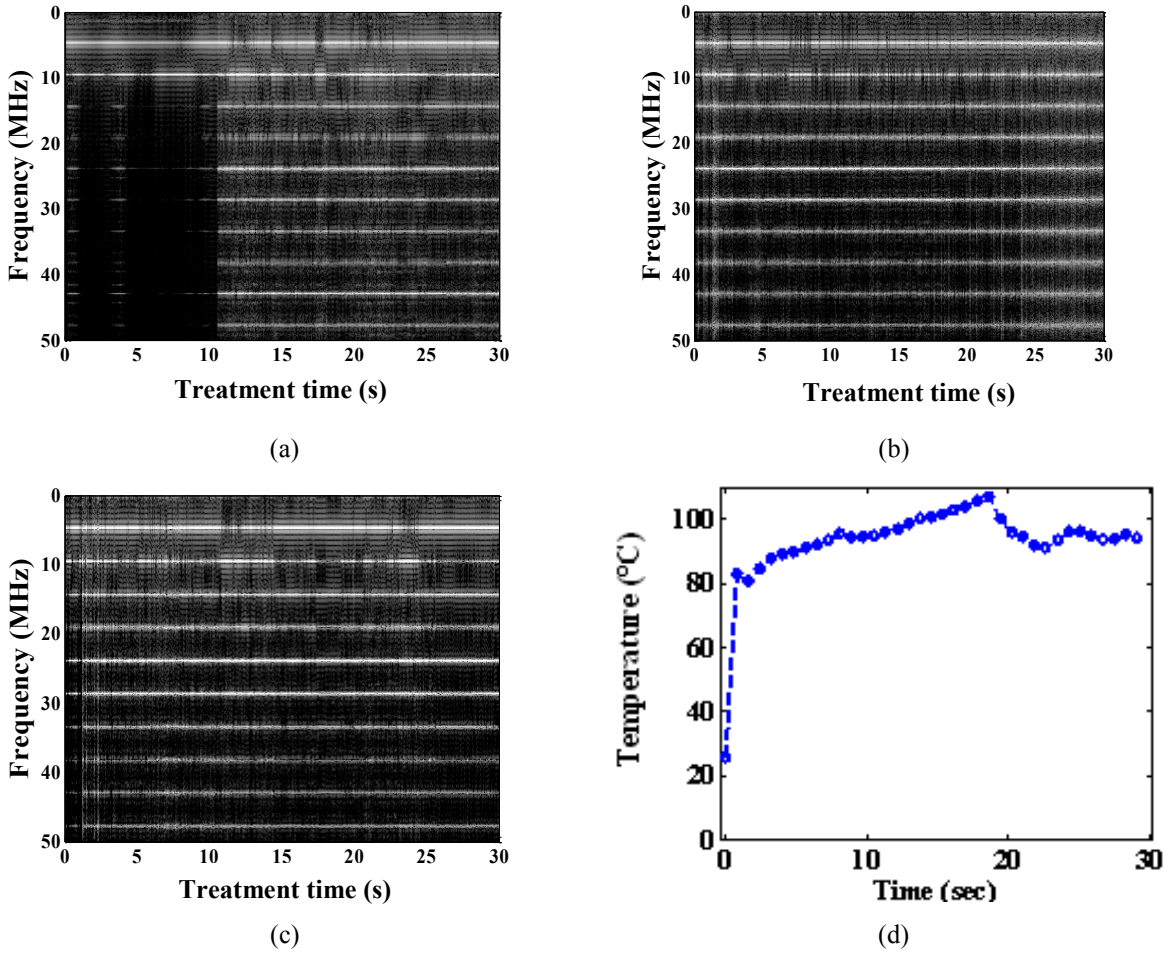

Figure 4.3. Passive Cavitation Detection (PCD) Spectrograms at acoustic power of 8W (b), 10W (c), and 11W (d) all showed significant increase in broadband noise energy, confirming formation of strong bubble dynamics due to boiling. (d) Representative temperature monitoring using T-type bare-wire thermocouple indicates boiling within the first several seconds from treatment onset, indicating presence of unsteady state throughout each monitoring case.

The thermocouple temperature measurement at the minimum power case of 8W also confirmed the presence of boiling; display of a sharp exponential increment followed by an unsteady trend around 100^{o} C, which is a result of the shielding effect due to bubble formation at

the focal region (Figure 4.3d). Consequentially, forty-three HIFU lesions were induced across all of the treatment power levels with the presence of boiling throughout this study. We first investigated our studies on nine HMIFU treatments on three pieces of *ex vivo* canine livers where HIFU treatments were repeated under acoustic intensity and power of 7164 W/cm^2 and 10 W for durations of 10-, 20-, and 30-s. As the treatment duration increased, both the relative change in peak-to-peak value of HMI focal displacement (-8.67±4.80, -14.44±7.77, -24.03±12.11 μm) and peak axial compressive strain (-0.16±0.06, -0.71±0.30, -0.68±0.36 %) exhibited decrease throughout the treatment, whereas the Δφ showed slight increase at 10 s and significant decrease at 20, 30-s cases (+1.80±6.80 º, -15.80±9.44 º, -18.62±13.14º) (Figures. 4.4 and 4.5) with a few monitoring time-points around the focal zone where Δφ exhibited an increase in spatial variation.

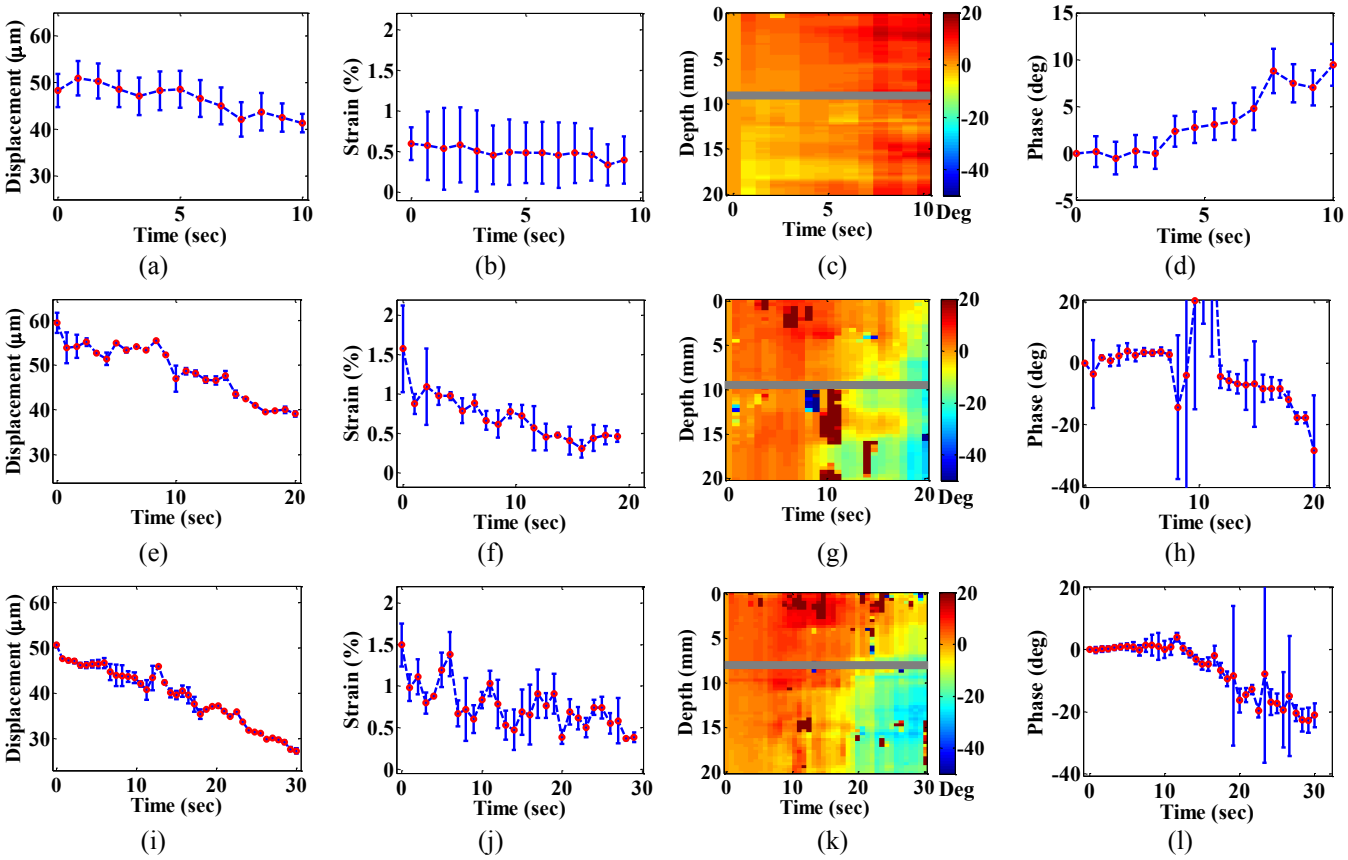

Figure 4.4. Example cases of multi-parametric HMIFU monitoring from first set of investigations. HIFU treatment of acoustic power were all set to be 10 W for 10 (a-d), 20 (e-h), and 30 second (i-l), respectively. Mean displacement, strain, and phase shift values were estimated across the HIFU focal zone (placed at approximately 10 mm from the surface of liver as indicated by the thick grey line on the Δφ M-mode (c,g, k). As shown, decrease trends were observed for both displacement (a,e,i) and strain. Δφ was observed to increase slightly amongst the 10 second cases but decrease significantly amongst the 20 and 30 second cases. The decorrelation points throughout the 2D phase shift M-mode (c,g,k) , as well as phase shifts at the focal zone (d,h,l), are likely to be linked to boiling.

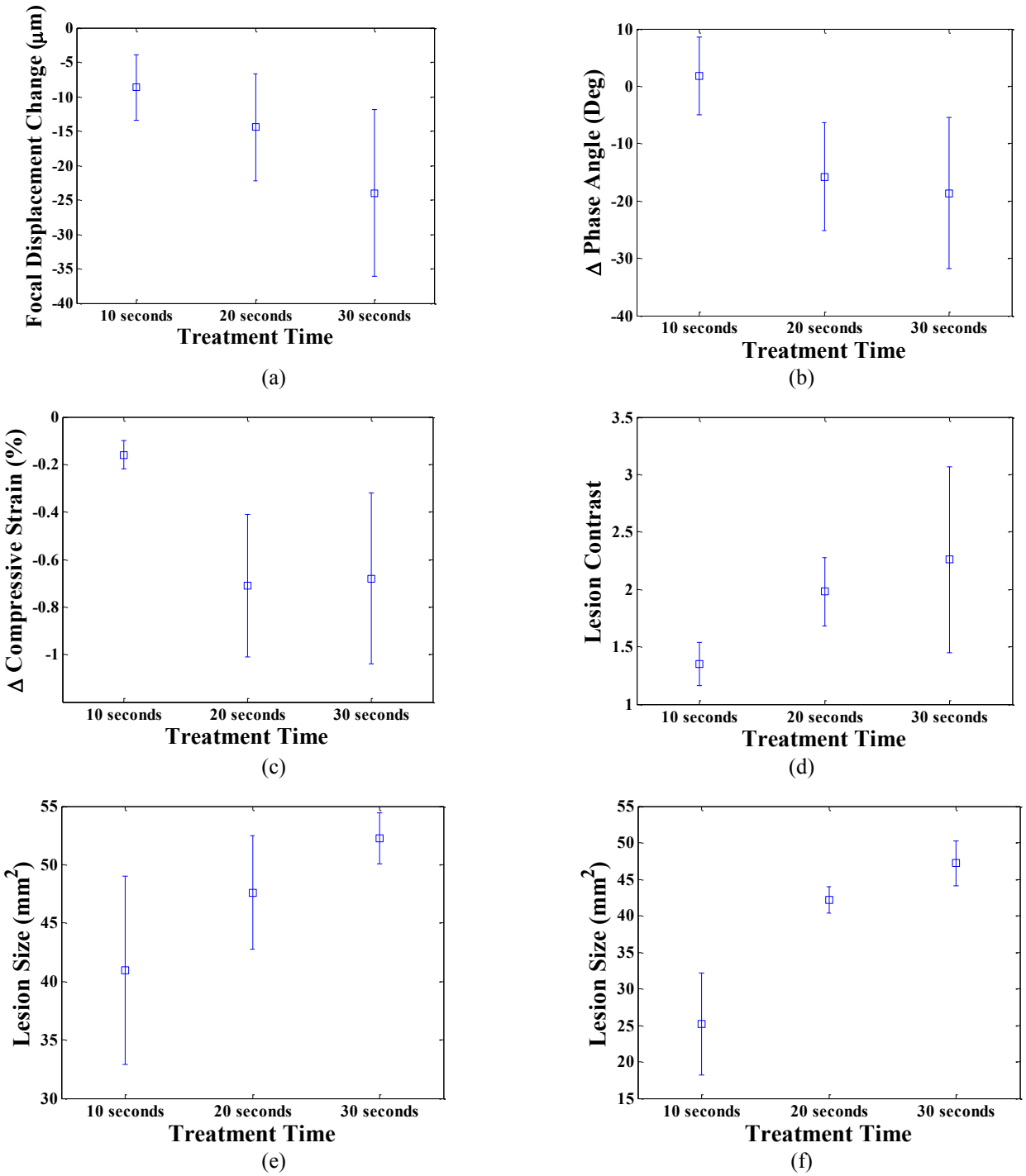

Figure 4.5. Statistical summary of the investigated treatment cases under 10W. Between three cases of HIFU treatments under 10, 20, and 30 seconds, decrease trend was observed in the peak-to-peak HMI focal displacement value (a) and compressive strain (c). Δφ (b) had a relatively increase, though unstable,

amongst the 10 second treatment cases but showed clear decrease trends amongst the 20 and 30 second treatment cases. 2D HMI displacement images observed increase in lesion-to-background displacement contrast (d) and lesion size (e), which was confirmed with pathology (f).

The standard deviation of both HMI focal displacement and phase shift monitoring curve refers to the average of measurements across the focal zone (2 mm) at the HIFU focusing depth inside the tissue. The 2D HMI displacement images also mapped an increase in lesion-to-background displacement contrast (1.34±0.19,1.98±0.30,2.26±0.80) and lesion size with treatment time (40.95±8.06, 47.6±4.87,52.23±2.19 mm^2), which was verified with pathology results (25.17±6.99, 42.17±1.77,47.17±3.10 mm^2) (Figures. 4.5 and 4.6.1).

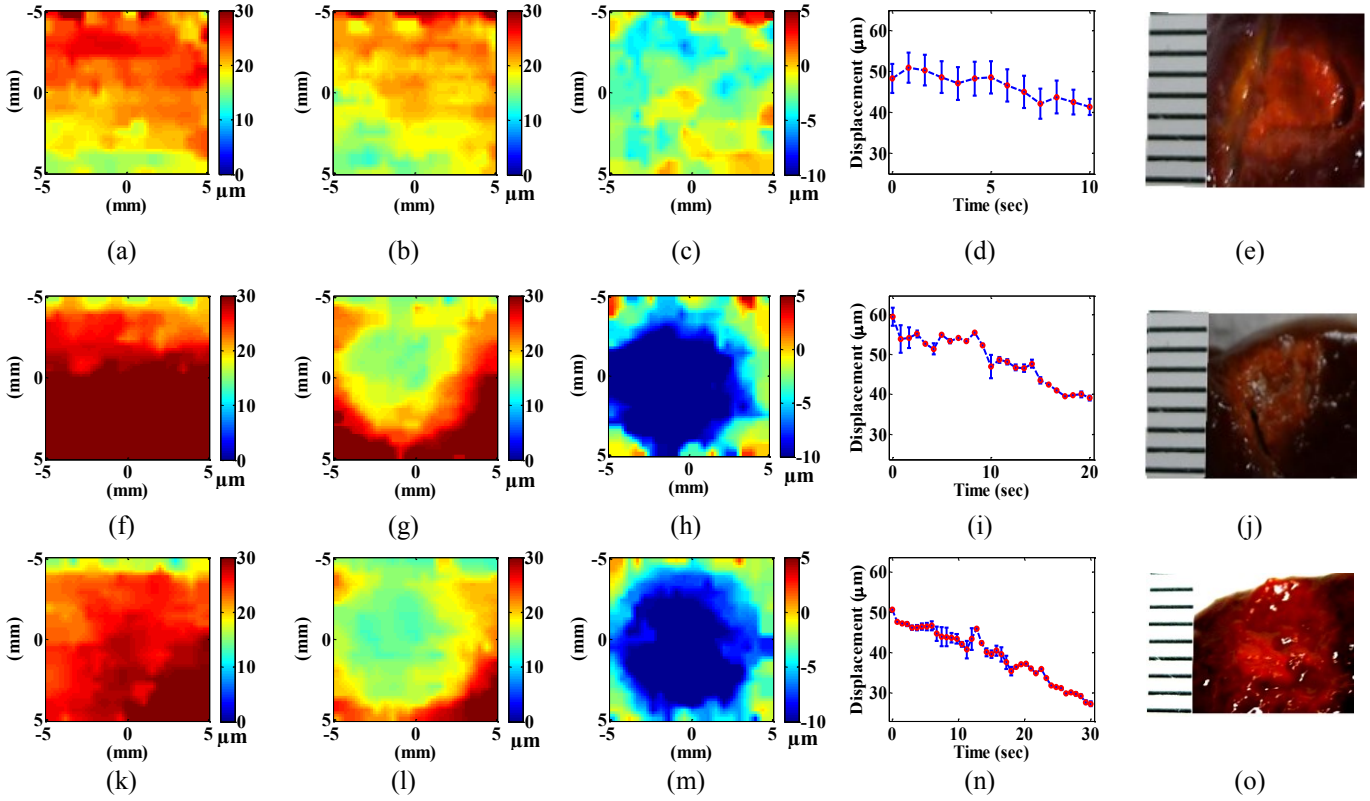

Figure 4.6.1. HMIFU monitoring and assessment images for cases with displacement decrease. HIFU treatment of acoustic power were set to be 10 W for 10 (a-e), 20 (f-j), and 30 second (k-o), respectively. The displacement contrast maps (c,h,m) are estimated from subtracting the displacement maps after lesion formation (b,g,l) from that of before (a,f,k) and displayed along with their corresponding monitoring curves (d,i,n). Both the lesion size and contrast increases with treatment time, lastly the increase in size was confirmed with corresponding gross pathology (e,j,o).

However, during the reproducibility studies as we repeated our multi-parametric HMIFU protocol across three different acoustic powers (8 W, 10 W, and 11 W) under treatment durations of 10-, 20-, and 30-s, there was a discrepancy in the distribution of the HMI lesion maps consisting of reversed lesion-to-background HMI displacement contrast, namely blue (HMI focal displacement decrease) lesion cases (Figure 4.6.1), where the 2D HMI displacement contrast

map (c,h,m) showed a decrease of displacement inside the thermal lesion and red (HMI focal displacement increase) (Figure 4.6.2) lesion cases were found (Figure 4.6.3).

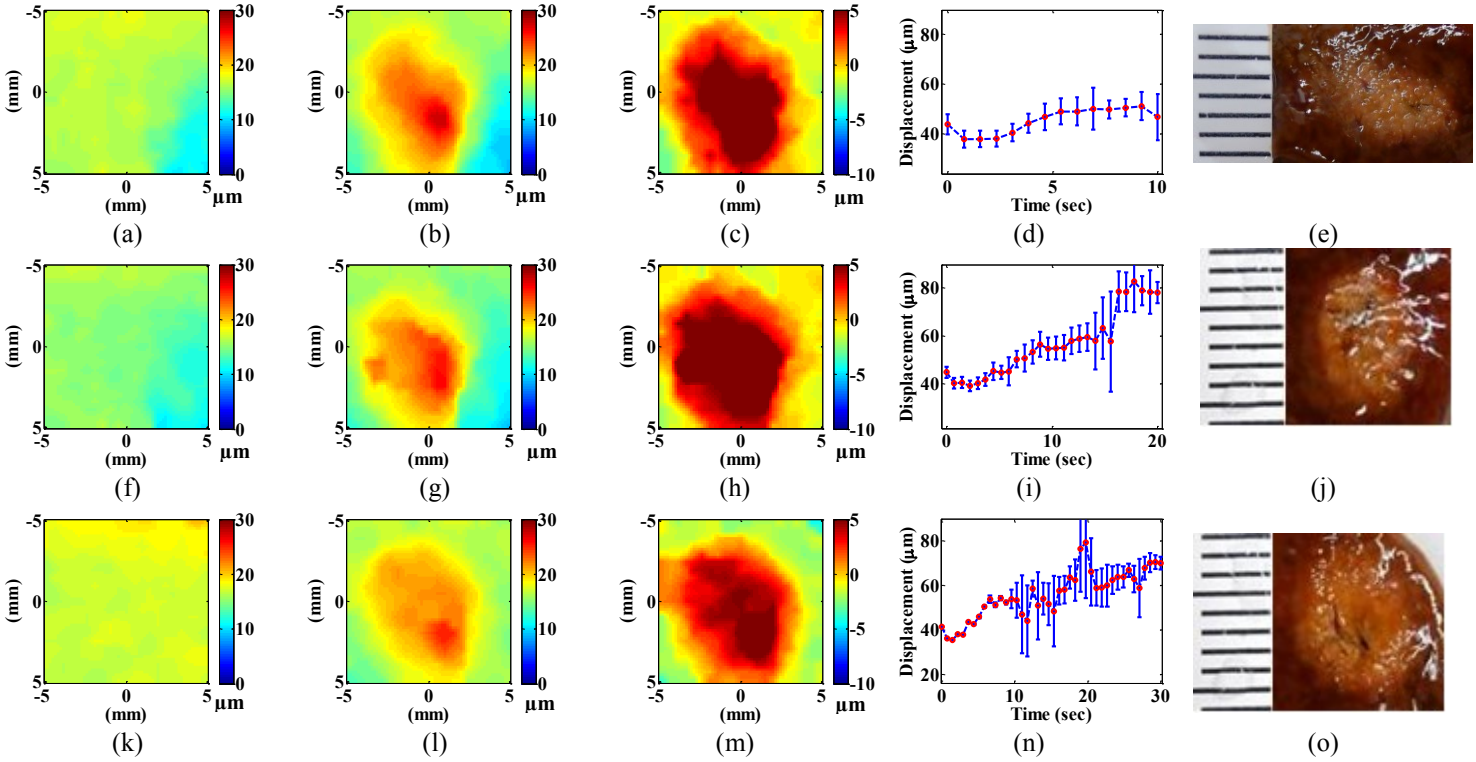

Figure 4.6.2. HMIFU monitoring and assessment images for cases with displacement increase. HIFU treatment of acoustic power were also set to be 10 W for 10 (a-e), 20 (f-j), and 30 second (k-o), respectively. The displacement contrast maps (c,h,m) along with their corresponding displacement monitoring curves (d,i,n) had reversed displacement-to-background contrast in comparison with Figure 4.6.1 across all of the treatment cases. Nevertheless, the mapped lesion sizes increased with treatment time and were confirmed with pathology images (e,j,o).

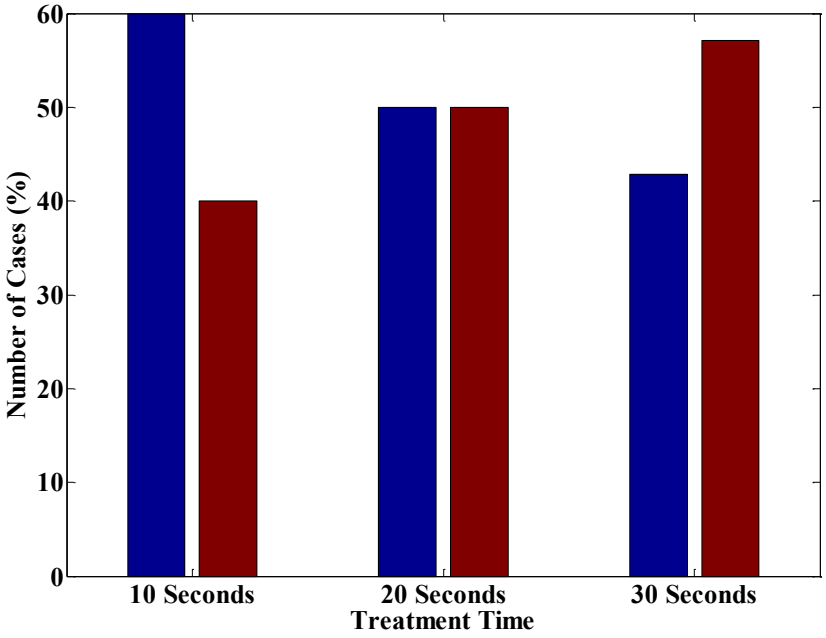

Figure 4.6.3. Statistical summary change in HMIFU displacement monitoring and contrast map for all treatment cases investigated under power of 10W. Each treatment time duration comprised of cases with both decrease (blue) and increase (red) displacement within the lesion compared to before treatment.

In addition, these results also confirmed that such a discrepancy was observed across all of the investigated treatment power and duration range where boiling was present (Figure 4.7a). The magnitude change of HMI displacement spanned from decreased (blue) to increased (red) cases amongst the 8W, 10W treatment cases and only increased cases were detected at 11 W under 10, 20, and 30 seconds treatment, respectively (Figures 4.7a,Table 4.1, 4.2, 4.3). For the $\Delta\varphi$, the range of the observed values also spanned across increased and decreased cases at 8W, 10W, whereas only decreased displacement and phase shift cases were detected at 11W treatment cases under 10, 20, and 30 seconds treatment (Figure 4.7b, Table 4.1, 4.2, 4.3). For the estimated lesion-to-background contrast, both increased and decreased cases were observed

across all the treatment power levels (Figure 4.7c, Table 4.1, 4.2, 4.3). Lastly, the mapped lesion size from the constructed 2D HMI image increased with treatment duration across all 8W, 10W, then slightly decreased for 11W treatment cases (Figure 4.7d, Table 4.1, 4.2, 4.3), confirmed with similar trends in gross pathology assessment (Figure 4.7e, Figure 4.7f, Table 4.1, 4.2, 4.3).

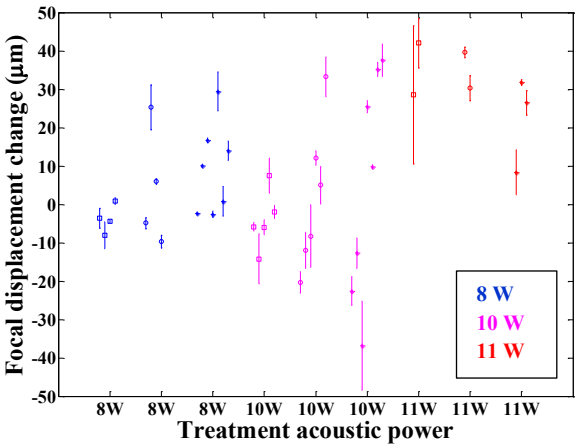

(a)

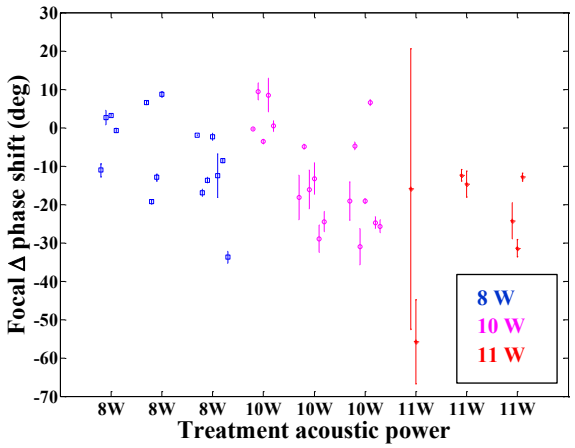

(b)

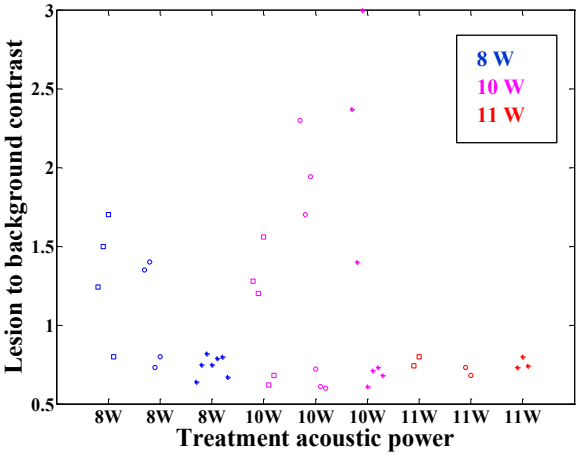

(c)

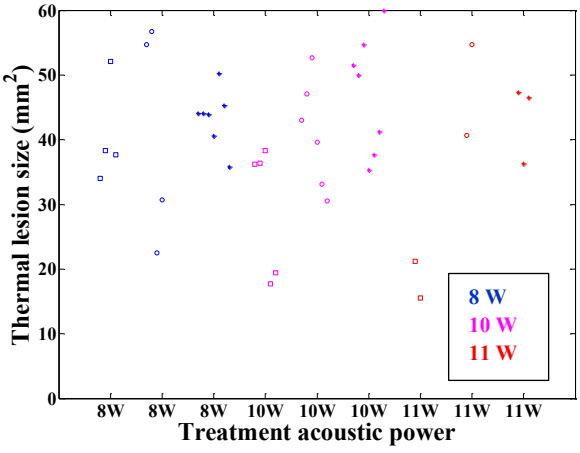

(d)

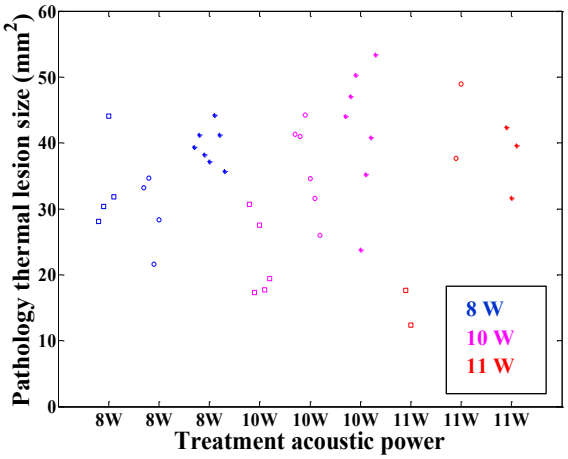

(e)

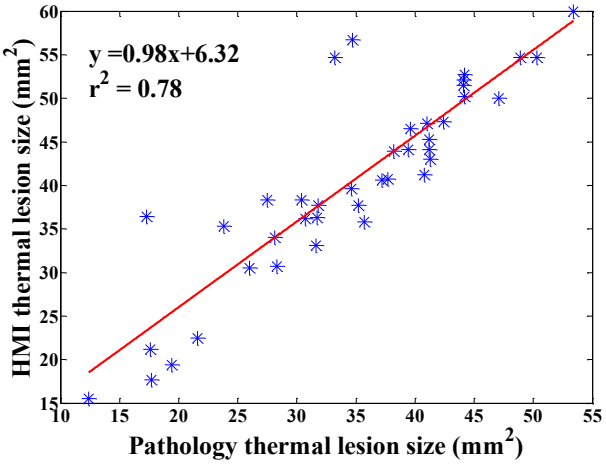

(f)

Figure 4.7. Statistical distribution of all of the investigated case at acoustic power of 8W (Blue), 10W (Magenta) and 11W (Red) for 10 (square), 20 (circle), and 30 (star) seconds. Focal displacement (a) increased and decreased across all treatment levels. However, the group of 10W seemed to host most of the decrease cases whereas 11W only had increase cases. Also, the magnitude of change increased as function of treatment time. Trends for $\Delta\varphi$ (b) showed a relatively unstable trend amongst the 10 sec cases with both increase and decrease trend, whereas decrease trend was observed amongst all other cases across all power levels. (c) Lesion-to-background contrast showed a reversed change, among the 8 W and 10 W cases whereas 11 W only consisted of increase trend (i.e., contrast < 1). (d) Lesion size increased with treatment time across all the investigated powers, which was confirmed with gross pathology results (e). (f) Linear regression analysis for comparing the thermal lesion size estimated with gross pathology and HMI mapping. It can be depicted that the HMI mapped size is well correlated with the pathological findings.

Acoustic Power / Parameter	8W		10W		11W
% of Displacement change during treatment (%)	**4.9±0.0 (n=1)**	**2.3±2.3 (n=4)**	**13.2± 6.0 (n=3)**	**27.3±6.0 (n=2)**	**50.0±23.6 (n=2)**
Δ Phase shift during treatment (°)	**-2.6±0.0 (n =1)**	**-2.9±7.4 (n=4)**	**4.5±6.9 (n=3)**	**1.7±6.1 (n=2)**	**-35.8±28.1 (n=2)**
Lesion-to-background contrast after treatment	**1.3±0.0 (n=1)**	**0.7±0.2 (n=4)**	**1.4±0.2 (n=3)**	**0.65±0.04 (n=3)**	**0.77±0.04 (n=2)**
Mapped HMI Lesion size (mm^2)	**34.0±0.0 (n=1)**	**42.7±8.1 (n=4)**	**36.9±1.1 (n=3)**	**18.6±1.2 (n=3)**	**18.3±4.0 (n=2)**

Table 4.1. Quantification of monitoring and assessment parameters across different acoustic powers for 10 seconds treatment duration. Note that red indicates cases where displacement increased and blue indicates cases where displacement decayed inside the thermal lesion, respectively.

Acoustic Power / Parameter	8W		10W		11W
% of Displacement change during treatment (%)	**4.9±0.0 (n=1)**	**2.3±2.3 (n=4)**	**13.2± 6.0 (n=3)**	**27.3±6.0 (n=2)**	**50.0±23.6 (n=2)**
Δ Phase shift during treatment (°)	**-2.6±0.0 (n =1)**	**-2.9±7.4 (n=4)**	**4.5±6.9 (n=3)**	**1.7±6.1 (n=2)**	**-35.8±28.1 (n=2)**
Lesion-to-background contrast after treatment	**1.3±0.0 (n=1)**	**0.7±0.2 (n=4)**	**1.4±0.2 (n=3)**	**0.65±0.04 (n=3)**	**0.77±0.04 (n=2)**
Mapped HMI Lesion size (mm^2)	**34.0±0.0 (n=1)**	**42.7±8.1 (n=4)**	**36.9±1.1 (n=3)**	**18.6±1.2 (n=3)**	**18.3±4.0 (n=2)**

Table 4.2. Quantification of monitoring and assessment parameters across different acoustic powers for 20 seconds treatment duration. Note that red indicates cases where displacement increased and blue indicates cases where displacement decayed inside the thermal lesion, respectively.

Acoustic Power / Parameter	8W		10W		11W
Δ Displacement during treatment (μm)	19.0±0.0 (n=1)	73.2±54.1 (n=5)	61.4±31.1 (n=4)	118.9±61.4 (n=5)	48.3±25.9 (n=3)
Δ Phase shift during treatment (°)	-1.9±0 (n=1)	-14.7±10.6 (n=5)	-18.5±10.1 (n=4)	-14.6±18.3 (n=5)	-22.8±9.4 (n=3)
Lesion-to-background contrast after treatment	1.7±0.0 (n=1)	0.76±0.05 (n=5)	2.3±0.8 (n=4)	0.7±0.05 (n=5)	0.76±0.04 (n=3)
Mapped HMI Lesion size (mm^2)	44.1±0.0 (n=1)	43.3±4.8 (n=5)	52.1±2.4 (n=4)	43.6±11.2 (n=5)	43.4±6.1 (n=3)

Table 4.3. Quantification of monitoring and assessment parameters across different acoustic powers for 30 seconds treatment duration. Note that red indicates cases where displacement increased and blue indicates cases where displacement decayed inside the thermal lesion, respectively.

4.1.5 Discussion

HIFU is an emerging technology that holds great promise as a cost effective, noninvasive, non-ionizing, extracorporeal tumor ablation method with a short recovery period. Across its three procedural stages, i.e., treatment planning, treatment monitoring, and treatment assessment, numerous assistive techniques have been developed in the field of MRI, ultrasound, and acousto-optics. Despite recent advancements for such guidance and assessment techniques, the treatment monitoring stage of HIFU especially during boiling remains as a critical challenge with respect to quantitative, localized, reliable, and real-time feedback requirements. HMIFU is a dynamic ultrasound-based elasticity imaging technique using a pair of confocally-aligned HIFU and pulse-echo transducers for inducing and tracking a stable focal oscillatory motion, which is directly related to the local mechanical property. This has provided the HMIFU with the

capability of performing localized HIFU monitoring without interrupting the treatment. In the past, the HMIFU feasibility was shown in the assessment of tissue relative stiffness as well as HIFU monitoring based on the displacement amplitude change. Throughout this study, we investigated the feasibility of a comprehensive HMIFU monitoring method with high energy HIFU treatment that induced boiling, which incorporated a mutli-parametric monitoring method including focal displacement, focal compressive axial strain, and relative change in focal phase shift ($\Delta\varphi$). We hypothesized the multi-parametric monitoring method improves the monitoring quality of HMIFU, i.e., 1) under boiling at high energy HIFU treatment 2) providing complementary analysis with each parameter for indication of various tissue response changes upon formation of a thermal lesion, 3) decoupling of acoustic and mechanical tissue parameters. Multi-parametric HMIFU was applied on HIFU treatment monitoring and assessment under three different acoustic powers (8W, 10W, and 11W) and durations (10 s, 20 s, and 30 s).

Although the previous studies [136, 202, 203] and our assessment of *ex vivo* liver [154, 204] showed a slow progressive elasticity deterioration under HIFU treatment with progressive decay in displacement or shear modulus, we found that across the HIFU treatment cases with boiling, the 2D HMI displacement images underwent reverse lesion-to-background displacement contrast. Figures 4.6.1-4.6.3 demonstrate a series of cases with discrepancy where lesions formed followed increased and decreased displacement under same HIFU treatment sequence. For HIFU treatment under 10W and lasting 10 s (a-e), 20 s (f-j), and 30 s (k-o), there were discrepancies where some cases with focal monitoring displacement decrease during treatment (Figure 4.6.1 d,i,n) whereas others exhibited an increase trend (Figure 4.6.2 d,i,n). The corresponding displacement contrast images of each treatment also mapped the consistent change of displacement increase (Figure 4.6.1 c,h,m) and decrease (Figure 4.6.2 c,h,m),

accordingly. We summarized our findings amongst the 10 W treatment cases, and found out that such discrepancies were present across all treatment durations where cases of both increase and decrease displacement were detected (Figure 4.6.3). Throughout our reproducibility studies, we also confirmed the consistency of such observation across all the treatment powers we have investigated in this study. Additionally, it is noteworthy that the changes in displacement were always consistent with its corresponding displacement monitoring curves across all of the treatment cases.

Figure 4.7 plots the outcome distribution of each parameter for all HIFU treatment cases performed at 8W (blue), 10W (magenta), and 11W (red). In Figure 7a and 7c, it was shown that, depending on the case, the HMI displacement will increase or decrease after lesioning but always reflect a change as a result of treatment regardless of the treatment or duration, indicating the consistent effect of boiling. Nevertheless, HMI was capable of detecting the lesion at all treatment durations and powers, i.e., the HMI displacement contrast ratio was different from one in every case where lesion was formed. The phase shift (Figure 4.7b), on the other hand, remained relatively consistent, despite a few outliers, indicating a consistent decrease trend (Table 4.1, 4.2, 4.3). In addition, the mapped lesion sizes from HMI contrast maps (Figure 4.7d) were consistent with the measurements in the gross pathology findings (Figure 4.7e). A good correlation was found between the thermal lesion sizes as mapped by HMI and gross pathology findings (Figure 4.7f). In addition, there was an increase of lesion size from 8W to 10W, then decrease in lesion size from 10W to 11W possibly due to the shielding effect associated with attenuation under strong boiling activity (Table 4.1, 4.2, 4.3). There can be several reasons for such reversal in displacement outcomes: Based on the measured focal temperature curve and PCD spectrograms, it was found that the focal region reaches boiling within first few seconds of

the treatment window. That said, there have been discussions that beyond a certain temperature threshold, e.g., boiling, as well as the mechanism such as tissue pulverization[205], gelatification [202, 203, 206], or shielding due to bubble occurrence and increase of acoustic absorption [207] can occur with continuous delivery of high thermal dosage [14]. The increase in attenuation can be due to either boiling and/or formation of thermal lesions [208], and the increase in attenuation can lead to higher displacement at the lesion, which generates an opposite lesion-to-background contrast. It is therefore concluded that the blue (or, displacement decrease) lesion maps may have been obtained in cases where the mechanical response change dominated (stiffening) over the structural and/or absorption change whereas the red lesion maps represented cases where the acoustic response change dominated (increase in attenuation). This finding can be supported from the aspect of change in the relative phase shift: It is noteworthy that the average phase shifts exhibited decrease with heating, especially for the 20-and 30-s treatment cases with the 2D HMI maps having either blue or red lesion-to-background displacement ratio, indicating a consistent tissue mechanical response change during acoustic property changes. Furthermore, we have completed a rheometer based mechanical testing study on HIFU lesions induced on *ex vivo* canine liver using the same treatment settings as previously described. In turn, we found the shear modulus of HIFU lesions samples to range between 10 to 15 times compared to that of the untreated samples[205]. Therefore, this validates the fact that all lesions investigated in this study did undergo mechanical stiffening, i.e., absorption changes were likely to be dominant amongst the cases where displacement increased.

In addition to displacement monitoring, we also investigated changes in strain during monitoring on a total number of nine treatment cases at 10W treatment, where we found a decrease in the axial compressive strain, which proved the feasibility of HMIFU to confirm

relative stiffness monitoring at a finer spatial resolution. However, not only does strain estimation rely on the displacement SNR, but also the SNR of the displacement profile across the focal zone inside the tissue, i.e., the end of the focal excitation zone must be clearly mapped in order to estimate for the axial compressive strain by calculating the spatial derivative. In this study, the strains were found to be noisier at other powers and the performance of HMI strain estimation is part of ongoing efforts in our group. The $\Delta\varphi$ also showed an interesting trend, where the 10-sec cases indicated a slight increase whereas both the 20 and 30 second cases indicated a significant decrease following an initial increase (Figure 4.7b, Table 4.1, 4.2, 4.3). Nevertheless, $\Delta\varphi$ consistently decreased amongst all lesions detected, confirming its strength as an independent biomechanical property marker. Additionally, the 2D HMI displacement images clearly mapped the relative increase of the lesion size and lesion-to-background contrast, which were comparable to previous studies [19, 146, 180, 181]. There was a slight decrease from the cases of treatment under 20 to 30 seconds, which could stem from either reduced thermal ablation at the pre-focal shielding effects (Table 4.1, 4.2, 4.3).

Despite the unpredictable change in acoustic properties in the presence of boiling, our results in treatment assessment also indicated the capability of HMIFU in displacement mapping across all treatment power levels and durations reaching boiling, demonstrating the robustness of HMIFU under high energy HIFU treatment. Moreover, the consistent decrease in $\Delta\phi$ amongst all of the formed lesion cases proved its usefulness as an independent biomechanical parameter for both monitoring and assessment. However, the strains were not estimated for lesion mapping during post-assessment phase due to the low SNR of the displacement when short lower pulse sequences were used compared to that of the monitoring study. Nevertheless, HMIFU was shown robust and reliable in mapping HIFU lesions formed with boiling despite the change in

acoustic absorption. Ongoing and future investigations include the study of the slow denaturation treatments where HMIFU monitoring showed a consistent trend where displacement increased then decreased, indicating tissue softening and stiffening [209] , and the change in tissue stiffness such as gelatification and pulverization at various thermal dose levels[205]. Furthermore, additional studies are being performed to study the relationship between the proposed monitoring parameters to both the PCD-based cavitation level as well as thermocouple-based focal temperature profile under the HIFU slow denaturation regime[200].Thermocouple measurements are not deemed reliable in the presence of boiling.

Additionally, in this study, 2D transverse HMI displacement maps were obtained before and after lesion formation through raster scanning on all treatment cases, where we utilized the displacement distribution for mapping both the lesion size and lesion-to-background displacement contrast. We also investigated the feasibility of mapping the lesion using the relative change in phase shift taken from the same displacement and input force acquired at the corresponding raster scan coordinate. Despite the changes in lesion-to-background displacement contrast across all of the treatment durations (Figure 4.A1. (a,d,g) vs. Figure 4.A2 (a,d,g)), $\Delta\varphi$ shows a consistent decrease within the thermal lesion (Figure 4.A1. (b,e,h) vs. Figure 4.A2. (b,e,h)), which indicates a consistent change in viscosity-to-elasticity ratio and its robustness as an independent biomechanical parameter.

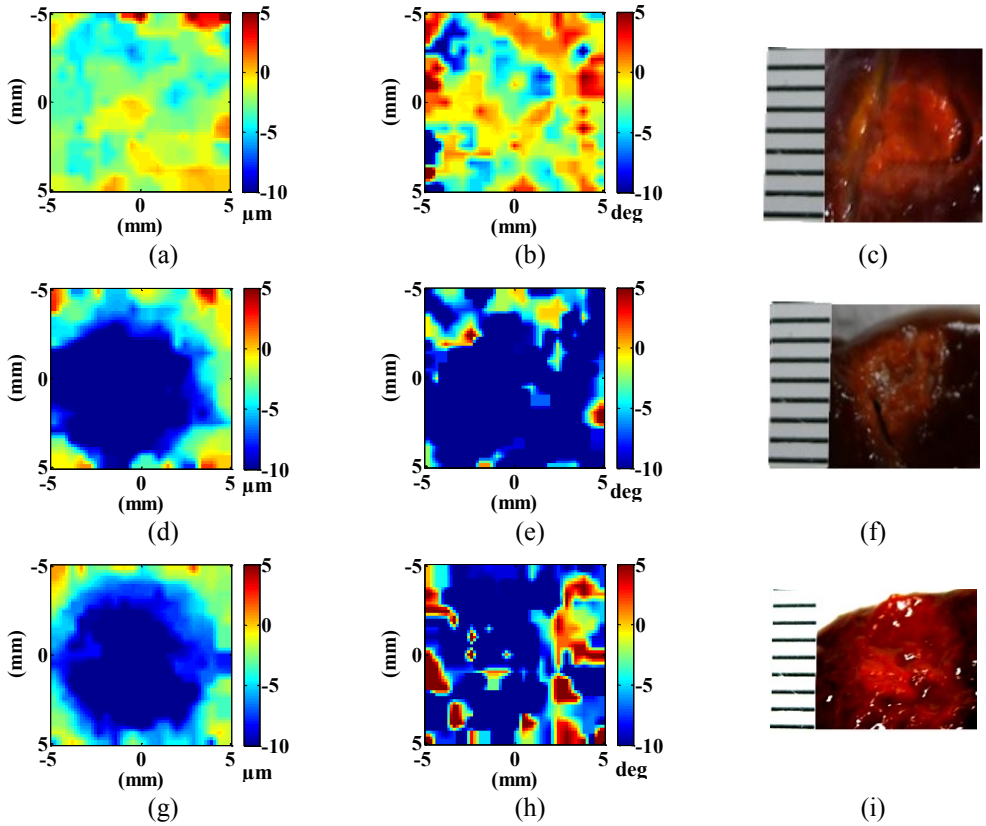

Figure 4.A1. Displacement map (a,d,g) and corresponding Δφ maps (b,e,h) for lesions with decreased displacement for the same cases as Figure 4.6.1 under HIFU treatment of 10W for 10 (a,b,c), 20(d,e,f), and 30(g,h,i) second. Note when displacement decays, the Δφ maps also indicates decrease in phase shift change within area of formed lesion (c,f,i).

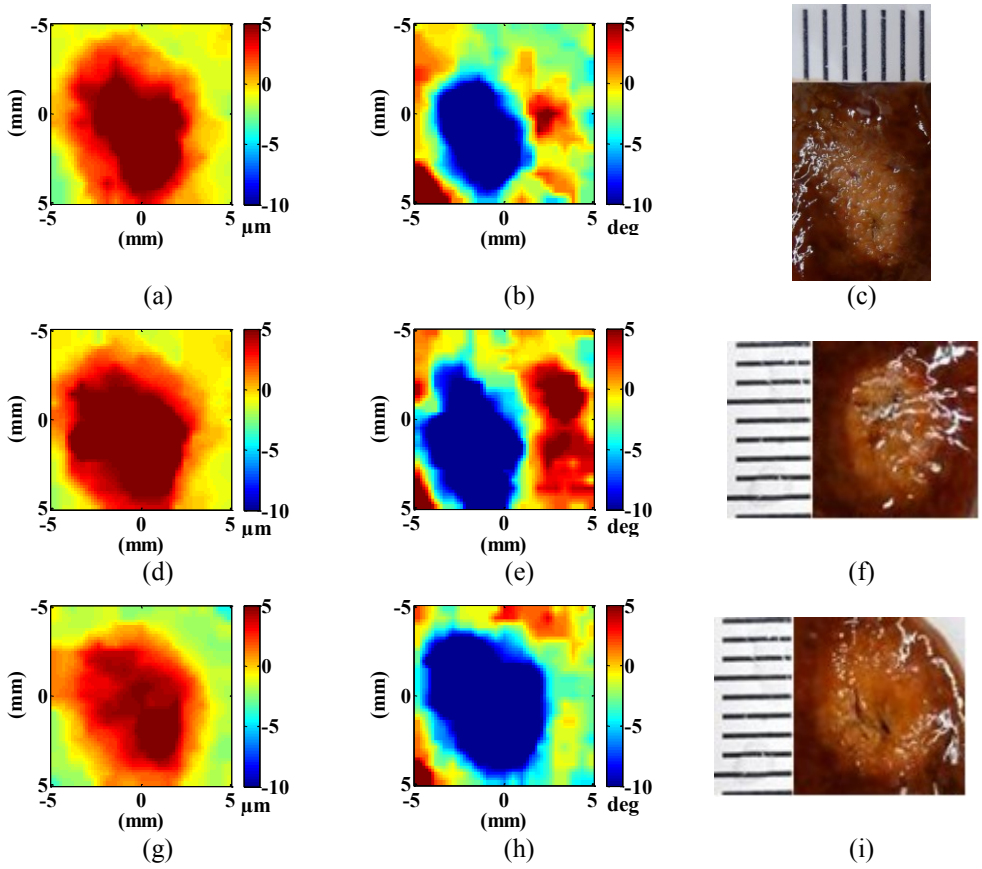

Figure 4.A2. Displacement contrast map (a,d,g) and corresponding Δφ maps (b,e,h) for lesions with increased displacement. Despite when displacement showed reversal trend, i.e., increase, the Δφ maps still showed consistent decrease inside the lesion (c,f,i), indicating a consistent biomechanical property change.

4.1.6 Conclusion and Summary

In subsection 4.1, a multi-parametric study was completed using the 1-D HMIFU framework through monitoring focal displacement, relative change in phase shift, and compressive strain in order to independently track the change in acoustic and viscoelastic tissue response under high energy HIFU treatment with boiling. Despite all studies were performed under boiling where displacement monitoring and lesion map contrast showed a consistent

reversal trend between increase and decrease, every parameter underwent a clear change in absolute magnitude upon lesion formation, indicating its feasibility in monitoring the drastic change of acoustic and/or mechanical property change throughout formation of HIFU lesion. In addition, relative change in phase shift showed a consistent decrease at longer treatment duration, indicating acoustically-independent mechanical change. Transverse 2D HMI images were also investigated and showed feasibility in mapping the increase in lesion size and lesion-to-background contrast. Nevertheless, two types of sequences are used for HIFU treatment in the clinic: Slow denaturation sequence with relatively lower power and longer duration, as well as the higher power and shorter duration HIFU treatment with boiling, which has been discussed for this study. Therefore, the next subsection will introduce another study which focuses on comparing the same multi-parametric HMIFU outcomes under the two different HIFU treatment sequences in order to comprehensively assess and compare the performance of HMIFU in monitoring both types of HIFU treatment sequences.

4.1.7 Monitoring of HIFU treatment with boiling and slow denaturation

In this subsection, another multi-parametric study will be summarized in order to assess the performance of HMIFU for monitoring of both HIFU treatment with slow denaturation and HIFU treatment with boiling. The motivation behind investigating the HIFU treatment with slow denaturation stems from the fact that the principle aim of HMIFU is to achieve consistent monitoring of progressive tissue elasticity, i.e., initial softening-then-stiffening elasticity phase change due to the denaturation of protein structures. More importantly, this type of elasticity change has been proposed to be the case of HIFU treatment with lower power and longer duration [136], and therefore we will refer to the treatment sequence type as slow denaturation sequence in this dissertation.

Despite the important aspect of HIFU treatment with slow denaturation sequence, there has yet to be a comprehensive study on assessing the reliability of HMIFU on consistently achieving the monitoring of this stiffness phase change along with validation assessments, i.e., monitoring of both acoustic and thermal property change in addition to mechanical change. Therefore, in this study, multiple techniques were implemented in order to perform the multi-parametric monitoring similar to the previous subsection. The acoustic monitoring is performed using Passive cavitation detection (PCD), which has been a standard approach to the detection of the acoustic response of tissue under HIFU treatment based on characteristics of backscattered HIFU signal spectrum [210]. The broadband noise is known to be present during tissue boiling with presence of strong bubble dynamics [211-213]. In addition, focal temperature measurement can be used in conjunction in order to provide quantitative information regarding the thermal property change and delivered thermal dosage. Hence, the objective of the present study is to

investigate the performance of HMIFU monitoring under both boiling (high power and short duration) as well as slow denaturation (low power and long duration) HIFU treatment sequence based on the change of HMI displacement and correlation coefficients across the HIFU treatment window.

In addition, we will couple both thermal and acoustic monitoring using thermocouple and PCD monitoring to our HMIFU monitoring in order to assess and justify an optimal power range for consistent monitoring of lesioning formed under slow denaturation elasticity change with minimum medium disturbance such as tissue boiling or acoustic cavitation. We hypothesize that the boiling sequence will possess a strong thermal and acoustic change that will affect the HMIFU assessment quality while the slow denaturation sequence will possess an optimal power and duration range that will enable a consistent monitoring of initial-stiffening-followed by-stiffening elasticity change as well as consistent phase shift during the lesion formation.

4.1.8 Materials and Methods

Canine livers (subject=8, lobes = 9, Treatment location = 43) were excised immediately upon animal sacrifice and immersed into a degassed Phosphate buffered saline (PBS) solution bath maintained at room temperature. All procedures were approved by the Institutional Animal Care and Use Committee (IACUC) of Columbia University. Each specimen was fixed using metallic needles onto an acoustic absorber placed inside of a de-ionized and degassed PBS container. The HMIFU system used for this subsection is and upgraded version from the previously mentioned framework (Figure 4.8). The transducers used were still comprised of a

4.75MHz focused Lead Zirconate Titanate (PZT) (outer diameter 80 mm, inner diameter 16.5 mm, focal depth 9 cm) transducer (Riverside Research Institute, New York, NY) for probing tissue with an AM frequency of 25 Hz, and a confocal 7.5 MHz single-element pulse-echo transducer (Olympus-NDT, Waltham, MA, U.S.A.) with a diameter of 15 mm and a focal length of 6 cm for simultaneous RF signals acquisition at a frame rate of 1 kHz; In comparison to our previous HMI and HMIFU studies with limited RF acquisition window, we have improved our acquisition system such that RF signals can now be acquired and saved continuously throughout the entire treatment window under the sampling rate of 100 MS/sec, which allows us to further investigate the detailed tissue property change throughout the entire HIFU treatment window. The HMIFU system was mounted and controlled through a 3D translational system (Velmex Inc., Bloomfield, NY, U.S.A.) for targeting purposes (Figure 4.8). The received RF signals were band-pass filtered (Reactel, Inc., Gaithersburg, Maryland, USA) with cutoff frequencies of f_{c1} = 5.84 MHz and f_{c2} = 8.66 MHz (at -60dB) and recorded along with the excitation signal representing the force profile and a dual-channel data acquisition unit (Gage applied, Lockport, IL, U.S.A.) at a sampling frequency of 80 MHz (Figure 4.8). Subsequently, a 1-D normalized cross-correlation (window size of 3.85 mm and 90% overlap) technique [177] was used to estimate the incremental HMI displacement and phase shift ($\Delta\varphi$).

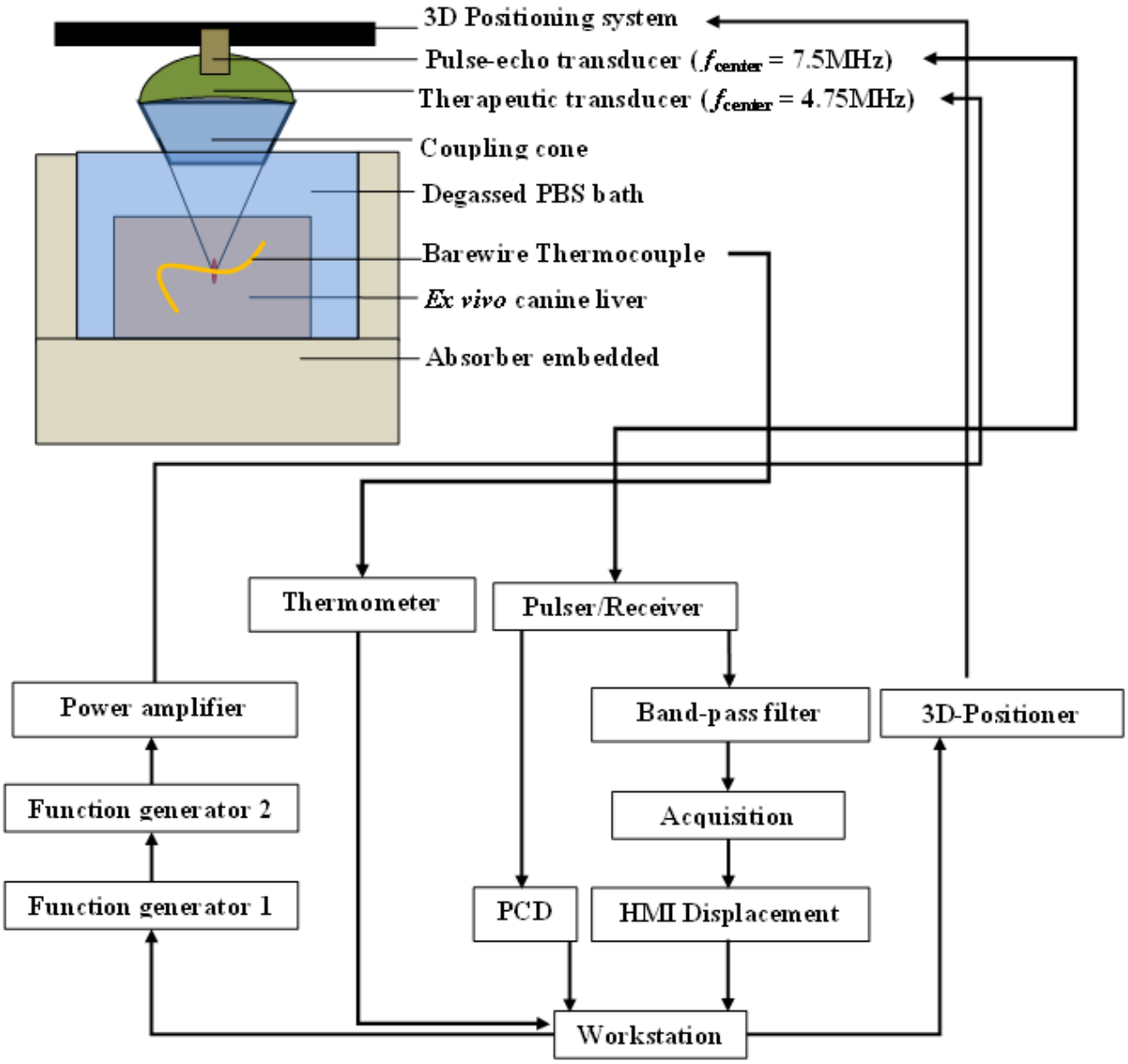

Figure 4.8. HMIFU experimental set up and data flow. The focal depth of the HIFU is 9 cm and the focal spot lies at 3.4 cm below of the tip of the coupling cone containing degassed water. Note the 3D positioning system is responsible for HMI raster scan.

Regarding the method for estimation of phase shift ($\Delta\varphi$), the readers can be referred to the previous subsection 4.1.3. Peak-to-Peak focal HMI displacements for each treatment case were estimated throughout the treatment window using a peak-detection algorithm: The displacement waveforms were divided into non-overlapping time segments of 1 s. For each segment the local maxima and minima were calculated. The collected local maxima and minima were linearly interpolated, respectively, and the resulting waveforms were smoothed using a moving average filter of 100 points. Constant extrapolation was used to fit and align the resulting waveforms with the displacement waveform. Finally, the peak to peak amplitude was calculated by subtracting the smoothed local minima waveform from the local maxima waveform. In order to assess the presence of tissue boiling at the proposed treatment level, PCD monitoring was also performed by operating the conically-aligned pulse-echo transducer in passive mode in conjunction with thermocouple measurement. Focal temperature monitoring was performed by inserting a T-type bare wire thermocouple with diameter of 25 μm (Omega Inc., Stamford, CT) inside the tissue through a customized needle gauge. The diameter of the thermocouple was chosen to be smaller than 1/10 of the carrier wavelength in order to minimize reflection and viscous heating artifacts [201].

Four additional parameters are introduced in this study to assess the performance of HMIFU monitoring in this study: Displacement contrast, Mean correlation coefficient, Minimum Correlation coefficient, and PCD Broadband Energy. The displacement contrast C is defined as:

$$C = \frac{Disp_{\max} - Disp_{\min}}{Disp_{\max} + Disp_{\min}} \tag{8}$$

where the $Disp_{\max}$, $Disp_{\min}$, are the maximum and minimum displacement during any monitoring displacement profile during a single treatment window. The mean correlation coefficient ρ_{mean} and minimum correlation coefficient $\rho_{\min}$ are defined as the average and minimum cross correlation value for the estimated displacement during a single treatment window:

$$\rho_{mean} = \frac{\sum_{t}^{T} \rho(t)}{T} \tag{9}$$

$$\rho_{\min} = \min(\rho(0) : \rho(T)) \tag{10}$$

Lastly, the PCD Broadband Energy is obtained simply by subtracting both the harmonic energy and ultra-harmonic energy from the total energy quantified across the PCD spectrograms. In this study, two HMIFU monitoring sequences were performed for HIFU treatment: boiling and slow denaturation, respectively. Monitoring HIFU treatments with slow denaturation were composed of sequences with treatment duration at 120 to 240 seconds under extrapolated *in situ* focal acoustic intensity and power of 2773 W/cm^2, 3582 W/cm^2, 5015 W/cm^2, at 4W, 5W, and 7W, respectively. Monitoring HIFU treatments with boiling were composed of sequences with treatment duration at 30 seconds under extrapolated *in situ* focal acoustic intensity and power of 5546 W/cm^2, 7164 W/cm^2, and 9067 W/cm^2, at 8W, 10W, and 11W for treatment with boiling sequence, respectively.

4.1.9 Results

In this study, a total of 43 HIFU treatment locations were performed on freshly excised canine liver specimens (subject = 8, lobes = 9) *ex vivo* . There were 34 treatments completed using the slow denaturation treatment sequence, where displacement, cross correlation coefficients, and phase shifts (Δφ) were monitored across the treatment window. It was observed that 21 cases or 62% of all the cases under slow denaturation sequence exhibited displacement decrease following HIFU treatment. On the other side, there were also 9 treatments completed using the HIFU treatment with boiling sequence, where 6 cases exhibited displacement increase and 3 cases exhibited displacement decrease following HIFU treatment with no case exhibited an increase-then-decrease progressive displacement change. Additionally, the averaged displacement change, displacement contrast, phase shift (Δφ), mean correlation, and minimum correlation during the slow denaturation HIFU treatment cases were -36.7±15 %, 0.34±0.18, 12.8 ± 2.0º, 0.97±0.079, and 0.81±0.19 (Figure 4.9) (Table 4.4), which were performed under *in situ* focal acoustic intensity and power ranged between 2773 W/cm^2, 3582 W/cm^2, 5015W/cm^2, at 4W, 5W, and 7W, respectively.

Monitoring Parameter / Treatment sequence	Change in HMI displacement before and after (%)	ΔPhase shift (º)	Mean correlation Coefficient	Min correlation Coefficient	Displacement contrast
Slow denaturation sequences	-36.7±15	12.9±2.0	0.97±0.08	0.81±0.14	0.34±0.18
Boiling sequence	197.4±315.3	7.0±16.3	0.81±0.19	0.26±0.4	0.46±0.37

Table 4.4. Summary of HMIFU monitoring parameters used in this study for both slow denaturation and boiling sequences. Note the average was taken across all of the cases with varied treatment durations and treatment powers.

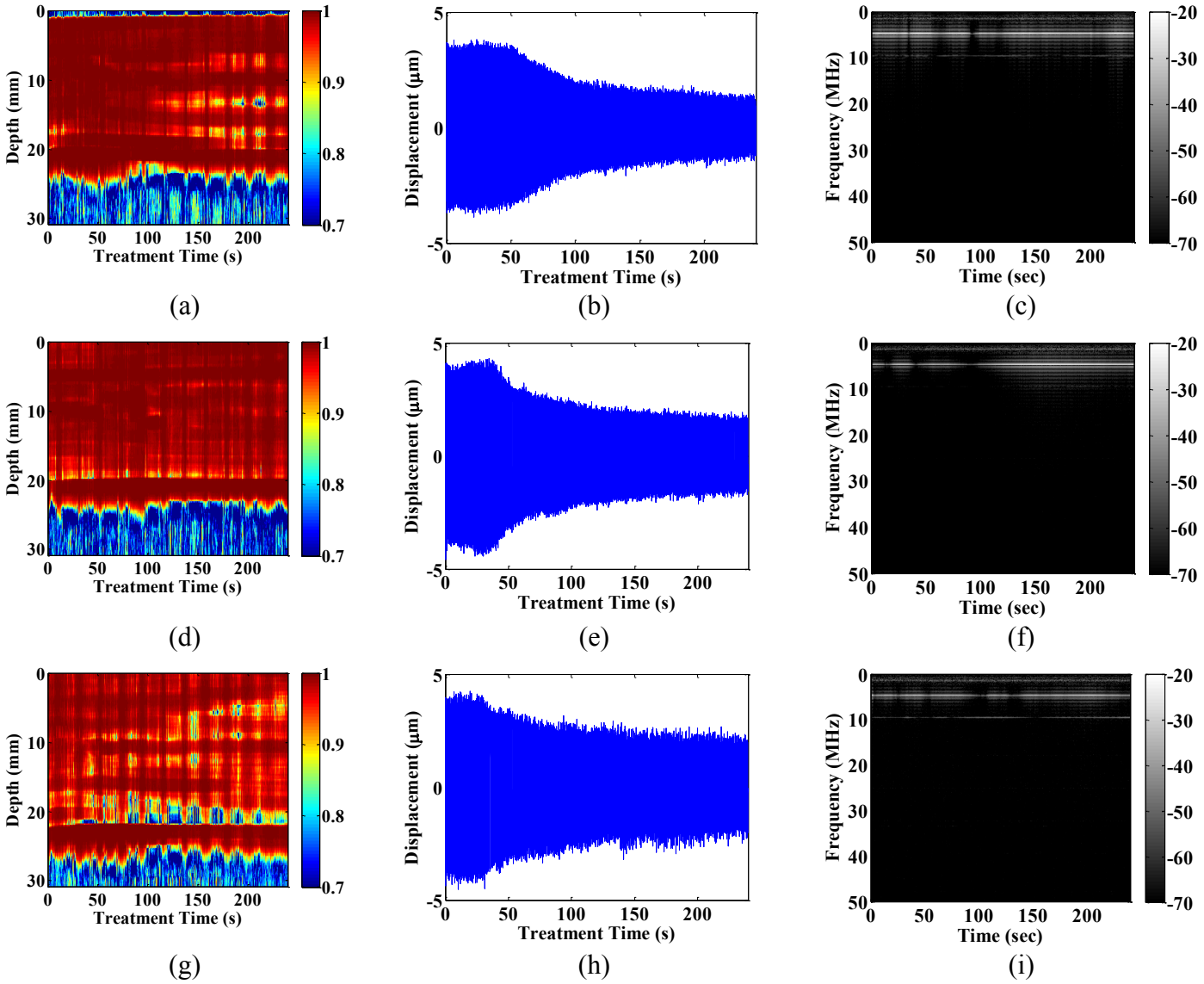

Figure 4.9. Multi-parametric monitoring of both focal HMIFU parameters and acoustic response under HIFU treatment with slow denaturation. The HMIFU correlation coefficient remained high for HIFU treatment with (a) 4W, (b) 5W, and (c) 7W as well as focal displacement (b,e,h). The PCD spectrogram observed minimum presence of bubble dynamics due to boiling, which was indicated by the presence of broadband level energy (c,f,i).

Contrarily, the averaged displacement change, displacement contrast, phase shift ($\Delta\varphi$), mean correlation, and minimum correlation during the HIFU treatment with boiling cases were 197.4±315.3 %, 0.46 ± 0.37, 7.0±16.3º, 0.81±0.14, and 0.26±0.40 (Figure 4.10) (Table 4.4), which were performed under *in situ* focal acoustic intensity and power ranged between 5546 W/cm^2, 7164 W/cm^2, and 9067 W/cm^2, at 8W, 10W, and 11W, respectively.

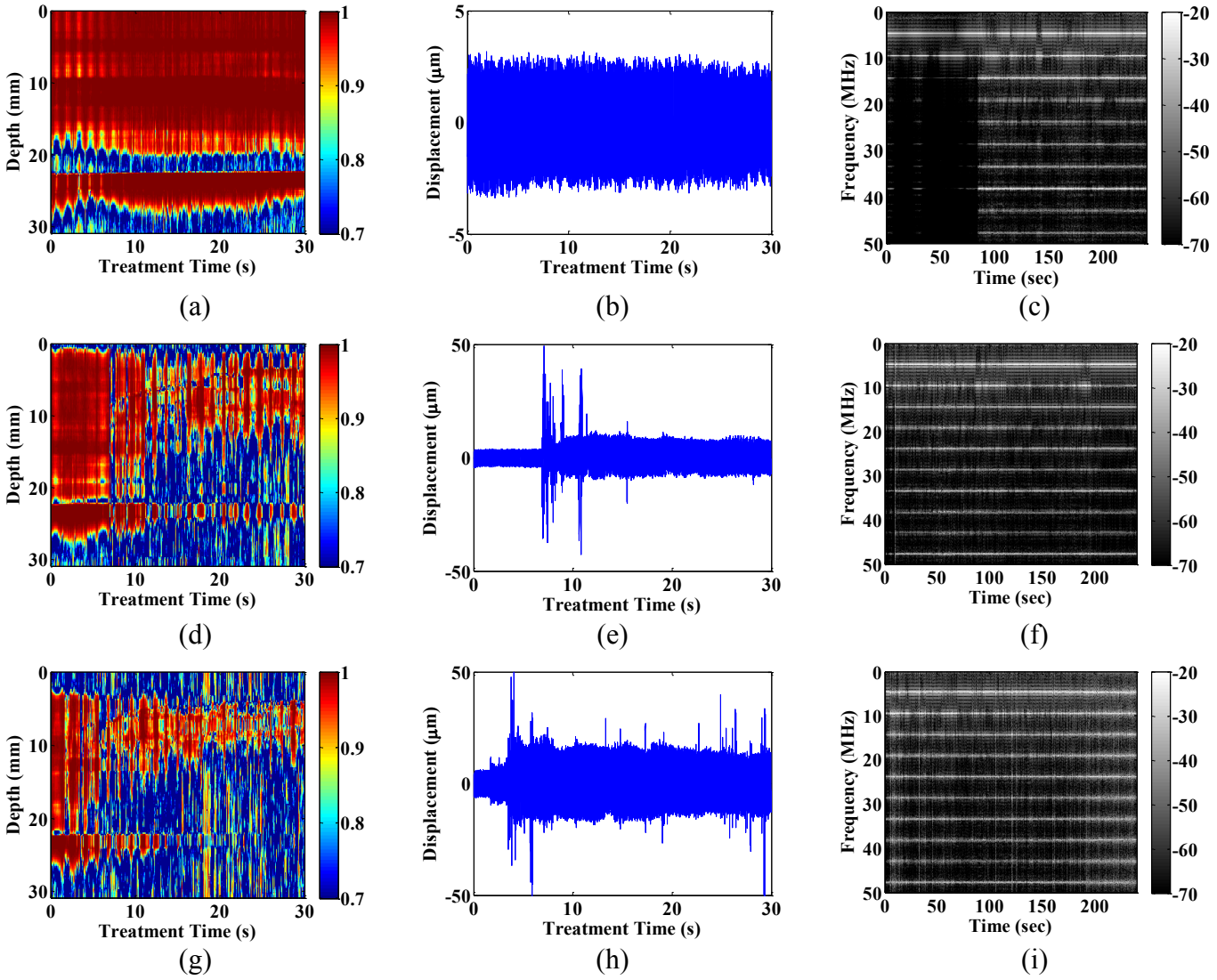

Figure 4.10. Passive Cavitation Detection (PCD) Spectrograms at acoustic power of 8W (b), 10W (c), and 11W (d) all showed significant increase in broadband noise energy, confirming formation of strong bubble dynamics due to boiling. (d) Representative temperature monitoring using T-type bare-wire thermocouple indicates boiling within the first several seconds from treatment onset, indicating presence of unsteady state throughout each monitoring case.

PCD monitoring was also performed on selected cases from both treatment sequences. No significant presence of broadband noise was detected in slow denaturation HIFU treatment

sequences (Figure 4.9c,f,i) (Figure 4.11a), where HIFU treatment with boiling cases observed the presence of broadband noise from the backscattered signal on PCD spectrograms with energy level reaching saturation point of the 40dB detection limit as temperature increases(Figure 4.10c,f,I) (Figure 4.11b).

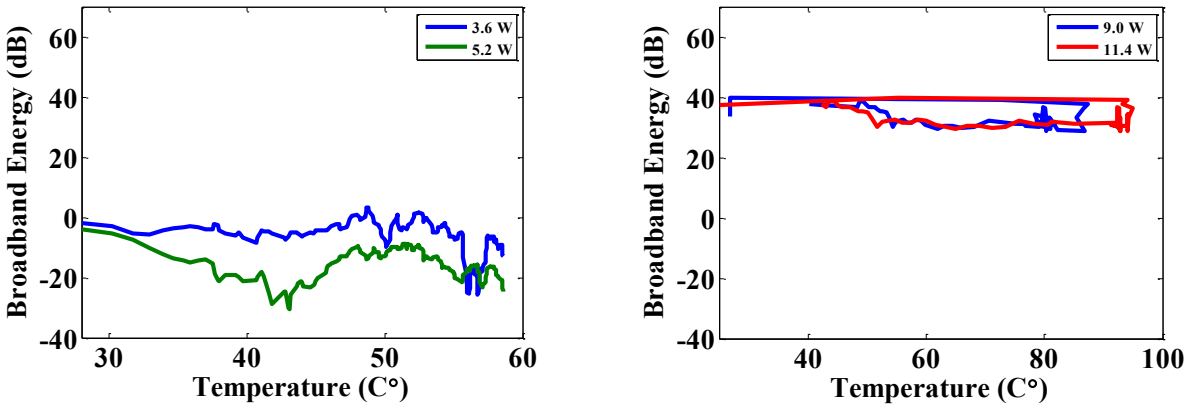

Figure 4.11. Quantification of broadband energy for PCD monitoring of both HIFU treatment with boiling (a) and slow denaturation (b) sequences. The blue and green represents the cases of 4W and 5W, respectively, whereas the red and blue represents the cases of 10W, and 11W, respectively.

Simultaneous monitoring of PCD and displacement with temperature monitoring were also conducted, where the energy of broadband noise in PCD spectrograms amongst slow denaturation HIFU treatment cases showed insignificant presence of broadband noise level ranging between -30 to -40 dB and HIFU treatment with boiling sequences exhibited strong and chaotic trend, reaching saturation of detection limit at 40dB along with drastic temperature increase up to around 100 degree Celsius (Figure 4.11b). All of the 21 cases under slow denaturation HIFU treatment sequence with displacement decrease also exhibited an increase-then-decrease displacement trend, i.e., the increase slope was 0.072±0.2 μm/sec while the

decrease slope was -0.0025± 0.03 µm/sec. An example of the slow denaturation displacement curve was shown with simultaneous temperature monitoring using bare-wire thermocouple. It can observed that the displacement increase reaches a peak range around 50-60 degree Celsius followed by the stiffening phase, and the formed thermal lesion is relatively uniform without significant mechanical tear as observed in the lesions formed by boiling treatment sequences (Figure 4.12a,b). In contrary, both displacement and temperature monitoring were chaotic in the HIFU treatment with boiling, where no consistent pattern between displacement variation and temperature change was observed (Figure 4.12c,d)

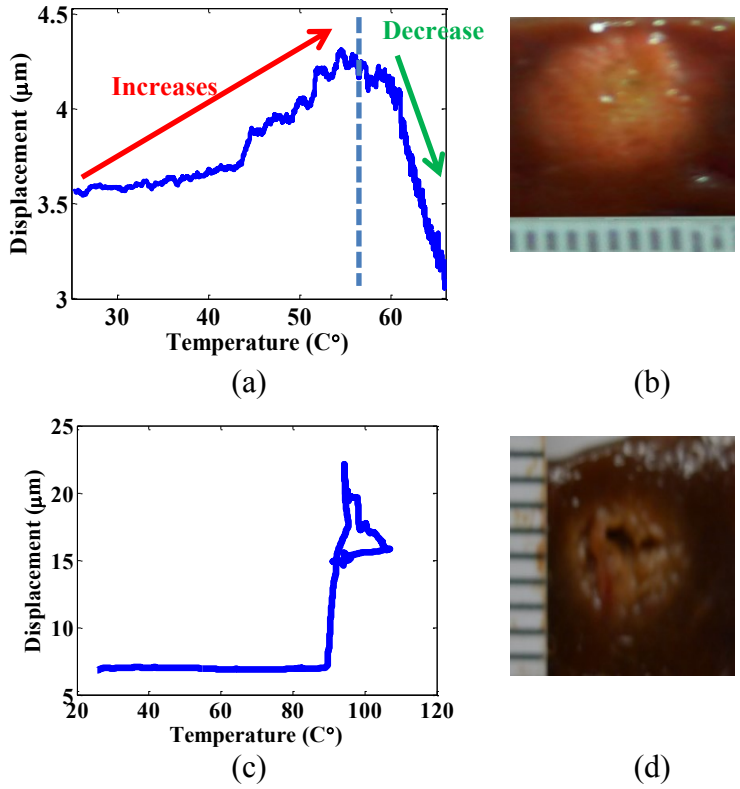

Figure 4.12. Comparative display between the HMIFU focal displacements with temperature monitoring and gross pathology of thermal lesion for both HIFU treatment with slow denaturation (a,b) and boiling (c,d) sequences, respectively.

4.1.10 Discussion

The objective of this study was to perform a comprehensive investigation in understanding the relationship between HMIFU monitoring parameters (i.e., focal displacement phase shift ($\Delta\varphi$), mean cross correlation coefficients, and minimum cross correlation coefficient) and its associated underlying acoustic and thermal property change for both boiling sequence (high power and short duration) as well as slow denaturation (low power and long duration) HIFU treatment sequence, where the thermal and acoustic monitoring were completed using thermocouple and PCD monitoring, respectively. We expected strong presence of thermal and acoustic changes will increase the variability of HMIFU assessment during boiling sequence, while a relatively stable change, i.e., a gradual of tissue softening-then-stiffening indicated by displacement increase then decrease will likely to be the outcomes amongst the slow denaturation sequence, where the presence of acoustic and thermal property change is gradual and minimized.

For or HIFU treatment with slow denaturation, example cases of cross correlation (Figure 4.9 a,d,g), focal displacement (Figure 4.9 b,e,h) and PCD spectrogram (Figure 4.9 c,f,i) were monitored under treatment protocol of 240 seconds with *in situ* focal acoustic intensity and power ranged between 2773 W/cm^2, 3582 W/cm^2, 5015W/cm^2, at 4W, 5W, and 7W, respectively. As we hypothesized, it was clear that all of the HMIFU parameters showed consistent trend across the HIFU treatment window: Cross correlation coefficients, especially both the mean (Figure 4.13a, blue) and minimum correlation coefficients (Figure 4.13a, green), remained high (Figure 4.9a, d, e) throughout the entire treatment window.

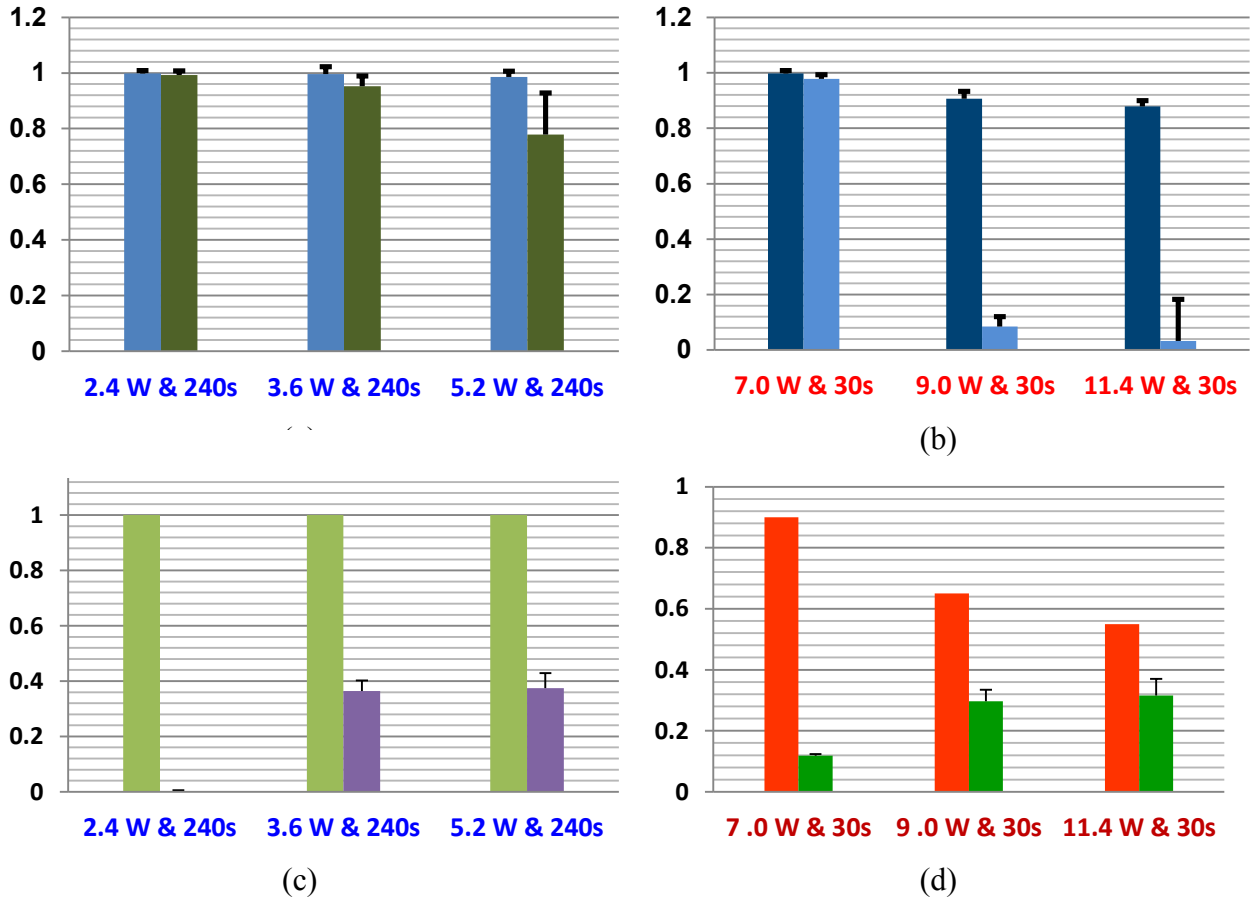

Figure 4.13. Quantification of HMIFU parameters used in this study for both HIFU treatment with slow denaturation (a,c) and boiling (b,d): Mean cross correlation coefficient across the entire treatment window (Light blue in (a) and Dark blue in (b)), Mean cross correlation coefficient across the entire treatment window (Dark green in (a) and light blue in (b)), Cases with displacement decrease or increase-then-decrease trend amongst the slow denaturation case (Light green in (c), Orange in (d)), and displacement contrast between maximum to minimum displacement monitored during the treatment window (Purple in (c) and Green on (d)).

Both focal displacement exhibited increase-then-decrease trend, indicating tissue softening-then-stiffening mechanical property change (Figure 4.9b, e, h). PCD spectrograms

showed minimized presence of boiling-associated bubble dynamics (Figure 4.9c, f, i)(Figure 4.11a), which is represented by the minimized level of broadband noise (Figure 4.11a). For HIFU treatment with boiling, example cases of cross correlation (Figure 4.10 a,d,g), focal displacement (Figure 4.10 b,e,h) and PCD spectrogram (Figure 4.10 c,f,i) were monitored under treatment protocol of 30 seconds with *in situ* focal acoustic intensity and power ranged between 5546 W/cm^2, 7164 W/cm^2, and 9067 W/cm^2, at 8W, 10W, and 11W, respectively. In contrast to the slow denaturation treatment cases, much more significant variations were observed amongst the HMIFU parameters across the HIFU treatment window: The mean cross correlation coefficients remained high (Figure 4.13b, dark blue); However, the minimum correlation coefficients (Figure 4.13b, light blue) dropped down significantly across numerous time points throughout the entire treatment window (Figure 4.10a, d, e). Further validating our hypothesis, the focal displacement exhibited either relatively unchanged (Figure 4.10b), or significant increase (Figure 4.10e, h) following HIFU treatment onset. In addition, the PCD spectrograms showed significant presence of boiling-associated bubble dynamics (Figure 4.10c, f, i), which is represented by a saturated level of broadband noise (Figure 4.11b) across the entire treatment window. The characteristic between displacement variation and temperature was also studied, where a gradual displacement increase-then-decrease trend was observed for HIFU treatment with slow denaturation, where displacement reached maximum around 55 °C following the tissue softening phase, then following a decrease trend indicating tissue softening phase (Figure 4.12a). This observation is consistent with previous findings from both our group and other groups [152-154, 202, 214]. Nevertheless, it is interesting to see the chaotic trend for the relationship between displacement change over temperature rise under HIFU treatment with boiling, where the temperature reading is strongly affected by the bubble dynamics and shielding

effect from the boiling mechanism, thus exhibits a chaotic trend with non-monotonic increase with treatment time (Figure 4.12b). Additionally, there is a distinct characteristic difference between the gross pathological lesion formed after the two different HIFU treatment sequences: The lesion formed under slow denaturation sequence is relatively uniform in shape and boundary (Figure 4.12b), whereas the lesion formed under HIFU treatment with boiling contains cavities, which can be due to either strong mechanical and thermal effect due to the boiling mechanisms around 100 degree Celsius (Figure 4.12d). The mean correlation coefficients remained high throughout the treatment duration for both HIFU treatment with slow denaturation and HIFU treatment with boiling (Figure 4.12 a,b), nevertheless, the minimum correlation dropped significantly in average down to 0.26 amongst the cases of HIFU treatment with boiling (Figure 4.12b) compared to the slow denaturation cases, where it remained above 0.8 in average (Figure 4.12a). As an increase-then-decrease displacement trend was observed for all of the slow denaturation with displacement decrease (Figure 4.13c), more cases amongst the HIFU treatment with boiling exhibited opposite trend of displacement increase or simply no significant change (Figure 4.13d). Nevertheless, there remained a strong displacement contrast across the monitoring displacements for all of the cases with HIFU treatment with boiling (Figure 4.13d), indicating that the robustness of HMI displacement even under the presence of strong broadband noise induced by the boiling bubble dynamics. From the present study, it is observed that the slow denaturation sequences are more suitable to use in order to monitor a steady viscoelasticity change under HIFU treatment using HMIFU, because of its advantage in maintaining a high cross correlation coefficient while minimizing the disturbance due to the mechanical and acoustical noise induced by boiling mechanism when temperature reached around or above 100 °C. Although there could potentially be other factors that can affect the level and occurrence

chance of boiling mechanism such as the degassing time, depth dependent attenuation effect, which are still being investigated, the fact that displacement contrast still remains amongst the cases with strong broadband energy level and low Minimum correlation coefficient validates the robustness of HMIFU to detect the formation of lesion even under HIFU treatment with boiling mechanism. Other areas of improvement includes the ability to simultaneously monitor all of the PCD, thermocouple, and HMIFU parameters as only either PCD or thermocouple with HMIFU parameters were able to be simultaneously studied in this work.

4.1.11 Conclusion and Summary

In this chapter, a comprehensive monitoring study has been performed in order to investigate the relationship between HMIFU parameters (focal displacement, phase shift ($\Delta\varphi$)) and thermal, acoustical, and mechanical effects within focal medium (i.e., boiling, cavitation, and nonlinearity) using barewire thermocouple and PCD on biological specimen *ex vivo*. HIFU treatment sequences with slow denaturation were performed with acoustic power ranged between 3.6 to 5.2 W for 120-240 s, where consistent displacement increase-then-decrease trend was observed, indicating tissue softening-then-stiffening and phase shift increased with treatment time in agreement with mechanical testing outcomes. The cross correlation parameter remained high throughout the entire treatment time under a minimized broadband energy and boiling mechanism. HIFU treatment sequences with boiling were performed with acoustic power ranged between 8 to 11W for 30 seconds, where both displacement and phase shift did not show

consistent trend under the presence of strong boiling mechanism confirmed by both PCD and thermocouple monitoring. Although the optimized sequence to perform consistent viscoelasticity monitoring seems to be the HIFU treatment with slow denaturation sequence, HMIFU parameters such as displacement contrast remained high amongst the HIFU treatment with boiling sequences, indicating the robustness of HMIFU in monitoring lesion formation under boiling mechanism. In summary, extensive investigations were performed in assessment and optimization of the feasibility of HMIFU monitoring for HIFU treatment sequence with slow denaturation and boiling by using a multi-parametric approach combining acoustic, mechanical, and thermal monitoring using the developed and optimized 1-D HMIFU system. Based on the studied fundamental mechanisms during HMIFU monitoring, the next step is to translate the HMIFU technique towards clinical implementation. Therefore, the following chapter 5 will describe the development and feasibility studies of a 2-D pre-clinical HMIFU system, which also incorporates the multi-parametric study protocols described throughout this chapter.

Chapter 5. 2D-HMIFU System based HIFU treatment monitoring

5.1 2-D HMIFU System

When it comes to the clinical translation of HMIFU, the fundamental limitation of the previously presented system lies in two aspects: 2-D imaging and real time display. The studies previously described in chapter 4 were performed by a 1-D HMIFU system utilizing a single element pulse echo transducer. Nevertheless, in a clinical setting where clinicians need to perform treatment localization, monitoring, and assessment, it is important to develop 2-D based HMIFU system because the target (e.g., tumor, organ) of HIFU treatment is usually a 3D object. In addition, the ability to perform 2-D avoids the necessity of mechanical raster scanning during targeting and assessment imaging stages, which can increase the efficiency of HIFU treatment procedure. Another previous limitation is the separate acquisition and processing units, where displacement estimation is performed offline by a different hardware unit. This is very time consuming and thus may significantly delay the HIFU treatment time, which in turn can potentially lead to further surgical risks. Therefore, in order to successfully translate the HMIFU technique towards a clinical setting, it is necessary to implement a clinically-oriented, fully-integrated, 2-D high frame rate platform capable of analyzing and streaming real time feedback of HMI assessment back to the user.

In order to develop any high frame rate ultrasound elasticity imaging modality, it is necessary to build a system with fast and efficient imaging acquisition, reconstruction (i.e., beam forming), and displacement estimation algorithm. Historically, the emergence of high frame rate

imaging stems from the concept of parallel beamforming, which was first proposed with reconstruction of an entire image from echoes generated after just a single acoustic transmission with frame rates up to kHz through parallel beamforming with fast analog multiplexers [215]. Later, the parallel processing technique was successfully implemented and validated *in vivo* using a phased array configuration, namely "Explososcan", where data acquisition rate was quadrupled with simultaneously reconstructing four receiving beams per single wide transmit beam [216-218]. Recently, several image acquisition techniques have also been developed and implemented onto commercial scanners to further increase the imaging frame rate such as plane-wave [219] or divergent transmit beam [220, 221]. In tissue elasticity imaging, high frame rate imaging has demonstrated a promising clinical value in quantitative imaging of tissue viscoelasticity with tracking sub-millimeters displacement produced by the shear waves imaged at high frame rate and generated from excitation source such as Transient Elastography [79, 222] or acoustic radiation force (SSI) [84, 219]. In addition, several Graphical Processing Unit (GPU) based beamforming approaches have also been developed to achieve high frame rate imaging such as Synthetic Aperture (SA) imaging [223-227], real-time small displacement estimation [228, 229], and Short-lag Spatial Coherence Imaging (SLCSC) [230].

Nevertheless, there has yet to be a novel beamforming algorithm developed for 2-D ultrasound elasticity imaging based HIFU monitoring application, where high-frame rate, high spatial resolution, real-time feedback over a continuous imaging window up to several minutes. Therefore, a fast parallel beamforming algorithm with further improvement in reconstruction speed is required for real time, 2D elasticity imaging based HIFU monitoring in order to detect the onset of effective treatment (i.e., cell necrosis) and stop the treatment to spare as much normal surrounding regions as possible. More importantly, monitoring feedback abilities in

HIFU treatment is also the key to maximizing the surgical efficiency because HIFU treatment is known to be a lengthy procedure especially when the target tumor volume is large compared to the focal spot size of the HIFU transducer, i.e., a series of treatment sequence is applied across the entire tumor volume in a raster scan manner. Therefore, the ability to detect the onset of lesion formation at each individual treatment location can decrease the total time of the ablation procedure.

The objectives in this chapter are first to develop a 2-D HMIFU system using a fully-integrated, clinically relevant commercial ultrasound scanner with high frame rate real time imaging capability by incorporating a GPU-based reconstruction algorithm. The algorithm allows for a real-time 2D HMIFU monitoring based on a sparse-matrix algorithm for parallel beamforming and scan conversion algorithm. The completed platform is expected to provide a quantitative real time 2D monitoring feedback during the HIFU treatment directly back to the user. We also aim at demonstrating the initial feasibility of the 2-D HMIFU in elasticity imaging and HIFU treatment monitoring through tissue-mimicking phantom and *in vitro* tissue experiments. We expect to observe under a real-time streaming mode, a reproducible range of displacement across our imaging measurement on the phantom study, as well as detect the onset and decrease of displacement throughout HIFU treatment, which indicates for stiffening of tissue upon lesion formation. Moreover, we aim at performing reproducibility study using the developed system and confirm the reliability of our treatment sequence from both the thermal and mechanical aspect, using thermocouple monitoring and mechanical testing, respectively.

5.2 Methods

Therapy and Imaging Unit (Hardware)

A 93-element, PZT-4 ceramic HIFU Array (H-178, Sonic Concept Inc., Bothell WA, U.S.A, Diameter $_{\text{individual element}}$ = 10 mm, Diameter$_{\text{overall outer}}$ = 110 mm, Diameter$_{\text{overall inner}}$ = 41 mm, f_{center} = 4.5 MHz, Focal depth = 70 mm) was used in this study. The transducer surface is covered with a polyurethane based membrane, which is coupled with a custom sterilization and degassing system (WDS-104, Sonic Concept, Bothell, WA, U.S.A.) with control of both volume and circulation flow of degassed cooling water within the transducer-tissue interface during HIFU treatment. All channels were synchronously excited by an AM-HIFU excitation signal was generated through a dual-channel arbitrary waveform generator (AT33522A, Agilent Technologies Inc., Santa Clara, CA, U.S.A.), and the extrapolated *in situ* focal acoustic pressure and intensity (I_{sptp}) was extrapolated to be 6.5 MPa and 9067 W/cm^2, respectively, based on priror hydrophone (HGN-0200; Onda Corporation, Sunnyvale, CA, U.S.A.) calibration procedure [204]. A 64-element phased array (ATL., Bothell, WA, U.S.A., f_{center} = 2.5 MHz) has been confocally fitted through a circular void or the HIFU transducer aperture through a custom built water-proof mechanical gasket with adjustable rotational positioning steps at every 36º steps for adaptive targeting and monitoring. The phased array transducer is operated through a 4-board VDAS system (Verasonics, Bothell, WA, U.S.A.) and a 260-pin header connector. The coupled transducer pair was mounted to a 3D translational system (Velmex Inc., Bloomfield, NY, U.S.A.) for mechanical translation during targeting. The excitation therapeutic sequence was synchronized with the VDAS system through a MATLAB-based (Mathworks, Natick, MA,

U.S.A.) custom algorithm on a host PC (Precision T7500, Dell Inc., Austin, TX, U.S.A.) (Figure 5.1a, 5.1b).

Figure 5.1a.

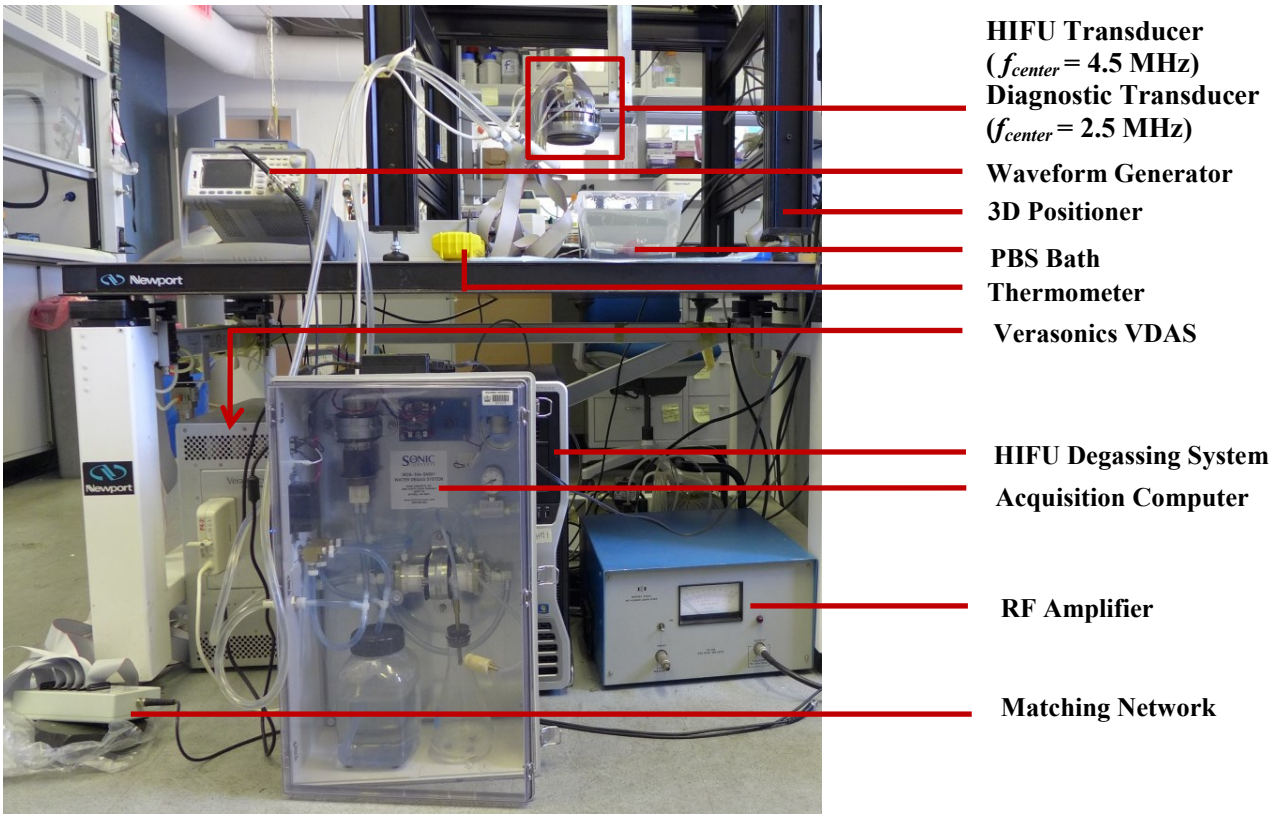

Figure 5.1a. 2D HMIFU system. The focal depth of the HIFU is 70 mm. Height of degassed water interface was adjusted around 35 mm, i.e., focal spot localized at 25 mm from surface of the target. The degassing circulation system was turned off during the experiment and turned on between trials to maintain degassing quality and transducer cooling.

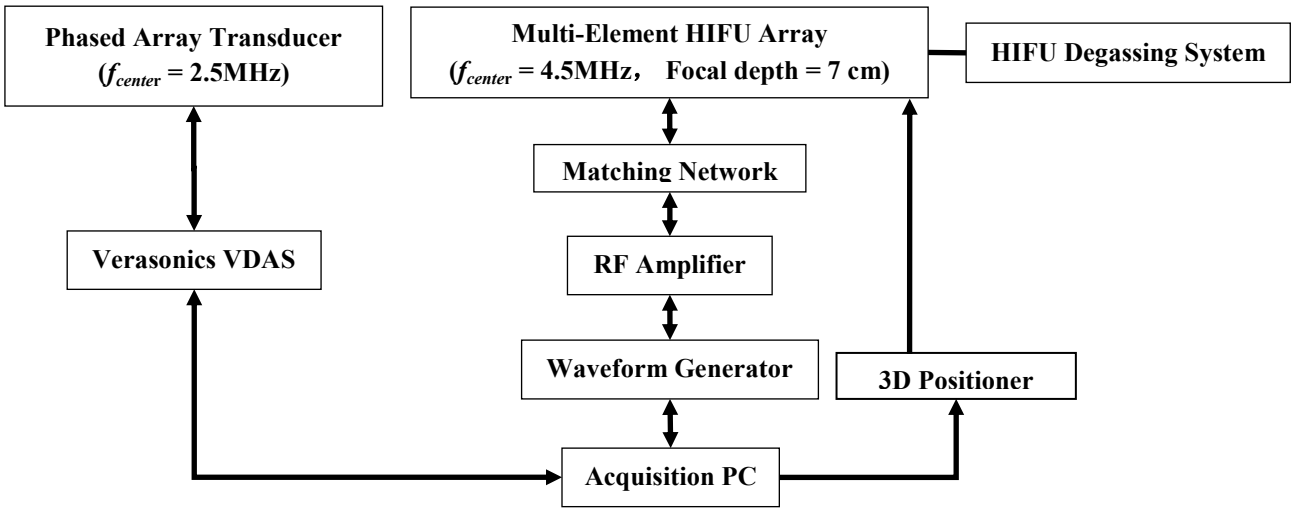

Figure 5.1b. Acquisition PC controls both transducers through waveform generator, Veraonics System, and the translational stage.

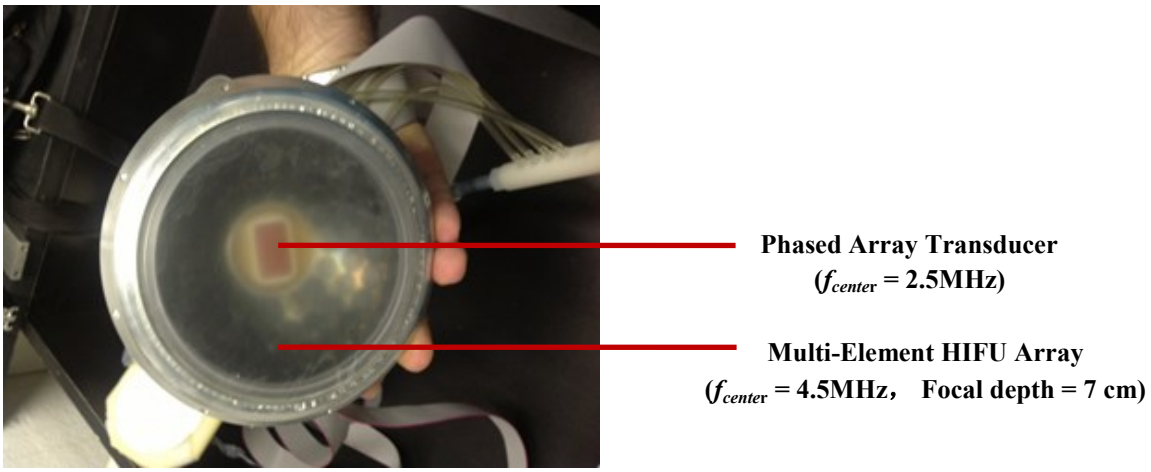

Figure 5.1c. Photo of the multi-element HIFU array with encasing of the confocally aligned phased array imaging probe.

Therapy and Imaging Unit (Software)

1a. Data acquisition and storage

The channel data signals were individually acquired through a 64-element phased array and Verasonics System using a custom divergent transmit imaging sequence [221]. The acquisition frame rate was set at 1000 frames/s (equivalent frame rate as the 1D-HMIFU study in 4.1.7), andthe analog-to-digital (A/D) sampling was chosen to be 4 samples per wavelength. The acquisition sequence is repeated continuously while the acquired frames were transferred in a stacked set of 10 frames through an external function operated within the host computer, where additional reconstruction algorithms will be applied. In this study, we have also chosen to store all beam-formed radio-frequency (RF) frames in order to demonstrate the reliability of our technique.

1b. GPU implementation of linear operators

GPU-based algorithms are formidable tools to drastically improve processing speeds, often by orders of magnitude when compared to standard MATLAB implementations. However, translating MALAB codes that often rely on pre-compiled proprietary functions to the Compute Unified Device Architecture (CUDA) language requires a significant amount of time and skill. Here, we have developed a simple approach to efficiently execute linear operations on the GPU with minimal effort and straightforward MATLAB integration. We have built our algorithm through the sparse matrix option of JACKET package (AccelerEyes, Atlanta, GA. U.S.A.) that can perform highly optimized sparse matrix-vector products on the GPU seamlessly in a MATLAB environment. As any linear operation can be recast as a matrix (from now on we will refer to this matrix as a "function matrix"), it suffices to find that function matrix to obtain a high

performance GPU function of said linear operation by using the JACKET package. More specifically, let's consider a function *f* with input *x* and output *y*, which can be a combination of any number of linear operations, including compiled functions such as interp2 in MATLAB. *x* and *y* are vectors (or matrices) containing a total of *N* and *M* elements, respectively. We have

$$y = f(x), \tag{1}$$

Since *f* is linear, there exists a matrix A such that

$$y = Ax, \tag{2}$$

where *y* and *x* are recast as vectors in R^M and R^N, respectively, without loss of generality. To find *A*, we apply *f* to the k^{th} standard basis vector e_k (i.e., a vector with zeros everywhere except in the k^{th} position) and obtain:

$$y = f(e_k), \tag{3}$$

$$y = \sum_j A_{ij} e_k, \ 1 \le i \le M, \tag{4}$$

$$y = A_{ik}, \ 1 \le i \le M, \tag{5}$$

or, in other words, $f(e_k)$ is the k^{th} column of the function matrix. By simply repeating this operation for all *k*, one can recover the matrix A. When working with images, the function matrix *A* can be very large, e.g., in our case ranging from 6×10^9 to 48×10^9 elements, depending on the upsampling rate and spatial size of displacement map reconstruction, hence the importance of using sparse matrix formats when possible, i.e., a regimen in which only non-zero elements are allocated. This case is very common, e.g., in the case of 2D linear interpolation: let vector *x* contain N elements corresponding to N pixels of a given image, and *y* contain M>N

elements corresponding to M pixels of the interpolated image. For a typical 4-neighbor interpolation scheme, an interpolated pixel y_i is given by a linear combination of 4 pixels of vector x. Therefore, the i^{th} line of $A_{ij,}$ used to compute pixel $y_{i,}$ contains 4 non-zero values and N-4 zeros, with N typically larger than 10,000. It is therefore highly beneficial both in terms of memory requirements and computational speeds to represent the matrix A in its sparse form. Generating the function matrix itself can be computationally expensive both in terms of time and memory; however, the function matrix has to be computed only once, which expedites the process of generating the function matrix to code compilation. Additionally, in many cases, smaller matrices can be obtained from larger matrices in a straightforward manner by removing appropriate lines of the function matrix, since each column of the function matrix correspond to one pixel of *x*, and each line of the function matrix corresponds to one pixel in *y*. This property can be used to adjust the angle field-of-view and the depth in real-time, without re-computing the function matrix.

1c. GPU based sparse matrix RF data reconstruction

In this study, we used this approach to recast the delay-and-sum beamforming [231] as well as the scan conversion in matrix-vector products since these operations are linear. In order to obtain every beamformed RF frame, two sparse matrices were generated for reconstruction and scan conversion, respectively. More specifically, every frame of RF data was reconstructed by first multiplying the channel data matrix with the reconstruction sparse matrix, then multiplying the product matrix by another sparse matrix for scan conversion (Figure 5.2), each performed as a single operation. The RF data were reconstructed on a 90° field of view with 128 beam lines for the gelatin phantom imaging studies, and reduced to 30° with 32 beam lines due to transfer and storage efficiency for HIFU treatment monitoring studies, respectively. It is also

noteworthy that the process of constructing the sparse matrix function matrix was itself performed on the GPU by using MATLAB GPU-compatible operations to limit processing times.

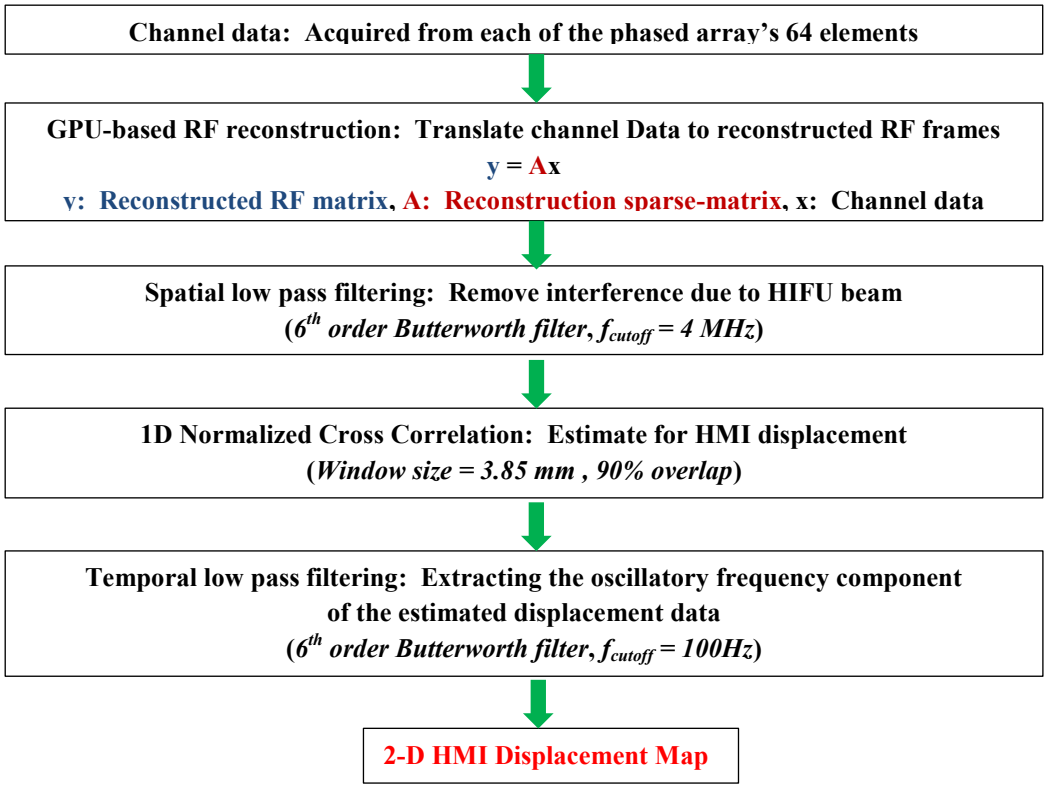

Figure 5.2. Flow chart of displacement image reconstruction algorithm. Note that frames were acquired and transferred from VDAS to host computer in a synchronous way, i.e., every acquisition is triggered by the completion of the previous processing.

1d. Displacement estimation

The same incremental displacement estimation algorithm described in Chapter 4 was used for every lateral beam line following the sparse-matrix based reconstruction algorithm scan conversion as described in section 2b (Figure 5.2). Note that the cross-correlation window size and overlap were 1.54 mm and 90%, respectively. In order to verify the reliability of the streamed data in this study, we have utilized another acquisition method where a separate set of 200 frames was acquired, transferred, and only beamformed before stored in the host computer.

2. Phantom and *ex vivo* experiment

2a. Gelatin phantom experiment

A gelatin phantom (n = 1, location = 3, measurement = 3) using gelatin bloom 50 powders (MP Biomedicals LLC., Santa Ana, CA, U.S.A.) was manufactured based on recipe from prior literature [232]. The constructed phantom was designed to cure with a cylindrical shape (Diameter 120 mm, Height 60 mm) with a Young's Modulus of 10 kPa. The phantom was placed on acoustic absorber in order to minimize any interface reflection interference and degassed echo gel (AQUASONIC®100, Parker Laboratories, Inc., Fairfield, NJ, U.S.A.) was placed above the phantom between the transducer membrane for impedance matching (Figure 5.1a). The imaging sequence consisted of a continuous 1.2 second excitation, and data were transferred back to the host PC for a set of 400 ms, equivalent to 20 cycles of HMI excitation. The water in coupling membrane of the HIFU transducer was degassed for 2 hours prior to the experiment using the circulation system, and acoustic gel was also degassed for one hour prior to the experiment.

2b. Ex vivo canine liver experiment

Canine livers (subject=2, lobes = 2, treatment location = 3) were excised immediately upon animal sacrifice and immersed into degassed Phosphate buffered saline (PBS) solution bath maintained at temperature of 25 ºC. The specimens were degassed for two hours prior to HIFU in order to prevent any air trapped inside. Each specimen was fixed using metallic needles onto an acoustic absorber submerged in a de-ionized and degassed PBS tank (Figure 5.1a). The HIFU treatment sequence consisted of a continuous 120-second excitation at 11W, and beamformed RF data frames were transferred back to the host PC at a rate of 100 fps, equivalent to 20 cycles of HMI excitation.

2c. In vitro reproducibility study with thermocouple monitoring and mechanical testing

Canine livers (subject=5, lobes = 5, treatment location = 19) were excised immediately upon animal sacrifice and immersed into degassed Phosphate buffered saline (PBS) solution bath maintained at temperature of 25 ºC. The specimens were then degassed for two hours prior to the HIFU in order to prevent any air trapped inside. Each specimen was fixed using metallic needles onto an acoustic absorber submerged in a de-ionized and degassed PBS tank (Figure 5.1a). The HIFU treatment sequence consisted of a continuous 120-second excitation, and beamformed RF data frames were transferred back to the host PC at a rate of 200 frames per second, equivalent to 40 cycles of HMI excitation. Focal temperature monitoring was performed by inserting a T-type bare wire thermocouple with diameter of 25 μm (Omega Inc., Stamford, CT) inside the tissue. The diameter of the thermocouple was chosen to be smaller than 1/10 of the carrier wavelength in order to minimize reflection and viscous heating artifacts [201]. The

setup framework of the 2-D HMIFU system was optimized by utilizing two acquisition PCs in order to synchronously acquire both the thermocouple reading and the RF signals, where the VDAS system was used as a trigger source (Figure 5.3). In addition, two raster scan HIFU treatments were performed on the 2 lobes from 2 additional subjects. Each raster scan treatment was performed on a 3 by 3 grid with 5 mm spacing. The repeated treatment sequence for each HIFU treatment was under same parameters as previously mentioned. All of the mechanical testing measurements were performed immediately following the HIFU treatment. The details of the mechanical testing apparatus are described in the Appendices section of this chapter.

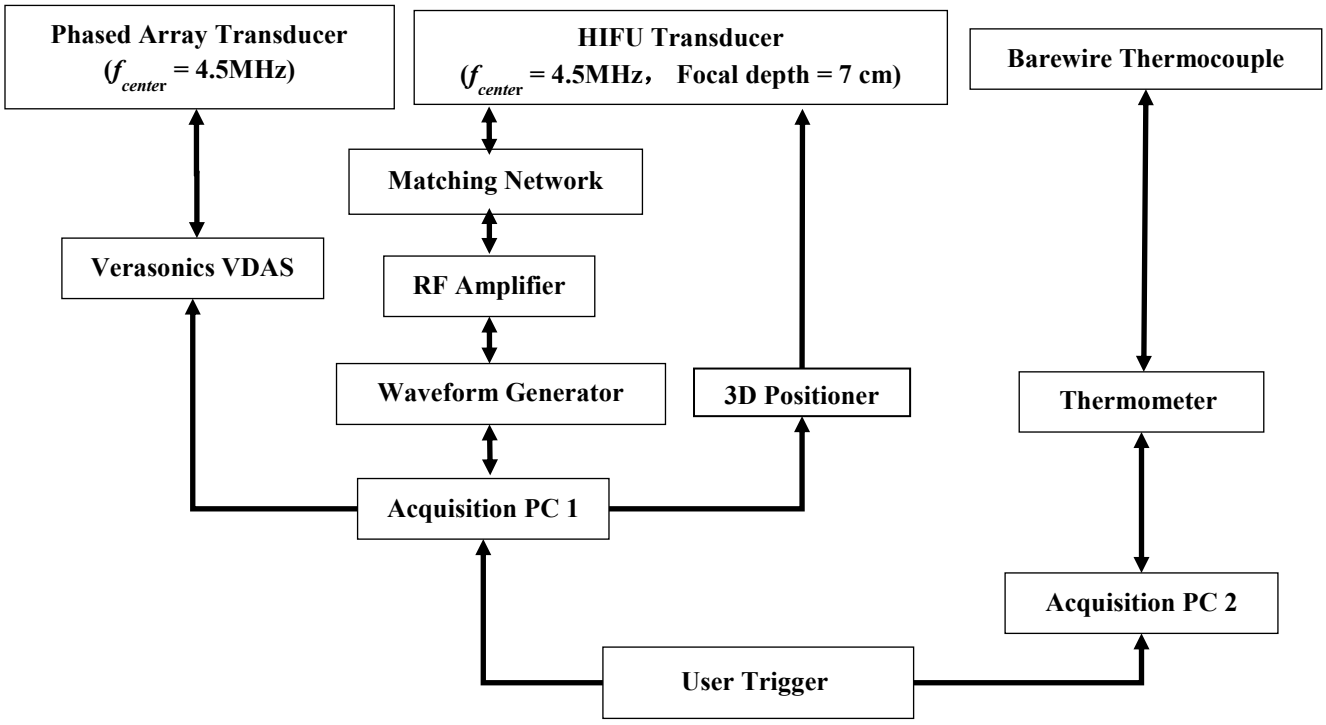

Figure 5.3. Upgraded 2D-HMIFU framework with two acquisition PCs controls both transducers through waveform generator, Veraonics System, thermometer, and the translational stage, respectively.

5.3 Results

GPU vs. CPU streaming speed

For both sets of experiments, the processing speed of GPU-based processing was compared against that of the CPU-based. In gelatin phantom experiment, the motion display (i.e., processing time from data acquisition to displacement estimation) frame rate was 1 Hz using the GPU-based sparse matrix algorithm and 0.01Hz using the CPU-based algorithm when reconstructing on a 90º field of view (128 lines) image from 50 to 90 mm deep (9.6 um axial grid step). In *ex vivo* canine liver experiment, the motion display (i.e., processing time from data acquisition to displacement estimation) frame rate was 15 Hz and 5 Hz with reconstructing 32 and 64 RF lines, respectively, using the GPU-based sparse matrix algorithm and 0.09 and 0.05 Hz using the CPU-based algorithm for a 40 mm range (9.6um axial grid step) and 30 degrees angle field of view image (Table 5.1).

Field of view	**Conventional CPU beamforming**	**Sparse-Matrix based GPU beamforming**
30°, 32 beams	0.09 Hz	15 Hz
30°, 64 beams	0.05 Hz	5 Hz
90°, 128 beams	0.01 Hz	1 Hz

Table 5.1. Online streaming frame rate using CPU-based reconstruction algorithm and GPU-based Sparse Matrix reconstruction algorithm under HMIFU imaging settings for a 40 mm range image with 9.6 um axial grid steps.

a. Gelatin Phantom experiment

Five displacement maps were obtained at three separate locations inside the gelatin phantom. B-mode imaging was performed before each imaging in order to optimize the field of view. For each displacement imaging, a 1.2 second continuous HMIFU excitation was applied and the RF signals were recorded at sets of 20-cycles (400 ms). The focal excitation zone was clearly imaged for every location investigated and also centered at the focusing depth of HIFU transducer, which is 70 mm with -6dB boundaries encompassing an ellipsoidal shape with diameters of 10 mm (axial) by 5 mm (lateral) (Figure 5.4). The distribution and magnitude range of the displacement profile at maximum excitation (Figure 5.4a, 4d), relaxation (Figure 5.4c, 4f), and zero (Figure 5.4b, 4e) force phase all remained reproducible for every cycle across the entire imaging sequence. The average peak-to-peak HMI displacement at each location was estimated to be 21.9±7.98 μm, 23.9±8.7 μm, and 21.6±2.4 μm, respectively (mean ± standard deviation).

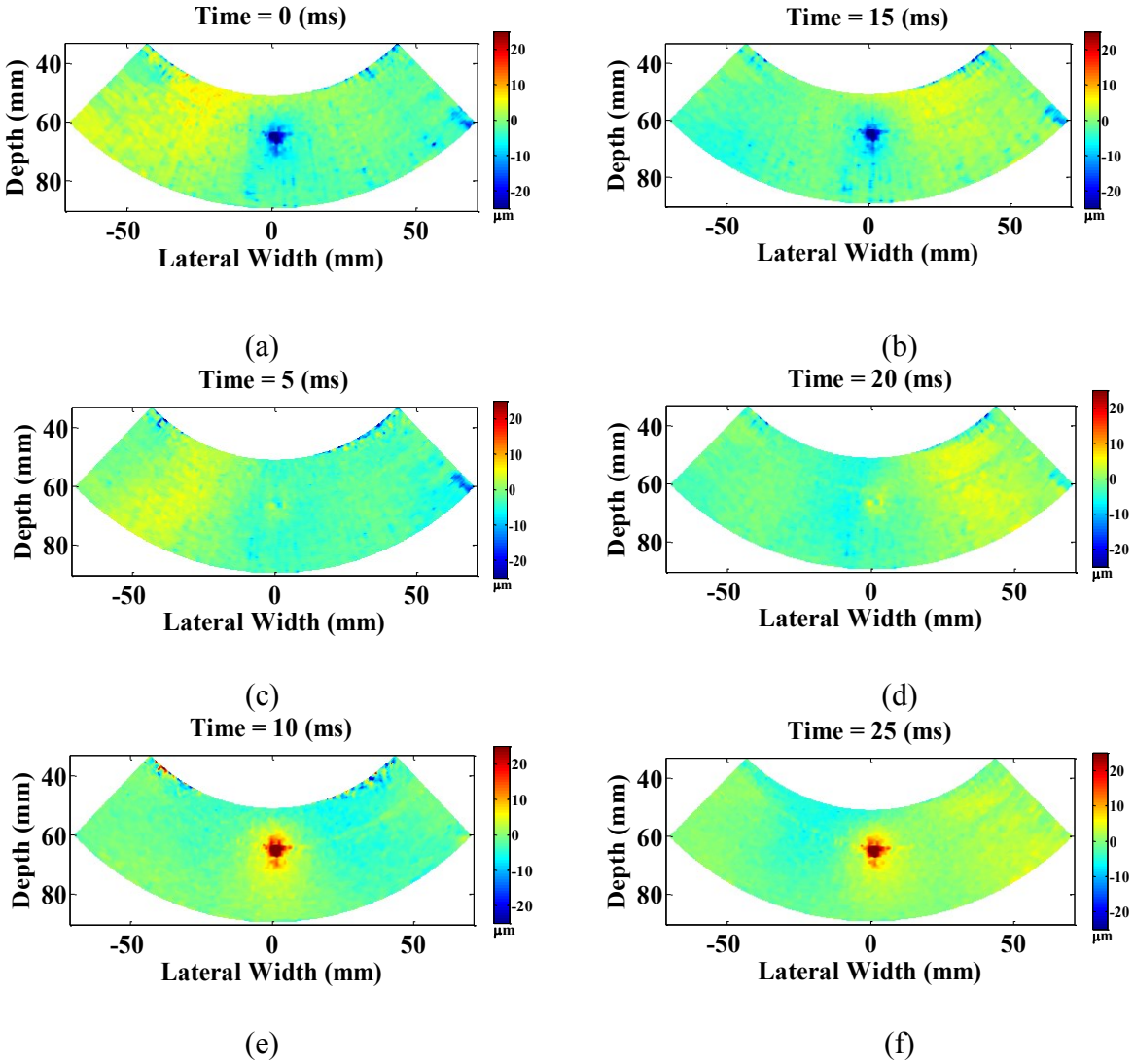

Figure 5.4. Displacement imaging using HMIFU on gelatin phantom. Three locations, peak negative (a,d), zero (b,e), and peak positive (c,f) displacement during a 50Hz-cycle across two independent period.

b. Ex vivo canine liver experiment

For each HIFU treatment, conventional B-mode imaging was used in order to target the focal zone within the region of interest inside the tissue. Three HIFU treatment sequences (8W, 120 s)at different locations across each of liver lobe using HMIFU monitoring, and a B-mode

image was acquired before and after the HIFU treatment (Figure 5.5, 6) and used for overlay with displacement image.

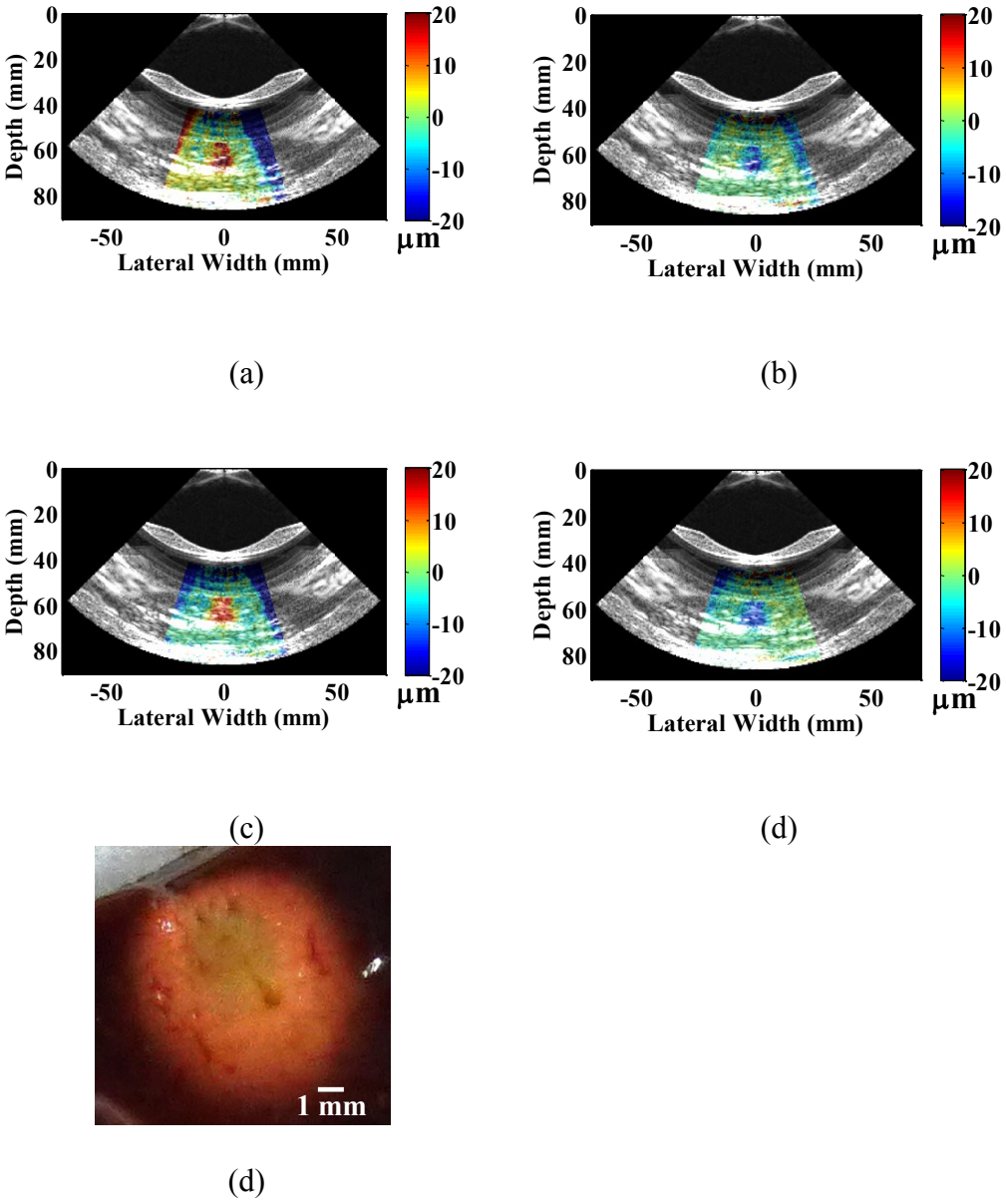

Figure 5.5. B-mode imaging with peak negative and positive displacement overlay at beginning (a,b), and ending (c,d) of a 120 second HIFU treatment for cases represented in Figure 5.4 (case 1) and the corresponding gross pathology images (e), respectively.

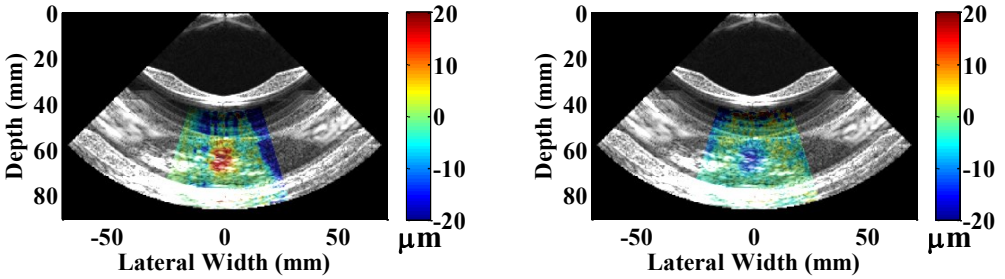

(a)

(b)

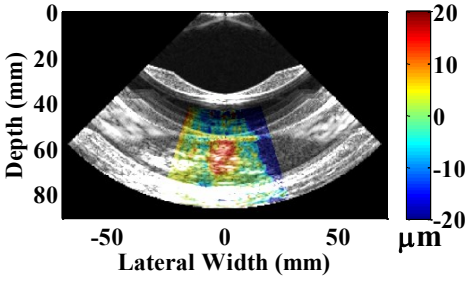

(c)

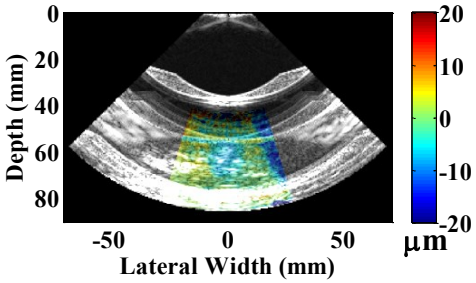

(d)

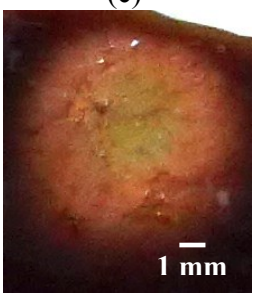

(d)

Figure 5.6. B-mode imaging with peak negative and positive displacement overlay at beginning (a,b), and ending (c,d) of a 120 second HIFU treatment for cases represented in Figure 5.5 (case 2) and the corresponding gross pathology images (e), respectively.

The peak-to-peak HMI displacements within the focal zone were monitored and processed using the same algorithm as the gelatin phantom experiment throughout the entire 2-

minute HIFU treatment period. For each of the three cases studied, a clear decrease in peak-to-peak HMI displacement of 40%, 30%, and 33% was observed, respectively. The same decrease trends were also clearly imaged in 2D, where individual single-cycle frame set consisting of maximum and minimum displacement profiles were shown in Figure 5.7, 5.8 representing each of the representative treated locations, respectively.

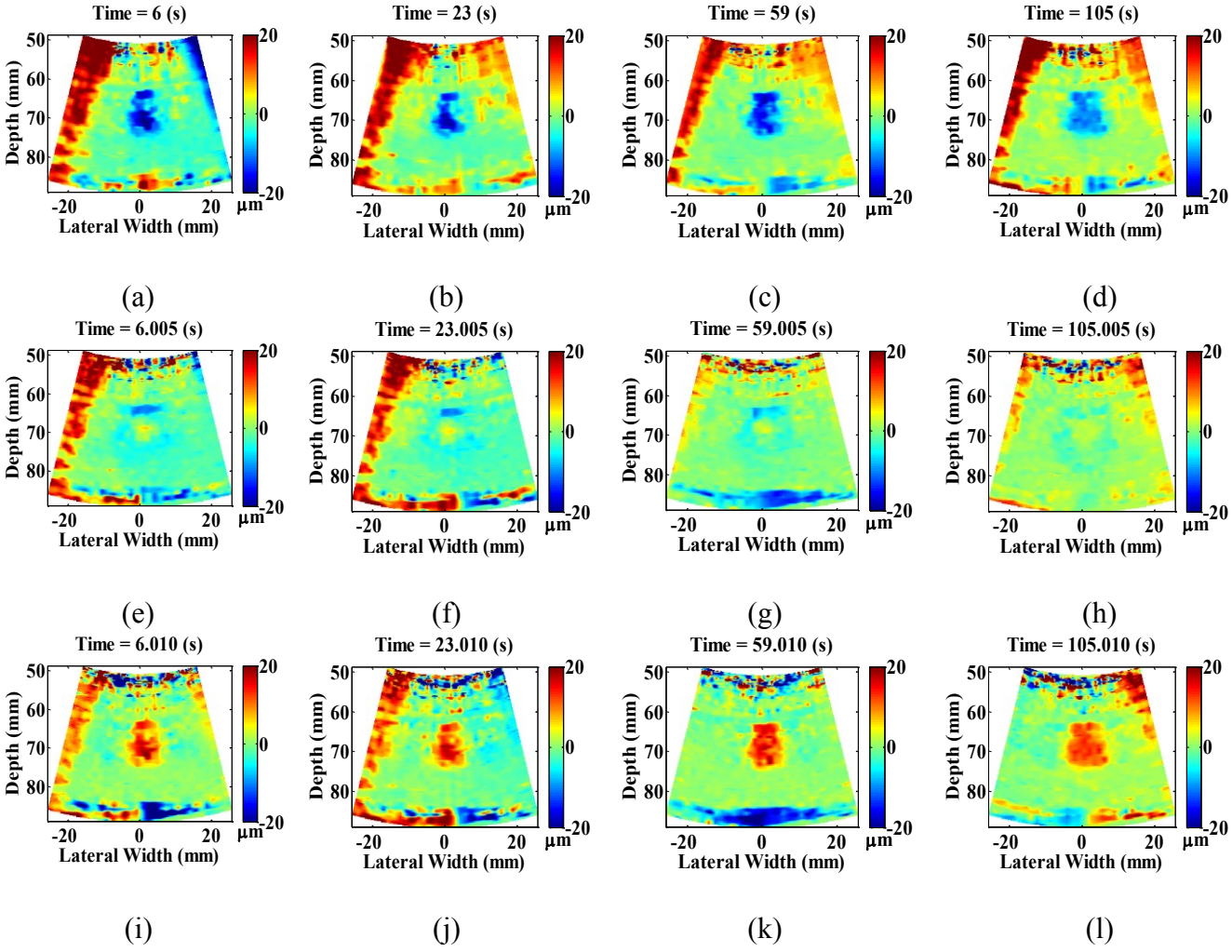

Figure 5.7. Displacement imaging and monitoring of HIFU treatment using 2D HMIFU platform. The peak negative (a-d), zero (e-h), and peak positive displacement (i-l) frames during a 50Hz-cycle at representative time points across the HIFU treatment sequence were selected to show the decrease of focal displacement as thermal lesion forms.

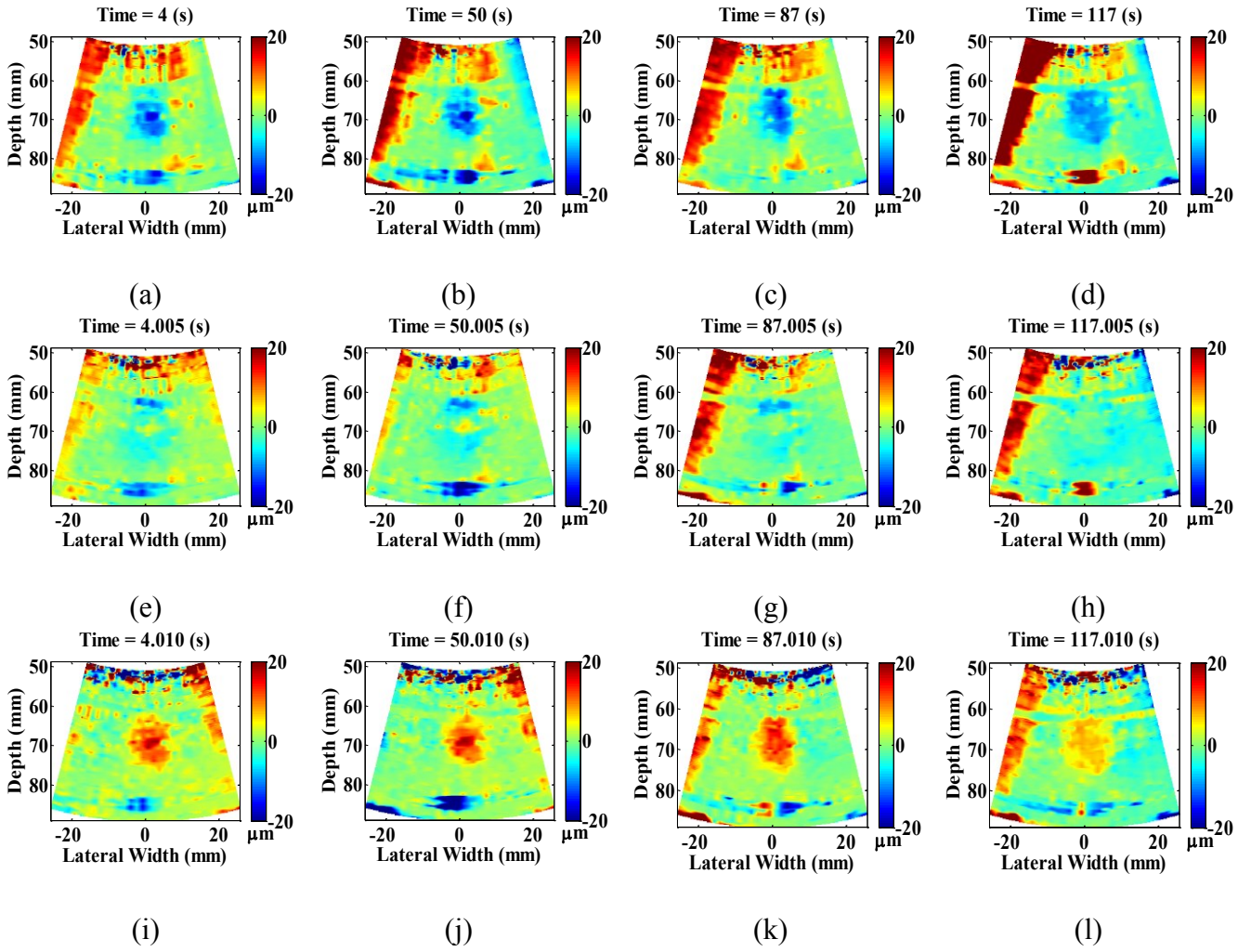

Figure 5.8. Displacement imaging and monitoring of HIFU treatment using 2D HMIFU platform at a second location. The peak negative (a-d), zero (e-h), and peak positive displacement (i-l).

The detected thermal lesion size were also imaged as 251, 254, and 226 mm^2 from gross pathology with an expected consistency given that the HIFU treatment parameters remained the same for all cases. In addition, the estimated diameter of HMI focal region from the displacement images across the three treatment cases increased both in axial and lateral direction from before (9.8 mm x 8.2 mm, 9.3 mm x 7.6 mm, 9.2 mm x 6.6 mm, respectively) to after (13.0

mm x 11.3 mm, 10.9 mm x 8.4 mm, and 10.0 mm x 10.5 mm, respectively) HIFU treatment, leading to an estimation of the confirmed thermal lesion diameter from gross pathology (9.0 mm x 8.0 mm, 9.0 x 8.5 mm, 7.5 x 6.5 mm, respectively) (Table 5.2).

Treatment Case	**Focal excitation diameter at T = 5s (Axial vs. Lateral) (T = 5 s)**	**Focal excitation diameter at T = 120s (Axial vs. Lateral) (T = 110 s)**	**Thermal lesion diameter from gross pathology (Axial vs. Lateral)**
1	9.8 mm x 8.2 mm	13.0 mm vs. 11.3 mm	9.0 mm vs. 8.0 mm
2	9.3 mm x 7.6 mm	10.9 mm vs. 8.4 mm	9.0 mm vs. 8.5 mm
3	9.2 mm vs. 6.6 mm	10.0 mm vs. 10.5 mm	7.5 mm vs. 6.5 mm

Table 5.2. Comparison table of HMI focal excitation region and the diameter of thermal lesion size from gross pathology analysis following *in vitro* experiment.

c. in vitro Reproducibility study with thermocouple monitoring and mechanical testing

18 of the 19 reproducibility study HIFU treatment cases exhibited average displacement decrease of 45.2±20.8% (Figure 5.9). In addition, 16 cases exhibited increase-then-decrease of displacement change during HIFU treatment, with average rate of increasing slope of 0.73±0.69 %/s, and average rate of decreasing slope of 0.60±0.19 %/s, respectively. In addition, the corresponding average rates of displacement increase with temperature were 0.84±1.15 %/ °C, and 2.03± 0.93%/ °C, respectively. The average size of all of the treated thermal lesion size was 236.6±140.2 mm^2 (Figure 5.11). The Under the same treatment parameters, the average Young's Modulus measured using mechanical testing were 2.1± 1.2 kPa and 38.8± 11.6 kPa, for the untreated and HIFU-treated specimens, respectively (Figure 5.12).

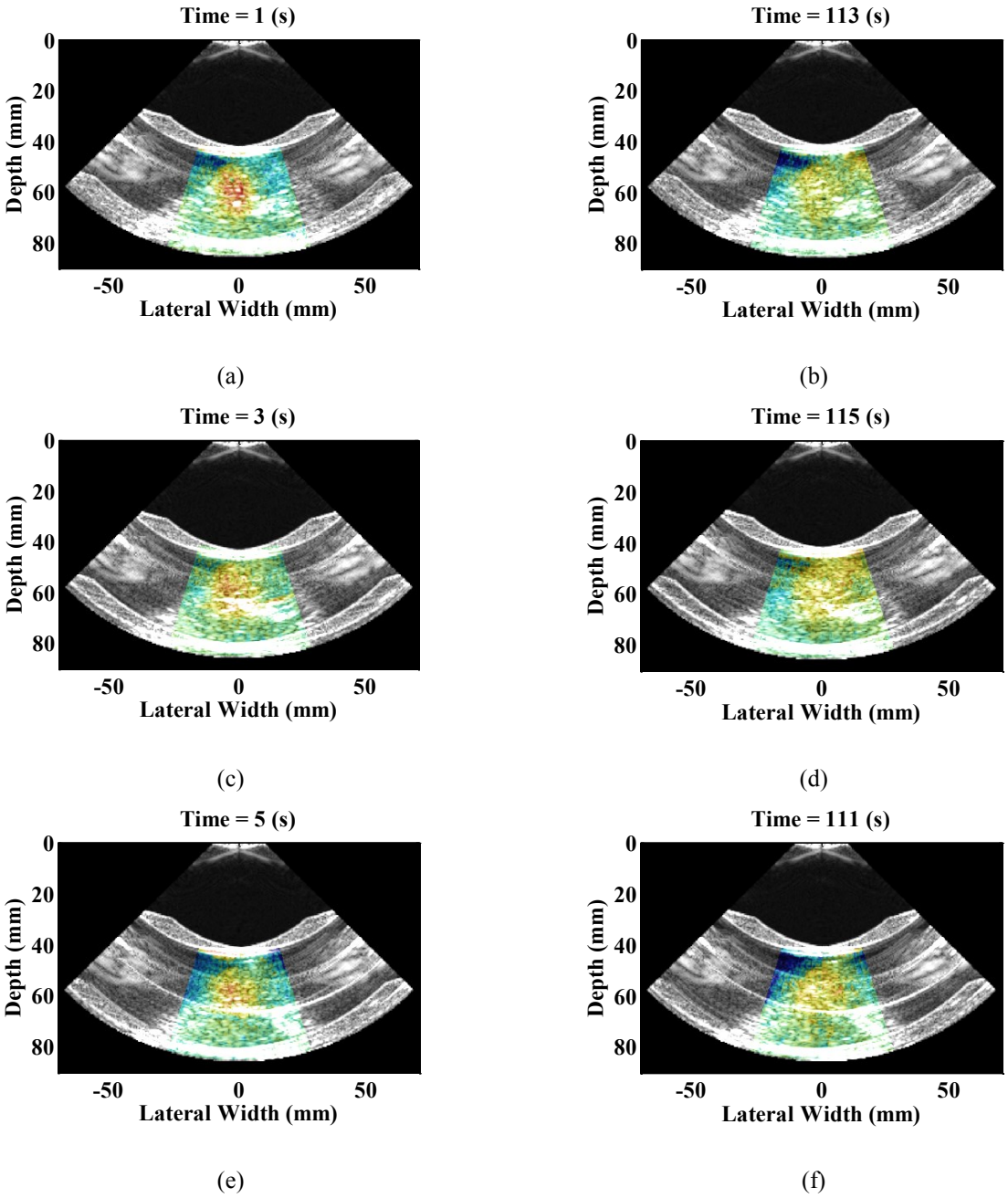

Figure 5.9. HMI displacement map with B-mode Overlay at peak positive displacement time point at beginning (a,c,e) and ending (b,d,f) of 120-s HIFU treatment using the 2D-HMIFU system for the same three example treatment cases as above (Case 1: a,b, Case 2: c,d, Case 3: e,f).

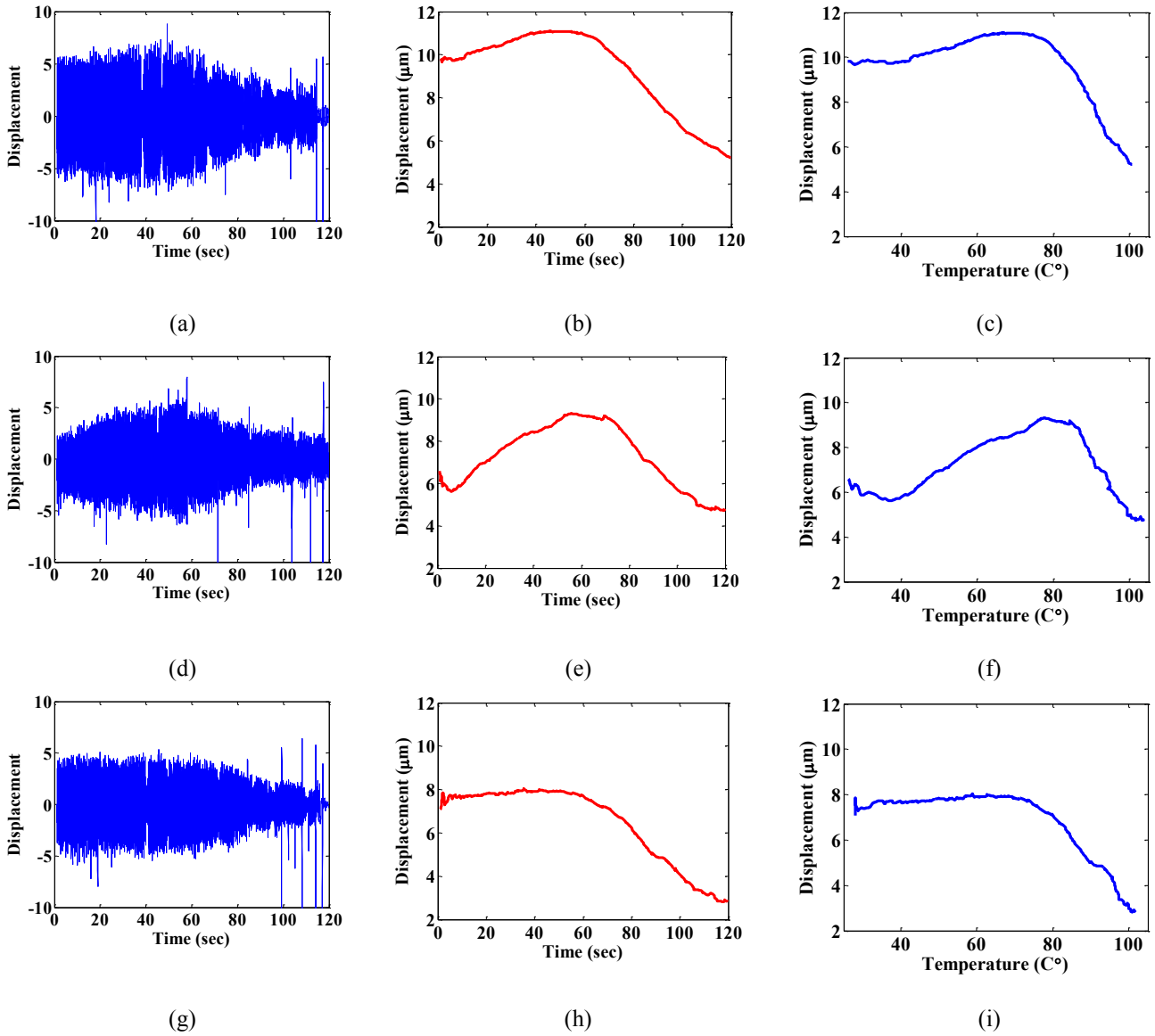

Figure 5.10. Focal displacement profile with temperature monitoring using the 2D-HMIFU system across three example treatment cases (Case 1: a,b,c, Case 2: d,e,f, Case 3: g,h,i). The peak-to-peak displacement profiles were also plotted against thermocouple readings for the corresponding cases (c,f,i).

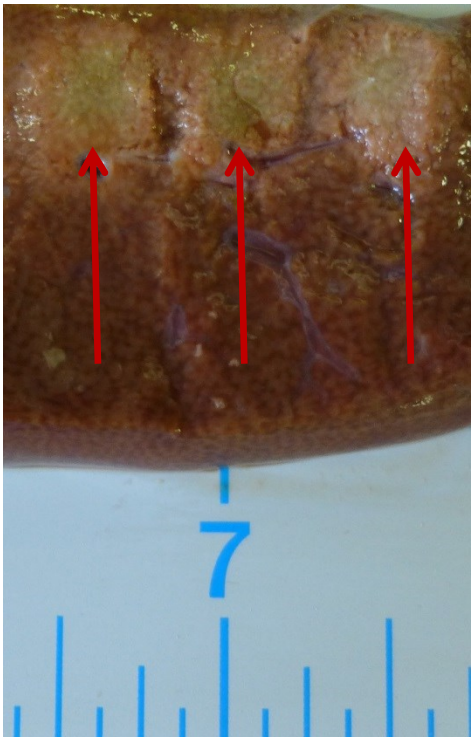

Figure 5.11. Gross pathology image of the respective HIFU lesions following HIFU treatment cases shown in Figure 5.9 and 5.10. Red arrow indicates the respective 3 individual HIFU treated thermal lesions. Note that each of the HIFU treatment was performed individually.

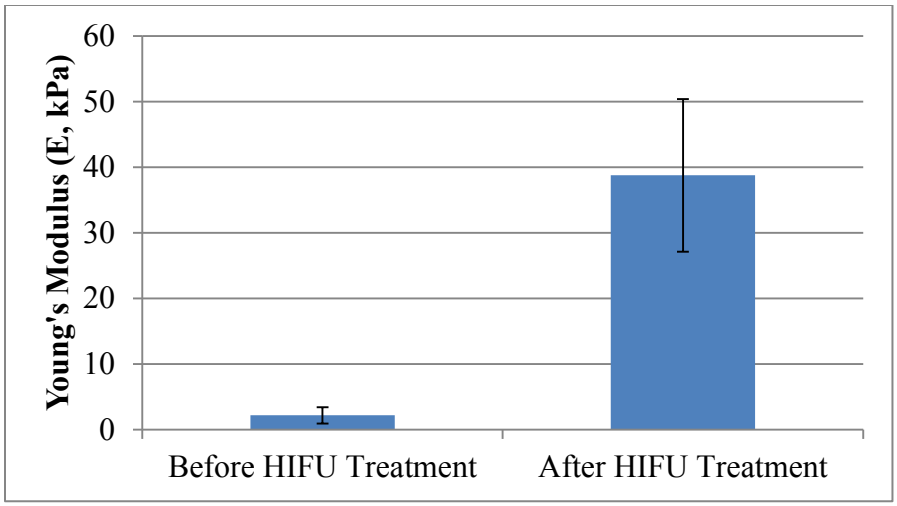

Figure 5.12. Measured Young's modulus using rheometer mechanical testing apparatus. The Young's modulus of *in vitro* canine liver after HIFU treatment using the 2D-HMIFU system showed significant increase relative to the untreated case.

5.4 Discussion

In this study, we have designed and built a 2D HMIFU system equipped with a real-time feedback capable of streaming the displacement image during the ablation procedure by incorporating a novel sparse matrix beamforming algorithm implemented on GPU. Both phantom and *in vitro* tissue experiments were performed in order to assess the quality and stability performance of the completed system. We hypothesized that our system was capable of producing reproducible high frame rate, 2D HMI displacement mapping in gelatin phantoms, as well as displacement variation during treatment upon and detecting thermal lesion formation.

To our knowledge, the capability of real-time monitoring and mapping thermal lesion formation at a frame rate of 5 to 15 Hz is currently the fastest amongst existing 2D HIFU

monitoring modalities. For example, MRgFUS provides temperature maps at sub-millimeter resolution but only at a frame rate between 0.1-1 Hz depending on slice thickness and spatial resolution. Echo shift imaging supersedes MRgFUS in both frame rate with ability to map temperature distribution up to 400 Hz [42]. Nevertheless, both modalities currently lack the ability to monitor the onset of lesion formation or perform real-time imaging of thermal lesion formation especially HIFU sequences with rapid temperature increase. Both ARFI and SSI methodologies implemented a cost-effective, all-ultrasound-based HIFU with a monitoring system capable of receiving beamformed RF signals between 11 to 17 kHz [151, 152]. However, ARFI utilizes a single transducer which must be excited at a low duty cycle (6%) in order to prevent transducer damage and the ARFI image were displayed interspersed between HIFU treatments with a 0.2 Hz frame rate following a single mechanical excitation[151], whereas SSI also requires the interruption of the treatment for HIFU beam during the its plane shear wave excitation, limiting its frame rate to be 0.333 Hz [152].

The HMI displacement images across the gelatin phantom were very consistent, and the largest variance amongst investigated locations was under 9.6 %. In addition, the focal excitation region was clearly imaged across all cases, where ellipsoidal shaped displaced regions were centered around 70 mm, in agreement with the expected geometrical focal depth of the HIFU transducer. The displacement profile maps and estimate across different locations showed a strong consistency, thus validating the reproducibility of our beamforming and motion estimation algorithm and ensuring the performance reliability of the new 2D HMIFU system. Despite the fact that the HMIFU excitation was continuous for 1.2 second, tissue heating and the associated changes such as in speed of sound were expected to be negligible within such a short time window and the associated low temperature changes [233]. For monitoring of HIFU

treatment studies, the focal excitation region was also clearly imaged across all cases, where focal displacement decreased by 40%, 30%, and 33% for each treatment monitoring upon lesion formation. These findings are also consistent with our previous work [154] as well as prior literature [136, 151]. The displacement decrease began around 60 to 80 seconds upon treatment initiation and progressively continued until the end. This study proved the significance of fast, continuous monitoring and lesion imaging of HIFU treatment, which allows physicians to identify the onset of lesion formation and the ability to either terminate the treatment or continue to monitor lesion growth. The progressive displacement decrease was also imaged clearly across all treatment cases, where the group of displacement at the focal zone showed a similar decrease trend. In comparison to the B-mode images (Figure 5.5, 5.6) acquired before and after HIFU treatment, the HMI displacement images were significantly more contrast-enhanced and informative in both providing the onset when thermal lesion formed as well as the growth of the thermal lesion as the treatment time elapsed (Table 4.2), which is believed to be associated with the change in mechanical boundary conditions during the formation of the stiffer thermal lesion. In addition, the displacement images reproducibly mapped the changes in mechanical property upon lesion formation.

Despite our successful implementation and feasibility study using the 2D system with streaming feedback ability, there are several limitations of the aforementioned HMIFU platform. All of the single variable sparse matrices used in this study were constructed offline using a separate algorithm in prior to the experiment, and the matrix computational cost can vary between few minutes to several hours, depending on the of upsampling rate, beam density, as well as the field of view. However, it is possible to circumvent the computational cost by first generating a single matrix at highest sampling rate and larger fields of view, and adapt the

reconstruction matrices with reshaping and down-sampling in respective to the specific imaging parameter. The reconstruction speed will also influence the streaming speed, where a larger field of investigation with high sampling rate than the presented case will have lower streaming frame rate. The data transfer rate from the VDAS to the host computer has also been a bottleneck issue in this platform (e.g. 930 ms is required to transfer every 200 frames acquired at 1 kHz frame rate), which is also another limiting factor to the streaming rate of HMI displacement because the upper limit of data transfer rate per channel in VDAS system is 18 M/s. Despite the additional hardware improvements streaming rate of 10-15 Hz deemed a suitable rate for HIFU guidance.

It is also important to emphasize that the proposed sparse-matrix based reconstruction method is very simple for rapid-prototyping and implementing on any conventional ultrasound system. Also, the nature of matrix-based algorithms allows for flexible adaptation of other types of linear functions. In addition, under the very fast frame rate available (1 kHz), we are capable of monitoring not only focal displacement, but also capturing the propagation of shear waves generated through our focal excitation. The ability to track shear waves will further unlock other application potentials for HMIFU such as simultaneous focal and peripheral-focal region shear-wave based elasticity imaging of lesion formation, as well as assessment of 2D viscoelasticity change during HIFU treatment using a previously developed method [182].

Amongst the cases our reproducibility study with simultaneous thermocouple monitoring, there was a good consistency with 95% of the cases exhibiting displacement decrease. More importantly, 84% of the cases exhibited increase-then-decrease trend, which indicates the underlying softening-then-stiffening tissue mechanical property change during HIFU treatment with slow denaturation sequence. In addition, the relative stiffening of the thermal lesion compared to the normal tissue was also confirmed with mechanical testing, where the Young's

Modulus of thermal lesions were higher than the normal, untreated tissues by a factor of 18 times. The monitoring findings are also in agreement with the previous studies performed using MRE [136], HMIFU [154], ARFI [151], and SSI [152, 153]. Both the slopes of displacement increase with time and temperature were less than the slope of decrease. This can be related to the findings from previous studies by Sapareto and Dewey., (1984) such that the threshold for total cellular death following the thermal dosage limit of 240 minutes of equivalent heating at 43 °C, which can be related to a gradual increase of thermal dose until the threshold of cell death when protein denaturation will then take place in a rapid manner. Furthermore, ultrasound elasticity imaging based studies investigating the softening-then-stiffening phase change by Arnal *et al.,* (2011) and Sapin-de Brosses *et al.,*(2010) also investigated and discussed that the collagen fibers denaturation took place around 60 °C where the hydrogen bonding maintaining the collagen helices will break [202, 203]. For the cases that did not exhibit the same displacement decrease or increase-then-decrease cases, we also speculate that the underlying structural differences across the liver tissue specimens could induce such variation in mechanical property change under thermal treatment. Another factor along with tissue structural characteristic that could interfere the measurement of our displacement and thermocouple reading is the depth-dependent attenuation, where we observed that surficial depth tend to have higher rise in temperature but good displacement focal localization reading compared to the depth extending towards the bottom half of the specimen, where temperature rise is steady but the focal location quality sometimes lacks defined boundary. It is also noteworthy that ARFI imaging technique has also previously investigated thermocouple measurement against their displacement findings across the HIFU treatment [151]. Nevertheless, the thermocouple used in their manuscript is 10 times the thickness of our barewire thermocouple, thus the measurement is expected to be inaccurate

due to artifact induced by reflection and viscous heating. In addition, the monitoring window is also extremely limited in ARFI due to the usage of only single diagnostic transducer to perform both HIFU treatment as well as the ARFI excitation. Other ongoing and future work includes implementation of a raster-ablation sequence for treatment of large tissue volume through electronic beam steering of the 93-element HIFU array, as well as a composite imaging with real time overlaying displacement image onto B-mode to perform simultaneous beam guidance and lesion assessment. Finally, clinical translation of this system is currently being explored and tailored towards breast and pancreatic tumor ablation.

5.5 Conclusion and Summary

In this study, a fully-integrated, clinically relevant ultrasound imaging platform was built for 2D real-time HIFU monitoring using HMIFU. A GPU-based sparse-matrix algorithm has been developed and implemented for beamforming and scan conversion, which capable of providing 2D real-time streaming during HIFU treatment up to 15 Hz without interruption. Reproducible HMI displacements were imaged and highlighted a clear excitation region across multiple locations from a gelatin phantom with a 10 kPa Young's Modulus. HIFU treatment monitoring was also performed and a clear decrease in focal displacements upon lesion formation was obtained in canine livers *in vitro*. Reproducibility studies also showed consistent successful monitoring of tissue-softening-then-stiffening phase change with thermocouple monitoring. The measurements from mechanical testing also confirmed the increase of Young's Modulus amongst the treated thermal lesions compared to the normal specimen. Ongoing

investigations will aim at raster ablation using beam steering with HIFU array, shear wave imaging, and the clinical translation of HMIFU for our upcoming studies.

Chapters 4 and 5 summarized the development and optimization of a 1-D based and 2-D based HMIFU system respectively for monitoring of both HIFU treatment with boiling and HIFU treatment with slow denaturation sequences with feasibilities shown on tissue mimicking phantom, *in vitro*, and *ex vivo* applications. As the HMIFU technique progressed towards the first completion phase of the system development, the next chapter (chapter 6) will be demonstrating a set of feasibility studies of the 2D HMIFU system on a preclinical application of transgenic pancreatic tumor mice model *in vivo*.

Chapter 6. *In vivo* pancreatic tumor HIFU treatment monitoring using 2D-HMIFU System

6.1 Introduction

In this chapter, the initial feasibility study of the previously described 2D-HMIFU system in monitoring HIFU treatment on pancreatic tumor is described. The chapter will first introduce an overview on pancreatic cancer, followed by the history of existing treatment strategies as well as previous studies applying HIFU for pancreatic tumor in pre-clinical and clinical studies. The chapter will then introduce the details of the preclinical models used, the treatment procedures, followed by the findings and discussions from the initial feasibility studies.

6.1.1 Pancreatic cancer

Pancreatic cancer is the 10th most common cancer, accounting for 5% of cancer deaths in the United States and is the fourth leading cause of cancer mortality with highest 5-year mortality rates amongst any cancer types [234, 235]. There are estimated 43,920 people diagnosed with pancreatic ductal adenocarcinoma (PDAC) in the U.S. with 33,790 associated deaths [236]. Current treatment options are of limited benefit with a 5-year survival rate of 4-5% following diagnosis. Pancreatic cancer treatment is considered as one of the most challenging cancer treatment as majority of the patients with advanced pancreatic cancer present remarkable intrinsic resistance to both standard and targeted chemotherapy as well as ionizing radiation [236]. A hallmark of pancreatic cancer is the fibrous inflammatory reaction, namely desmoplasia,

which form a prominent stromal matrix that separates blood vessels from tumor cells resulting in to insufficient delivery of chemotherapy drugs into the tumor. The stromal component, which includes fibroblasts, leukocytes, endothelial cells, and extracellular matrix proteins can comprise up to 90% of the tumor mass[236]. This in turn limits the ability of chemotherapeutic agents, which must penetrate the tumors in effective quantities without causing significant toxicity to normal tissues while is required to kill malignant tumor cells *in vivo.*

Although extensive testing in pancreatic cancer cell cultures and *in vivo* mouse models of pancreatic cancer have demonstrated that gemcitabine has activity against pancreatic cancer, this has not translated into an effective systemic treatment in humans. It is hypothesized that this ineffectiveness is in part due to changes in the expression of genes involved in gemcitabine transport leading to chemoresistance [237]. In addition to chemoresistance at the cellular level, recent studies using a genetically modified mouse model of pancreatic cancer that appears to recapitulate more closely the human disease compared to other transplantation mouse models (xenograft or syngenic autograft), suggesting that insufficient delivery of gemcitabine into the tumor is also an important mechanism for the apparent chemoresistance [238]. Therefore, developments of novel therapeutic techniques are urgently needed in the field of pancreatic cancer.

6.1.2 HIFU treatment for pancreatic cancer

High Intensity Focused Ultrasound (HIFU), with its wide range of application capabilities in treating various types of tumor types has also been previously shown feasible in ablating pancreatic tumor, mostly for providing palliative effect [239]. Numerous clinical studies reported using HIFU for palliative treatment on pancreatic patients, including a 251 advanced

pancreatic cancer patients study which indicated 84% of the patient population showing significant pain relief while some cases exhibited significant reduction of tumor volume without significant adverse effects or pancreatitis [240].

In terms of pre-clinical studies, HIFU has been applied in several studies using swine models in vivo due to its relevance in size and anatomy with respect to that of the human case. Hwang *et al.*, were the first to show that HIFU treatment can induce effective necrosis in the pancreas without significant adverse effects such as skin burns or pancreatitis during a 7-day post-treatment observation period [241]. Similar findings were confirmed with another study using both light microscopy and electron microscopy. Recently, other multi-treatment studies have shown combination of HIFU treatment with radiation therapy in the swine model *in vivo* [242], as well as using the combination of a pulsed HIFU treatment sequence with chemotherapeutic drug (Gemcitabine) to induce enhanced cell apoptosis on xenograft mouse tumor model *in vivo* [243].

Despite the aforementioned clinical and preclinical studies, there has yet a comprehensive clinical trial validation on assessment on whether HIFU alone is capable of providing effective local tumor response or providing longer survival rate of pancreatic tumor patients. Moreover, no previous studies have yet to perform real-time monitoring and mapping of the underlying pancreatic tumor stiffness throughout HIFU treatment, which can serve as an important indicator for assessing the treatment outcome. Therefore, our objective in this study is to investigate the feasibility of applying the 2-D HMIFU system for HIFU treatment and monitoring of pancreatic tumor on genetically engineered pancreatic model *in vivo* in order to facilitate the future preclinical and clinical HIFU studies. We hypothesize that our preclinical system is capable of

both inducing effective cell necrosis through thermal ablation, monitor the associated elastic changes from variation of HMI displacement, and verify our findings with gross pathological and histological analysis.

6.2 Methods

6.2.1 The kP(f)c and KPC models

In order to better understand and gain insights to the underlying biology and mechanism of pancreatic tumor development, which in turn leads to development of innovative therapeutic approaches, numerous preclinical models have been developed in the past to generate pancreatic cancer in mice. In this study, two types of transgenic models developed by the laboratory of Dr. Kenneth Olive at Columbia University Irving Cancer Research Center, were used for HIFU treatment with HMIFU monitoring. The first model is bearing a homozygous p53 conditional knockout allele (K-rasLSL.G12D/+, p53Flox/+, PdxCre) or, namely kp(f)C or "KP-flox" model, while the second model harboring a heterozygous conditional mutant allels of K-rasLSL.G12D/+, p53R172H/+, PdxCre, namely "KPC" model mice [236]. It is noteworthy that one of the barriers to drug delivery appears to be due to the presence of a prominent stromal matrix that separates blood vessels from tumor cells. This stromal barrier is present in human pancreatic cancer and in a genetically engineered mouse model (KPC mice); but is absent in xenograft and syngenic autograft models. More importantly, the value of KPC model comes from the fact that "it is the only model that recapitulated many aspects of the human disease, including histopathologic similarities in neoplastic tissue, common occurrence of metastasis to relevant site,

comorbidities such as cachexia, activation of biochemical pathway, and evidence for genomic instability" [244].

6.2.2 2-D HMIFU System for HIFU monitoring *in vivo*

In vivo study procedure

The same 2D-HMIFU system along with the acquisition and processing algorithm and parameters as previously described in Chapter 5 were used for this study. Each HIFU treatment was performed continuously for 2 minutes with HMIFU monitoring, and every treatment location was separated by 2 mm using the 3D positioning system. A total of three mice (n=3, kp(f)C =1, KPC =2) were used in this study. The 2-D HMIFU based HIFU treatment procedure for every *in vivo* study was based on the following procedure (Figure 6.1): First, the animal was placed on an adjustable stage covered by a waterproof pad and underneath an electrically heating pad embedded while being anesthetized (Figure 6.3b). The tumor targeting was first performed using a 25-MHz high frequency ultrasound probe (RMV-707B, Visualsonics Inc. Toronto, Canada) in order to characterize the tumor dimension and boundary characteristics. Then, a water bath with adjustable height (Figure 6.2) was placed onto the mice with acoustic gel coupling, while the high frequency ultrasound probe was fixed to the translational stage. In turn, a metallic washer was placed inside the water bath and adjusted such that the center aperture lies right above the entry path to the tumor from above mice (Figure 6.3b). The high frequency probe was then relocated above the entry point in order to confirm visualization of tumor through the aperture (Figure 6.3c,d). Once the target was confirmed, the HMIFU transducers were

replaced with the high frequency probe and fixed onto the translational stage, where the 2.5 MHz phased array of the 2-D HMIFU system was used to provide final targeting of the tumor based on the backscattering signatures from the metallic washer on the B-mode imaging. Next, the HIFU treatment was performed across numerous locations in a raster scan format, where individual treatment locations were separated by 2 mm in order to avoid treatment overlaps. The mouse was immediately sacrificed upon completion of all HMIFU treatments, followed by necropsy procedures to extract the tumor for gross pathological analysis and paraffin embedding. Hematoxylin and eosin (H&E) staining was performed in order to assess the presence of necrosis of PDAC cells due to thermal ablation damage by the HIFU treatment. Cleaved-Caspase 3 staining was also performed in order to assess the apoptotic cell death, which is due to collateral damage from the HIFU treated region.

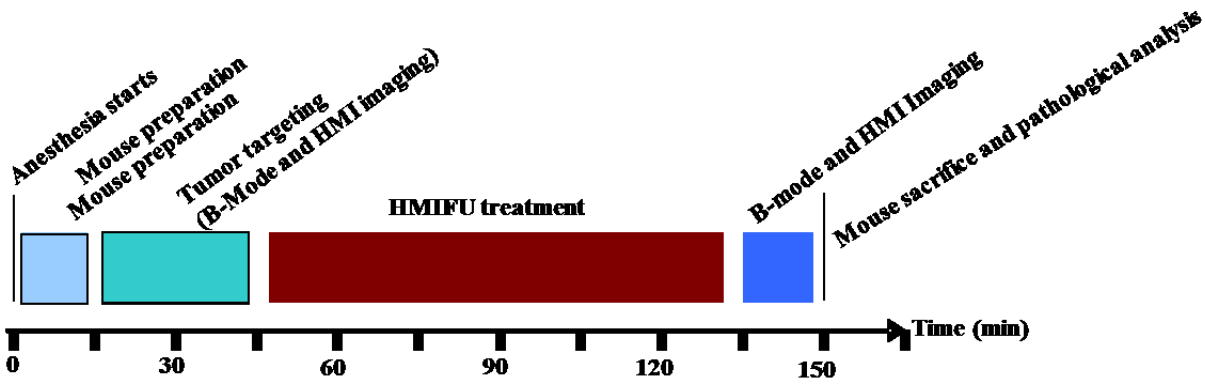

Figure 6.1. Procedure time line of the *in vivo* experiments. Both high frequency and regular B-mode images will be acquired before and after the treatments, followed by the immediate sacrifice with necropsy and gross pathology analysis.

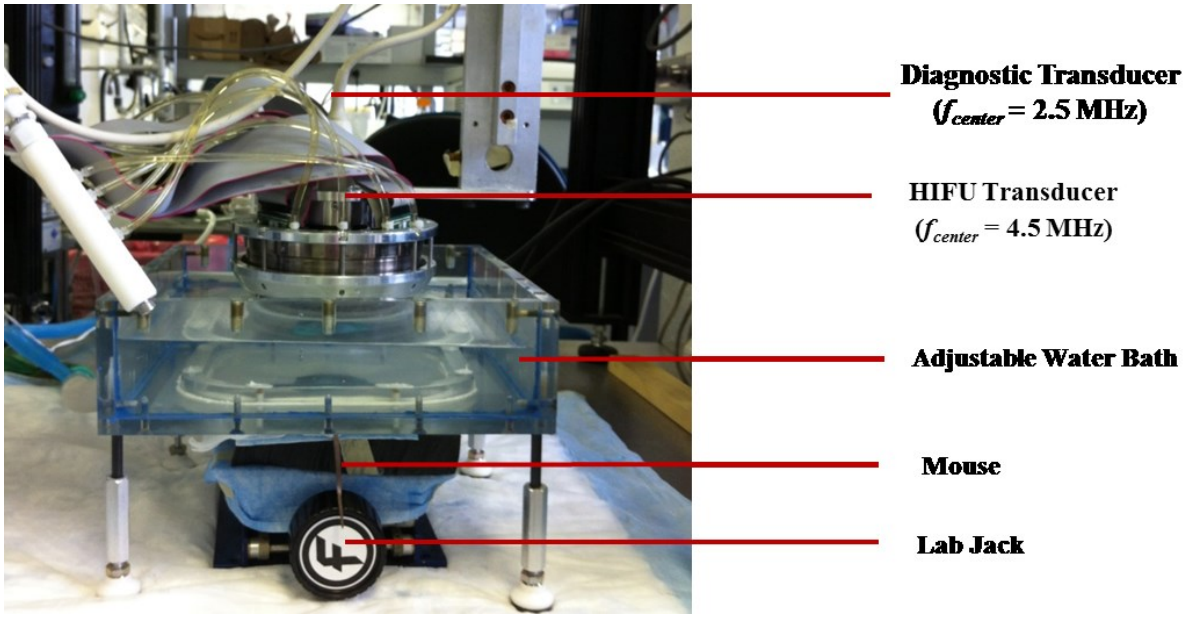

Figure 6.2. Coupling set up for *in vivo* mice study. The mouse is placed on top of an electrical heating waterproof pad fixed to a lab jack, while an adjustable water tank is placed from top in order to provide the acoustic coupling with the 2D HMIFU system with the animal.

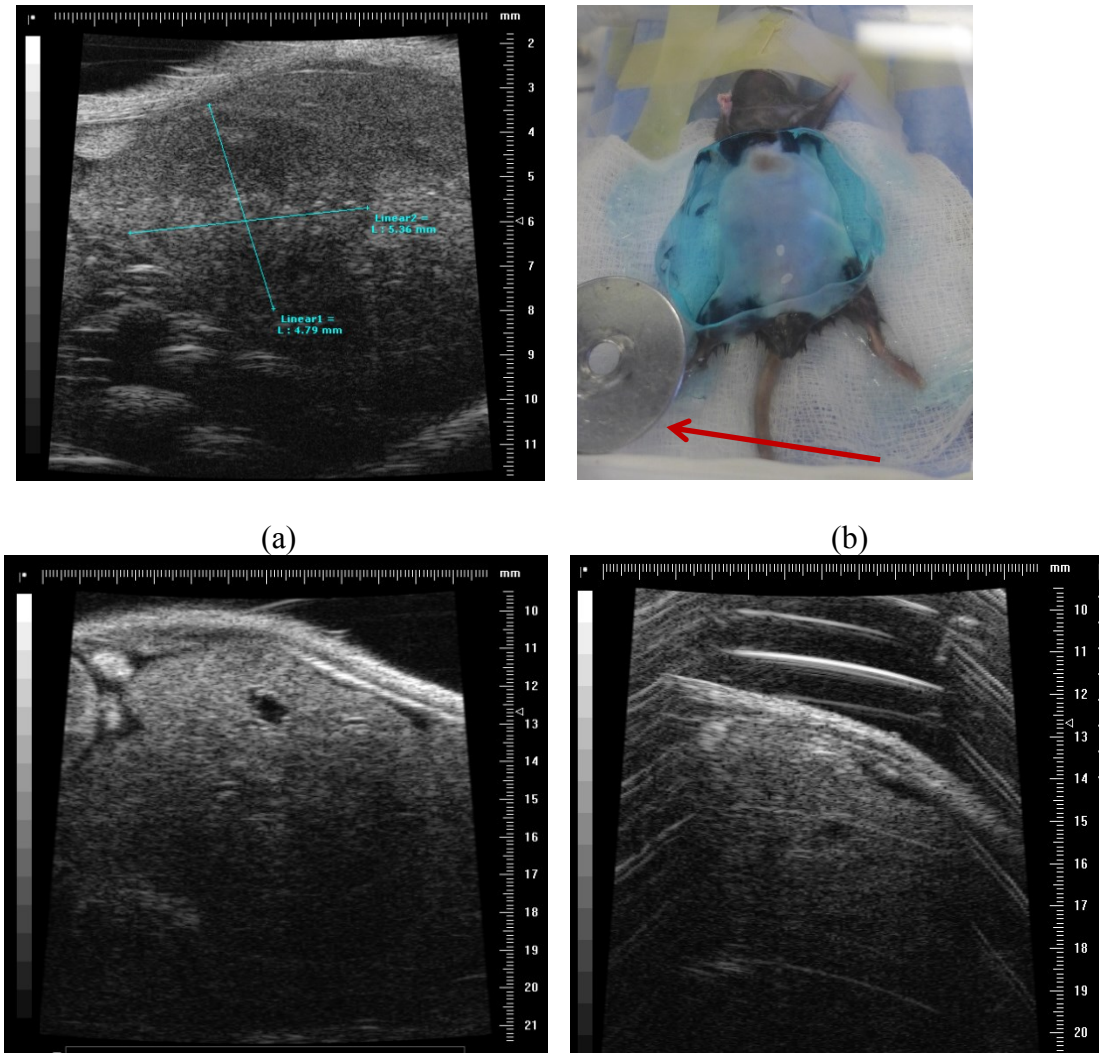

Figure 6.3. High frequency imaging based targeting of pancreatic tumor: High frequency probe fixed onto the translational stage will first capture B-mode image to characterize the tumor (a), followed by placing the metallic washer indicated by red arrow above the mice inside the water bath (b). Upon confirming the view matching between the high frequency B-mode before washer placemen (c) and through the washer aperture (d), the high frequency probe will be replaced by the HMIFU transducers to perform HIFU treatment.

6.3 Results

Three mice were subjected to HIFU treatment using the 2-D HMIFU platform. Both the focal displacement curves as well as the peak-to-peak displacement values were monitored throughout the treatment time. For the kP(f)c mice, five locations across the tumor region were subjected to HIFU treatment, where three locations showed peak-to-peak HMI displacement decrease during HIFU treatment. The respectively representative focal displacement monitoring curves were shown in Figure 6.4 (a,c,e) as well as the corresponding peak-to-peak HMI displacement, which indicated displacement decrease of 20.8±6.84, 18.6±1.46, and 24.0±5.43%, for each of the three treatment locations, respectively (Figure 6.4b,d,f). Upon sacrifice of the mice, gross pathology images also confirmed two regions of the hemorrhage, each spanning a region of 1 to 2 mm and separated by 2 mm, which was in agreement with the raster ablation step size of 2 mm, indicated by the red arrows (Figure 6.5).

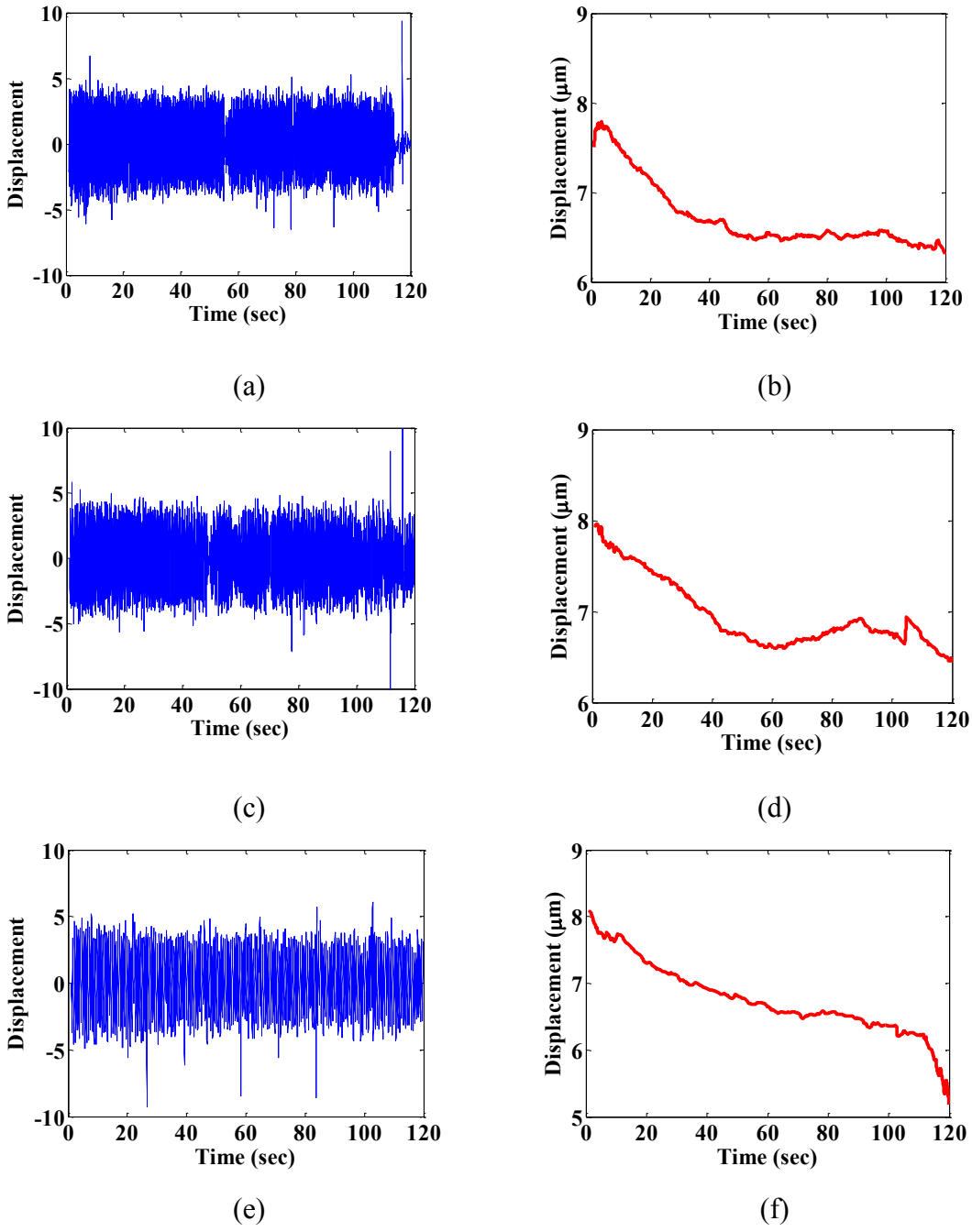

Figure 6.4. 1D focal displacement across two treatment locations on a kP (f) c mouse. Both location 1(a,b) and location (d,e) exhibited a decrease in peak-to-peak HMI displacement over treatment time.

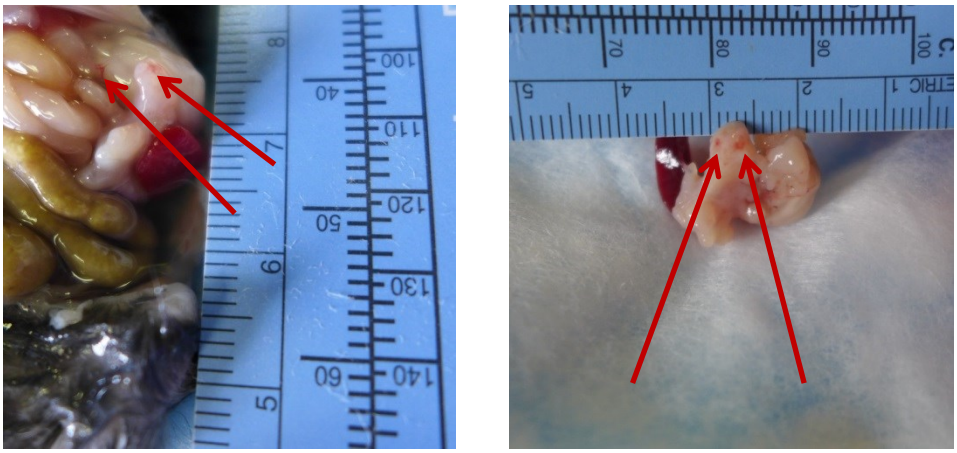

(a) (b)

Figure 6.5. kP(f)c mice gross pathology confirmation with tumor intact (a) and detached (b). The red arrows points to the treated regions where surface hemorrhages were observed.

Similar findings were observed for the two KPC mice as well. A total of seven treatment locations were performed, where peak-to-peak HMI displacement decrease was observed in four locations, at 39.5±2.98%, 34.5±21.5%, 16.0±3.05%, and 35.0±3.12%, respectively. Two representative focal displacement monitoring curves were shown in Figure 6.6 (a,c) as well as the corresponding peak-to-peak HMI displacement, which indicated displacement decrease of 40 and 34%, for each of the two treatment locations, respectively(Figure 6.6 b,d). In addition, focal HMI displacement images at the beginning of the treatment (Figure 6.7a,c,e) and towards the end of the treatment (Figure 6.7b,d,f) were also shown overlayed onto the B-mode images for the displacement case with 39.5±2.98% focal peak-to-peak HMI displacement decrease. Upon sacrifice of the mice, gross pathology images also confirmed lesion regions lesion, each spanning a region of 1 to 2 mm and separated by 2 mm, which was in agreement with the treatment location adjustment (Figure 6.8a). Furthermore, histological assessment using H&E staining also

indicated effective region of necrosis, indicated by the unnatural regions of cell death with defined boundaries, which is due to thermal ablation damage by HIFU treatment (Figure 6.9 a,b). At 20x and 40x magnification, the histology images also confirmed cell denucleation within the PDA cells was detected across the HIFU treated region (Figure 6.9 c,d).

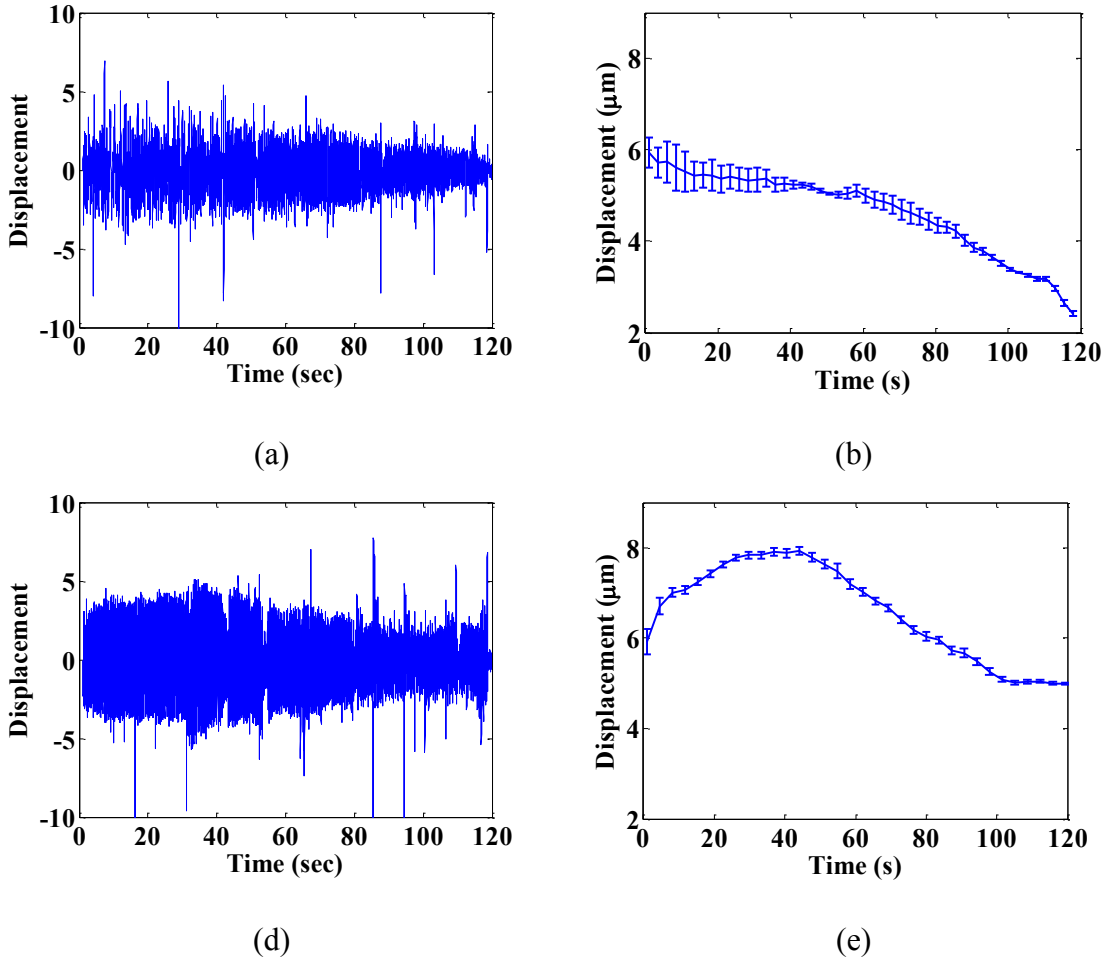

Figure 6.6. 1D focal displacements across two treatment locations on a KPC mouse. Both location 1(a,b) and location (d,e) exhibited a decrease in peak-to-peak HMI displacement over treatment time (Please see Chapter 5 for details on peak-to-peak HMI displacement calculation).

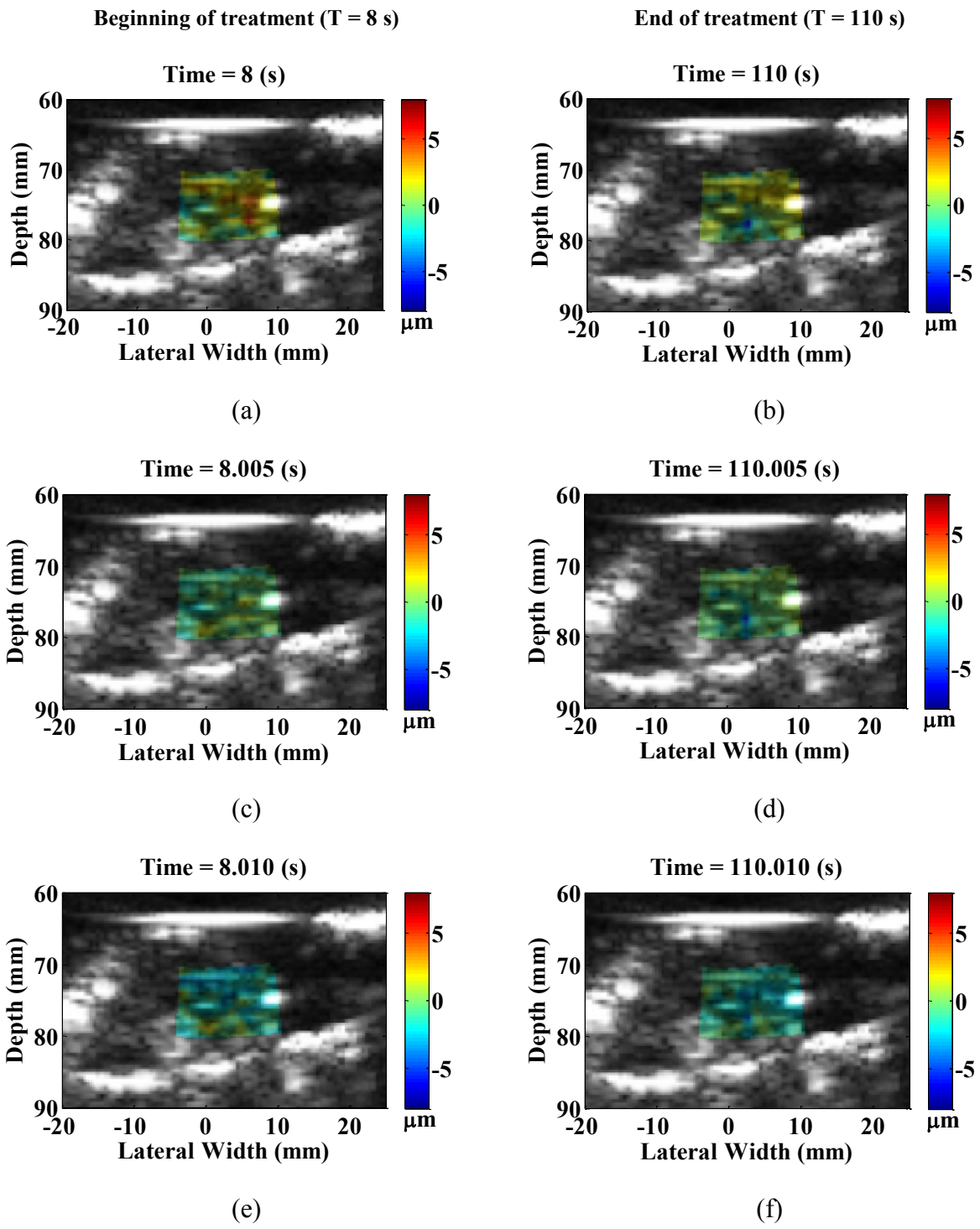

Figure 6.7. 2D displacement cycle maps with B-mode overlay. The tumor is depicted by the dark region on the center. The targeted focal region was towards the right half of the tumor. Clear displacement decrease was observed before (a,c,e) and after the treatment (b,d,f).

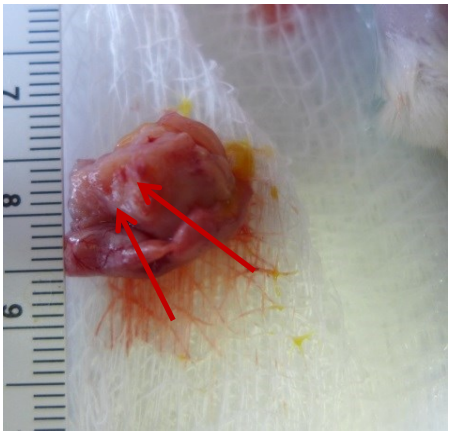

(a)

(b)

(c)

Figure 6.8. KPC mice gross pathology Confirmation. The red arrows on the tumor image (a) point to the treated regions where surface hemorrhages were observed. Note that the tumor was surrounded by a complex structure of intestine (b,c).

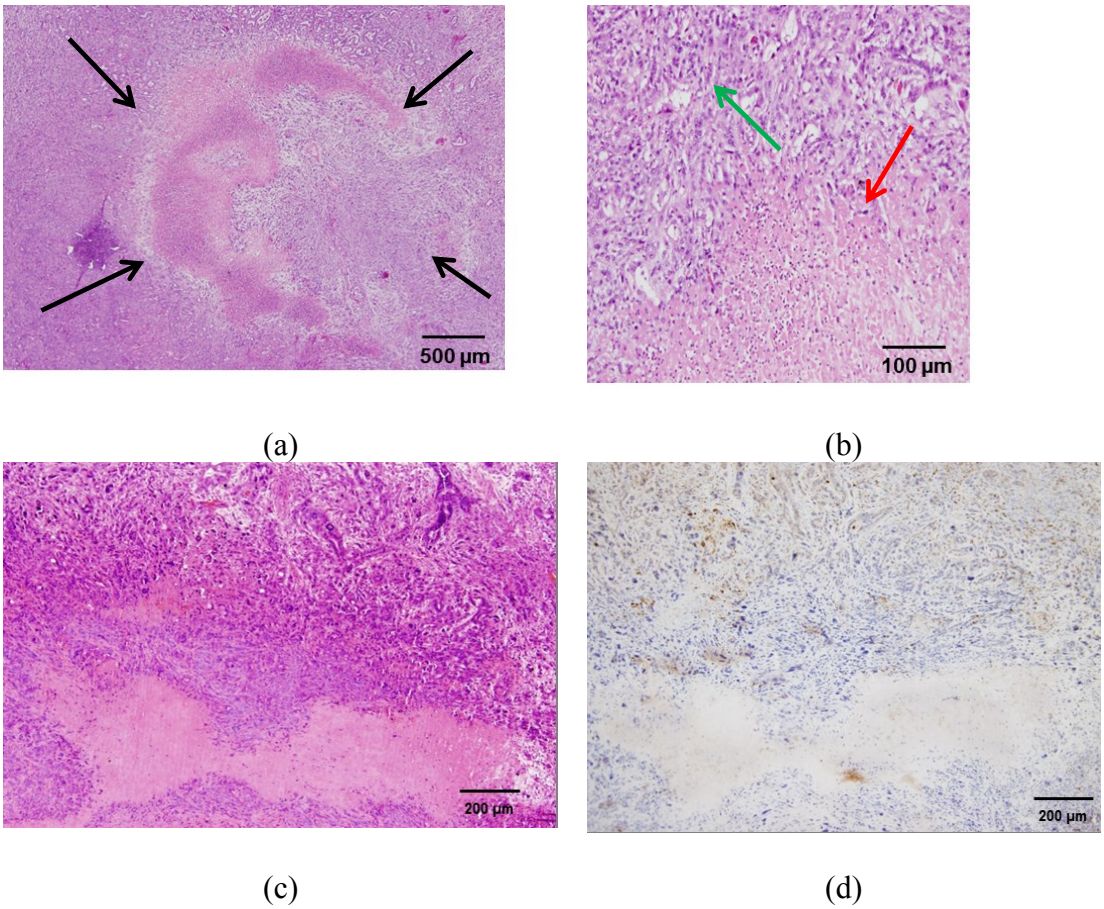

Figure 6.9. H&E histological images of KPC tumor at (a) 1x, (b) 4x , (c) 10x, and Cleaved Caspase-3 staining histological image at (d) 10x magnifications. Black arrows indicated unnatural necrotic regions of PDA cell death due to the thermal damage by the HIFU treatment. Furthermore, clear cell denucleations were observed across the high magnification images at the HIFU treated region (red arrow) compared to peripheral regions (green arrows) in (b). (d) The Cleaved Caspase-3 staining image from the same serial section indicated the regions of apoptotic cell death (brown) surrounding the HIFU treated region. The slides shown are between 400-500 µm from the top of the tumor specimen, with thickness of 60 µm each, respectively.

6.4 Discussion

Pancreatic ductal adenocarcinoma (PDAC) is currently the fourth leading cause of cancer mortality with highest 5-year mortality rates [234, 235] and very limited treatment options. Due to the strong resistance nature of standard and targeted cancerous therapies, [236], the 5-year survival rate following diagnosis has been one of the lowest amongst all cancer types between 4-5%. Therefore, development of new alternative techniques with clinical promise is crucial in treatment of PDACs. Over the past few decades, High Intensity Focused Ultrasound (HIFU) treatment has been applied to treat a wide range of cancer tumor types in both preclinical and clinical models. Several studies have reported the use of HIFU in treating pancreatic tumors both in clinical model and preclinical models. Nevertheless, all of the previous clinical studies have been mainly focused on providing palliative relief aspect of pancreatic patients [239], instead of targeting for effective necrosis of the PDAC tumor cells. The preclinical studies on the other hand, were performed either using normal pancreatic applications [241], or xenograft based preclinical models that lacked the traits of human PDAC tumors [243]. Most importantly, none of the previous studies were performed with real-time monitoring in order to assess the tumor characteristic change during the HIFU treatment. In this work, we have investigated the feasibility of treating PDAC tumors *in vivo* using HIFU alone using a usage of a preclinical real time 2-D monitoring platform based on the HIMFU technique in treating PDAC tumors using *in vivo* transgenic PDAC model mice that mimics the characteristics of human PDAC tumor characteristics [238]. Two models have been used in this study, a heterozygous p53 conditional knockout allele (K-rasLSL.G12D/+, p53Flox/+, PdxCre) or, namely kp(f)C or “KP-flox” model,

and another model harboring a heterozygous conditional mutant allels of K-rasLSL.G12D/+, p53R172H/+, PdxCre, called "KPC" model that mimics the characteristics of human PDAC tumor such as the presence of prominent stromal matrix that separates blood vessels from tumor cells. Our objective of this study is to first show the feasibility our developed 2-D HMIFU system for HIFU treatment and monitoring of pancreatic tumor on genetically engineered pancreatic model *in vivo*.

Three mice (1 kp(f)C model, 2 KPC models) were treated with HIFU treatment with monitoring using the 2-D HMIFU system. Both the focal displacement curves and the peak-to-peak HMI displacement values were analyzed through the entire HIFU treatment window. For the HIFU treatment of the kp(f)C model, a displacement decrease was observed across three of the five treatment locations at 20.8±6.84, 18.6±1.46, and 24.0±5.43%, respectively (Figure 6.4). For the HIFU treatment of KPC model, the displacement decrease was found across four of seven treatment locations at 39.5±2.98%, 34.5±21.5%, 16.0±3.05%, and 35.0±3.12%, respectively (Figure 6.6). In addition, the decrease of focal displacement profiles at the focal zone inside the KPC tumor was also mapped by the 2-D HMIFU system before (Figure 6.7a,c,e) and after (Figure 6.7b,d,f) the HIFU treatment. The confirmation of the tumor stiffness change was first validated by the agreement with both gross pathological findings, where multiple locations of speculated thermal lesion with hemorrhages, separated by the raster ablation step of 2 mm. The displacement increase-then-decrease from the monitoring displacement profiles (Figure 6.6) can be correlated with the liquefaction of the treated tumor region (Figure 6.9 c,d). This proves the effective localization of the HIFU focal region inside the tumor, indicating the displacements were representative of the tumor tissue (Figure 6.5, 6.8). Moreover, for the KPC models, the H&E histological assessment also confirmed regions of effective HIFU treatment,

i.e., region with unphysiological necrosis of PDAC cells and delineated by clear boundary which symbolize the circular cross sectional view of a HIFU focal zone (Figure 6.9 a,b,c). The Cleaved-Caspase-3 also confirms the cell apoptosis surrounding the HIFU treated region, which is due to the lack of blood and nutritional supply that is induced by the collateral damage of the HIFU (Figure 6.9 d). To our knowledge, this study shows the first effective treatment of PDAC cells by HIFU alone with real-time monitoring using a clinically relevant transgenic pancreatic tumor model (KPC model) *in vivo*.

Several limitations must also be discussed for the aforementioned outcomes. First of all, the inability to monitor stiffness changes across all of the treatment cases could stem from several sources. It is noteworthy that the initial peak-to-peak displacements amplitude (lower than 10 μm) was relatively much lower in comparison to our other application studies using canine liver[233] and breast tumor models[188]. As mentioned previously, we know that the unique hypoxic nature of the PDAC tumors with extensive stromal matrix, which is composed of fibroblasts, leukocytes, endothelial cells, and extracellular matrix proteins, provides the tumor with a mechanically stiff environment. This environment is not only challenging to delivery of standard chemotherapeutic or radiotherapy treatments, but also for HIFU treatment, which requires delivery of effective thermal dosage in order to achieve cell necrosis, as well as for HMIFU monitoring which requires effective energy delivery to provide mechanical probing of the tissue during thermal ablation. This can be confirmed with all of the gross pathological assessment, where the diameter of treated region were no more than a millimeter or two (Figure 6.5, 6.8), which is much lower than any of the previously reported thermal lesions using HMIFU technique. In turn, such a limited HIFU beam energy will also limit the ability of performing HMIFU monitoring due to the attenuated radiation force *in situ*. Furthermore, the location of the

PDAC tumor is another significant factor that limits the delivery of the HIFU beam energy. As we can observe from the gross pathological assessment upon sacrifice (Figure 6.5a, Figure 6.8b,c), the tumor is often adjacent or even covered by organs such as liver or intestines, which can create significant problems in the HIFU wave propagation despite the implementation of the aforementioned custom targeting protocol.

Despite the existing limitation mentioned above, several improvements can be implemented in order to improve the outcome quality of HIFU treatments with HMIFU monitoring for the ablation of PDAC tumor. In terms of both targeting and monitoring the focal displacement, the high frequency imaging probe (f_{center} = 25 MHz) can be implemented as the confocally aligned imaging probe inside the HMIFU system in order to improve both the imaging and monitoring resolution at the tumor site given the small excitation nature inside of the very stiff PDA tumors. Moreover, this will in turn reduce the prolonged targeting time with the aforementioned custom targeting involving both the high frequency imager and the 2D HMIFU system (Figure 6.3). For delivery of higher thermal dosage, the HMIFU system is currently being upgraded with an external power supply that can enhance the acoustic emission power up to an order of magnitude, and we are also investigating the usage of higher AM frequencies in stiffer regions in order to create larger mechanical response due to the frequency dependency of biological tissues. Lastly, we expect to perform long term study with assessing both the tumor size change as well as the survival performance of the mice in order to optimize the treatment strategy of HIFU alone or possible HIFU-Drug combinational strategies for treatment of the PDA tumors.

Nevertheless, the present study validates the first proof-of-concept study of HIFU alone effective PDAC tumor ablation on a clinically relevant transgenic KPC model *in vivo* with real-

time monitoring using a 2-D HMIFU system. It is believed that the findings are promising in paving a translational path to the usage of the HIFU system and HMIFU monitoring for treatment of pancreatic tumor as well as other types of tumor models in both preclinical and clinical setting.

6.5 Conclusion and Ongoing work

In this work, the feasibility of inducing cell necrosis on clinically relevant KPC model has been demonstrated using the developed 2-D HMIFU system *in vivo*. A total of three mice (1 kp(f)C and 2 KPC models) were subjected to HIFU treatment with HMIFU monitoring. HMI displacement decreases was observed at 3 of 5 treatment locations across the kP(f)c model at 28, 20, and 30%, respectively, as well as at 4 out of the 7 treatment locations across the KPC model at 40, 34, 19, and 36%, respectively. The apparent stiffening of the tumor observed by HMIFU monitoring were also confirmed with gross pathological findings, which indicated clear regions of thermal lesions with hemorrhage, as well as H&E histological assessment, which indicated well delineated regions of unnatural cell necrosis due to thermal ablation. Ongoing work includes improvement of the targeting and monitoring system using a high frequency imager as well as progressive long term study on tumor size change as well as the survival study for optimization of treatment strategy.

In Chapters 4 and 5, we have successfully demonstrated the design, development, and optimization of both a 1-D and 2-D based HMIFU system with initial feasibilities in monitoring HIFU treatment sequences with both boiling and slow denaturation. In this chapter, we further showed successful feasibility of using the developed 2-D HMIFU system in treating and

monitoring HIFU treatment for pre-clinical KPC pancreatic tumor models in vivo. Despite the vast amount of optimization efforts described in our previous chapters, the ultimate dream for any biomechanical based imaging modalities is to perform quantitative assessment of biological tissues. Therefore, the next chapter (Chapter 7) will focus on the development and implementation of a model-independent fundamental algorithm for estimation of HMI-based Young's modulus through HMI displacement and strain, where we will demonstrate both the theoretical and experimental validation studies.

Chapter 7. Modulus Estimation using HMIFU

7.1 Introduction

As the HMIFU system has been assessed fundamentally in Chapter 3, the development of both the 1-D and 2-D HMIFU system have been described in the Chapters 4, 5, along with initial feasibilities in preclinical pancreatic tumor model mice *in vivo* in chapter 6. In this chapter, the work is focused on demonstrating the feasibility of implementing a novel technique for estimating the Young's modulus is presented utilizing the principle of HMI and HMIFU. The motivation behind this work stems from the lack of *in vivo* indentation based method for estimating of localized quantitative stiffness index such as Young's Modulus for biological tissue assessment. The further details have been previously summarized and can be found in the section of Appendix B of this chapter.

The objective of this chapter is to investigate a new role for HMIFU, namely, a mechanical testing tool, where a known dynamic force is applied and the resulting displacement is measured. In the previous work (described in Appendix B), three objectives were being investigated: (1) Proposal of a stiffness index, namely, the HMI modulus E_{HMI}, based on the applied force and the measured strains, (2) Evaluation of the correlation between E_{HMI} and the true Young's modulus E with finite-element simulations, and (3) Evaluation of the quality and the experimental feasibility of the proposed method on phantoms, by comparing E_{HMI} to the Young's modulus measured by mechanical testing. Nevertheless, further validation of the proposed modulus estimation method is required on biological specimen as well as implementation onto the clinically-translatable 2-D HMIFU system. Therefore, the main

objective of this work is to (4) demonstrate the feasibility of the proposed method on *ex vivo* biological tissue for elasticity imaging using both the developed 1-D and 2-D HMIFU system. The estimated modulus using 1-D and 2-D HMIFU system will be referred as the E_{HMI}, namely HMI modulus throughout this chapter. The 1-D HMI modulus as the ratio of the maximum $\sigma_{compression}$ divided by the maximum measured axial normal strain ε_{zz} . E_{HMI} is therefore defined as:

$$E_{HMI} = \frac{\max(\sigma_{Compressio\ n})}{\max(\varepsilon_{zz})}, \quad (1)$$

whereas the 2-D HMI modulus, which is estimated from both axial normal strain and axial shear strain, can be defined as:

$$\iiint f_v dV = E(2\pi R^2 \varepsilon_{zz} + \frac{1}{3}\varepsilon_{xz} * 2\pi Rh) \quad (2)$$

2-D HMI modulus will be described in the following section of 7.2 in detail. It is important to re-emphasize that our general objective of the proposed method is to provide an HMI-based mechanical testing setup that is particularly relevant for biomechanics as it is non-contact, non-invasive, and it can be used *in vivo*.

7.2 Materials and Methods

As mentioned in the introduction, much of the previous work, which focused on the demonstration of the fundamental assessment of the modulus estimation methodology using

Finite Element Analysis (FEA) modeling, and the feasibility study using polyacrylamide phantoms with mechanical testing validation, have been previously demonstrated and is described on the Appendix B of this chapter.

Calculation of the 2D HMI Elastic Modulus

Upon development of the 2-D HMIFU system, it is possible to estimate both the axial strain (ε_{zz}) and axial shear (ε_{xz}) strain, which allows us to utilize another model independent, close formula as follows:

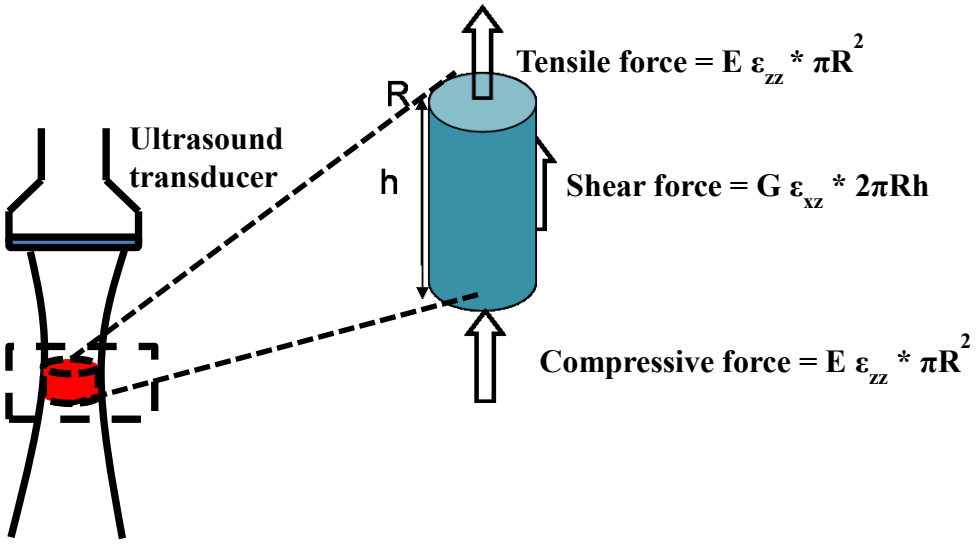

Figure 7.1. Summary of how the 2D HMI modulus is calculated. Note that focal region is assumed to be a volumetric force distributed across a cylindrical piston-like shape in highlighted in pink. Green region indicates the force piston. R, h indicates the radius and the height of piston shaped force, respectively.

The closed form equation for estimating 2-D HMI modulus is as follows:

$$\iiint f_v dV = E(2\pi R^2 \varepsilon_{zz} + \frac{1}{3}\varepsilon_{xz} * 2\pi Rh) \quad (2)$$

where f_v is the volumetric force, E would be the HMI modulus, R and h indicates the radius and height of the force piston, respectively, and lastly ε_{zz} and ε_{xz} indicating axial and axial-shear strain. Note assumption of both incompressibility as well as homogeneous medium is assumed for this equation to hold. The confirmation study for incompressibility has been completed previously and is described in Appendix B.

Ex vivo Study using 1-D HMIFU system

For the 1-D modulus estimation study, two canine liver lobes were excised from the animals immediately after sacrifice. All procedures were approved by the Institutional Animal Care and Use Committee of Columbia University. The tissue specimens were immersed in a degassed Phosphate Buffered Saline bath upon excision and throughout the experimental procedure. Both the HMI imaging experimental protocol used here has been described in details previously [154]. AM frequency was 25 Hz, resulting in an excitation frequency of f=50Hz. The excitation transducer has a characteristic beam profile of 4 mm by 1 mm at -6dB, which results in approximately 10 mm of excitation in the axial direction (Figure 7.2). Note that this transducer also used in the study described in Chapter 3. Due to the similar order of axial excitation range and the thickness of liver specimen, the transducer was intentionally positioned near the top surface of the liver in order to facilitate the measurement of axial compressive strain. Axial and shear strains were obtained from axial displacements using a gradient operator. More

specifically, a least square estimator implemented with a Savitzky-Golay filter was used to estimate the strains. (Figure 7.3). The size of the window for incremental HMI displacement estimation was equal to 3.85 mm, with an overlap of 90%. The size of the window for strain estimation was varied between 0.12 mm to 0.58 mm for axial strain, and 0.94 mm to 1.56 mm for axial shear strain, depending on the profile of the focal displacement.

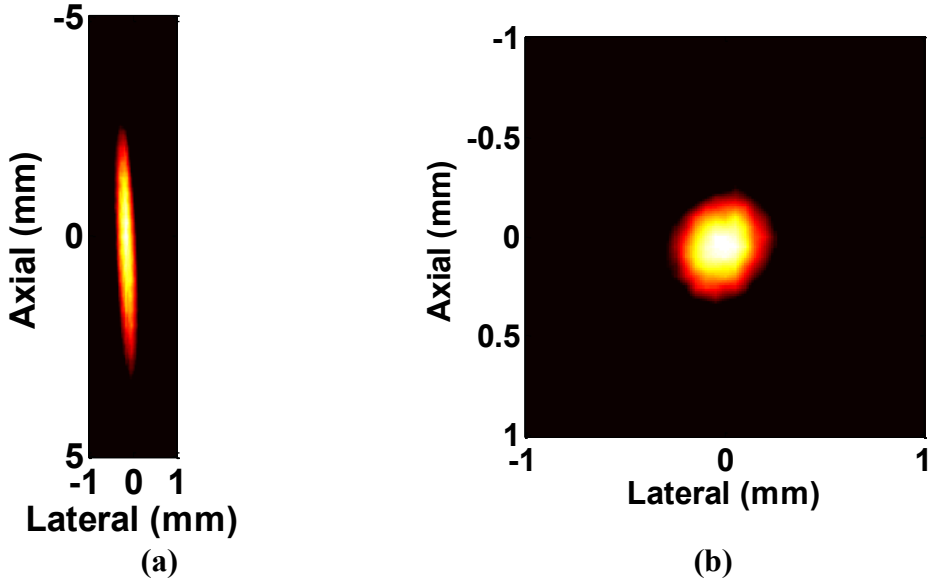

Figure 7.2. Beam profile of 1-D system HIFU transducer (a): On axis view, (b): Cross-sectional view. The -6dB region consists of focal length of 4 mm in the axial and 0.6 mm in the lateral direction.

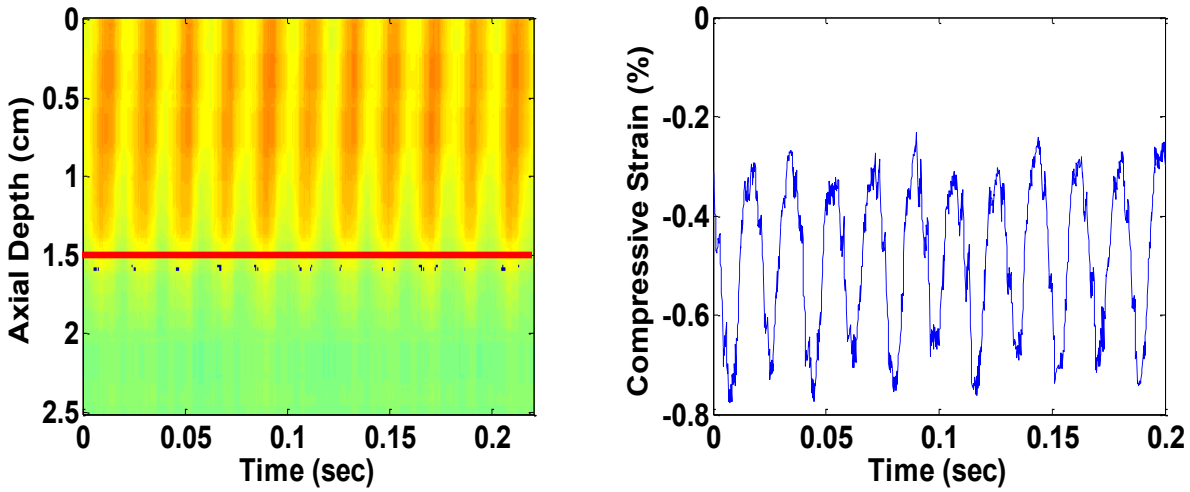

(a) **(b)**

Figure 7.3. (a) Estimated displacement using 1D cross correlation and (b) Estimated axial compressive strain using least square estimator algorithm. Red line indicates the region of investigation for compressive strain, i.e., end of acoustic focal zone. Note that the displacement profile is plotted in m-mode.

Mechanical tests were carried out in order to obtain the Young's modulus of freshly-excised canine liver tissue ex vivo. Samples were collected from the same livers as those tested by HMI, and were constantly kept in Phosphate Buffered Saline (PBS) (Fischer Scientific, Pittsburgh, PA) during ex vivo transportation and mechanical testing. To minimize the variations in tissue properties, all tests were completed within 12 hours post-mortem. Five cylindrical test specimens of diameter $d = 5.19 \pm 0.41$mm and height $h = 4.22 \pm 0.80$mm (N=3 and N=2 for liver 1 and 2, respectively) were prepared using a biopsy punch. The specimens were placed unconfined between the top/bottom plates, pre-compressed (to induce enough grip between the tissue and grip surfaces) (ε=5%), and tested under oscillatory shear test (ε=1%, f=1Hz-10Hz) in order to measure the shear modulus ($G_{Mech.Test.}$). The value of the shear storage modulus $G_{Mech.Test.}$ measured at f=10Hz was chosen as the reference value, and the Young's modulus was

obtained by $E_{Mech.Test.} = 3\ G_{Mech.Test.}$ under the assumption of quasi-incompressibility, as in the phantom study.

Numerical, phantom and ex vivo Study for 2-D HMIFU system

Both the methods for numerical and phantom studies are described in the Appendix B. For the 2-D modulus estimation study, another set of numerical study was first performed under the same simulation parameters and implementation approach as discussed in the method section of A1. Two modifications were made, where excitation was made under static mode, and the excitation force was modified with the force profile simulated using a previously developed custom simulation algorithm [245]. Both phantom and liver specimen based study was performed. Three locations were investigated on a co-polymer phantom with custom manufacturing method [246] with holds Young's modulus of 5.5 kPa, and the liver specimen (n=3, treatment location 3) preparation was the same as the procedure using the 1-D HMIFU system. Both imaging HMIFU sequence as well as HIFU treatment sequence was used for phantom and liver study. Further information on the detail of the HMIFU sequence can be found on Chapter 5. The excitation transducer has a characteristic beam profile of 1.7 mm by 0.4 mm at -6dB (Figure 7.4). The size of the window for incremental HMI displacement estimation was equal to 1.54 mm, with an overlap of 90%. The processing algorithm and parameters for strain estimation were same as the 1-D system study mentioned in Chapter 4.

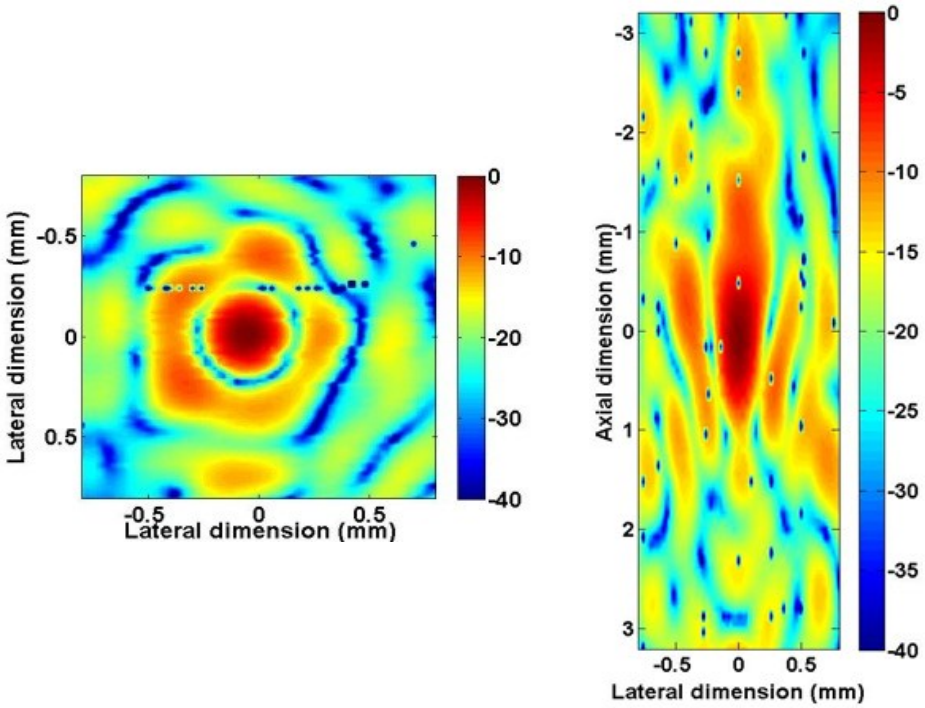

(a) (b)

Figure 7.4. (a) Beam profile of the 2-D system's HIFU transducer (a): On axis view, (b): Cross-sectional view. The -6dB intensity (-3dB Pressure) region consists of focal length of 1.7 mm in the axial and 0.4 mm in the lateral direction.

7.3 Results

The outcomes from the numerical study of 1-D HMIFU system including assumption error estimation, correlation between E and Young's Modulus based on simulation as well as polyacrylamide phantom studies, as well as investigation on inhomogeneity dependency have been described further in Appendix B.

Ex vivo Study using 1-D HMIFU system

The estimated E_{HMI} and the measured Young's Modulus of two sets of liver specimens are listed on Tables 7.1 and 7.2, respectively. The average value of the modulus was 33.9±15.2 kPa whereas the measured Young's Modulus from mechanical testing was 4.20±2.58 kPa. The average ratio between the two moduli is found to be $E_{HMI}/E \approx 8.1$.

Specimen #	*Compressive Strain %*	*E_{HMI} (kPa)*
1	**0.76±0.02**	**44.6**
2	**1.31±0.02**	**23.1**
Average	**0.78±50.0**	**33.9±15.2**

Table 7.1. Estimated compressive strain using HMI and E_{HMI}

Specimen #	*Estimated E (kPa)*
1	**2.64**
2	**2.19**
3	**2.16**
4	**7.29**
5	**6.72**
Average	**4.2±2.58**

Table 7.2. Measured Young's Modulus of ex vivo liver tissue using rhometry mechanical testing

Numerical, phantom, and ex vivo Study using 2-D HMIFU system

From the ABAQUS simulation, we simulated for the excitation force, axial displacement, axial strain and axial shear strain. The resulting force was 2 x 10^6 N/m3, the resulting peak

positive displacement was around 2.0 μm, the axial strains were varied between 0.69 to 0.82 %, and the axial shear strain was around 2.2% (Figure 7.5).

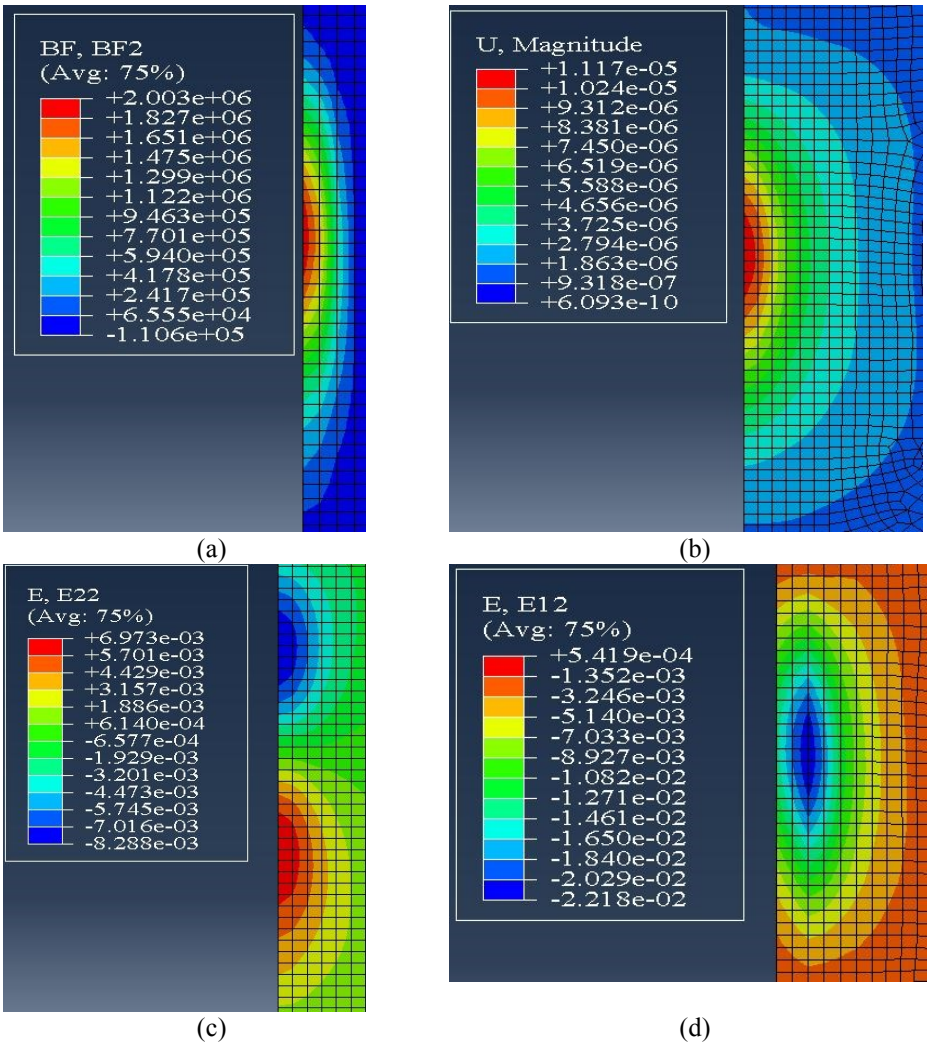

Figure 7.5. Theoretical simulation of HMI body force (a), axial displacement (b), axial strain (c), and axial shear strain (d) using a axi-symmetric based model on ABAQUS. Note the magnitude is in SI.

Displacement mapping was performed across three locations on the co-polymer phantom, and clear peak positive HMI focal displacement (Figure 7.6a) was mapped and used for estimation of both axial strain (Figure 7.6b) and axial shear strain (Figure 7.6c) The mapped displacement focal size were found to be 3 mm (axial) by 1.5 mm (lateral). The estimated E_{HMI} across three measurements on the copolymer phantom are listed on Table 7.3, respectively. The average value of the modulus was 167±8.61 kPa whereas the manufactured Young's Modulus from mechanical testing was 5.5±0.5 kPa. The average ratio between the two moduli is found to be $E_{HMI}/E \approx 30.4$.

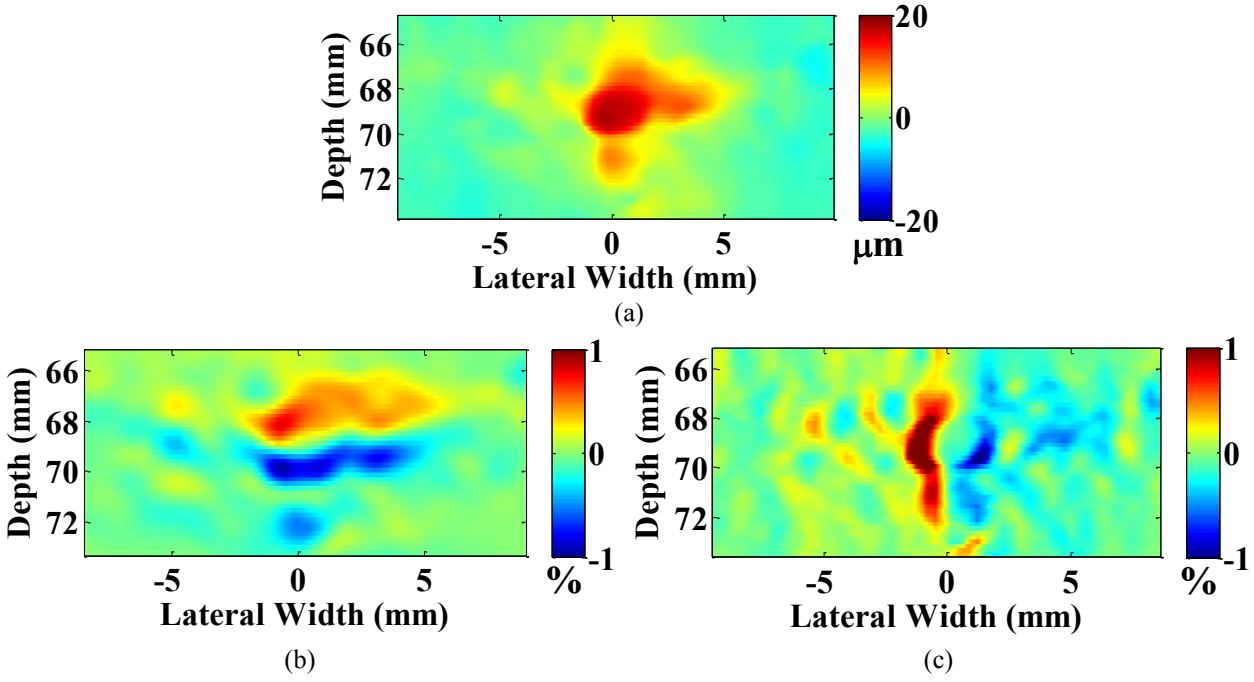

Figure 7.6. 2D HMI displacement map (a) , axial strain (b), and axial shear strain (c) using the 2D HMIFU system on copolymer phantom.

Phantom Location	Axial Compressive Strain (%)	Axial Tensile Strain (%)	Axial Shear Strain (%)	Piston Size (Height x Radius) (mm)	Estimated HMI Modulus (kPa)
1	0.5	0.51	2.06	3 x 1.5	159.7
2	0.96	0.8	1.41	3 x 1.5	164.8
3	0.8	1.4	0.9	3 x 1.5	176.5

Table 7.3. Strain and modulus computation on copolymer phantom

Similar to the copolymer phantom study, displacement mapping was performed across three treatment locations on three different live specimens, and clear peak positive HMI focal displacement (Figure 7.7a,b) was mapped and used for estimation of both axial strain (Figure 7.7 c,d) and axial shear strain (Figure 7.7 e,f) at beginning (Figure 7.7 a,c,e) and ending during (Figure 7.7 b,d,f) HIFU treatment time. The average mapped displacement focal size were found to be 5.07 mm (axial) by 2.54 mm (lateral) at beginning of the treatment, and 10.6 mm (axial) by 0.98 mm (lateral) at ending of the HIFU treatment. The estimated E_{HMI} across three measurements on the liver specimens are listed on Table 7.4, respectively. The average value of the modulus was 887.3±542.15 kPa and 5291.2±3384.4 kPa at beginning and ending during HFU treatment, respectively. The modulus contrast before and after HIFU treatment was found to be $E_{HMI,after}/E_{HMI,after} \approx 5.96$.

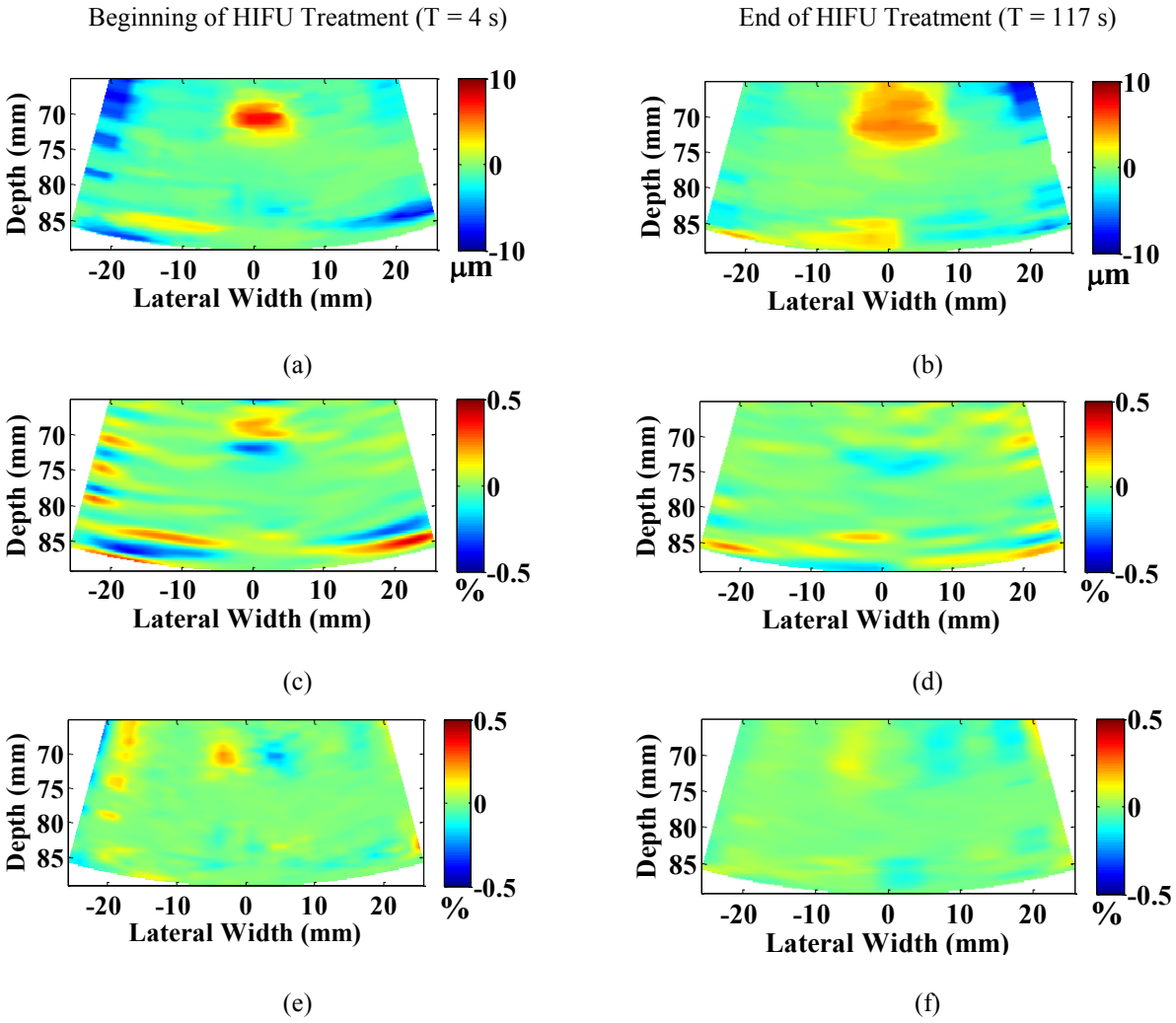

Figure 7.7. 2D HMI displacement map (a,b) , axial strain (c,d), and axial shear strain (e,f) on canine liver using the 2D HMIFU system at beginning (T=4 s) and end (T =117s) of a 2 min HIFU treatment sequence.

Liver Sample	Axial Compressive Strain (%)		Axial Shear Strain (%)		Piston Size (Height x Radius) (mm)		Estimated HMI Modulus (kPa)	
	Beginning	End	Beginning	End	Beginning	End	Beginning	End
1	0.3	0.15	0.24	0.12	3.7 x 3.0	10.0 x 5.0	822.2	2941.2
2	0.15	0.087	0.26	0.15	8.0 x 2.6	11.7 x 3.9	1459.3	3762.1
3	0.5	0.06	0.37	0.07	3.5 x 2.2	10.0 x 7.0	380.9	9170.3

Table 7.4. Strain and modulus at beginning and end of HIFU treatment on canine liver tissue

7.4 Discussion

In this chapter, a methodology using the acoustic radiation force for internal, non-contact indentation of soft tissues was proposed and investigated both theoretically and experimentally. Currently, no techniques are available for a noninvasive internal, non-contact identation based mechanical property assessment for biological specimens. Utilizing the principle of HMIFU, our method utilized the applied force and by measuring the resulting deformation, a stiffness modulus was proposed, namely, the HMI modulus E_{HMI}. It is noteworthy that the E_{HMI} differs from the Young's modulus E by definition, and thus our goal here is to assess the feasibility of estimating E_{HMI} using both 1-D HMIFU system and 2-D HMIFU system as well as investigating the correlation between the two.

Discussions regarding the previous work on 1-D HMIFU based modulus estimation can be found in Appendix B. The preliminary *ex vivo* experiments using 1-D HMIFU system were performed on liver specimens in order to demonstrate the feasibility of the method on soft tissue. It is important to keep in mind that mechanical testing experiments were performed on a very limited number of samples (N=5), and the following conclusions should be therefore considered

with caution. A high contrast ratio was obtained between the E_{HMI} and the Young's modulus ($E_{HMI}/E \approx 8.1$). This ratio is substantially higher than the one measured in phantoms, and it could be related to the alteration of mechanical properties due to sample preparation and conditioning. Due to the limited number of tested livers, no correlation could be clearly established between E_{HMI} and E in this ex vivo study. Nevertheless, the feasibility of the method was demonstrated on soft tissue.

Preliminary experiments using 2-D HMIFU system were also performed on both copolymer phantom as well as liver specimens in order to demonstrate the feasibility of the 2D modulus estimation method. Both the axial and axial shear strain profiles were clearly mapped across all of the cases. Nevertheless, the estimated E_{HMI} values were much higher than the manufacturer's value of ($E_{HMI}/E_{Manufacturer} \approx 30.3$). Similar findings were observed amongst the liver specimen cases, where the estimated E_{HMI} values of 887.3±542.1 kPa were much higher than the mechanical-testing based Young's modulus of 4.2±2.58 kPa. Nevertheless, the contrast remained high between the E_{HMI} at beginning of the HIFU treatment and ending of the HIFU treatment $E_{HMI,after}/E_{HMI,after} \approx 5.96$). This indicated the clear stiffening of the underlying tissue elasticity, which is confirmed with both previous literatures [136, 138, 139, 154, 174], as well as our mechanical testing results presented in Chapter 5.

Several reasons could be associated with the difference between the E_{HMI} and the mechanical testing measured Young's modulus: For modulus estimation based on 1-D system, by definition, the modulus that was proposed in this study (E_{HMI}) differs from the actual Young's modulus. E_{HMI} was defined as the ratio of compressive stress to underlying compressive strain. In reality, the acoustic radiation volumetric force acting within the focal region yields both compressive and shear deformation around the focal region, and the full balance of forces written

for the focal region should be written accordingly. Therefore, the 2-D system studies were performed in order to measure the actual Young's modulus by HMI using the measurements of both compressive and shear deformations. Nevertheless, the 2-D system studies led even a larger error between the estimated E_{HMI} and the underlying Young's Modulus. In regards to the aforementioned outcomes, we would like to discuss a few sources of error and the potential improvement on our technique which addresses such issues.

From the material property aspect, a major source of uncertainty in E_{HMI} estimation is related to the value of the acoustic absorption. The acoustic absorption can be estimated according to the different sources existing in the literature, but this will result most probably in an approximation of its actual value. However, due to the linear relationship between acoustic radiation force and acoustic attenuation, an inaccurate estimation of α will not affect the correlation that exists between E_{HMI} and the intrinsic Young's modulus E. A limitation to this method would be the example of an organ where the acoustic absorption varies dramatically within the tissue, since in that case, the spatial variation of E_{HMI} not be only related to spatial variation of E, but also to the spatial variation of the absorption. Other than attenuation, factors such as anisotropic, tissue inhomogeneity, viscosity, and nonlinearity properties of soft tissue can also contribute to the estimation error.

From the estimation algorithm perspective, a significant error also lies in the estimation of both the axial and shear strain. First, the displacement is affected by tissue inhomogeneity such as blood vessels and boundary effects when focal zone is localized near the surface or bottom edge on the specimen. In addition, we discussed in Chapter 5 that the size of the focal zone excitation increases with treatment time as thermal lesion grows. Therefore, the window size of the Savitzky-Golay filter is required to be adjusted depending on the displacement

profiles, which can induce estimation error both intra- and inter- treatment location measurement error across different treatments. It can be clear from both Tables 7.3 and 7.4 that experimental strains are generally much lower than that of the simulated. This could come from both limited axial and lateral resolution, which requires even a higher reconstruction resolution (80 MHz is used for this study) and beam density. In addition, the signal-to-noise (SNR) ratio can be improved in order to facilitate the delineation of the focal excitation displacement profile using a high frame rate, focused wave transmission imaging sequence in order to map the true focal displacement distribution. Another important aspect is the frequency dependency of strain, which has been discussed further in Appendix C.

Despite the fact that E_{HMI} differs from E by definition, it is important to insist on its high significance. The high correlation between these two moduli was demonstrated in this study. Therefore, relative contrast in terms of E_{HMI} is particularly interesting as it will be the same as the contrast in terms of actual elasticity. Moreover, E_{HMI} is a simple-to-measure, quantitative parameter that can be easily followed in time, and would therefore constitute a valuable quantitative parameter for HIFU monitoring directly at the focus. Ongoing work is being carried out in the relevance of E_{HMI} for therapy monitoring.

7.5 Conclusion

In this chapter, a noninvasive, noncontact, model-independent method for the measurement of tissues elasticity is presented based on the principle of indentation by applying the principle of HMIFU. The method is capable of estimating the Young's Modulus from estimated focal strain profiles and the applied focal volumetric force. The method has been

validated theoretically with Finite Element Analysis (FEA), and feasibility studies have been completed experimentally using both phantoms and liver specimens with the developed 1-D and 2-D HMIFU system. Good correlation was found between the E_{HMI} and assigned Young's Modulus in simulation ($E_{HMI}/E \approx 2.3$), as well as between the E_{HMI} and rheometer measured Young's Modulus using the 1-D HMIFU system. Strong discrepancies were observed between the estimated E_{HMI} using 2-D HMIFU system on both copolymer phantom($E_{HMI}/E \approx 30.4$), and liver specimen (($E_{HMI}/E \approx 211.3$), which were mainly due to limitation of imaging resolution, SNR, and accuracy in estimating the acoustic properties of imaging medium. Nevertheless, clear contrast remained between E_{HMI} at beginning of the HIFU treatment and E_{HMI} at the end of HIFU treatment ($E_{HMI,end}/E_{HMI,beginning} \approx 5.96$), indicating underlying stiffening of tissue upon HIFU treatment. Ongoing work includes both the improvement on resolution and SNR or imaging sequence and reconstruction, as well as estimation of tissue acoustic properties.

In the following and last chapter of this dissertation, we will summarize the findings from all of the aforementioned studies as well as discuss the potential area for improvement and recommended directions for the future development of HMIFU technique.

Chapter 8. Conclusion summary and future works

8.1 Conclusion & summary

The scope of this dissertation has been focused on the theoretical, system, and application development of a biomechanical assessment and monitoring of thermal ablation with a noninvasive ultrasound based technique, namely Harmonic Motion Imaging for Focused Ultrasound (HMIFU). HMIFU is an acoustic radiation force based technique for assessment and monitoring of tumor thermal ablation procedures such as High Intensity Focused Ultrasound (HIFU) treatment. In this dissertation, the performance of HMIFU in detecting the formation of HIFU thermal lesion has been assessed theoretically with experimental validation (Chapter 3) [204], followed by the development of both a 1-D and 2-D HMIFU system for pre-clinical and clinical study have been developed with feasibility shown ex vivo (Chapter 4, Chapter 5) [199, 233] and *in vivo* (Chapter 6) [247], and lastly a quantitative mechanical mapping method has been proposed and implemented onto both the HMIFU framework (Chapter 7) [183].

In chapter 3, a 3D, FE-based interdisciplinary simulation framework comprised of a nonlinear wave propagation model coupled with a Bioheat Transfer (BHT) module to simulate for acoustic pressure maps and thermal lesion size, a finite-element (FE) based mechanics module to simulate for the mechanical response, and an image-formation model is used to evaluate the HMIFU estimated displacement, in order to assess the feasibility of HMIFU in thermal lesion mapping. For the simulated HIFU treatment cases, the modulus contrast of lesion-to-background were assigned for 3,6, and 9 for HIFU treatment with 10,20, and 30 seconds, both the HMIFU simulation framework and validation experiments showed capability

in depicting the lesion size increase (Simulation: 16.2, 73.1, 334.7 mm^2, Experiment: 28.2, 83.3, 201.1 mm^2) (Figure 3.11, Table 3.4) as well as the lesion-to-background displacement contrast (Simulation: 1.65, 3.19, 4.59, Experiment: 1.19, 1.28, 1.78) (Figure 3.10, Table 3.5).

In Chapter 4, the 1-D HMIFU system has been upgraded and optimized in order to investigate the relationship between HMIFU parameters (focal displacement, phase shift ($\Delta\varphi$)) and thermal, acoustical, and mechanical effects within focal medium (i.e., boiling, cavitation, and nonlinearity) using barewire thermocouple and PCD on biological specimen *ex vivo*. The multi-parametric HMIFU monitoring studies were performed under HIFU treatment sequences with slow denaturation and boiling. For HIFU treatments with slow denaturation, which were performed with acoustic power ranged between 3.6 to 5.2 W for 120-240 seconds, consistent displacement increase-then-decrease trend was observed, indicating tissue softening-then-stiffening and phase shift increased with treatment time in agreement with mechanical testing outcomes. The cross-correlation parameter remained high throughout the entire treatment time under a minimized broadband energy and boiling mechanism. In contrast, HIFU treatment sequences with boiling were performed with acoustic power ranged between 8 to 11W for 30 seconds, where both displacement and phase shift change lacked consistency under the presence of strong boiling mechanism confirmed by both PCD and thermocouple monitoring. Nevertheless, HMIFU parameters such as displacement contrast remained high amongst the HIFU treatment with boiling sequences, indicating the robustness of HMIFU in monitoring lesion formation under boiling mechanism.

In chapter 5, we have further designed and developed a fully-integrated, clinically 2D real-time HMIFU system, which incorporated a GPU-based sparse-matrix reconstruction algorithm capable of providing 2D real-time streaming during HIFU treatment up to 15 Hz

without interruption. To our knowledge, the developed HMIFU platform is currently the fastest real-time feedback system in the field of HIFU treatment monitoring. Reproducibility studies also showed consistent displacement estimation on tissue-mimicking phantoms (21.9±7.98 μm, 23.9±8.7 μm, and 21.6±2.4 μm) as well as monitoring of tissue-softening-then-stiffening phase change across 16 out of 19 liver specimens (Increasing rate in phase shift ($\Delta\varphi$): 0.73±0.69 %/s, Decreasing rate in phase shift ($\Delta\varphi$): 0.60±0.19 %/s) along with thermocouple monitoring (Increasing: 0.84±1.15 %/°C, Decreasing: 2.03± 0.93%/°C). The underlying stiffening assessments were also confirmed with mechanical testing as well (Untreated: 2.1± 1.2 kPa, HIFU treated: 38.8± 11.6 kPa).

In chapter 6, the feasibility of using the developed 2-D HMIFU system on pancreatic (kP(f)c and KPC) models has been demonstrated *in vivo*. HMI displacement decreases were observed at three of five treatment locations across the kP(f)c model at 20.8±6.84, 18.6±1.46, and 24.0±5.43%, as well as at four of the seven treatment locations across the KPC model at 39.5±2.98%, 34.5±21.5%, 16.0±3.05%, and 35.0±3.12%. Gross pathological findings and H&E histological assessment also confirmed the well delineated regions of treated tissue with cell death confirmation. Cleaved-Caspase-3 staining also confirmed the apoptotic cell death surrounding the HIFU treated regions due to the collateral damage from the HIFU treatment. Ongoing and future work will be focused on long-term study to monitor the progressive change in tumor characteristics following HIFU treatment with HMIFU monitoring.

In chapter 7, a novel model-independent method for the estimating Young's modulus based on strain profile was implemented onto both 1-D and 2-D HMIFU system. The method was first validated with Finite Element Analysis (FEA), where good correlations were found between the E_{HMI} and assigned Young's Modulus in simulation, as well as between the E_{HMI} and

rheometer measured Young's Modulus using the 1-D HMIFU system on both polyacrylamide phantom ($E_{HMI}/E \approx 2.3$) and liver ($E_{HMI}/E \approx 8.1$). Strong discrepancies were observed between the estimated E_{HMI} using 2-D HMIFU system on both copolymer phantom ($E_{HMI}/E \approx 30.4$), and liver specimen ($E_{HMI}/E \approx 211.3$) due to the limited imaging resolution and SNR. Clear contrast was also detected between E_{HMI} at beginning of the HIFU treatment and E_{HMI} at the end of HIFU treatment ($E_{HMI,end}/E_{HMI,beginning} \approx 5.96$), indicating underlying stiffening of tissue upon formation of thermal lesion. The 2-D HMIFU system is currently being investigated to improve both the spatial resolution and SNR in order to facilitate estimation of focal strain profiles.

In summary, the outcomes from the aforementioned studies successfully showed the feasibility of both the 1-D and 2-D HMIFU system in monitoring both HIFU treatment with slow denaturation and boiling. The monitoring capabilities of HMIFU have been improved to a multi-parametric approach involving focal displacement, phase shift, strain, temperature, PCD on *ex vivo* and *in vivo* applications.

8.2 Future directions

Ever since the conceptualization of Localized Harmonic Motion Imaging (LHMI)[81], there have been many studies extensively on this subject from many different aspects. From the perspective of HIFU treatment, as mentioned earlier, there are three stages for every ablation therapy treatment: 1) Treatment planning, 2) Treatment monitoring, and 3) Treatment Assessment. As for the stages of treatment planning and assessment, two important missions are required to be completed: target localization (or mapping) and beam localization (or mapping). From the aspect of target localization, extensive diagnostic imaging modalities using ultrasound,

acousto-optical imaging, MRI, or CT have been developed that are capable of localizing/mapping thermal lesion based on its unique tissue property such as echogenicity, speed of sound, attenuation coefficient. Despite the aforementioned targeting modalities, imaging techniques to localize the HIFU focal zone, in other words the beam localization of the therapeutic ultrasound is relatively underdeveloped. Previously developed beam localization techniques have been based on MRI as well as the noninvasive temperature imaging using echo-shift based method. A recent study demonstrated feasibility the application of both Synthetic Aperture (SA) and Single Focused Transmission (STF) imaging in order to monitor the change in echogenicty to localize HIFU focus and assess lesion formation *in vivo* [248]. With respect to the developed techniques, HMIFU can also establish a beam localization sequence in order to improve the targeting accuracy prior to the treatment procedure. It is noteworthy that the sequence is required to detect any shift of the focal beam spot while incapable of producing any unintended irreversible therapeutic effects at the focal region. The treatment monitoring aspect, however, remains the most challenging and therefore underdeveloped where further improvements can be made to optimize the performance of HIFU treatment. Despite the development of other techniques such as MRgFUS, MRE, ARFI Imaging, SSI, HMIFU remains as the only modality capable of imaging the focal information without interruption of the treatment. Over the past decade, an extensive range of assessment approaches have been proposed such as focal displacement, focal phase shift, and focal strain. Despite the previously feasibility studies with these parameters, these parameters are heavily dependent on system parameters such as carrier frequency, modulation frequency, treatment power, motion estimation parameter, as well as medium parameters such as boundary condition, viscoelasticity, and nonlinearity. As all of these parameters play significant role and can vary drastically across

different biological media and conditions, it is important to assess their quality and reliability on pathological tissue *ex vivo* or *in vivo* during the preclinical stage in order to confirm the optimal assessment strategy in a clinical setting. Another major area of interest can be utilization of the shear waves generated using the HMIFU focal excitation. However, due to the complex boundary conditions especially following treatment, where focal region is comprised of lesion, tumor, and normal tissue as well as the nature of a spherical source excitation, the design of the corresponding inverse problem for complex modulus reconstruction can be challenging.

Despite the previously work in Localized Harmonic Motion monitoring of HIFU treatment [160], it is also important to develop an in-house customized theoretical model specifically designed for simulating focal environment during the HMIFU-monitored HIFU treatment. The model should base on a customized wave propagation model tailored for HMIFU condition in order to predict the medium change in acoustic, thermodynamic, mechanic, and ultrasonic property utilizing the input of HMIFU treatment and system parameters.

From the system aspect, numerous areas can be developed both the 1-D HMIFU and 2-D HMIFU system. The 1-D HMIFU system is already optimized to perform multi-parametric monitoring across the entire HIFU treatment window, so the unmet needs lie on the capability of online real-time assessment. This requires the modification of the data acquisition unit and can be potential achieved by a parallel-processing algorithm based on GPU. Another area of improvement is the simultaneous PCD, thermocouple, and HMIFU utilizing the four channel system which can be utilized to capture RF, thermometer reading, PCD detector signal, and input voltage (for viscoelasticity assessment such as phase shift). For the 2-D HMIFU system, the focus should lie more on increasing the buffer memory of the VDAS system to host as many frames during the treatment as possible, and transforming the reconstruction algorithm using

machine languages such as C++/CUDA in order to further improve the lag and stability of the processing performance. Such software optimization can also lead to potential 3D HMIFU monitoring with a confocally-aligning a 2D imaging array, which requires an optimized memory allocation and algorithm stability. In addition, the therapeutic module of the 2-D HMIFU system is expected to be replaced by a VDAS-based unit combined with a HIFU-module capable for dual mode of therapy and diagnostic performance, which further transforms clinical applicability of HMIFU system. The upgraded system is expected to access each of the individual elements of the array HIFU transducer in order to perform tasks such as electronic steering and focal size or shape adjustment for tasks such as raster ablation, mutli-focal monitoring, or shear wave imaging. As versatile as the applicability of HIFU treatment, the potential application of HMIFU can also span across a wide range of anatomical parts such as breast, pancreas, liver, heart, brain, prostate, kidney, and muscle. That said, the respective monitoring imaging sequence is a major area which requires through investigation: For example, current imaging sequence are composed of a divergent single transmit wave, which more suitable for cardiovascular and shear wave application that requires a wider field of view in the lateral direction. Nevertheless, other imaging sequences such as plane wave imaging (Figure 8.1 b,d,f) has shown potential improvement in focal signal-to-noise (SNR) while suppressing lens-effect like displacement artifact (Figure 8.1 a,c,e) and can serve to increase the frame rate by avoiding the scan conversion processing.

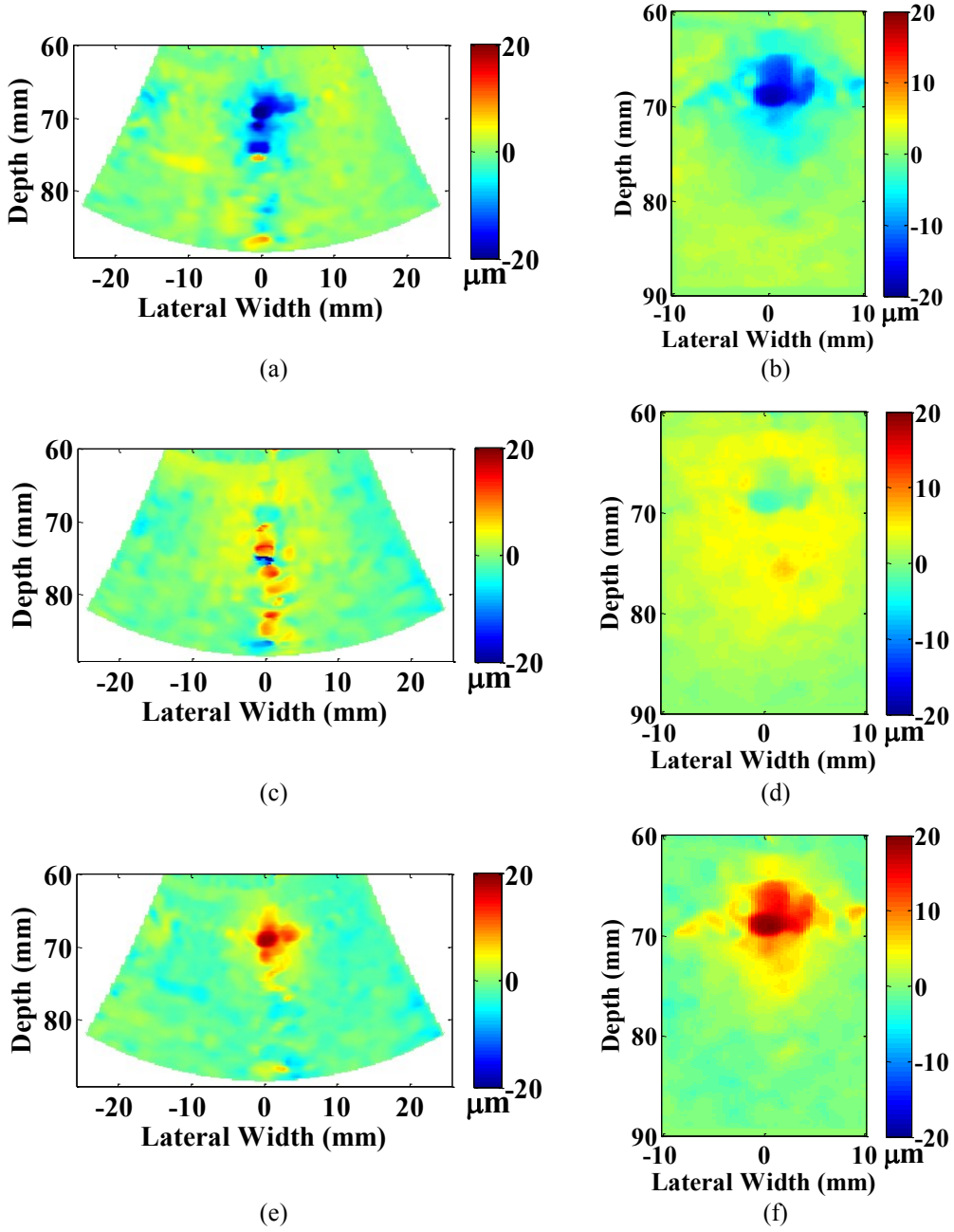

Chapter 8.1. One cycle of peak-to-peak HMI displacement frames between divergent wave imaging (a,c,e) and plane wave imaging (b,d,f) using 2.5 wavelengths cross correlation window size.

Nevertheless, estimation of localized parameters such as axial and shear strain requires not only high frame rate but also high SNR at the focal region. In the case of plane wave, despite the well delineation of focal zone, the focal displacement profile may be over filtered and lose the true distribution characteristics. Therefore, other imaging and reconstruction sequence such as synthetic aperture [225, 249], wide beam with reduced aperture [250], or Hadamard coding [227, 251] can also be investigated to achieve an optimized imaging sequence with enough SNR and frame rate to perform the desired parametric monitoring. Another important aspect of the imaging component is the choice of motion estimation parameters, i.e., the window size for the search kernel used during cross correlation algorithm. It can be observed that for the case of a homogenous medium such as the studied case using copolymer phantom, the displacement profiles are much smoother and delineate the shape of a HIFU focal zone using a window size of 6.16 mm or 10 wavelength (Figure 8.2) compared to the case of 1.54 mm (Figure 8.1) under both divergent wave and plane wave imaging sequence. Nevertheless, this is not applicable for any target (e.g., *in vivo* mice) or any inhomogeneous mediums (e.g., Cyst bearing tumor), where larger window size may lead to averaging of the displacement across the entire field of interest thus the mapped profile will lose the ability to map the intrinsic displacement distribution, which is also closely linked with the reliability of strain estimation algorithm. Therefore, the adjustment and optimization of motion estimation parameters will further need to be performed in the future.

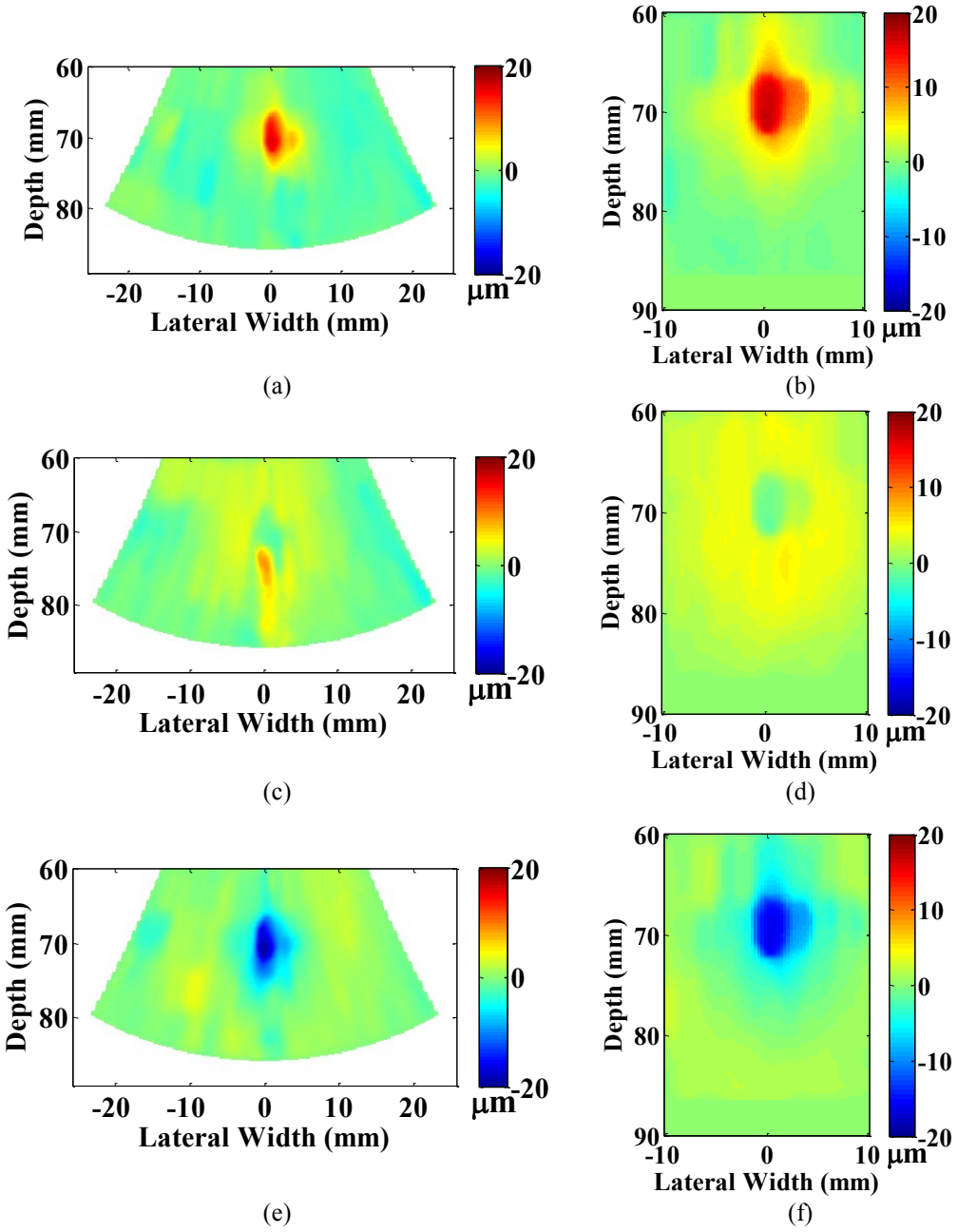

Chapter 8.2. HMI displacement profile between divergent wave imaging and plane wave imaging using 10 wavelengths cross correlation window size.

In the ultimate ending of this dissertation, we sincerely hope the findings presented in this dissertation contribute to the clinical and commercial translation of HMIFU in the near future.

BIBLIOGRAPHY

1. Jemal, A., et al., *Cancer statistics, 2008.* Ca-a Cancer Journal for Clinicians, 2008. **58**(2): p. 71-96.
2. Chaplain, M.A.J. and B.D. Sleeman, *Modeling the growth of solid tumors and incorporating a method for their classification using nonlinear elasticity theory.* Journal of Mathematical Biology, 1993. **31**(5): p. 431-473.
3. Jain, R.K. and K. Wardhartley, *Tumor Blood-Flow - Characterization, Modifications, and Role in Hyperthermia.* IEEE Transactions on Sonics and Ultrasonics, 1984. **31**(5): p. 504-526.
4. Jain, R.K., *Determinants of Tumor Blood-Flow - a Review.* Cancer Research, 1988. **48**(10): p. 2641-2658.
5. Jain, R.K., *Parameters Governing Tumor Blood-Flow.* Tumor Blood Supply and Metabolic Microenvironment, 1991. **20**: p. 27-36.
6. Nguyen, D.X., P.D. Bos, and J. Massague, *Metastasis: from dissemination to organ-specific colonization.* Nature Reviews Cancer, 2009. **9**(4): p. 274-U65.
7. Urruticoechea, A., et al., *Recent Advances in Cancer Therapy: An Overview.* Current Pharmaceutical Design, 2010. **16**(1): p. 3-10.
8. Mauri, D., N. Pavlidis, and J.P.A. Ioannidis, *Neoadjuvant versus adjuvant systemic treatment in breast cancer: A meta-analysis.* Journal of the National Cancer Institute, 2005. **97**(3): p. 188-194.
9. Grzankowski, K.S. and M. Carney, *Quality of Life in Ovarian Cancer.* Cancer Control, 2011. **18**(1): p. 52-58.

10. Baskar, R., et al., *Cancer and Radiation Therapy: Current Advances and Future Directions.* International Journal of Medical Sciences, 2012. **9**(3): p. 193-199.

11. Niu, L., et al., *The role of cryosurgery in palliative care for cancer.* Annals of Palliative Medicine, 2013. **2**(1): p. 26-34.

12. Izzo, F., *Other thermal ablation techniques: Microwave and interstitial laser ablation of liver tumors.* Annals of Surgical Oncology, 2003. **10**(5): p. 491-497.

13. Ni, Y., et al., *A review of the general aspects of radiofrequency ablation.* Abdominal Imaging, 2005. **30**(4): p. 381-400.

14. Ter Haar, G., D. Sinnett, and I. Rivens, *High-Intensity Focused Ultrasound - a Surgical Technique for the Treatment of Discrete Liver-Tumors.* Physics in Medicine and Biology, 1989. **34**(11): p. 1743-1750.

15. Al-Bataineh, O., J. Jenne, and P. Huber, *Clinical and future applications of high intensity focused ultrasound in cancer.* Cancer Treatment Reviews, 2012. **38**(5): p. 346-353.

16. Kennedy, J.E., G.R. ter Haar, and D. Cranston, *High intensity focused ultrasound: surgery of the future?* British Journal of Radiology, 2003. **76**(909): p. 590-599.

17. Hill, C.R. and G.R. Ter Haar, *Review article: High intensity focused ultrasound-potential for cancer treatment.* British Journal of Radiology, 1995. **68**(816): p. 1296-1303.

18. Kennedy, J.E., *High-intensity focused ultrasound in the treatment of solid tumours.* Nature Reviews Cancer, 2005. **5**(4): p. 321-327.

19. Dasgupta, S., et al., *HIFU volume as function of time, as determined by MRI, histology, and computations.* Journal of Biomechanical Engineering, 2010. **132**: p. 081055.

20. Burov, A.K. and G.D. Andreevskaya, *Effect of High Intensity Supersonic Oscillations on Malignant Tumors in Man and Animals.* Doklady Akademii Nauk Sssr, 1956. **106**(3): p. 445-448.

21. Linke, C.A., et al., *Localized Tissue Destruction by High-Intensity Focused Ultrasound.* Archives of Surgery, 1973. **107**(6): p. 887-891.

22. Fry, F.J. and L.K. Johnson, *Tumor irradiation with intense ultrasound.* Ultrasound in Medicine & Biology, 1978. **4**(4): p. 337-341.

23. Bamber, J.C. and C.R. Hill, *Ultrasonic attenuation and propagation speed in mammalian tissues as a function of temperature.* Ultrasound in Medicine & Biology, 1979. **5**(2): p. 149-157.

24. Corry, P.M., et al., *Human cancer-treatment with ultrasound.* IEEE Transactions on Sonics and Ultrasonics, 1984. **31**(5): p. 444-456.

25. Goss, S.A. and F.J. Fry, *The Effect of High-Intensity Ultrasonic Irradiation on Tumor-Growth.* IEEE Transactions on Sonics and Ultrasonics, 1984. **31**(5): p. 491-496.

26. Frizzell, L.A., *Threshold Dosages for Damage to Mammalian Liver by High-Intensity Focused Ultrasound.* IEEE Transactions on Ultrasonics, Ferroelectrics, and Frequency Control, 1988. **35**(5): p. 578-581.

27. Taylor, K.J.W. and C.C. Connolly, *Differing Hepatic Lesions Caused by Same Dose of Ultrasound.* Journal of Pathology, 1969. **98**(4): p. 291-293.

28. Cline, H.E., et al., *Focused US System for MR Imaging-Guided Tumor Ablation.* Radiology, 1995. **194**(3): p. 731-737.

29. Huber, P.E., et al., *A new noninvasive approach in breast cancer therapy using magnetic resonance imaging-guided focused ultrasound surgery.* Cancer Research, 2001. **61**(23): p. 8441-8447.

30. Hynynen, K., et al., *MR imaging-guided focused ultrasound surgery of fibroadenomas in the breast: A feasibility study.* Radiology, 2001. **219**(1): p. 176-185.

31. Gianfelice, D., et al., *MR imaging-guided focused ultrasound surgery of breast cancer: correlation of dynamic contrast-enhanced MRI with histopathologic findings.* Breast Cancer Research and Treatment, 2003. **82**(2): p. 93-101.

32. Takeuchi, T., Ishii, M., Takeuchi, K. *The experimental study of stereotaxic destruction on the cat brain by intense focused ultrasound: Detection of ultrasonic focal lesion by ultrasonic echo method*. in *The 4th Meeting of Japanese Society of Ultrasoics in Medicine*. 1963.

33. Lele, P.P., *Concurrent detection of the production of ultrasonic lesions.* Medical and Biological Engineering, 1966. **4**: p. 451-456.

34. Yang, R., et al., *Sonographic and Computed-Tomography Characteristics of Liver Ablation Lesions Induced by High-Intensity Focused Ultrasound.* Investigative Radiology, 1993. **28**(9): p. 796-801.

35. Furusawa, H., et al., *Magnetic resonance-guided focused ultrasound surgery of breast cancer: Reliability and effectiveness.* Journal of the American College of Surgeons, 2006. **203**(1): p. 54-63.

36. Ishihara, Y., et al., *Precise and Fast Temperature Mapping Using Water Proton Chemical-Shift.* Magnetic Resonance in Medicine, 1995. **34**(6): p. 814-823.

37. Vaezy, S., et al., *Liver hemostasis using high-intensity focused ultrasound.* Ultrasound in Medicine and Biology, 1997. **23**(9): p. 1413-1420.

38. Chavrier, F., et al., *Modeling of high-intensity focused ultrasound-induced lesions in the presence of cavitation bubbles.* Journal of the Acoustical Society of America, 2000. **108**(1): p. 432-440.

39. Simon, C., P. VanBaren, and E.S. Ebbini, *Two-dimensional temperature estimation using diagnostic ultrasound.* IEEE Transactions on Ultrasonics, Ferroelectrics, and Frequency control, 1998. **45**(4): p. 1088-1099.

40. Pernot, M., et al., *Temperature estimation using ultrasonic spatial compound imaging.* IEEE Transactions on Ultrasonics, Ferroelectrics, and Frequency Control, 2004. **51**(5): p. 606-615.

41. Liu, D. and E. Ebbini, *Real-Time 2-D Temperature Imaging Using Ultrasound.* IEEE Transactions on Biomedical Engineering, 2010. **57**(1): p. 12-16.

42. Casper, A., D.L. Liu, and E.S. Ebbini, *Realtime Control of Multiple-focus Phased Array Heating Patterns Based on Noninvasive Ultrasound Thermography.* IEEE Transactions on Biomedical Engineering, 2012. **59**(1): p. 95-105.

43. Lai, P.X., et al., *Real-Time Monitoring of High-Intensity Focused Ultrasound Lesion Formation Using Acousto-Optic Sensing.* Ultrasound in Medicine and Biology, 2011. **37**(2): p. 239-252.

44. Cui, H.Z. and X.M. Yang, *Real-time monitoring of high-intensity focused ultrasound ablations with photoacoustic technique: An in vitro study.* Medical Physics, 2011. **38**(10): p. 5345-5350.

45. Palmeri, M.L. and K.R. Nightingale, *What challenges must be overcome before ultrasound elasticity imaging is ready for the clinic?* Imaging in Medicine, 2011. **3**(4): p. 433-444.

46. Tomeno, W., et al., *Evaluation of the Liver Fibrosis Index calculated by using real-time tissue elastography for the non-invasive assessment of liver fibrosis in chronic liver diseases.* Hepatology Research, 2013. **43**(7): p. 735-742.

47. Carver, W. and E.C. Goldsmith, *Regulation of Tissue Fibrosis by the Biomechanical Environment.* Biomed Research International, 2013.

48. Foucher, J., et al., *Diagnosis of cirrhosis by transient elastography (FibroScan): a prospective study.* Gut, 2006. **55**(3): p. 403-408.

49. Huwart, L., et al., *Liver fibrosis: Noninvasive assessment with MR elastography versus aspartate aminotransferase-to-platelet ratio index.* Radiology, 2007. **245**(2): p. 458-466.

50. Yin, M., et al., *Quantitative assessment of hepatic fibrosis in an animal model with magnetic resonance elastography.* Magnetic Resonance in Medicine, 2007. **58**(2): p. 346-353.

51. Rouviere, O., et al., *MR elastography of the liver: Preliminary results.* Radiology, 2006. **240**(2): p. 440-448.

52. Fung, Y.C., *Biomechanics: Mechanical Properties of Living Tissues*1993, New York: Springer-Verlag.

53. Krouskop, T.A., et al., *Elastic Moduli of Breast and Prostate Tissues under Compression.* Ultrasonic Imaging, 1998. **20**: p. 260-274.

54. Anderson, W.A.D., *Pathology*. 3rd Edition ed1957, St. Louis: The C. V. Mosby Company.

55. Blacher, J., et al., *Arterial calcifications, arterial stiffness, and cardiovascular risk in end-stage renal disease.* Hypertension, 2001. **38**(4): p. 938-942.

56. Weinberg, E.J., D. Shahmirzadi, and M.R.K. Mofrad, *On the Multiscale Modeling of Heart Valve in Health and Disease.* Biomechanics and Modeling in Mechanobiology, 2010. **9**(4): p. 373-387.

57. Marra, S.P., et al., *Elemental composition, morphology and mechanical properties of calcified deposits obtained from abdominal aortic aneurysms.* Acta Biomaterialia, 2006. **2**(5): p. 515-520.

58. Shahmirzadi, D. and E.E. Konofagou, *Detection of Aortic Wall Inclusions Using Regional Pulse Wave Propagation and Velocity In Silico.* Artery Research, 2012. **6**(3): p. 114-123.

59. Ariel, I.M. and B.B. Cleary, *Breast cancer diagnosis and treatment* 1987, New York: McGraw-Hill.

60. Famaey, N. and J.V. Sloten, *Soft tissue modelling for applications in virtual surgery and surgical robotics.* Computer Methods in Biomechanics and Biomedical Engineering, 2008. **11**(4): p. 351-366.

61. Cobbold, R.S.C., *Foundations of Biomnedical Ultrasound* 2007, New York: Oxford Univ. Press.

62. Sarvazyan, A.P., et al., *Shear wave elasticity imaging: a new ultrasonic technology of medical diagnostics.* Ultrasound in Medicine and Biology, 1998. **24**(9): p. 1419-35.

63. Ophir, J., et al., *Elastography: Imaging the Elastic Properties of Soft Tissues with Ultrasound.* Journal of Medical Ultrasound, 2002. **29**(Winter): p. 155-171.

64. Ophir, J., et al., *Elastography: A Quantitative Method for Imaging the Elasticity of Biological Tissues.* Ultrasonic Imaging, 1991. **13**: p. 111–134.

65. Parker, K.J., et al., *Tissue response to mechanical vibrations for sonoelasticity imaging.* Ultrasound in Medicine and Biology, 1990. **16**: p. 241–246.

66. Shi, X.G., et al., *Detection of high intensity focused ultrasound liver lesions using dynamic elastometry.* Ultrasonic Imaging, 1999. **21**: p. 107–126.

67. Lewa, C.J., *Magnetic-resonance-imaging in the presence of mechanical waves.* Spectroscopy Letter, 1991. **24**: p. 55–67.

68. Kruse, S.A., et al., *Tissue characterization using magnetic resonance elastography: Preliminary results.* Physics in Medicine and Biology, 2000. **45**: p. 1579–1590.

69. Sinkus, R., et al., *High-resolution tensor MR elastography for breast tumour detection.* Physics in Medicine and Biology, 2000. **45**(6): p. 1649-1664.

70. Muthupillai, R., et al., *Magnetic-Resonance Elastography by Direct Visualization of Propagating Acoustic Strain Waves.* Science, 1995. **269**(5232): p. 1854-1857.

71. Catheline, S., et al., *Measurement of viscoelastic properties of homogeneous soft solid using transient elastography: An inverse problem approach.* Journal of the Acoustical Society of America, 2004. **116**(6): p. 3734--3741.

72. Sandrin, L., et al., *Transient elastography: A new noninvasive method for assessment of hepatic fibrosis.* Ultrasound in Medicine and Biology, 2003. **29**(12): p. 1705-1713.

73. Fatemi, M. and J.F. Greenleaf, *Ultrasound-stimulated vibro-acoustic spectrography.* Science, 1998. **280**: p. 82-85.

74. Lizzi, F.L., et al., *Radiation-force technique to monitor lesions during ultrasonic therapy.* Ultrasound in Medicine and Biology, 2003. **29**(11): p. 1593-1605.

75. Michishita, K., H. Hasegawa, and H. Kanai, *Ultrasonic measurement of minute displacement of object cyclically actuated by acoustic radiation force.* Japanese Journal of Applied Physics Part 1-Regular Papers Short Notes & Review Papers, 2003. **42**(7A): p. 4608-4612.

76. Fatemi, M. and J.F. Greenleaf, *Probing the dynamics of tissue at low frequencies with the radiation force of ultrasound.* Physics in Medicine and Biology, 2000. **45**(6): p. 1449-1464.

77. Chen, S., et al., *Shearwave Dispersion Ultrasound Vibrometry (SDUV) for measuring tissue elasticity and viscosity.* IEEE Transactions on Ultrasonics, Ferroelectrics and Frequency control, 2009. **56**(1): p. 55-62.

78. Bercoff, J., et al., *Monitoring thermally-induced lesions with supersonic shear imaging.* Ultrasonic Imaging, 2004. **26**(2): p. 71-84.

79. Bercoff, J., et al., *In vivo breast tumor detection using transient elastography.* Ultrasound in Medicine and Biology, 2003. **29**(10): p. 1387-1396.

80. Konofagou, E., J. Thierman, and K. Hynynen, *A focused ultrasound method for simultaneous diagnostic and therapeutic applications - a simulation study.* Physics in Medicine and Biology, 2001. **46**(11): p. 2967-2984.

81. Konofagou, E.E. and K. Hynynen, *Localized harmonic motion imaging: Theory, simulations and experiments.* Ultrasound in Medicine and Biology, 2003. **29**(10): p. 1405-1413.

82. Konofagou, E.E. and K. Hynynen. *Localized harmonic motion imaging: theory, simulations and experiments*. in *IEEE Symposium Ultrasonics*. 2002. Munich, Germany.

83. Mitri, F., et al., *Prostate cryotherapy monitoring using vibro-acoustography: Preliminary results of an ex vivo study and technnical feasibility.* IEEE Transactions on Biomedical Engineering, 2008. **55**(11): p. 2584-2592.

84. Bercoff, J., M. Tanter, and M. Fink, *Supersonic shear imaging: A new technique for soft tissue elasticity mapping.* IEEE Transactions on Ultrasonics, Ferroelectrics, and Frequency Control, 2004. **51**(4): p. 396-409.

85. Sapin de Brosses, E., et al., *Temperature dependence of the shear modulus of soft tissues assessed by ultrasound.* Physics in Medicine and Biology, 2010. **55**: p. 1701-1718.

86. Sapin de Brosses, E., M. Pernot, and M. Tanter, *The link between tissue elasticity and thermal dose in vivo.* Physic in Medicine and Biology, 2011. **56**: p. 7755-7765.

87. Wang, T.-Y., et al., *Imaging Feedback of Histotripsy Treatments Using Ultrasound Shear Wave Elastography.* IEEE Transaction on Ultrasonics, Ferroelectronics, and Frequency Control, 2012. **59**(6): p. 1167-1181.

88. Nightingale, K.R., et al., *On the feasibility of remote palpation using acoustic radiation force.* Journal of Acoustic Society of America, 2001. **110**: p. 625–634.

89. Meunier, J., et al., *Local Myocardial Deformation Computed from Speckle Motion*, in IEEE Proceedings in Computers in Cardiology 1988. p. 133-136.

90. Konofagou, E.E., J. D'hooge, and J. Ophir, *Myocardial Elastography- A Feasibility Study in vivo.* Ultrasound in Medicine and Biology, 2002. **28**(4): p. 475-482.

91. Couade, M. and e. al., *Quantitative assessment of arterial wall biomechanical properties using shear wave imaging* Ultrasound in Medicine and Biology., 2010. **36**: p. 1662–1676.

92. Pernot, M., et al., *Real-time assessment of myocardial contractility using shear wave imaging.* Journal of the American College of Cardiology, 2011. **58**: p. 65–72.

93. Shahmirzadi, D., R.X. Li, and E.E. Konofagou, *Pulse-Wave Propagation in Straight-Geometry Vessels for Stiffness Estimation: Theory, Simulations, Phantoms and In Vitro Findings.* Journal of Biomechanical Engineering, 2012. **134**(11): p. 1145021-1145026.

94. Garra, B.S., et al., *Elastography of Breast Lesions: Initial Clinical Results.* Radiology, 1997. **202**: p. 79–86.

95. Alizad, A., et al., *Potential applications of vibro-acoustography in breast imaging.* Technology in Cancer Research & Treatment, 2005. **4**(2): p. 151-157.

96. Antolin, G.S., et al., *FibroScan Evaluation of Liver Fibrosis in Liver Transplantation.* Transplantation Proceedings, 2009. **41**(3): p. 1044-1046.

97. Damianou, C., et al., *MRI monitoring of lesions created at temperature below the boiling point and of lesions created above the boiling point using high intensity focused ultrasound.* Biomedical Science and Engineering, 2010. **3**: p. 763-775.

98. Ter Haar, G., et al., *Trackless surgery using focused ultrasound: Technique and case report.* Minimally Invasive Therapy and Allied Technologies, 1991. **1**(1): p. 13-19.

99. Frizzell, L.A., et al., *Thresholds for Focal Ultrasonic Lesions in Rabbit Kidney, Liver, and Testicle.* IEEE Transaction on Biomedical Engineering, 1977. **24**(4): p. 393-396.

100. Emelianov, S.Y., et al., *Elasticity Imaging for Early Detection of Renal Pathology.* Ultrasound in Medicine and Biology, 1995. **21**(7): p. 871-883.

101. Cespedes, I., et al., *Elastography - Elasticity Imaging Using Ultrasound with Application to Muscle and Breast in-Vivo.* Ultrasonic Imaging, 1993. **15**(2): p. 73-88.

102. Nightingale, K., et al., *Acoustic Radiation Force Impulse imaging of in vivo vastus medialis muscle under varying isometric load.* Ultrasonic Imaging, 2002. **24**(2): p. 100-108.

103. Granke, M., et al., *Change in porosity is the major determinant of the variation of cortical bone elasticity at the millimeter scale in aged women.* Bone, 2011. **49**(5): p. 1020-1026.

104. Kallel, F., et al., *Elastographic imaging of the normal canine prostate in vitro.* Ultrasonic Imaging., 1999. **21**(3): p. 201-215.

105. Zhai, L., et al., *Acoustic Radiation Force Impulse Imaging of Human Prostates: Initial in Vivo Demonstration.* Ultrasound in Medicine and Biology, 2012. **38**(1): p. 50-61.

106. Bharat, S., et al., *Monitoring stiffness changes in lesions after radiofrequency ablation at different temperatures and durations of ablation.* Ultras Med Biol, 2005. **31**: p. 415-422.

107. Fahey, B.J., et al., *In Vivo Guidance and Assessment of Liver Radio-Frequency Ablation with Acoustic Radiation Force Elastography.* Ultrasound in Medicine and Biology, 2008. **34**(10): p. 1590-1603.

108. Bharat, S., et al., *Three-dimensional electrode displacement elastography using the Siemens C7F2 four Sight four-dimensional ultrasound transducer.* Ultrasound in Medicine and Biology, 2008. **34**(8): p. 1307–1316.

109. Varghese, T., J. Zagzebski, and F. Lee, *Elastographic imaging of thermal lesions in the liver in vivo following radiofrequency ablation: preliminary results.* Ultrasound in Medicine and Biolology, 2002. **28**: p. 1467–1473.

110. Kallel, F., et al., *The feasibility of elastographic visualization of HIFU-induced thermal lesions in soft tissues.* Ultrasound in Medicine and Biology, 1999. **25**: p. 641–647.

111. Righetti, R., et al., *Elastographic characterization of HIFU-induced lesions in canine livers.* Ultrasound in Medicine and Biolology, 1999. **25**: p. 1099–1113.

112. Wu, T., et al., *Assessment of thermal tissue ablation with MR elastography.* Magnetic Resonance in Medicine, 2001. **45**: p. 80–87.

113. Souchon, R., et al., *Monitoring the formation of thermal lesions with heat-induced echo-strain imaging: A feasibility study.* Ultrasound in Medicine and Biology, 2005. **31**(2): p. 251-259.

114. Chenot, J., et al., *Intra-operative ultrasound hand-held strain imaging for the visualization of ablations produced in the liver with a toroidal HIFU transducer: first in vivo results.* Physics in Medicine and Biology, 2010. **55**(11): p. 3131-3144.

115. Arnal, B., M. Pernot, and M. Tanter, *Monitoring of Thermal Therapy Based on Shear Modulus Changes: II. Shear Wave Lesion Imaging of Thermal Lesions.* IEEE Transaction on Ultrasonics, Ferroelectronics, Frequency Control, 2011. **58**(8): p. 1603-1611.

116. Thittai, A.K., B. Galaz, and J. Ophir, *Visualization of Hifu-Induced Lesion Boundaries by Axial-Shear Strain Elastography: A Feasibility Study.* Ultrasound in Medicine and Biology, 2011. **37**(3): p. 426-433.

117. Fry, W.J., et al., *Production of Focal Destructive Lesions in the Central Nervous System with Ultrasound.* Journal of Neurosurgery, 1954. **11**(5): p. 471-478.

118. Warwick, R. and J. Pond, *Trackless Lesions in Nervous Tissues Produced by High Intensity Focused Ultrasound (High-Frequency Mechanical Waves).* Journal of Anatomy., 1968. **102**: p. 387-405.

119. Basauri, L. and P.P. Lele, *A simple method for production of trackless focal lesions with focused ultrasound: statistical evaluation of the effects of irradiation on the central nervous system of the cat.* . Journal of Physiology., 1962. **160**(3): p. 513–534.

120. Gellermann, J., et al., *Methods and potentials of magnetic resonance imaging for monitoring radiofrequency hyperthermia in a hybrid system.* International Journal of Hyperthermia, 2005. **21**(6): p. 497-513.

121. Parsons, J.E., et al., *Pulsed cavitational ultrasound therapy for controlled tissue homogenization.* Ultrasound in Medicine and Biology., 2006. **32**: p. 115-129.

122. Kieran, K., et al., *Refining histotripsy: Defining the parameter space for the creation of nonthermal lesions with high intensity, pulsed focused ultrasound of the in vitro kidney.* Journal of Urology., 2007. **178**: p. 672–676.

123. Roberts, W., et al., *Pulsed cavitational ultrasound: a noninvasive technology for controlled tissue ablation (histotripsy) in the rabbit kidney.* Journal of Urology., 2006. **175**(2): p. 734–738.

124. Mitri, F., et al., *Prostate cryotherapy monitoring using vibroacoustography: Preliminary results of an ex vivo study and technnical feasibility.* IEEE Transaction on Biomedical Engineering, 2008. **55**: p. 2584–2592.

125. Vallancien, G., et al., *Focused extracorporeal pyrotherapy: Feasibility study in man.* Endourology, 1992. **6**: p. 173-181.

126. Wu, F., W. Chen, and J. Bai, *Effect of high-intensity focused ultrasound on patients with hepatocellular cancer–preliminary report.* Chinese Journal of Ultrasonogy, 1999. **8**: p. 213-216.

127. Li, C.X., et al., *Analysis of clinical effect of high-intensity focused ultrasound on liver cancer.* World Journal of Gastroenterology, 2004. **10**(15): p. 2201-2204.

128. Wu, F., et al., *Advanced hepatocellular carcinoma: Treatment with highintensity focused ultrasound ablation combined with transcatheter arterial embolization.* Radiology, 2005. **235**(5): p. 659-667.

129. Wu, F., et al., *Extracorporeal high intensity focused ultrasound treatment for patients with breast cancer.* Breast Cancer Research and Treatment, 2005. **92**(1): p. 51-60.

130. Kiss, M.Z., D.M. J., and T. Varghese, *Investigation of Temperature-Dependent Viscoelastic Properties of Thermal Lesions in ex vivo Animal Liver Tissue.* Journal of Biomechanics, 2009. **42**: p. 959-966.

131. Fahey, B.J., et al., *Acoustic radiation force impulse imaging of thermally- and chemically-induced lesions in soft tissues: Preliminary ex vivo results.* Ultrasound in Medicine and Biology, 2004. **30**: p. 321–328.

132. Maleke, C. and E.E. Konofagou, *Harmonic motion imaging for focused ultrasound (HMIFU): A fully integrated technique for sonication and monitoring of thermal ablation in tissues.* Physics in Medicine and Biology, 2008. **53**: p. 1773–1793.

133. Lewa, C.J., *Magnetic-resonance-imaging in the presence of mechanical waves.* Spectroscopy Letters, 1991. **24**(1): p. 55-67.

134. Multhupillai R., L.D., Rossman PJ., Greenleaf JF., Manduca A., RL Ehman, *Magnetic resonance elastography by direct visualization of propagating acoustic strain waves.* Science, 2001. **269**(5232): p. 1854-1857.

135. Kruse SA, S.J., Lawrence AJ, Dresner MA, Manduca A, Greenleaf JF, Ehman RL, *Tissue characterization using magnetic resonance elastography: preliminary results.* Physics in Medicine and Biology, 2000. **45**(6): p. 1579-1590.

136. Wu, T., et al., *Assessment of thermal tissue ablation with MR elastography.* Magnetic Resonance in Medicine, 2001. **45**(1): p. 80-87.

137. Parker, K.J., et al., *Tissue response to mechanical vibrations for Sonoelasticity Imaging.* Ultrasound in Medicine and Biology, 1990. **16**: p. 241-246.

138. Righetti, R., et al., *Elastographic characterization of HIFU-induced lesions in canine livers.* Ultrasound in Medicine and Biology, 1999. **25**(7): p. 1099-1113.

139. Shi, X.G., et al., *Detection of high-intensity focused ultrasound liver lesions using dynamic elastometry.* Ultrasonic Imaging, 1999. **21**(2): p. 107-126.

140. Ophir, J., et al., *Elastography: A quantitative method for imaging the elasticity of biological tissues.* Ultrasonic Imaging, 1991. **13**(2): p. 111--134.

141. Curiel, L., et al., *Elastography for the follow-up of high-intensity focused ultrasound prostate cancer treatment: Initial comparison with MRI.* Ultrasound in Medicine and Biology, 2005. **31**(11): p. 1461-1463.

142. Stafford, R.J., et al., *Elastographic imaging of thermal lesions in soft tissue: A preliminary study in vitro.* Ultrasound in Medicine and Biology, 1998. **24**(9): p. 1449-1458.

143. Kallel, F., et al., *The feasibility of elastographic visualization of HIFU-induced thermal lesions in soft tissues.* Ultrasound in Medicine and Biology, 1999. **25**(4): p. 641-647.

144. Bharat, S., et al., *Monitoring stiffness changes in lesions after radiofrequency ablation at different temperatures and durations of ablation.* Ultrasound in Medicine and Biology, 2005. **31**(3): p. 415-422.

145. Souchon, R., et al., *Visualisation of hifu lesions using elastography of the human prostate in vivo: Preliminary results.* Ultrasound in Medicine and Biology, 2003. **29**(7): p. 1007-1015.

146. Chenot, J., et al., *Intra-operative ultrasound hand-held strain imaging for the visualization of ablations produced in the liver with a toroidal HIFU transucer: first in vivo results.* Physics in Medicine and Biology, 2010. **55**(11): p. 3131-3144.

147. Fatemi, M. and J.F. Greenleaf, *Ultrasound-stimulated vibro-acoustic spectrography.* Science, 1998. **280**(5360): p. 82-85.

148. Nightingale, K.R., et al., *On the feasibility of remote palpation using acoustic radiation force.* Journal of the Acoustical Society of America, 2001. **110**(1): p. 625-634.

149. Fahey, B.J., et al., *Acoustic radiation force impulse imaging of thermally- and chemically-induced lesions in soft tissues: Preliminary ex vivo results.* Ultrasound in Medicine and Biology, 2004. **30**(3): p. 321-328.

150. Fahey, B.J., et al., *Liver ablation guidance with acoustic radiation force impulse imaging: challenges and opportunities.* Physics in Medicine and Biology, 2006. **51**(15): p. 3785-3808.

151. Bing, K.F., et al., *Combined Ultrasonic Thermal Ablation with Interleaved ARFI Image Monitoring Using a Single Diagnostic Curvilinear Array: A Feasibility Study.* Ultrasonic Imaging, 2011. **33**(4): p. 217-232.

152. Arnal, B., M. Pernot, and M. Tanter, *Monitoring of Thermal Therapy Based on Shear Modulus Changes: I. Shear Wave Thermometry.* IEEE Transactions on Ultrasonics, Ferroelectrics, and frequency control, 2011. **58**(2): p. 369-378.

153. Arnal, B., M. Pernot, and M. Tanter, *Monitoring of Thermal Therapy Based on Shear Modulus Changes: II. Shear Wave Imaging of Thermal Lesions.* IEEE Transactions on Ultrasonics, Ferroelectrics, and Frequency control, 2011. **58**(8): p. 1603-1611.

154. Maleke, C. and E.E. Konofagou, *Harmonic motion imaging for focused ultrasound (HMIFU): a fully integrated technique for sonication and monitoring of thermal ablation in tissues.* Physics in Medicine and Biology, 2008. **53**(6): p. 1773-1793.

155. Maleke, C., M. Pernot, and E.E. Konofagou, *A Single-element focused ultrasound transducer method for harmonic motion imaging.* Ultrasonic Imaging, 2006. **28**(3): p. 144-158.

156. Curiel, L., R. Chopra, and K. Hynynen, *In vivo monitoring of focused ultrasound surgery using local harmonic motion.* Ultrasound in Medicine and Biology, 2009. **35**(1): p. 65-78.

157. Maleke, C. and E.E. Konofagou, *In vivo feasibility of real-time monitoring of focused ultrasound surgery (FUS) using Harmonic Motion Imaging (HMI).* IEEE Transactions on Biomedical Engineering, 2009. **57**(1): p. 7-11.

158. Konofagou, E., J. Thierman, and K. Hynynen, *The use of ultrasound-stimulated acoustic emission in the monitoring of modulus changes with temperature.* Ultrasonics, 2003. **41**(5): p. 337-345.

159. Maleke, C., et al., *Simulation study of amplitude-modulated (AM) harmonic motion imaging (HMI) for stiffness contrast quantification with experimental validation.* Ultrasonic Imaging, 2010. **32**(3): p. 154-76.

160. Heikkila, J., L. Curiel, and K. Hynynen, *Local harmonic motion monitoring of focused ultrasound surgery--a simulation model.* IEEE Transaction on Biomedical Engineering, 2010. **57**(1): p. 185-93.

161. Konofagou, E.E., et al., *Estimating localized oscillatory tissue motion for assessment of the underlying mechanical modulus.* Ultrasonics, 2004. **42**(1-9): p. 951-6.

162. Maleke, C., et al., *Simulation Study of Amplitude-Modulated (AM) Harmonic Motion Imaging (HMI) for Stiffness Contrast Quantification with Experimental Validation.* Ultrasonic Imaging, 2010. **32**(3): p. 154-176.

163. Soneson, J.E. *A User-Friendly Software Package for HIFU Simulation*. in *8th* International Symposim on Therapeutic Ultrasound. 2009. AIP Conference Proceedings.

164. Zabolotskaya, E. and R.V. Khokhlov, *Quasi-planes waves in the nonlinear acoustic of confined beam.* Soviet Physics Acoustics-Ussr, 1969. **15**(1): p. 35-40.

165. Marquet, F., *Echographic methods of correcting and monitoring therapeutic treatments using high-intensity focused ultrasound*, in *Langevin Institute*2009, Univeristy Paris VII: Paris.

166. Goodman, J., *Statistical Optics*1985, New York: Wiley-Interscience.

167. Duck, F.A., ed. *Physical Properties of Tissue. A Comprehensive Reference Book*. 1990, Academic Press: San Diego. 346.

168. Lu, Z.F., et al., *Ultrasound attenuation and backscatter in the liver during prednisone administration.* Ultrasound in Medicine and Biology, 1997. **23**(1): p. 1-8.

169. Lee, Y.S., *Numerical solution of the KZK equation for pulsed finite amplitude sound beams in thermoviscous fluids*, in *Mechanical Engineering*1986, University of Texas: Austic. p. 216.

170. Canney, M.S., et al., *Acoustic characterization of high intensity focused ultrasound fields: A combined measurement and modeling approach.* Journal of the Acoustical Society of America, 2008. **124**(4): p. 2406-2420.

171. Nyborg, W.L., *Acoustic Streaming near a Boundary.* Journal of the Acoustical Society of America, 1958. **30**(4): p. 329-339.

172. Palmeri, M.L., et al., *A finite-element method model of soft tissue response to impulsive acoustic radiation force.* IEEE Transactions on Ultrasonics Ferroelectrics and Frequency Control, 2005. **52**(10): p. 1699-1712.

173. Palmeri, M.L. and K.R. Nightingale, *Acoustic radiation force-based elasticity imaging methods.* Interface Focus, 2011. **1**(4): p. 553-564.

174. Zhang, M., et al., *Real-time sonoelastography of hepatic thermal lesions in a swine model.* Medical Physics, 2010. **35**(9): p. 4132-4141.

175. Bamber, J.C. and R.J. Dickinson, *Ultrasoonic B-scanning - A computer - simulation.* Physics in Medicine and Biology, 1980. **25**(3): p. 463-479.

176. Seggie, D.A., S. Leeman, and R.E. Burge. *Realistic Simulation of B-Scan Images*. in *Proc IEEE Ultrasonics Symp*. 1983. Atlanta, GA.

177. Luo, J.W. and E.E. Konofagou, *A Fast Normalized Cross-Correlation Calculation Method for Motion Estimation.* IEEE Transactions on Ultrasonics, Ferroelectrics, and Frequency Control, 2010. **57**(6): p. 1347-1357.

178. Fleury, G., et al., *New piezocomposite transducers for therapeutic ultrasound*, in *2nd International Symposium on Therapeutic Ultrasound*2002: Seattle, U.S.A.

179. Smith, W.A., A.A. Shaulov, and B.A. Auld, *Design of Piezocomposites for Ultrasonic Transducers.* Ferroelectrics, 1989. **91**: p. 155-162.

180. Hou, G.Y., et al. *Simulation of HMIFU (Harmonic Motion Imaging for Focused Ultrasound) with in-vitro validation*. in *Bioengineering Conference, Proceedings of the 2010 IEEE 36th Annual Northeast*. 2010.

181. Kun, G. and M.X. Wan, *A comparison of HIFU-induced lesion size measurement based on gross histological examination and image of bovine thigh in vitro.* Ultrasonics, 2005. **43**(5): p. 351-355.

182. Vappou, J., C. Maleke, and E.E. Konofagou, *Quantitative viscoelastic parameters measured by Harmonic Motion Imaging.* Physics in Medicine and Biology, 2009. **54**(11): p. 3579-3594.

183. Vappou, J., et al., *Measuring elastic properties of biological tissues by using Focused Ultrasound-based internal indentation. (In preparation)*, 2014.

184. Kallel, F. and J. Ophir, *A least squares estimator for elastography.* Ultrasonic Imaging, 1997. **19**: p. 195-208.

185. Smith, D.N., et al., *MRI guided focused ultrasound surgery (FUS) of fibroadenomas in the breast.* Radiology, 2000. **217**: p. 268-268.

186. Nandlall, S.D., E. Jackson, and C.C. Coussios, *Real-Time Passive Acoustic Monitoring of Hifu-Induced Tissue Damage.* Ultrasound in Medicine and Biology, 2011. **37**(6): p. 922-934.

187. Anand, A. and P.J. Kaczkowski, *Monitoring formation of high intensity focused ultrasound (HIFU) induced lesions using backscattered ultrasound.* Acoustics Research Letters Online-Arlo, 2004. **5**(3): p. 88-94.

188. Maleke, C. and E.E. Konofagou, *In Vivo Feasibility of Real-Time Monitoring of Focused Ultrasound Surgery (FUS) Using Harmonic Motion Imaging (HMI).* IEEE Transactions on biomedical Engineering, 2010. **57**(1): p. 7-11.

189. Maleke, C., M. Pernot, and E.E. Konofagou, *Single-element focused ultrasound transducer method for harmonic motion imaging.* Ultrasonic Imaging, 2006. **28**(3): p. 144-158.

190. Bailey, M.R., et al., *Physical mechanisms of the therapeutic effect of ultrasound - (A review).* Acoustical Physics, 2003. **49**(4): p. 369-388.

191. Khokhlova, T.D., et al., *Magnetic resonance imaging of boiling induced by high intensity focused ultrasound.* Journal of the Acoustical Society of America, 2009. **125**(4): p. 2420-2431.

192. Ter Haar, G., et al., *High-Intensity Focused Ultrasound for the Treatment of Rat-Tumors.* Physics in Medicine and Biology, 1991. **36**(11): p. 1495-1501.

193. Wu, F., et al., *Pathological changes in human malignant carcinoma treated with high-intensity focused ultrasound.* Ultrasound in Medicine and Biology, 2001. **27**(8): p. 1099-1106.

194. Wu, F., et al., *Changes in biologic characteristics of breast cancer treated with high-intensity focused ultrasound.* Ultrasound Med Biol, 2003. **29**(10): p. 1487-92.

195. Chen, L.L., et al., *Histological study of normal and tumor-bearing liver treated with focused ultrasound.* Ultrasound in Medicine and Biology, 1999. **25**(5): p. 847-856.

196. Chen, L.L., et al., *Histological-Changes in Rat-Liver Tumors Treated with High-Intensity Focused Ultrasound.* Ultrasound in Medicine and Biology, 1993. **19**(1): p. 67-74.

197. Jensen, C.R., et al., *Spatiotemporal Monitoring of High-Intensity Focused Ultrasound Therapy with Passive Acoustic Mapping.* Radiology, 2012. **262**(1): p. 252-261.

198. Marquet, F., et al. *Boiling Effects on the Performance of Harmonic Motion Imaging for Focused Ultrasound*. in *IEEE International Ultrasonics Symposium*. 2012. Dresden, Germany.

199. Hou, G.Y., et al., *Optimization of Real-Time Acoustical and Mechanical Monitoring of High Intensity Focused Ultrasound (HIFU) treatment using Harmonic Motion Imaging for High Intensity Focused Ultrasound (HMIFU) (In preparation).* 2013.

200. Hou, G., et al., *Optimization of Real-Time Acoustical and Mechanical Monitoring of High Intensity Focused Ultrasound (HIFU) treatment using Harmonic Motion Imaging for High Intensity Focused Ultrasound (HMIFU)*, in *35th Annual International Conference of the IEEE Engineering in Medicine and Biology Society*2013: Osaka, Japan.

201. Wang, S.T., V. Frenkel, and V. Zderic, *Optimization of pulsed focused ultrasound exposures for hyperthermia applications.* Journal of the Acoustical Society of America, 2011. **130**(1): p. 599-609.

202. Sapin-de Brosses, E., et al., *Temperature dependence of the shear modulus of soft tissues assessed by ultrasound.* Physics in Medicine and Biology, 2010. **55**(6): p. 1701-1718.

203. Sapin-de Brosses, E., M. Pernot, and M. Tanter, *The link between tissue elasticity and thermal dose in vivo.* Physics in Medicine and Biology, 2011. **56**(24): p. 7755-7765.

204. Hou, G.Y., et al., *Performance Assessment of Hifu Lesion Detection by Harmonic Motion Imaging for Focused Ultrasound (Hmifu): A 3-D Finite-Element-Based Framework with Experimental Validation.* Ultrasound in Medicine and Biology, 2011. **37**(12): p. 2013-2027.

205. Shahmirzadi, D., G.Y. Hou, and E.E. Konofagou, *Ex Vivo Characterization of Canine Liver Tissue Viscoelasticity Following High Intensity Focused Ultrasound (HIFU) Ablation.* Ultrasound in Medicine and Biology, 2012.

206. Kiss, M.Z., M.J. Daniels, and T. Varghese, *Investigation of temperature-dependent viscoelastic properties of thermal lesions in ex vivo animal liver tissue.* Journal of Biomechanics, 2009. **42**(8): p. 959-966.

207. Damianou, C.A., et al., *Dependence of ultrasonic attenuation and absorption in dog soft tissues on temperature and thermal dose.* Journal of the Acoustical Society of America, 1997. **102**(1): p. 628-634.

208. Sokka, S.D., R. King, and K. Hynynen, *MRI-guided gas bubble enhanced ultrasound heating in in vivo rabbit thigh.* Physics in Medicine and Biology, 2003. **48**(2): p. 223-241.

209. Hou, G.Y., et al., *Performance optimization of High Intensity Focused Ultrasound (HIFU) treatment monitoring using Harmonic Motion Imaging for Focused Ultrasound (HMIFU).* Physics in Medicine and Biology, 2012.

210. Coussios, C.C., et al., *Role of acoustic cavitation in the delivery and monitoring of cancer treatment by high-intensity focused ultrasound (HIFU) (vol 23, pg 105, 2007).* International Journal of Hyperthermia, 2007. **23**(3): p. 327-327.

211. Zhang, S.Y., et al., *Dynamic Changes of Integrated Backscatter, Attenuation Coefficient and Bubble Activities during High-Intensity Focused Ultrasound (Hifu) Treatment.* Ultrasound in Medicine and Biology, 2009. **35**(11): p. 1828-1844.

212. Zhou, Y. and X. Wilson Gao, *Variations of bubble cavitation and temperature elevation during lesion formation by high-intensity focused ultrasound.* The Journal of the Acoustical Society of America, 2013. **134**(2): p. 1683-94.

213. Jensen, C.R., R.O. Cleveland, and C.C. Coussios, *Real-time temperature estimation and monitoring of HIFU ablation through a combined modeling and passive acoustic mapping approach.* Physics in Medicine and Biology, 2013. **58**(17): p. 5833-50.

214. Sapin-De Brosses, E., et al., *Subject-specific numerical estimation of the temporomandibular joint reaction force during mouth opening and closing movements.* Computer Methods in Biomechanics and Biomedical Engineering, 2011. **14**: p. 125-127.

215. Delannoy, B., et al., *Acoustical Image-Reconstruction in Parallel-Processing Analog Electronic Systems.* Journal of Applied Physics, 1979. **50**(5): p. 3153-3159.

216. Shattuck, D.P., et al., *Explososcan - a Parallel Processing Technique for High-Speed Ultrasound Imaging with Linear Phased-Arrays.* Journal of the Acoustical Society of America, 1984. **75**(4): p. 1273-1282.

217. Smith, S.W., H.G. Pavy, and O.T. Vonramm, *High-Speed Ultrasound Volumetric Imaging-System .1. Transducer Design and Beam Steering.* IEEE Transactions on Ultrasonics, Ferroelectrics, and Frequency Control, 1991. **38**(2): p. 100-108.

218. Vonramm, O.T., S.W. Smith, and H.G. Pavy, *High-Speed Ultrasound Volumetric Imaging-System .2. Parallel Processing and Image Display.* IEEE Transactions on Ultrasonics Ferroelectrics and Frequency Control, 1991. **38**(2): p. 109-115.

219. Montaldo, G., et al., *Coherent Plane-Wave Compounding for Very High Frame Rate Ultrasonography and Transient Elastography.* IEEE Transactions on Ultrasonics, Ferroelectrics, and Frequency Control, 2009. **56**(3): p. 489-506.

220. Hasegawa, H. and H. Kanai, *High-frame-rate echocardiography using diverging transmit beams and parallel receive beamforming.* Journal of Medical Ultrasonics, 2011. **38**(3): p. 129-140.

221. Provost, J., et al., *Electromechanical wave imaging for arrhythmias.* Physics in Medicine and Biology, 2011. **56**(22): p. L1-L11.

222. Sandrin, L., et al., *Time-resolved 2D pulsed elastography. Experiments on tissue-equivalent phantoms and breast in-vivo.* Medical Imaging 2001: Ultrasonic Imaging and Signal Processing, 2001. **2**(30): p. 120-126.

223. Li, Y.F. and P.C. Li, *Software Beamforming: Comparison between a Phased Array and Synthetic Transmit Aperture.* Ultrasonic Imaging, 2011. **33**(2): p. 109-118.

224. Chang, L.W., K.H. Hsu, and P.C. Li, *Graphics Processing Unit-Based High-Frame-Rate Color Doppler Ultrasound Processing.* IEEE Transactions on Ultrasonics, Ferroelectrics, and Frequency Control, 2009. **56**(9): p. 1856-1860.

225. Hansen, J.M., D. Schaa, and J.A. Jensen, *Synthetic aperture beamformation using the GPU,* Ultrasonics Symposium (IUS), 2011: p. 373-376.

226. Yiu, B.Y.S., I.K.H. Tsang, and A.C.H. Yu, *Real-Time GPU-Based Software Beamformer Designed for Advanced Imaging Methods Research.* 2010 IEEE International Ultrasonics Symposium Proceedings, 2010: p. 1920-1923.

227. Choe, J.W., et al., *GPU-Based Real-Time Volumetric Ultrasound Image Reconstruction for a Ring Array.* IEEE Transactions on Medical Imaging, 2013. **32**(7): p. 1258-1264.

228. Rosenzweig, S., M. Palmeri, and K. Nightingale, *GPU-Based Real-Time Small Displacement Estimation With Ultrasound.* IEEE transactions on ultrasonics ferroelectrics and frequency control, 2011. **58**(2): p. 399-405.

229. Yang, X., S. Deka, and R. Righetti, *A Hybrid CPU- GPGPU Approach for Real-Time Elastography.* IEEE Transactions on Ultrasonics Ferroelectrics and Frequency Control, 2011. **58**(12): p. 2631-2645.

230. Hyun, D., G.E. Trahey, and J. Dahl, *A GPU-based real-time spatial coherence imaging system* SPIE Proceedings, 2013. **8675**.

231. Thomenius, K.E., *Evolution of ultrasound beamformers.* 1996 IEEE Ultrasonics Symposium, Proceedings, Vols 1 and 2, 1996: p. 1615-1622.

232. Hall, T.J., et al., *Phantom materials for elastography.* IEEE Transactions on Ultrasonics, Ferroelectrics, and Frequency Control, 1997. **44**(6): p. 1355-1365.

233. Hou, G.Y., et al., *Multi-parametric monitoring and assessment of High Intensity Focused Ultrasound (HIFU) boiling by Harmonic Motion Imaging for Focused Ultrasound (HMIFU): An ex vivo feasibility study.* Physics in Medicine and Biology (in press), 2013.

234. Hidalgo, M., *Pancreatic Cancer.* New England Journal of Medicine, 2010. **362**(17): p. 1605-1617.

235. Vincent, A., et al., *Pancreatic cancer.* Lancet, 2011. **378**(9791): p. 607-620.

236. Westphalen, C.B. and K.P. Olive, *Genetically Engineered Mouse Models of Pancreatic Cancer.* Cancer Journal, 2012. **18**(6): p. 502-510.

237. Rauchwerger, D.R., et al., *Equilibrative-sensitive nucleoside transporter and its role in gemcitabine sensitivity.* Cancer Research, 2000. **60**(21): p. 6075-6079.

238. Olive, K.P., et al., *Inhibition of Hedgehog Signaling Enhances Delivery of Chemotherapy in a Mouse Model of Pancreatic Cancer.* Science, 2009. **324**(5933): p. 1457-1461.

239. Khokhlova, T.D. and J.H. Hwang, *HIFU for palliative treatment of pancreatic cancer.* Journal of gastrointestinal oncology, 2011. **2**(3): p. 175-84.

240. He SX, W.G., *The noninvasive treatment of 251 cases of advanced pancreatic ancer with focused ultrasound surgery*, in *2nd International Symposium on Therapeutic Ultrasound* 2002. p. 51-56.

241. Hwang, J.H., et al., *Preclinical in Vivo Evaluation of an Extracorporeal Hifu Device for Ablation of Pancreatic Tumors.* Ultrasound in Medicine and Biology, 2009. **35**(6): p. 967-975.

242. Liu, C.X., et al., *A Preclinical in Vivo Investigation of High-Intensity Focused Ultrasound Combined with Radiotherapy.* Ultrasound in Medicine and Biology, 2011. **37**(1): p. 69-77.

243. Lee, E.S., et al., *Pulsed High-Intensity Focused Ultrasound Enhances Apoptosis of Pancreatic Cancer Xenograft with Gemcitabine.* Ultrasound in Medicine and Biology, 2013. **39**(11): p. 1991-2000.

244. Olive, K.P. and D.A. Tuveson, *The use of targeted mouse models for preclinical testing of novel cancer therapeutics.* Clinical Cancer Research, 2006. **12**(18): p. 5277-5287.

245. Jiménez, N., et al., *Nonlinear acoustics FDTD simulation of radiation force fields in soft tissue under HIFU treatment monitoring using HMIFU* 2013.

246. Oudry, J., et al., *Copolymer-in-Oil Phantom Materials for Elastography.* Ultrasound in Medicine and Biology, 2009. **35**(7): p. 1185-1197.

247. Hou, G.Y., et al., *Ex vivo and In vivo performance validation of a 2D pre-clinical HIFU treatment monitoring system using Harmonic Motion Imaging for Focused Ulrasound (HMIFU).* IEEE Transactions on Biomedical Engineering, 2013.

248. Casper, A.J., et al., *Real-Time Implementation of a Dual-Mode Ultrasound Array System: In Vivo Results.* IEEE Transactions on Biomedical Engineering, 2013. **60**(10): p. 2751-2759.

249. Rasmussen, M.F., et al., *Preliminary comparison of 3D synthetic aperture imaging with Explososcan.* Medical Imaging 2012: Ultrasonic Imaging, Tomography, and Therapy, 2012. **8320**.

250. Provost, J., et al., *Single-heartbeat electromechanical wave imaging with optimal strain estimation using temporally unequispaced acquisition sequences.* Physics in Medicine and Biology, 2012. **57**(4): p. 1095-1112.

251. Choe, J.W., et al., *Volumetric Real-Time Imaging Using a CMUT Ring Array.* IEEE Transactions on Ultrasonics Ferroelectrics and Frequency Control, 2012. **59**(6): p. 1201-1211.

252. Fung, Y.C.B., *Elasticity of Soft Tissues in Simple Elongation.* American Journal of Physiology, 1967. **213**(6): p. 1532-&.

253. Holzapfel, G.A., T.C. Gasser, and R.W. Ogden, *A new constitutive framework for arterial wall mechanics and a comparative study of material models.* Journal of Elasticity, 2000. **61**(1-3): p. 1-48.

254. Sakuma, I., et al., *In vitro measurement of mechanical properties of liver tissue under compression and elongation using a new test piece holding method with surgical glue.* Surgery Simulation and Soft Tissue Modeling, Proceedings, 2003. **2673**: p. 284-292.

255. Haslach, H.W., *Nonlinear viscoelastic, thermodynamically consistent, models for biological soft tissue.* Biomechanics and Modeling in Mechanobiology, 2005. **3**(3): p. 172-189.

256. Klatt, D., et al., *Noninvasive assessment of the rheological behavior of human organs using multifrequency MR elastography: a study of brain and liver viscoelasticity.* Physics in Medicine and Biology, 2007. **52**(24): p. 7281-7294.

257. Green, M.A., L.E. Bilston, and R. Sinkus, *In vivo brain viscoelastic properties measured by magnetic resonance elastography.* Nmr in Biomedicine, 2008. **21**(7): p. 755-764.

258. Atay, S.M., et al., *Measurement of the dynamic shear modulus of mouse brain tissue in vivo by magnetic resonance elastography.* Journal of Biomechanical Engineering-Transactions of the ASME, 2008. **130**(2).

259. Pattison, A.J., et al., *Time-harmonic magnetic resonance elastography of the normal feline brain.* Journal of Biomechanics, 2010. **43**(14): p. 2747-2752.

260. Vappou, J., et al., *Assessment of in vivo and post-mortem mechanical behavior of brain tissue using magnetic resonance elastography.* Journal of Biomechanics, 2008. **41**(14): p. 2954-2959.

261. Jenkyn, T.R., R.L. Ehman, and K.N. An, *Noninvasive muscle tension measurement using the novel technique of magnetic resonance elastography (MRE).* Journal of Biomechanics, 2003. **36**(12): p. 1917-1921.

262. Domire, Z.J., et al., *Feasibility of Using Magnetic Resonance Elastography to Study the Effect of Aging on Shear Modulus of Skeletal Muscle.* Journal of Applied Biomechanics, 2009. **25**(1): p. 93-97.

263. Gennisson, J.L., et al., *Human muscle hardness assessment during incremental isometric contraction using transient elastography.* Journal of Biomechanics, 2005. **38**(7): p. 1543-1550.

264. Schmitt, C., A.H. Henni, and G. Cloutier, *Characterization of blood clot viscoelasticity by dynamic ultrasound elastography and modeling of the rheological behavior.* Journal of Biomechanics, 2011. **44**(4): p. 622-629.

265. Deffieux, T., et al., *Shear Wave Spectroscopy for In Vivo Quantification of Human Soft Tissues Visco-Elasticity.* IEEE Transactions on Medical Imaging, 2009. **28**(3): p. 313-322.

266. Palmeri, M.L., et al., *Quantifying hepatic shear modulus in vivo using acoustic radiation force.* Ultrasound in Medicine and Biology, 2008. **34**(4): p. 546-558.

267. Zhai, L., et al., *An integrated indenter-ARFI imaging system for tissue stiffness quantification.* Ultrasonic Imaging, 2008. **30**(2): p. 95-111.

268. Chen, S.G., et al., *Shearwave Dispersion Ultrasound Vibrometry (SDUV) for Measuring Tissue Elasticity and Viscosity.* IEEE Transactions on Ultrasonics, Ferroelectrics, and Frequency Control, 2009. **56**(1): p. 55-62.

269. Oliver, W.C. and G.M. Pharr, *An Improved Technique for Determining Hardness and Elastic-Modulus Using Load and Displacement Sensing Indentation Experiments.* Journal of Materials Research, 1992. **7**(6): p. 1564-1583.

270. Nightingale, K., et al., *Acoustic radiation force impulse imaging: In vivo demonstration of clinical feasibility.* Ultrasound in Medicine and Biology, 2002. **28**(2): p. 227-235.

271. Sarvazyan, A.P., et al., *Shear wave elasticity imaging: A new ultrasonic technology of medical diagnostics.* Ultrasound in Medicine and Biology, 1998. **24**(9): p. 1419-1435.

272. Vappou, J., et al., *Dynamic viscoelastic shear properties of soft matter by magnetic resonance elastography using a low-field dedicated system.* Journal of Rheology, 2006. **50**(4): p. 531-541.

Appendices

Appendix A. Rheometry Mechanical Testing

After completion of the ablation, both unablated and ablated tissues were sectioned for mechanical testing using shear rheometry (TA Instrument, DE) (Figure 5.A1). A 6 mm biopsy punch was used to extract a total of 8 samples from the unablated tissues as well as 10 samples from the ablated tissues. First, a 5% compressional strain was applied on the samples to increase the shear surface grip between the tissue-fixture interfaces. The oscillatory shear test was performed by applying a periodic shear strain as follows:

$$\gamma(\omega) = \gamma_0 \sin(\omega t) = \gamma_0 \sin(2\pi f t)\ , \tag{1}$$

and measuring the resultant shear stress in the form of:

$$\tau(\omega) = \tau_0 \sin(\omega t + \delta) = \tau_0 \sin(2\pi f t + \delta)\ . \tag{2}$$

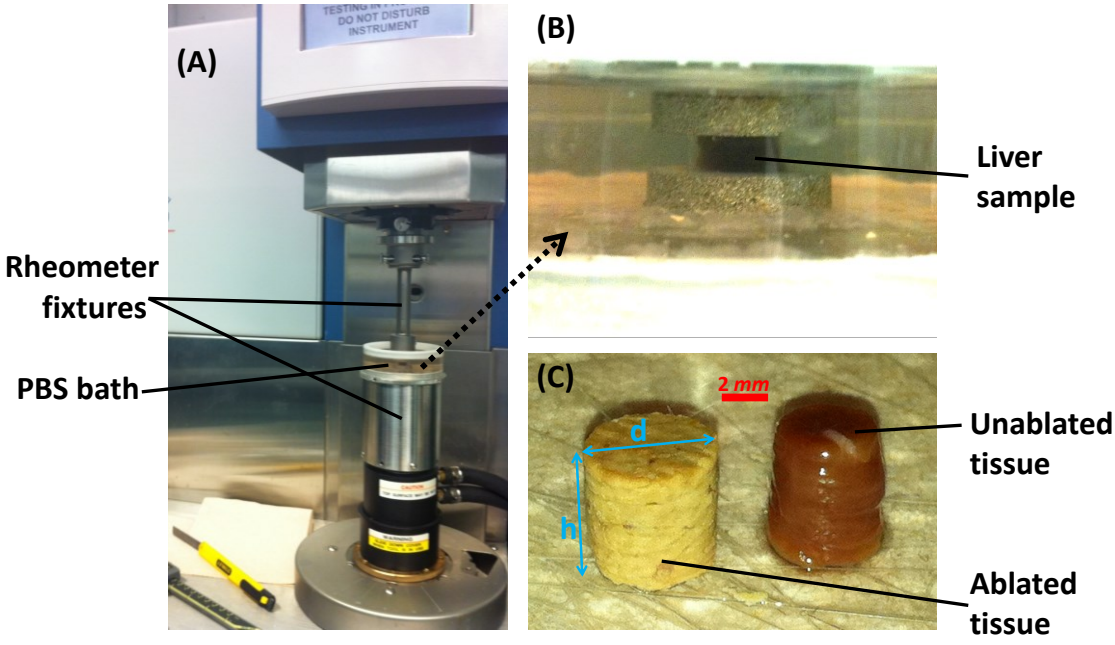

Figure A1. (A) The rheometer experimental set up used to characterize the viscoelastic properties of canine liver tissues *in vitro*. (B)Close up of the liver sample between the rheometer fixtures. (C)Representative biopsy samples from unablated and ablated canine liver tissues.

The applied shear strain was set at $\gamma_0 = 0.01$ with a frequency of 10Hz. The strain and stress magnitudes were used to calculate the complex shear modulus as following:

$$G^* = \frac{\tau}{\gamma}. \tag{3}$$

The complex shear modulus and phase shift were also used to compute the shear loss (viscous) modulus and storage (elastic) modulus as following, respectively:

$$G^{"} = G^* sin\delta = \frac{\tau_0}{\gamma_0} sin\delta\ , \tag{4}$$

$$G' = G^* cos\delta = \frac{\tau_0}{\gamma_0} cos\delta\ . \tag{5}$$

Additionally, the ratio of the viscosity to elasticity as represented by $tan\delta$, and the dynamic shear viscosity coefficient were calculated as following, respectively:

$$tan\delta = \frac{G^{"}}{G'}, \tag{6}$$

$$\eta = \frac{G^{"}}{\omega} = \frac{\tau_0}{\gamma_0 \omega} sin\delta\ . \tag{7}$$

Appendix B. Modulus estimation using Harmonic Motion Imaging (HMI)

Measuring material properties with noninvasive, nondestructive methods has always been a challenging field in materials science. For biological tissues, conventional mechanical testing methods are external and limited to either superficial tissues or to in vitro testing [252-255], and hence, do not allow to measure mechanical properties of major organs *in vivo*. This is a critical hurdle to overcome as underlying mechanical properties can often be used to diagnose disease and treatment conditions.

Elasticity Imaging is a research field that has been continuously expanding since its initial development more than two decades ago. The aim of such methods was initially to combine the principle of palpation with medical imaging modalities. As of today, this research field has been progressively expanding with development of numerous medical imaging modalities aim to estimate the mechanical properties of biological mediums. Additionally, the past research in this field has developed beyond the sole initial objective of diagnosis by palpation, and a large number of methods have been proposed that offer more complex applications. In particular, there has been increasing interest in the use of elasticity imaging methods in biomechanics, as they offer the valuable advantage of measuring mechanical properties *in vivo* in a noninvasive manner. Examples of the use of elasticity imaging methods for biomechanical applications include: Magnetic Resonance Elastography (MRE) for the determination of brain and liver tissue viscoelastic properties *in vivo* [256-258] evaluation of differences in elastic properties between brain tissue white and grey matter [259] and comparison between *in vivo* and post-mortem brain properties [260]; MRE for the measurement of skeletal muscle contraction and muscle stiffness changes with aging [261, 262]; Transient Elastography

to assess skeletal muscle stiffness during contraction [263]; Dynamic ultrasound elastography for the rheological characterization of blood clots [264]; Supersonic Shear Imaging (SSI) for the measurement of shear wave dispersion curves for characterization of soft tissues viscoelasticity[265]; Acoustic Radiation Force Impulse (ARFI) Imaging to evaluate stiffness of soft tissues such as liver *in vivo* [266], or *ex vivo* colon cancer specimen based on tissue relaxation characteristics following acoustic radiation force excitation [267] ; Shearwave Dispersion Ultrasound Vibrometry (SDUV) for investigation of *in vivo* viscoelastic properties in porcine liver [268]. In this chapter, an ultrasound-based method for the measurement of tissues elasticity is presented based on the principle of indentation.

Indentation is a widely used material testing method that allows to measure the Load-Displacement curve. Analytical solutions were proposed by Sneddon (Sneddon, 1965) in the case of penetration of axisymmetric indenters in an elastic half space. Based on these relationships, several methods have been proposed to derive the Young's modulus of the tested material. For example, as proposed by Oliver and Pharr [269], the Young's modulus can be estimated using a complex iterative procedure and calibration process. While indentation is commonly used for materials such as polymers and metallic samples, the application of such an experimental approach is limited *in vivo*, due to the external nature of indentation. In order to address this issue, we hereby propose a non-invasive internal indentation method that uses the acoustic radiation force resulting utilizing the simultaneous measurement of the resulting displacement from focused ultrasound. Moreover, this can be achieved with the basic principle of the Harmonic Motion Imaging (HMI) method [189]. A stiffness index equal to the ratio between the applied stress and the resulting uniaxial strain is defined as the HMI modulus (E_{HMI}). In order to validate the developed methodology, correlation between the HMI modulus and the actual

Young's modulus is evaluated both theoretically using numerical studies, and experimentally using a 1D and 2D imaging system on physical phantoms as well as biological specimens.

HMI and HMIFU are an ultrasound-based method that uses an amplitude modulated signal in order to generate an oscillating radiation force at the focal region using a focused ultrasound (FUS) transducer. The original objective of HMIFU was to constitute an all-in-one tool for tumor detection, characterization, targeting and monitoring of the thermal ablation. Within the small ellipsoidal-shape focal region composed of few millimeters in axial and millimeter or sub-millimeters in the lateral and elevational dimensions, a volumetric force oscillates at a single frequency within typically the 10-200Hz range. At the same time, an imaging transducer concentric and confocal with the FUS transducer allows to acquire ultrasound radiofrequency (RF) data. Displacements resulting from the oscillating acoustic radiation force are estimated by using cross-correlation techniques. Further details on the methods of HMIFU can be found in the method of both chapter 4 and 5.

Calculation of the 1D HMI Elastic Modulus

As mentioned in Chapter 2, the modulus estimation method is based on the localized, internal acoustic radiation force, instead of an external mechanical indenter, as the source of stress. In HMIFU, a focused ultrasound (FUS) transducer is used to generate an oscillating force at the focal region. The volumetric force can be measured experimentally as part of the transducer calibration, and its spatial profile can be therefore known. In the 1-D HMIFU system,

the resulting displacement is measured using the consecutive RF signals acquired by a pulse-echo transducer (f = 7.3 MHz). The general experimental setup is summarized in Figure B1.1(a).

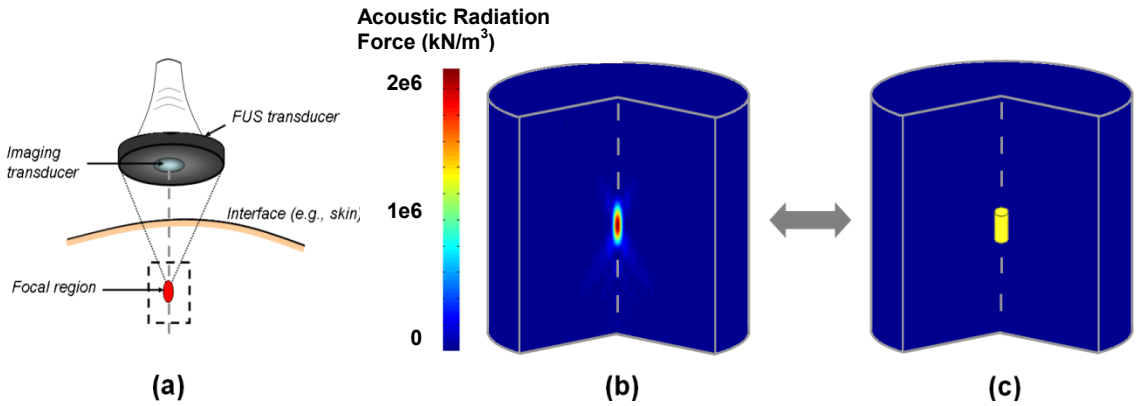

Figure B1.1. (a) General HMI setup, (b) actual distribution of the acoustic radiation force field, and (c) equivalent volumetric force modeled as uniform within the focal region[183].

In the proposed method, the focal region is modeled as a cylindrical region where the volumetric acoustic radiation force is uniform. This is an approximation since the actual radiation force has a well-defined spatial distribution (Figure B1.1 b,c). This cylindrical region is therefore assumed to act as an oscillating rigid piston. We propose to define the 1D HMI elastic moduli E_{HMI} as the ratio between the compressive stress $\sigma_{compression}$ experienced by the tissue exerted by the piston and the axial strain ε_{zz} measured in an infinitesimal volume located below the focal region (Figure B1.2):

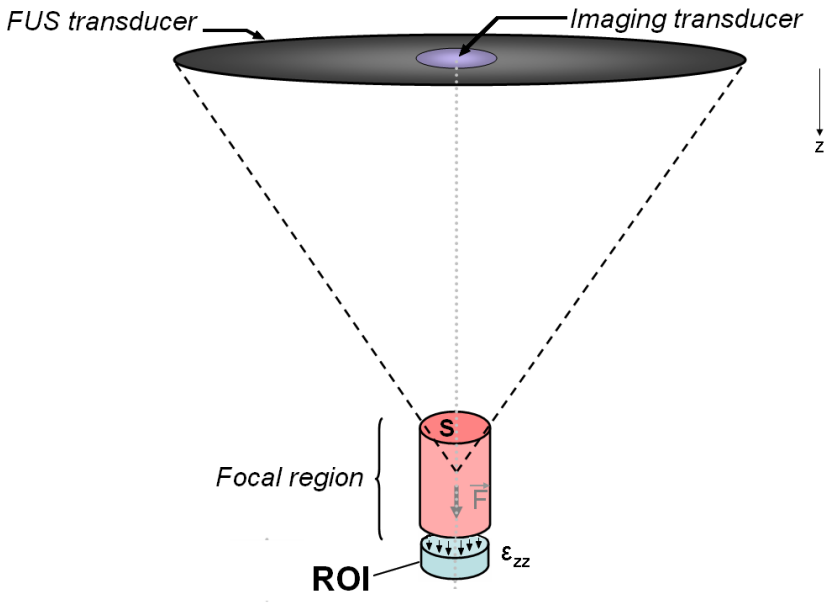

Figure B1.2. Summary of how the 1-D HMI modulus is calculated. Note that focal region is assumed to be a volumetric force distributed across a cylindrical piston-like shape in highlighted in pink.

$$E_{HMI}(t) = \frac{\sigma_{Compressio\ n}(t)}{\varepsilon_{zz}(t)} \quad (1)$$

where $\sigma_{compression}$ can be expressed as the total force exerted by the piston over the cross-sectional surface S of the focal region:

$$\sigma_{compressio\ n} = \frac{\iiint_{volume} f_v\, dV}{S} \quad (2)$$

where f_v is the volumetric acoustic radiation force within the focal region. The experimental setup used in this study is dynamic (hence, f_v is time-dependent). In this study, as a first

approximation, E_{HMI} is defined as the ratio of the maximum $\sigma_{compression}$ divided by the maximum measured strain ε_{zz} . E_{HMI} is therefore defined as:

$$E_{HMI} = \frac{\max(\sigma_{Compressio\ n})}{\max(\varepsilon_{zz})} (3)$$

This method requires knowledge of the acoustic radiation force. In this study, we used the experimental pressure profile obtained using a needle hydrophone in water, as described previously [188]. The corresponding 3D acoustic radiation force distribution was used as input in both simulations and experiments throughout the study. Acoustic radiation force f_{exp} was then calculated as:

$$f_{\exp} = \frac{2\alpha I}{c_s}, \quad (4)$$

where I is the acoustic intensity, c_s the speed of sound (c_s = 1530 m/s), and α the acoustic absorption of the medium. Absorption α was measured by transmission on the same polyacrylamide gels as those used in the phantom study. It was found to be equal to α=0.25 cm^{-1} at f=4.5 MHz. This value was chosen for the calculation of the input force for both finite-element and phantom studies. The absorption value for force calculation from *ex vivo* studies was chosen to be α=0.75 cm^{-1} at f =4.5 MHz based on previous literature [204].

The volumetric force distribution was modeled as a cylindrical region Ω inside which the volumetric force f_Ω was assumed to be uniform (hence acting as a rigid piston). The size of this region was chosen as the region outside which the volumetric force is inferior to one tenth of the maximum force, resulting in a region 3mm in height by 0.9mm in diameter. The uniform volumetric force f_Ω was calculated as the average of the actual experimentally measured volumetric force f_{exp} within Ω:

$$f_\Omega = \frac{\iiint_\Omega f_{\exp} dV}{V_\Omega}, \quad (5)$$

where V_Ω is the volume of the cylindrical region Ω. This f_Ω was used as input volumetric force in equation 2 for both simulations and experiments.

Materials and Methods for 1-D HMI Elastic Modulus Estimation

Numerical Study

For both Finite-element simulations were performed using a commercial software (Abaqus 6.8, Simulia, Providence, RI, USA). Initially, the accuracy of the assumption of having a uniform acoustic radiation force within the focal region was evaluated. Next, the correlation between the HMI modulus, E_{HMI}, and the actual Young's modulus, E, was estimated in homogeneous numerical phantoms. Finally, the influence of heterogeneity of the medium was evaluated. For all the studies, axisymmetric models were used, and the geometry of the medium was chosen as cylindrical (50 mm in height * 50 mm in diameter). The dynamic problem was

solved in an implicit scheme (time step=0.005 s, total duration = 1s). Excitation frequency was chosen to be f=10Hz in order to match the study frequency of rheometer. The focal region was set at the center of the axis of revolution (height = 10mm, radius = 2mm) with mesh refinement around this focal region.

1) Evaluation of the approximation of uniform radiation force distribution

In reality, the spatial distribution of the acoustic radiation force is non-uniform, although almost all of the energy is concentrated in the focal spot region. Here, we evaluate the error related to the assumption of uniformity. A homogeneous numerical phantom was used, where force profiles were implemented, namely, the actual experimental force and the resulting uniform equivalent force. The average strain values measured below the focus at the center line were compared. The Young's modulus of the medium was chosen to E=2kPa for the 1-D system parameters and E=10kPa for the 2-D system parameters.

2) Evaluation of the correlation between Young's modulus and HMI modulus

The Young's modulus E of the numerical phantom was varied (0.5kPa, 1kPa, 2kPa, 5kPa, 10kPa, 20kPa). For each case, the average strain in the center line was measured, allowing calculation of the HMI modulus. E_{HMI} was compared to the input E in each case.

3) Influence of Heterogeneity

We evaluated the influence of medium heterogeneity on the measurement of E_{HMI}. A spherical inclusion was embedded within the numerical phantom around the focal region. The background stiffness was fixed to $E_{background}$ = 1kPa while $E_{inclusion}$ = 10kPa. The diameter of the

inclusion was varied between 4, 6, 8, 10 and 12 mm. For each case, E_{HMI} was calculated.

Phantom Study using 1-D HMIFU system

1-D HMIFU system was first used for polyacrylamide (PA) phantoms The HMI modulus was measured on six PA phantoms (concentrations of 15%, 20%, 25%, 30%, 35% and 40%), and compared to the Young's modulus measured by mechanical testing. For each gel, the same liquid mixture (before cross-linking) used for the construction of HMI phantoms was used to make samples for mechanical testing.

For HMI experiments, parallelepiped-shaped phantoms were prepared (approx. 10cm x 5cm x 5cm). Agar powder (4%) was added to each mixture for scattering. The HMI experimental protocol used here has been described in details previously. The amplitude-modulated (AM) frequency was 20Hz, resulting in an excitation frequency of f=40Hz. The size of the window for displacement estimation was equal to 1.8 mm, with an overlap of 90%. The compressive strain was calculated as the 1D gradient of the axial displacement by using the least square estimator method.

For mechanical testing, cylindrically-shaped samples were prepared for each gel (N=5-8 per gel, diameter = 12mm, thickness = 2.5-3.5 mm) and were tested on an ARES rheometer (TA Instruments, NewCastle, DE, USA). Dynamic analysis was performed at frequencies between 1Hz and 10Hz at ε=0.5% strain. The value of the shear storage modulus $G_{Mech.Test.}$ measured at f=10Hz was chosen as the reference value, and the Young's modulus was obtained by $E_{Mech.Test.} = 3\ G_{Mech.Test.}$ under the assumption of quasi-incompressibility.

Results for 1-D HMI Elastic Modulus Estimation

1) Evaluation of the error under the uniform force assumption

The maximum compressive strain values ε_{zz} were compared in two cases, namely, (1) using the actual force field derived from experimental measurements and (2) using the corresponding modeled force field uniform within the focal region. Figure B1.3 illustrates the strain profile around the focal region (zoomed) for both cases. The two strain distributions were found to be very similar. Compressive strain ε_{zz} was averaged within a ROI of approximately 0.5mm in height and 0.2mm in diameter. The values of ε_{zz} in the uniform case differs from the ε_{zz} measured using the actual force field, but this difference was deemed to be relatively limited (≈ 13% relative error).

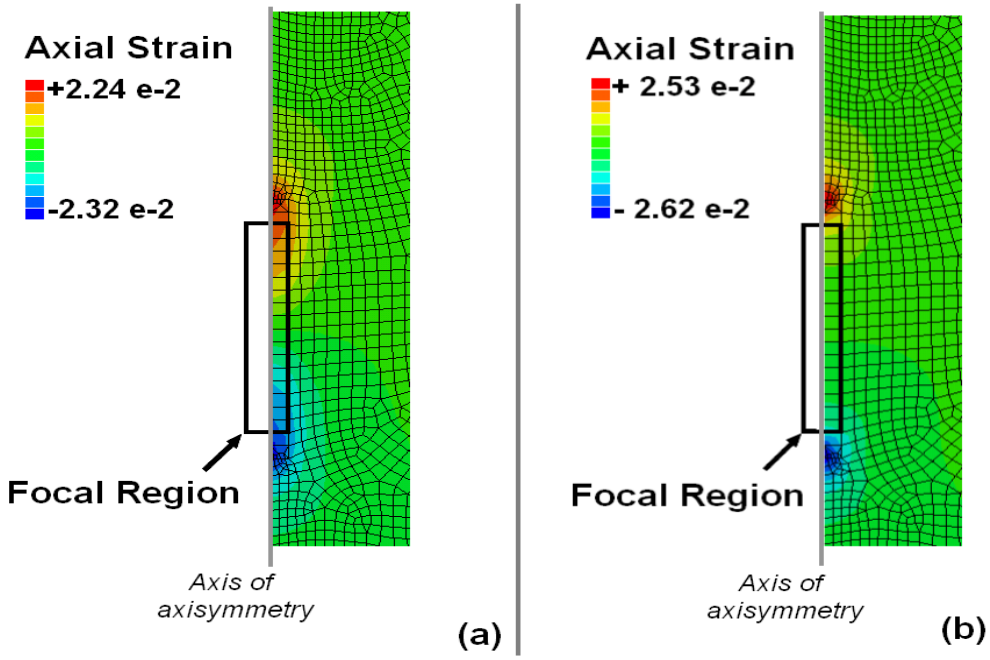

Figure B1.3. Axial strain fields around the focal region for both input force field profiles (a): Actual force field, (b): Corresponding force field modeled as being uniform within the focal region.

2) Correlation between HMI modulus and Young's modulus

Excellent correlation was found between HMI modulus E_{HMI} and the pre-defined Young's modulus E. Figure B1.4 illustrates E_{HMI} versus E for E varying between 0.5 kPa and 20kPa.

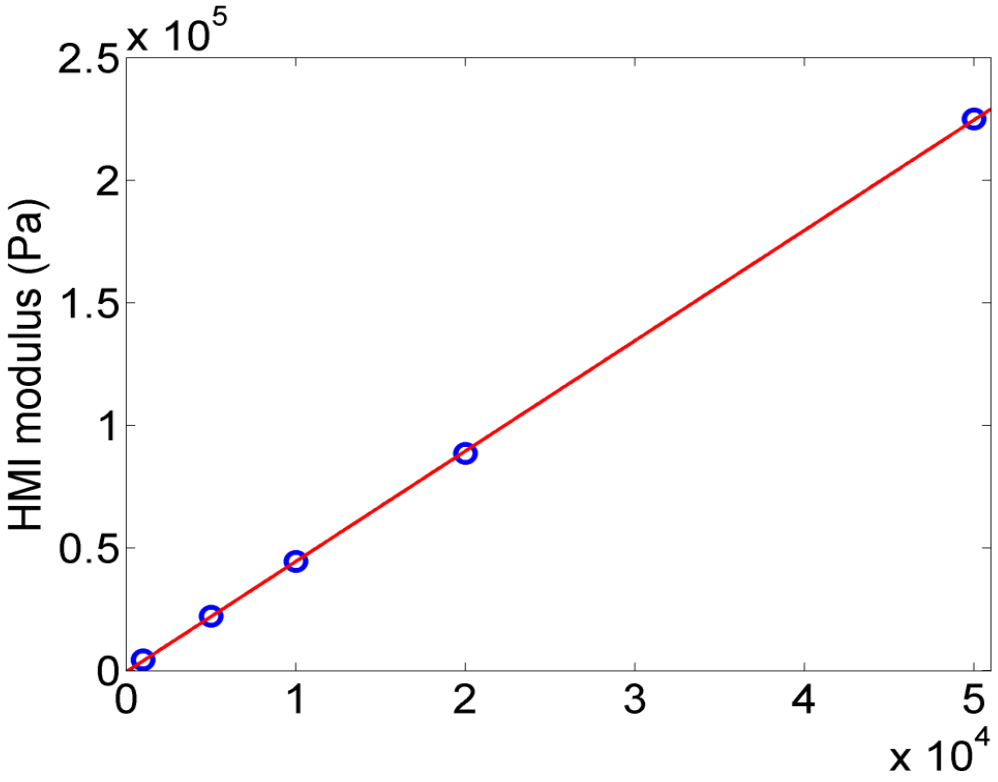

Figure B1.4. HMI modulus versus Young's modulus obtained in the numerical study.

3) Dependence on heterogeneity

The inclusion size was varied between 4mm and 12mm in diameter (focal region height = 4mm). Results are shown in figure 7A1.6. For an inclusion size of 6 mm or higher, the HMI modulus was found to be very similar to the HMI modulus found in the uniform case (average relative difference=12%). For an inclusion size of 4mm, the HMI modulus was found to be significantly different. This shows that E_{HMI} is independent of the inclusion size as long as the inclusion is approximately two times larger than the focal region.

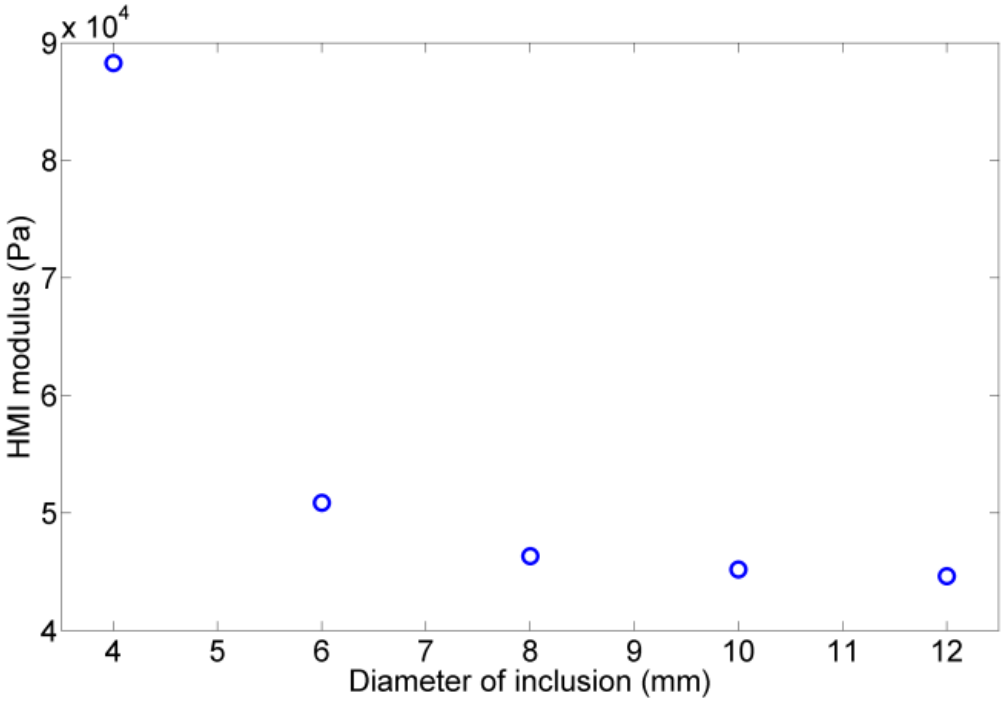

Figure B1.5. HMI modulus obtained when focusing within the inclusion in the case of the heterogeneous numerical phantom.

Phantom Study

Very good correlation ($r^2 = 0.95$) was found between the Young's modulus and the HMI modulus. The average ratio between the two moduli as found to $E_{HMI}/E \approx 2.3$. Figure 7A1.6 illustrates the HMI modulus versus the Young's modulus for the 6 tested gels.

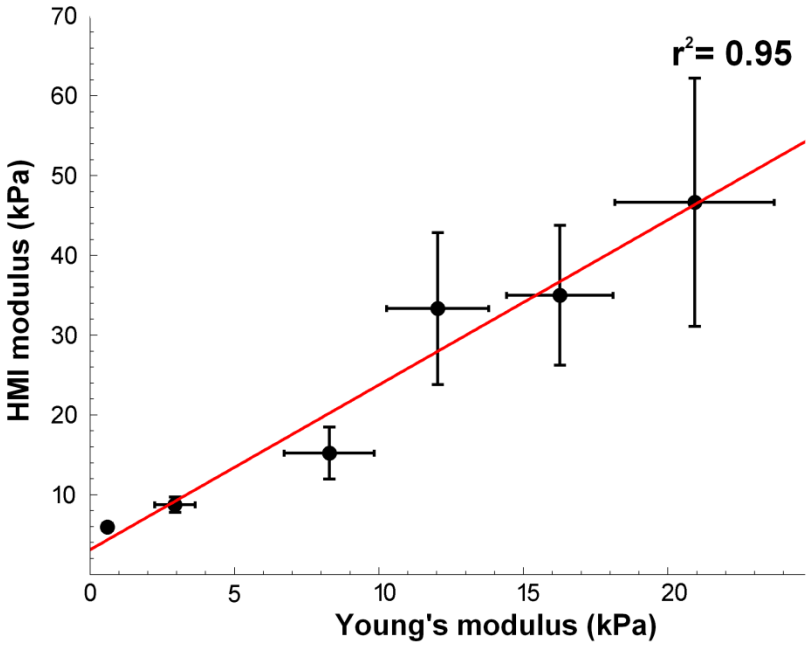

Figure B1.6. HMI modulus measured on polyacrylamide phantom versus Young's modulus measured by mechanical testing on the same gels.

Discussion and Conclusions for 1-D HMI Elastic Modulus Estimation

The numerical study has established the very high correlation between E_{HMI} and E, and has shown the robustness of E_{HMI} as it is independent on the heterogeneity of the medium. In other words, E_{HMI} can be measured locally point-by-point almost independently of the elasticity distribution around this point, as long as the typical heterogeneity size is larger than the focal region (typically > 5mm at 4.5 MHz). Such independency makes the method particularly robust, allowing to map the elasticity of a medium by changing the point of measurement.

Furthermore, phantom experimental results also indicated a high correlation between E_{HMI} and E. The standard deviation of the measurements was significant, especially in the most rigid phantoms (30%, 35% and 40% concentration), where the measured strain values were lower and the SNR was poorer than in softer gels. In order to overcome this uncertainty and enhance the accuracy of the method, the input force can be increased so that the SNR increases as well. However, in this phantom study, the same input force was used for all the phantoms in order to allow direct comparison in the same conditions. Nevertheless, this study has shown on both numerical, physical phantoms a very good correlation between these two values.

Several methods use the acoustic radiation force for estimating mechanical response of biological tissues. For example, Acoustic Radiation Force Impulse Imaging [270] and traditional HMI [189] consist in measuring the tissue displacement resulting from an internal excitation. However, the displacement alone is only a qualitative indicator of tissue elasticity, since it is highly sensitive to boundary conditions and heterogeneity of the medium. Displacement can therefore particularly be useful for certain clinical diagnostic purposes, but it remains limited for biomechanical applications that aim at quantitatively measuring tissue elasticity.

A legitimate question about the proposed method is why measuring a stiffness parameter E_{HMI} that is strongly correlated with but not equal to the actual elasticity, while several shear-wave based methods exist that allow to measure quantitatively the local shear modulus by using the acoustic radiation force, such as Shear Wave Elasticity Imaging [271], Supersonic Shear Imaging [84], and shear wave-based HMI [182]. Although shear wave methods allow in theory to estimate quantitatively viscoelastic properties, they are intrinsically related to the inverse problem and are associated with significant limitations such as wave reflections due to heterogeneity, diffraction, and mode conversion. Moreover, they have important resolution limitations that are directly related to wavelength limitations. Such resolution limitations can be pushed by increasing the excitation frequency, but this is turn brings increased attenuation and decreased SNR. In general, the frequency range that can be effectively used in shear wave based methods is a complex issue, where both physical and inverse problem-related constraints are involved [272]. In contrast, the proposed method measures the local elasticity at a submillimetric scale in a relatively straightforward way. This ability can offer interesting new applications, including the measurement of local elastic properties of small samples or organs. It is interesting to note that the focal size could be decreased even further by using a higher FUS frequency. As mentioned previously, ongoing work is focused on improving both the material property estimation, imaging sequence, and strain estimation algorithm, as well as investigating the relevance of E_{HMI} for therapy monitoring. Another interesting use of the dynamic information can infer to additional information such as viscoelastic properties, as well as their dependence on the excitation frequency.

Appendix C. Poisson's ratio measurement

Methods:

A Digital Image Correlation (DIC) system (Correlated Solutions Inc., SC, USA) was used to measure the surface axial and lateral strain fields under a cyclic uniaxial tension in order to measure the Poisson's ratio. Each axial and lateral strain was considered as the average of strain measurements at 9 different local points on the specimen's surface. The accuracy of DIC measurements was verified under a zero strain field, *e.g.* rigid body motion.

Results:

Figures C.A and C.B show the DIC-based axial and lateral strain fields, respectively, for a representative specimen. The average strain from surface strain fields was used to plot the axial versus lateral strains curves (Figure C.C), whose slope –obtained as the linear fit to data– was taken as the Poisson's ratio, v. The measurements resulted in a $v = 0.49 \pm 0.06$ ($n=6$), which makes the nearly-incompressibility a valid assumption in this study.

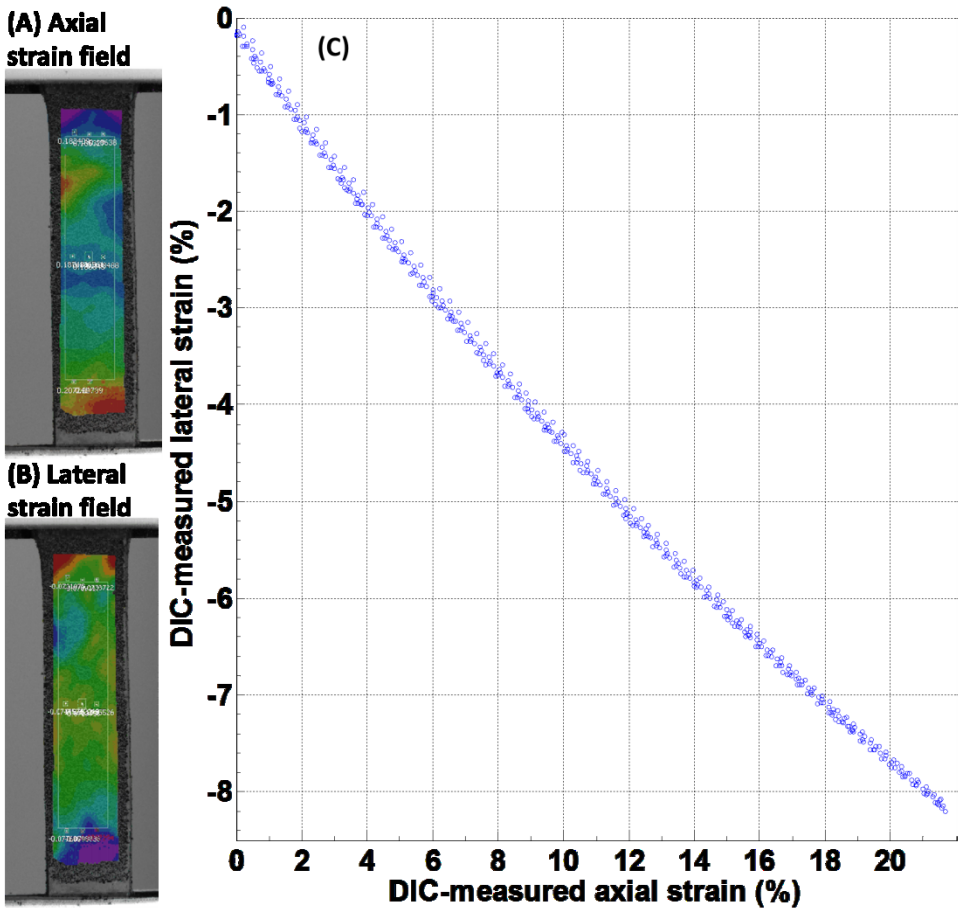

Fig C. Representative surface of (A) axial strain, and (B) lateral strain fields obtained on a phantom specimen; (C) lateral vs. axial strains curves used to compute the Poisson's ratio.

Appendix D. Effects of Frequency and Strain in Rheological measurements

Methods:

Canine liver specimens (N=2) were freshly excised immediately after sacrifice and kept immersed in degassed PBS throughout the experiments *ex vivo*. A 6 *mm* biopsy punch was used to extract a total of eight (n=8) cylindrical samples of height h=5.39±0.71 *mm* and diameter d=5.08±0.24 *mm*. A rheometry mechanical testing machine *(ARES-G2, TA Instrument, DE, USA)* was used to examine the shear behavior of the tissue specimens under two protocols: (a)under constant shear frequency of f=5 *Hz* and a sweeping shear strain of ε=1-10 *%*, and (b)under constant shear strain of ε=1 *%* and a sweeping shear frequency of f=0.1-10 *Hz*. The entire *ex vivo* experiments were completed within 2-3 hours post-mortem. All procedures were approved by the Institutional Animal Care and Use Committee (IACUC) at Columbia University.

Results:

Figure 7A3 shows the variations in dynamic shear modulus and tangent of the phase shift on liver tissue samples for increasing shear strain and frequency, separately. The results show that the liver shear modulus decreases only slightly with increasing strain (Figure. D.A) and can be safely assumed as strain-independent; however, it increases exponentially with increasing shear frequency and therefore it is strain-rate-dependent (Figure. D.C). On the other hand, the tangent of the phase shift is seen to increase with increasing strain (Figure. D.B) –indicating increasing dominance of viscosity over elasticity but it is found to be largely strain-rate-

independent (Figure. D.D). Therefore, further studies are required to investigate the HMI excitation frequency dependence of the strain values.

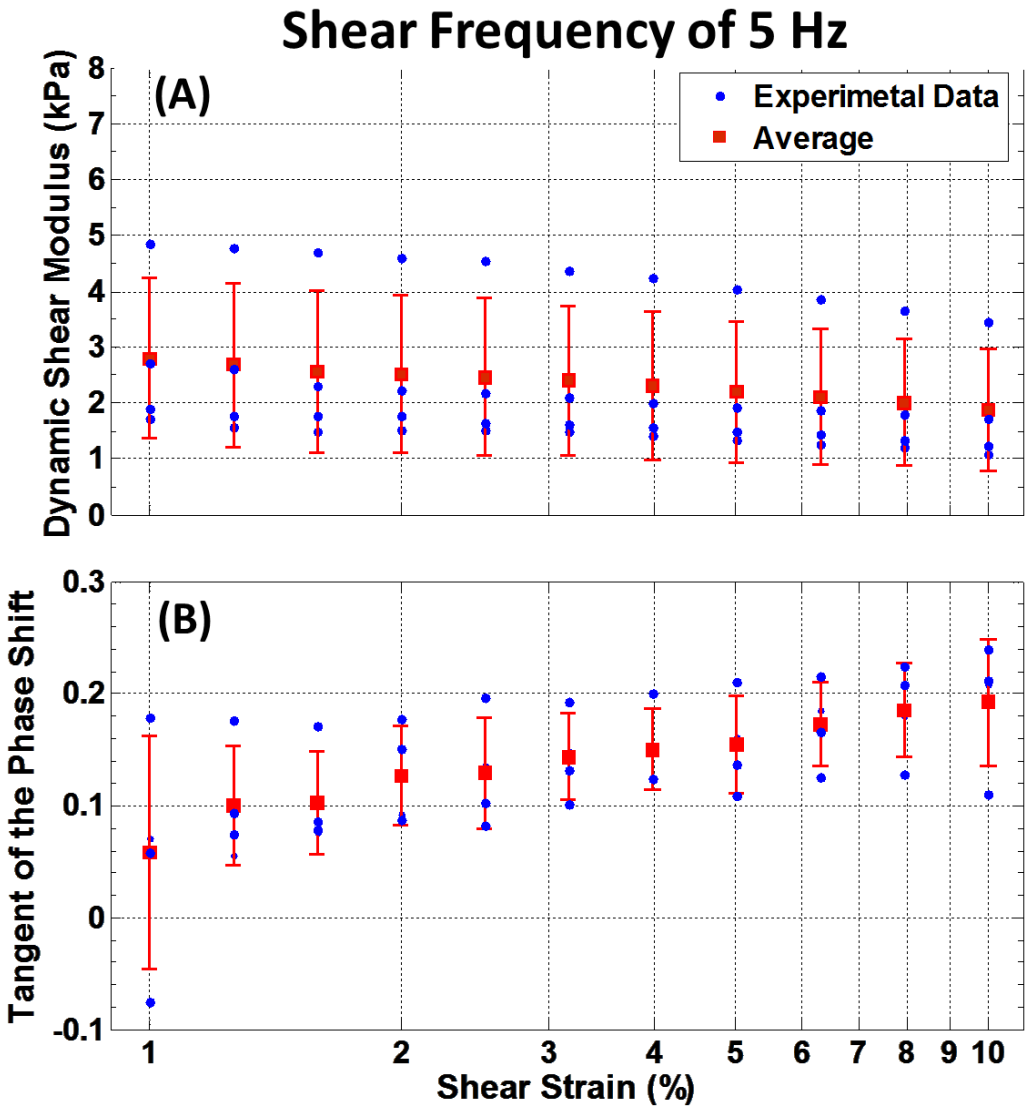

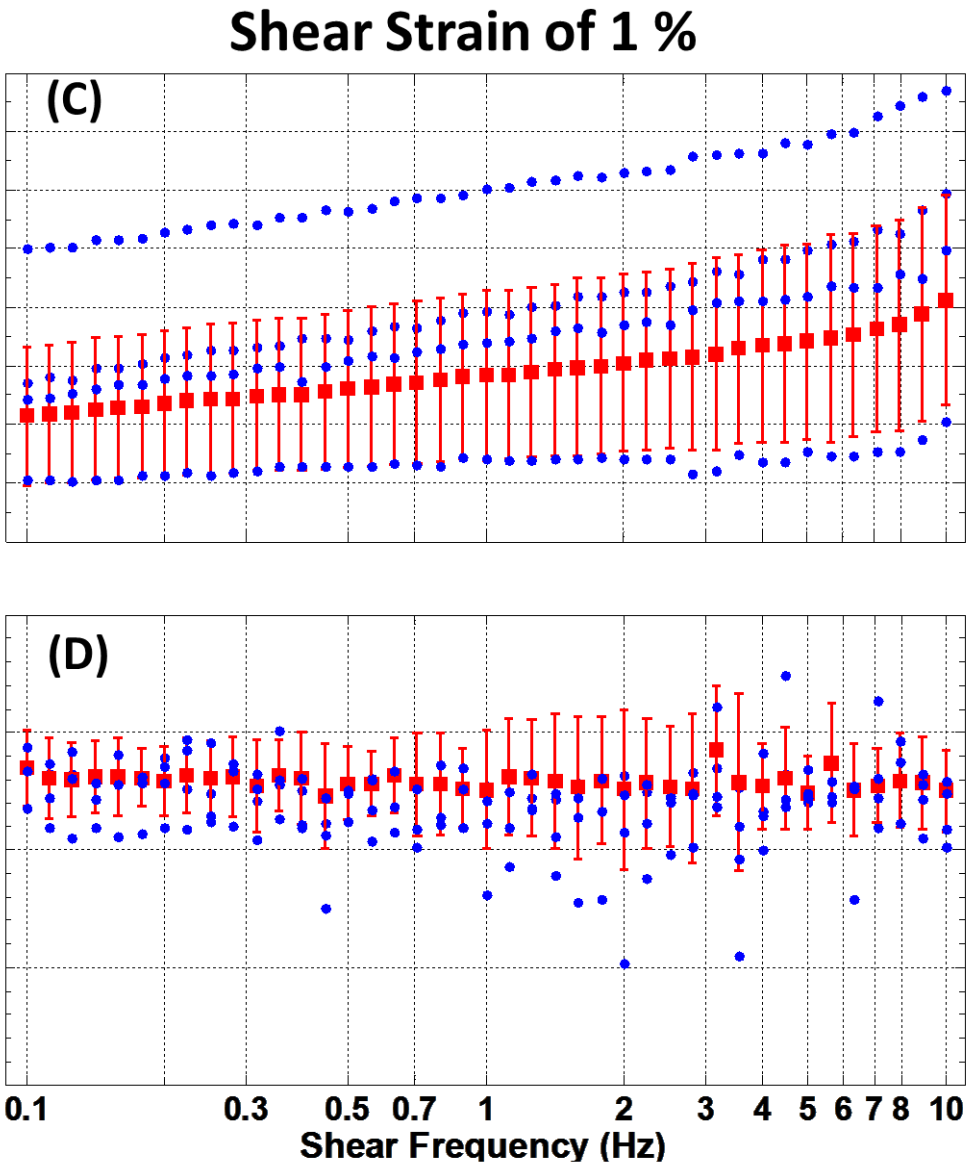

Fig D. Rheometrical measurements on 'dynamic shear modulus' and 'tangent of the phase shift' from canine liver tissue *ex vivo*, tested in a range of (D.A-D.B) Shear Strain and (D.C-D.D) Shear Frequency.